LONG-TERM STRUCTURAL PERFORMANCE MONITORING OF BRIDGES

Phase II: Development of Baseline Model and Methodology for Health Monitoring and Damage Assessment

- Report to the California Department of Transportation –

By

Maria Q. Feng, Professor

Yoshio Fukuda, Post-doctoral Researcher

Yangbo Chen, Serdar Soyoz, and Sungchil Lee, Graduate Students

Department of Civil & Environmental Engineering

University of California, Irvine

October 31, 2006

STATE OF CALIFORNIA · DEPARTMENT OF TRASPORTATION

TECHNICAL REPORT DOCUMENTAION PAGE

TR0003 (REV. 9/99)

1. REPORT NUMBER	2. GOVERNMENT ASSOCIATION NUMBER	3. RECIPIENT'S CATALOG NUMBER
4. TITLE AND SUBTITLE LONG-TERM STRUCTURAL PERFORMANCE MONITORING OF BRIDGES		5. REPORT DATE October, 2006 6. PERFORMING ORGANIZATION CODE UC Irvine
7. AUTHOR Maria Q. Feng, Yoshio Fukuda, Yangbo Chen, Serdar Soyoz, and Sungchil Lee		8. PERFORMING ORGANIZATION REPORT NO.
9. PERFORMING ORGANIZATION NAME AND ADDRESS Civil and Environmental Engineering E4120 Engineering Gateway University of California, Irvine Irvine, CA 92697-2175		10. WORK UNIT NUMBER 11. CONTACT OR GRANT NUMBER
12. SPONSORING AGENCY AND ADDRESS California Department of Transportation (Caltrans) Sacramento, CA		13. TYPE OF REPORT AND PERIOD COVERED Final Report 14. SPONSORING AGENT CODE

15. SUPPLEMENTARY NOTES

16. ABSTRACT

This project explores the use of the sensor technology for long-term bridge structural health monitoring. In Phase I of the project, sensors were installed on two highway bridges, and vibration data analysis was reported in a Catlrans technical report. In this Phase-II study, an additional highway bridge was instrumented, but the focus was on to develope methodologies for analyzing the sensor data and diagnosing the on-going "health" of the structure. Stiffness of structural elements of a bridge is considered as an indicator of structural "health". As a structure deteriorates due to aging or suffers from damage caused by extreme loads such as earthquakes, stiffness of the damaged structural elements would decrease, and as a result, the global vibration characteristics of the structure would change. Therefore, by monitoring the structural vibration, one can identify the change in structural vibration characteristics and then further identify the element stiffness. A number of system identification methods were developed in this study for identifying the structural element stiffness based on measurement of bridge vibrations caused by traffic and seismic excitations. A unique traffic excitation model was proposed for more reliable stiffness identification based on traffic-induced vibrations. The effectiveness of these methods in evaluating seismic damage on a bridge structure was demonstrated through seismic shaking table tests of a multi-bent multi-column concrete bridge model. Long-term monitoring data from the instrumented bridges were analyzed and developed into a structural stiffness database using a software platform developed in this study.

17. KEYWORDS	18. DISTRIBUTION STATEMENT	
Structural Health Monitoring, Stiffness Identification, Database, Shaking table test	No restrictions.	
19. SECURITY CLASSIFICATION (*of this report*) Unclassified	20. NUMBER OF PAGES	21. COST OF REPORT CHARGED

DISCLAIMER: The contents of this report reflect the views of the authors who are responsible for the facts and the accuracy of the data presented herein. The contents do not necessarily reflect the official views or policies of the State of California or the Federal Highway Administration. This report does not constitute a standard, specification or regulation.

The United States Government does not endorse products or manufacturers. Trade and manufacturers' names appear in this report only because they are considered essential to the object of the document.

SUMMARY

This project explores the use of the sensor technology for long-term bridge structural health monitoring. In Phase I of the project, accelerometers and other types of sensors were installed on two new highway bridges in Orange County, CA, and vibration measurement data were analyzed, as reported to Caltrans by Feng and Kim (2001). In this Phase-II study, an additional highway bridge was instrumented with sensors, but the focus is on the development of methodologies for analyzing the vibration data gathered by the sensors and, based on the results, diagnosing the on-going "health" of the structure. In this study, the stiffness of structural elements of the bridge structure is considered as an indication of structural "health". As a structure deteriorates due to aging or suffers from damage caused by extreme loads such as earthquakes, stiffness of the damaged structural elements would decrease, and as a result, the global vibration characteristics of the structure would change. Therefore, by monitoring the structural vibration, one can identify the change in structural vibration characteristics and furthermore change in element stiffness. As the change exceeds certain threshold, the structure is considered damaged. Identification of structural stiffness enables assessment of not only extent but also locations of structural damage. A stiffness established when the structure is new can be used as a baseline for long-term structural health monitoring. The baseline based on vibration measurement can also be used for verifying the design of the structure.

In this report, Chapter 1 provides background information for the project and Chapter 2 a literature review on the sensor-based monitoring technology. Chapter 3 describes

the installation of sensors, data logs, and communication devices on the three highway bridges. Chapter 4 presents acceleration data recorded at the instrumented bridges including traffic- and earthquake-induced vibration data, including 1712 sets of traffic-induced vibration data collected at the Jamboree Road Overcrossing. Chapter 5 presents measured strain data and comparison between the results obtained from strain and acceleration data analyses.

Chapter 6 develops a number of methods and algorithms for identifying element stiffness of a bridge structure based on vibration measurement. The chapter is divided into two sections: one focuses on bridge super-structures and the other on bridge sub-structures (columns). The super-structure stiffness is identified based on traffic excitations, while sub-structure stiffness is identified by earthquake excitations for the purpose of seismic damage assessment and thus nonlinear identification methods become necessary. A Bayesian updating method and a neural network method were developed for identifying super-structure stiffness based on traffic-induced vibration measurement. In this regard, an innovative traffic excitation model was proposed in this study that is more realistic and thus reliable than the conventional white noise model because of the use of available traffic information from video monitoring. For identifying bridge column stiffness, the neural network method and the extended Kalman filter method were formulated based on earthquake vibration data. These system identification methods can also be categorized as frequency-domain and time-domain methods. Some of these methods can be performed online in real time and deal with nonlinear structural response.

Chapter 7 presents experimental validation of the system identification methods developed in Chapter 6. Two shaking table tests were performed on large-scale concrete bridge models involving multiple bents and multiple columns, progressively inducing seismic damage to the models. The stiffness reduction at the bridge columns

identified based on the measured vibration data is consistent with the actual damage, in terms of the damage extents and locations. These shaking table tests represent the first effort in experimentally validating such damage identification methods using realistic structural models suffering from realistic seismic damage.

In Chapter 8, a vibration test under controlled traffic excitation was performed on one of the instrumented bridges, and the results were compared with those obtained from a similar test performed when the bridge was new. Chapter 9 develops a database for modal frequencies and furthermore for element stiffness values for each of the instrumented bridges based on vibration measurement. The stiffness values were identified using the neural network-based system identification method, and the results are consistent with those identified by the other methods presented in Chapter 6. Variations in the identified frequencies (as large as +/-10%) and in stiffness values (as large as 6%) for one of the bridges were observed over a four-year period, due to change in environmental conditions. From the element stiffness database, it is observed that the superstructure stiffness identified from vibration measurement fluctuates around 95% of the design values, while the column stiffness is 85% of the design value. Similar observations were made for the other two bridges. The stiffness database serves as the baseline for long-term monitoring.

Chapter 10 describes a software platform developed in this project based on the stiffness identification methods developed in this study for automated data processing, analysis, stiffness identification, baseline updating, and database development. Finally, Chapter 11 summarizes the conclusions made in this project and suggests important topics for future study such as estimation of remaining capacity of bridges based on stiffness evaluation.

List of Figures

Figure 1.1.1 Visual Inspection

Figure 3.1.1 Sensors on JRO

Figure 3.1.2 Web Pages of the Wireless Bridges

Figure 3.1.3 Directional Antennas

Figure 3.1.4 TS-Terminal Software

Figure 3.1.5 Server Software

Figure 3.1.6 Java Applet – Client Software

Figure 3.1.7 Battery Box

Figure 3.2.1 Configuration of Wireless Transmission

Figure 3.3.1 Location of the FROO

Figure 3.3.2 Plan view of the FROO

Figure 3.3.3 Elevation of the FROO

Figure 3.3.4 Bearing at Abutment 1

Figure 3.3.5 Typical Cross-section of the Box-girder

Figure 3.3.6 Schematic Layout of the Accelerometers

Figure 3.3.7 Picture of a Uni-axial Accelerometer

Figure 3.3.8 Pictures of a Bi-axial Accelerometer

Figure 3.3.9 Pictures of a Tri-axial Accelerometer

Figure 3.3.10 Pictures Accelerometers Mounted in the Box-girder

Figure 3.3.11 Picture of the Data-logger Container and the Junction Box

Figure 3.3.12 Data-logger and the Strain Meter Conditioner in the Container

Figure 3.3.13 Accelerometer Splicing in the Junction Box

Figure 3.3.14 LVDT Type Strain Meters Installation

Figure 3.3.15 Position of the Strain Meters on the Deck

Figure 3.3.16 Strain Meter Splicing in the Junction Box

Figure 3.3.17 Conventional Strain Gauge and LVDT Strain Meter installed in Column 3

Figure 3.3.18 Conventional Strain Gauges Installed in Footings

Figure 3.3.19 Installation of Signal Box for Conventional Strain Gauges

Figure 3.3.20 Soil Pressure Sensor

Figure 3.3.21 Backfilling at Abutment 1

Figure 3.3.22 Displacement Sensor

Figure 3.3.23 Thermocouple and Signal Conditioner

Figure 3.3.24 Thermocouple Wiring Map

Figure 3.3.25 Map of Channel Assignment of the Data-logger

Figure 4.1.1 Traffic-Induced Vibrations Saved at JRO

Figure 4.1.2 Traffic-Induced Vibrations Streamed at JRO

Figure. 4.2.1 Instrumental Intensity Map by Shake-Map

Figure 4.2.2 Earthquake Response Records at JRO

Figure 4.3.1 Traffic-Induced Vibrations Saved at WSO

Figure 4.4.1 Ground Motion of a Moderate Earthquake at WSO

Figure 4.5.1 Traffic-Induced Vibrations Saved at FROO

Figure 5.1.1 Strain Gauge Locations of WSO

Figure 5.2.1 Influence Line for R1 and R10

Figure 5.2.2 Strain Time History of R1

Figure 5.2.3 Strain Time History of R10

Figure.5.2.4 Influence Line of R2

Figure. 5.2.5 Influence Line of R3

Figure.5.2.6 Strain Time History of R2

Figure. 5.2.7 Strain Time History of R3

Figure.5.2.8 Influence Line of R4

Figure.5.2.9 Strain Time History of R4

Figure. 5.2.10 Strain Time History of R5

Figure.5.2.11 Strain Time History of R6

Figure. 5.2.12 Influence Line of R7

Figure. 5.2.13 Influence Line of R8 and R9

Figure. 5.2.14 Strain Time History of R7

Figure. 5.2.15 Strain Time History of R8

Figure. 5.2.16 Strain Time History of R9

Figure.5.3.1 Maximum Strain of R1 and R10

Figure. 5.3.2 Maximum Strain of R2 and R3

Figure. 5.3.3 Maximum and Minimum Strain of R4

Figure. 5.3.4 Maximum Strain of R5 and Minimum Strain of R6

Figure. 5.3.5 Maximum Strain of R6 and Minimum Strain of R5

Figure. 5.3.6 Minimum Strain of R7

Figure. 5.3.7 Maximum Strain of R8 and R9

Figure. 5.3.8 Finite Element Model of WSO

Figure. 5.3.9 HS 20-44 Load

Figure. 5.3.10 Lanes for Moving Load Analysis

Figure. 5.3.11 Strain R1 and R10 due to Vehicle Locations

Figure. 5.3.12 Strain R2 and R3 due to Vehicle Locations

Figure. 5.3.13 Strain R4 due to Vehicle Locations

Figure. 5.3.14 Strain R5 due to Vehicle Locations

Figure. 5.3.15 Strain R6 due to Vehicle Locations

Figure. 5.3.16 Strain R7, R8, and R9 from Finite Element Analysis

Figure. 5.3.17 Long-term Monitored Data of R5

Figure. 5.3.18 Monitored Time Histories and Their Power Spectral Density (6/28/2006)

Figure. 5.3.19 Third Mode Shape (Transverse Direction)

Figure. 5.3.20 The Fourth Mode Shape (Transverse Direction)

Figure 6.2.1 System Identification Methodologies

Figure 6.3.1 Beam-Moving Force Model

Figure 6.3.2 ENFs at Node i.

Figure 6.3.3 Geometry of a FE Model

Figure 6.3.4 $\mathrm{cov}[F_1^Q(t)F_i^Q(s)]$ for Case 1: γ =2 /s, SP = 1, μ_v = 20 m/s, σ_v = 5 m/s

Figure 6.3.5 $\mathrm{cov}[F_1^Q(t)F_i^Q(s)]$ for Case 2: γ =2 /s, SP = 1, μ_v = 30 m/s, σ_v = 5 m/s

Figure 6.3.6 $\mathrm{cov}[F_1^M(t)F_i^Q(s)]$ for Case 1: γ =2 /s, SP = 1, μ_v = 20 m/s, σ_v = 5 m/s

Figure 6.3.7 $\mathrm{cov}[F_1^M(t)F_i^Q(s)]$ for Case 2: γ =2 /s, SP = 1, μ_v = 30 m/s, σ_v = 5 m/s

Figure 6.3.8 Distortion of the Response Spectrum

Figure 6.3.9 Captured Video Images of a Vehicle Traveling on the Bridge

Figure 6.3.10 Infer Parameters from Traffic Video Information

Figure 6.3.11 Sensor System and Finite Element Model of JRO

Figure 6.3.12 Elements from Excitation Covariance $\mathbf{\Sigma}^F(t)$

Figure 6.3.13 Element of Predicted Response Covariance $\mathbf{\Sigma}_1^Y(t-s)$

Figure 6.3.14 Element of Experimental Response Covariance $\mathbf{\Sigma}_{ex}^Y(t-s)$

Figure 6.3.15 Results Using 0-60 Second Data

Figure 6.3.16 Results Using Entire 0-360 Second Data

Figure 6.3.17 Distribution of β at Selected Instants

Figure 6.4.1 Architecture of the Neural Network

Figure 7.1.1 Layout of the Specimen in Experiment 1

Figure 7.1.2 Reinforcement Details of the Specimen in Experiment 1

Figure 7.1.3 Schematic Plot of Experiment 1

Figure 7.1.4 Damage at Flared Portion of Columns

Figure 7.1.5 Design of the Bridge Specimen in Experiment 2

Figure 7.1.6 Design of the Post-tension Ducts in Experiment 2

Figure 7.1.7 Design of the Three Bents in Experiment 2

Figure 7.1.8 Illustration of Experiment 2

Figure 7.1.9 Schematic Plot of the Sensor Layout in Experiment 2

Figure 7.1.10 Damage Observed at a Column of Bent 1

Figure.7.1.11 Strain Measurements at Bent-3 During Test 14

Figure 7.2.1 Measured Acceleration Responses at Ch-5 to Ambient Excitations

Figure 7.2.2 Peak-Picking of Power Spectrum Density Functions

Figure 7.2.3 Free vibration II (after 100% Sylmar) and Its Time-frequency Plot

Figure 7.2.4 Simulated and Measured Responses for 15% Sylmar Motion

Figure 7.2.5 Acceleration Responses at Ch-4 to White Noise Disturbances at Various Damage Stages

Figure 7.2.6 Simulated and Measured Ch-4 Responses for WN-X-2 Motion

Figure 7.2.7 Simulated and Measured Ch-4 Responses for WN-X-5 Motion

Figure.7.3.1 Fourier Spectral Results Obtained from White Noise Input

Figure 7.3.2 Sensor Locations and System Identification Methodology

Figure 7.3.3 Time History Portion Used for the Identification

Figure 7.3.4 Identified Natural Frequency with Different Starting Points of the Ending Portion

Figure 7.3.5 Identified Natural Frequencies Using End Portions

Figure.7.3.6 Schematic View of Finite Element Model

Figure.7.3.7 Comparison of Responses at DOF 10 for T-13

Figure.7.3.8 Stiffness Reduction During T-13

Figure.7.3.9 Comparison of Responses at DOF 10 for T-13 (Filtered)

Figure.7.3.10 Stiffness Reduction During T-14

Figure.7.3.11 Stiffness Reduction During T-15

Figure.7.3.12 Stiffness Reduction During T-19

Figure.7.3.13 Comparison of Responses at DOF 10 for Test-19

Figure 8.1.1 Test Vehicle Locations in Transverse Direction

Figure 8.1.2 Test Vehicle Locations in Longitudinal Direction

Figure 8.1.3 Axle Load of the Test Vehicle

Figure 8.1.4 Strain Time History of All Sensors

Figure 8.2.1 Exciting Force Location of Braking and Bumping Test

Figure 8.2.2 Locations of Fiber Optic Accelerometers

Figure 8.2.3 Acceleration Time History from Braking Test

Figure 8.2.4 PSD from Conventional Accelerometer

Figure 8.2.5 PSD from Fiber Optic Accelerometer

Figure 8.2.6 Mode Shape from Braking Test (Vertical Direction)

Figure 8.2.7 Mode Shape from Braking Test (Transverse Direction)

Figure 8.2.8 Time History of Acceleration of A10

Figure 8.2.9 Time History of Acceleration of A3

Figure 8.2.10 Time History of Acceleration of A5

Figure 8.2.11 PSD from Bumping Test

Figure 8.3.1 Time History of Strain at R3

Figure 8.3.2 Time History of Strain at R5

Figure 8.3.3 Time History of Strain at R8

Figure 8.3.4 Time History of Acceleration at A10

Figure 8.3.5 Time History of Acceleration at A5

Figure 8.3.6 Time History of Acceleration at A3

Figure 9.1.1 First Modal Identification Results

Figure 9.1.2 Second Modal Identification Results

Figure 9.1.3 Third Modal Identification Results

Figure 9.1.4 Fourth Modal Identification Results

Figure 9.1.5 Distribution of Data Recording Time

Figure 9.1.6 Typical Traffic-induced Accelerations in Middle of Spans 1 and 2

Figure 9.1.7 Mode Frequency Change at WSO

Figure 9.1.8 Ground Motion of the Yucaipa Earthquake

Figure 9.1.9 Frequency Response Functions of WSO under Earthquake

Figure 9.1.10 Finite Element Model for FROO

Figure 9.1.11 Mode Shapes of FROO

Figure 9.1.12 Typical Traffic-induced Accelerations

Figure 9.1.13 Mode Frequency Change at FROO

Figure. 9.1.14 Acceleration Time History of the FROO

Figure. 9.1.15 PSD from All Acceleration Channels

Figure. 9.1.16 PSD from Vertical Acceleration Channels

Figure. 9.1.17 PSD from Transverse Acceleration Channels

Figure 9.2.1 Architecture of the Neural Network

Figure 9.2.2 Column Stiffness Correction Coefficient

Figure 9.2.3 Superstructure Stiffness Correction Coefficient

Figure 10.1.1 Major Functions of the Software

Figure 10.1.2 Bridge Selection Window

Figure 10.1.3 Bridge Selection Window

Figure 10.1.4 Main Interface for the Software

Figure 10.2.1 Data Format Conversion Window

Figure 10.2.2 Time History Display Window

Figure 10.2.3 Data Combination Window

Figure 10.2.4 FDD Analysis Window

Figure 10.2.5 Neural Network Analysis Window

Figure 10.2.6 Animation Window

Figure 10.2.7 Location Map Window

Figure 10.2.8 Sensor Configuration Window

Figure 10.2.9 File Naming Window

List of Tables

Table 3.3.1 Installation of Accelerometers

Table 3.3.2 Splicing and Wiring Map

Table 4.1.1 Summary of Triggered Data on the JRO

Table 4.1.2 Summary of Streamed Data on the JRO

Table 4.3.1 Summary of Triggered Data on the WSO

Table 4.4.1 Peak Ground Motion at the WSO

Table 4.5.1 Summary of Collected data on the FROO

Table 5.1.1 Strain Gauge Specification

Table 5.3.1 Measured Strain

Table 5.3.2 Strain from Measurement and Analysis

Table 6.3.1 Traffic Information Extracted from the Video Images

Table 7.1.1 Test Procedure

Table 7.2.1 Damping Ratios ζ

Table 7.2.2 Identified Correction Coefficients

Table 7.2.3 Comparison of the Modal Characteristics

Table 7.2.4 Identified Correction Coefficients

Table 7.3.1 Comparison of Identified Natural Frequency Using White Noise and End Portions

Table 7.3.2 Finite Element Model Calibration

Table.7.3.3 Comparison of First Modal Frequency

Table 8.1.1 Test Vehicle Locations in Longitudinal Direction

Table 8.1.2 Measured Strain from Static Test

Table 8.1.3 Computed Maximum Strain

Table 8.2.1 Mode Frequency from Braking Test

Table 8.2.2 Mode Frequency from Bumping Test

Table 8.3.1 Dynamic Load Cases

Table 8.3.2 Measured Dynamic Strain

Table 8.3.3 Comparison of Strain

Table 9.1.1 Modal Frequencies from Controlled Vibration Test

Table 9.1.2 Modal Frequencies Identified from Ambient Vibration Records

Table 9.1.3 Modal Frequencies Identified from the Yucaipa Earthquake

Table 9.1.4 Modal Frequencies of FROO

Table 9.1.5 Mode Frequencies Identified from Ambient Vibration Records

Table 9.2.1 Moments of Inertia of JRO

Table 9.2.2 Moments of Inertia of WSO

Table 9.2.3 Spring Stiffness of Abutment Boundary Conditions

Table 9.2.4 Training Patterns for the WSO

Table 9.2.5 Verification of Trained Neural Network

Table 9.2.6 Modal Frequencies Identified from Ambient Vibration Records

Table 9.2.7 Updated Moment of Inertia of Column and Superstructure

Table 9.2.8 Updated Spring Stiffness of Abutment Boundary Conditions

TABLE OF CONTENTS

TECHNICAL REPORT PAGE…….....ii

DISCLAMER……..……...iii

SUMMARY…….…….....iv

LIST OF FIGURES……viii

LIST OF TABLES…….…….xvi

TABLE OF CONTENTS……..…….....xviii

1. INTRODUCTION……..…….....1

1.1 Vibration-Based Bridge Structural Health Monitoring: Concept and Advantages…….……..1

1.2 Objective and Scope……...…5

1.3 Overview of Phase-I Work and Phase-II Report……6

2. LITERATURE REVIEW…….…….8

3. MONITORING SYSTEM INSTALLATION AND UPGRADES…….15

3.1 Upgrades of Phase-I JRO Monitoring System……15

3.1.1 Addition of Temporary Sensors……..15

3.1.2 Installation of Wireless Remote Data Acquisition System…….16

3.1.3 Development of Communication Software TS-Terminal……...20

3.1.4 Development of Server/Client Solution for Real-Time Internet Waveform Display and Data Acquisition…….….21

3.1.5 Power System Upgrade……..…….22

3.2 Upgrades of Phase-I WSO Monitoring System……...23

3.3 Instrumentation of the 3rd Bridge: FROO…….24

3.3.1 Bridge Description……..24

3.3.2 Monitoring System Design and Installation……29

4. VIBRATION DATA……...47

4.1 Ambient Vibration Data on JRO……..48

4.1.1 Triggered Data……...……..48

4.1.2 Streamed Data……..……...49

4.2 Moderate Earthquake on JRO……..…51

4.3 Ambient/Traffic-Induced Vibration on WSO……..53

4.4 Moderate Earthquake on WSO…….53

4.5 Ambient Vibration Data on FROO……..55

5. STRAIN DATA AND ANALYSIS…….57

5.1 Strain Sensors and Locations…….57

5.2 Characteristics of Dynamic Strain Data…….59

5.2.1 R1 and R10……59

5.2.2 R2 and R3……..60

5.2.3 R4, R5 and R6……...62

5.2.4 R7, R8 and R9……...64

5.3 Comparison of Measured and Computed Strain……...66

5.3.1 Measured Maximum Strain……..66

5.3.2 Finite Element Analysis under Design Live Load……...72

5.3.3 Comparison of Strain Data……...80

5.4 Summary……...84

6. DEVELOPMENT OF STRUCTURAL HEALTH MONITORING METHODOLOGIES……..…..85

6.1 Definition of Structural Health and Damage……85

6.2 System Identification Methodologies……...86

6.3 Traffic Excitation Modeling and Super-Structure Condition Assessment…...89

6.3.1 Output only System Identification……89

6.3.2 Physical Formulation of Traffic Loads on a Bridge……...91

6.3.3 Traffic Excitation Covariance Model……95

6.3.4 Distortion on the Response Spectrum due to Spatially Correlated Excitation……...…...101

6.3.5 Video Based Traffic Monitoring and Processing……104

6.3.6 Structural Condition Assessment……..……...106

6.3.6.1 Bayesian Updating……..….107

6.3.6.2 Estimation of Response Covariance Matrix……111

6.3.6.3 Validation on a Test-bed Bridge…….....112

6.3.7 Summary……..118

6.4 Sub-Structure Condition Assessment……121

6.4.1 Frequency Domain Identification……121

6.4.1.1 Least Squares Estimation for Modal Parameters…….121

6.4.1.2 Neural Network Based Identification……...123

6.4.2 Time Domain Identification…….125

6.4.2.1 Least Squares Estimation for Structural Parameters……125

6.4.2.2 Extended Kalman Filter Based Identification……..126

7. EXPERIMENTAL VERIFICATION OF METHODOLOGIES……..131

7.1 Large-Scale Shake Table Test Verification……131

7.1.1 Two Column Bent Test (Experiment 1)……131

7.1.2 Full Bridge Test (Experiment 2)……...134

7.2 Damage Identification Based on Low-Level Excitation……140

7.2.1 Frequency Domain Identification…….141

7.2.2 Time Domain Identification…….143

7.2.2.1 Experiment 1……...143

7.2.2.2 Experiment 2……...145

7.3 Damage Identification Based on Earthquake Excitations…….149

7.3.1 Frequency Domain Identification……149

7.3.1.1. Frequency Domain Identification Using White Noise Input..149

7.3.1.2. Frequency Domain Identification Using Ending Portions of Earthquake Motions……..…….150

7.3.2 Time Domain Identification……....154

8. FIELD TEST ON WEST STREET ON-RAMP……161

8.1 Static Load Test……161

8.1.1 Load Cases……..161

8.1.2 Test Vehicle…….163

8.1.3 Static Test Results and Comparison with Analysis……163

8.2 Braking and Bumping Tests……..165

8.2.1 Test Procedure…….166

8.2.2 Braking Test Results……...166

8.2.3 Bumping Test Results…….172

8.3 Dynamic Load Test……...174

8.3.1 Dynamic Load Cases……...174

8.3.2 Dynamic Strain Results……...174

8.3.3 Mode Frequency……..177

9. DEVELOPMENT OF DATABASE…….179

9.1 Database for Modal Parameters……..179

9.1.1 JRO……179

9.1.2 WSO……..182

9.1.3 FROO……189

9.1.3.1 Finite Element Modeling and Analysis…….189

9.1.3.2 Ambient Vibration Data and Modal Frequency Identification.192

9.2 Database for Structural Parameters…….197

9.2.1 JRO……199

9.2.2 WSO……...201

9.3 Summary and Design Recommendations……206

10. DEVELOPMENT OF SOFTWARE……207

10.1 List of Software Modules…….207

10.2 Description of Usage of Modules…….211

11. CONCLUSIONS AND RECOMMENDED FUTURE WORK….....216

11.1 Conclusions…….217

11.2 Recommended Future Work……219

REFERENCES……...……220

Chapter 1

INTRODUCTION

This chapter first describes motivations of this research project on long-term performance monitoring of Caltrans highway bridges, by introducing the concept of vibration-based highway bridge structural health monitoring and its potential advantages. Then, this chapter summarizes the overall scope of this two-phased project. As this is the second report focusing on the Phase-II research, the work accomplished in Phase I of this project will then be briefly reviewed.

1.1 Vibration-Based Bridge Structural Health Monitoring: Concept and Advantages

Structural condition assessment of highway bridges has long relied on visual inspection (Fig. 1.1.1, courtesy of FHWA), which involves subjective judgment of inspectors and detects only local and visible flaws. The frequency of visual inspection and the qualification of the inspectors are regulated by a standard, the National Bridge Inspection Standards (NBIS 1996). And the Federal Highway Administration (FHWA) Recoding and Coding Guide (FHWA, 1995) was also provided to guide the procedure including the condition ratings and the documentation in current practice. Even with these provisions, a recent investigation initiated by FHWA to examine the reliability of visual inspections reveals significant

variability in the structural condition assignments by inspectors (Phares et al., 2004). Moreover, visual inspection cannot quantitatively evaluate the strength and/or deformation capacity reservation of a bridge. Local defects or flaws might or might not have a significant effect on the bridge global performance.

Figure 1.1.1 Visual Inspection

Sensor-based structural health monitoring can revolutionize the traditional way we inspect structures, in a more timely, objective, and quantitative fashion. By installing appropriate sensors at critical locations on a bridge structure, transmitting the sensor data through a communications network, and analyzing the data through a software platform, the location and severity of bridge deterioration and damage can be automatically, remotely, and rapidly assessed, without sending inspection crews to the site. As the sensor, networking, and communication technologies advance, the sensor-based structural health monitoring (SHM) has become an intensively investigated subject (e.g., Aktan et al, 1997; Doebling et al, 1998, Feng and Kim, 1998, Feng and Bhang, 1999, Aktan et al, 2000; Park, et al, 2001, Peeters et al, 2001,

Catbas and Aktan, 2002; Chang and Liu, 2003; Chen and Feng, 2003, Kim, et al, 2003, Sohn, et al, 2003, Feng, et al, 2004).

In addition to the potential benefits to bridge inspection and maintenance, sensor-based monitoring results can also be used to verify the current bridge design approaches and suggest future improvement. The monitoring results can be used for making more scientific decisions in terms of prioritization of bridges for structural retrofit and strengthening. Furthermore, the sensor-based continuous monitoring will potentially enable real-time and remote post-event damage assessment of highway bridges and early warning, significantly improving emergency response operations.

As a branch of the wide-ranging subjects in SHM research, many researchers seek to measure the structural vibration behavior (dynamic response of a structure with or without measuring the exerting excitations), and infer from the vibration data the level of structural global and/or local integrity. This is partially because vibration sensors (such as accelerometers) can be easily attached to the surface of an existing structure, compared with other sensors (such as strain sensors) that require embedment during the construction (for concrete structures). The concept of vibration-based SHM comes from a fact that, when the structure is subjected to damage or deterioration, the stiffness of some structural components or the support conditions will change, and as a result, the global vibration characteristics of the structure will change accordingly. Therefore, by monitoring the vibration and detecting changes in the vibration characteristics, and further interpreting such changes in terms of element stiffness changes, one can assess quantitatively the structural health condition. Besides its global and quantitative natures, vibration

monitoring is a nondestructive condition assessment method that can be implemented continuously on highway bridges without interrupting traffic. This has made it particularly attractive.

However, two major obstacles remain against successful implementations of the vibration-based SHM in real-life bridge structures. One is the lack of low-cost high-performance vibration sensors and data acquisition systems, the other is the lack of proper methodologies to interpret vibration data in terms of structural integrity.

1.2 Research Object and Scope

The overall objective of this project is to explore the use of the sensor technology for long-term bridge structural performance monitoring, by (1) demonstrating the installation of sensor and monitoring systems on three typical highway bridges and (II) developing methodologies and software for vibration data analysis and interpretation. As reported by Feng and Kim (2001), the Phase-I effort focuses on the instrumentation of two highway bridges and preliminary data measurement and analysis. The Phase-II research included the instrumentation of an additional highway bridge, upgrade of communication links for the monitoring systems, but the major focus was on the development of methods for interpreting bridge vibration data into the on-going structural health, defined as element stiffness of the bridge structure in this study. The methods are mainly based on bridge responses to traffic loads. Using traffic-induced vibration data has a few practical advantages over other bridge structural condition assessment methods: (I) It does not interrupt traffic; (II) It captures the *in-situ* dynamic behavior of the bridge undergoing its normal service; (III) It can be performed continuously, scheduled periodically or triggered automatically and (IV) It requires no special experimental arrangement or a heavy shaker/hammer.

During Phase II of the research, the authors obtained unique opportunities to verify the SHM methods developed in this study by performing seismic shake table tests on large-scale realistic bridge models. These experiments demonstrate that the proposed vibration-based methods can quantitatively assess the bridge structural conditions, locate the damage zone and provide a mean to evaluate the bridge remaining capacity.

1.3 Overview of Phase-I Work and Phase-II Report

The Phase-I work of this project has been summarized in a Caltrans report by Feng and Kim (2001). In Phase I, sensor systems for long-term structural performance monitoring were installed on two new highway bridges in Orange County, California: the Jamboree Road Overcrossing (JRO) and the West Street On-Ramp (WSO). They include accelerometers, strain gauges, pressure sensors, displacement sensors, installed or embedded at strategic locations of both super- and substructures. Data recorders and power supplies were also installed at the bridge sites. Preliminary vibration measurement and data analysis were performed on these two instrumented bridges. On the JRO bridge, ambient or traffic-induced vibration data were collected, based on which natural frequencies and mode shapes were extracted using peak-picking, randomdec and frequency domain decomposition methods, assuming the excitation is a spatially uncorrelated white noise process. These results were compared with those obtained by the preliminary finite element analysis. On the WSO bridge, braking and bumping vibration tests were carried out using a water truck. Natural frequencies were derived using similar methods as for the JRO bridge.

The JRO bridge and the WSO bridge instrumented in Phase I, are short or medium span reinforced concrete box girder bridges, where the mechanical properties of the abutments, including its support condition, mass and interaction with soil and foundations, and its constrain stiffness to the superstructure, have significant influence of the bridge dynamic behavior. To enrich the spectrum of the monitoring bridges, a 3rd bridge, the Fairview Road On-Ramp Overcrossing (FROO), with longer span length and more number of spans, was instrumented with a denser sensor system in Phase II.

In Phase II, the existing monitoring system on the JRO and the WSO underwent major upgrades to accommodate wireless remote data acquisition. Such upgrades ease the data collection, and are highly valuable for establishing a database to monitor the long-term behaviors of these bridges. They also enable on-line real-time data visualization and sharing on the Internet.

This report documents the Phase-II study. A literature review on structural instrumentation and performance monitoring in provided in Chapter 2. The instrumentation of the FROO and the system upgrades in the JRO and WSO are documented in Chapter 3. Recorded data from ambient vibration and due to earthquakes are shown in Chapter 4. As stated before measurements are taken not only from accelerometers but also from strain gauges. In chapter 5 results obtain from strain measurement and analysis are discussed. More importantly, the Phase-II research focus on the development methods for analyzing and interpreting the vibration data into structural health. Chapter 6 describes the vibration-based SHM methods proposed and developed in this study, and Chapter 7 documents the unique shaking table tests performed in this study to verify the SHM methods. Chapter 8 discusses the field tests conducted on WSOO using water trucks under controlled environments. It has been well known that the environmental changes have considerable effects on modal identification results. Chapter 9 shows the variation in modal identification results throughout the last four years. Chapter 10 describes the software developed in this study that implements the proposed and developed SHM methods. Finally, Chapter 11 summarizes this project by providing concluding remarks and suggesting future research topics.

Chapter 2

LITERATURE REVIEW

Structural condition assessment of highway bridges has long relied on visual inspection, which involves subjective judgment of inspectors and detects only local and visible flaws. The frequency of visual inspection and the qualification of the inspectors were regulated by a standard, the National Bridge Inspection Standards (NBIS 1996). The Federal Highway Administration (FHWA) Recoding and Coding Guide (FHWA, 1995) was also provided to guide the procedure including the condition ratings and the documentation in current practice. Even with these provisions, a recent investigation initiated by FHWA to examine the reliability of visual inspections reveals significant variability in the structural condition assignments by inspectors (Phares et al., 2004). Moreover, visual inspection cannot quantitatively evaluate the strength and/or deformation capacity reservation of a bridge.

In order to investigate the global structural condition of bridges in an automated, continuous, objective and quantitative manner, structural health monitoring (SHM) has been promoted by researchers (e.g., Aktan et al, 1997; Doebling et al, 1998, Feng and Kim, 1998, Feng and Bhang, 1999, Aktan et al, 2000; Park, 2001, Peeters et al, 2001, Catbas and Aktan, 2002; Chang and Liu, 2003; Chen and Feng, 2003, Kim, et al, 2003, Sohn, et al, 2003, Feng, et al, 2004). Recently, SHM has been an intensively investigated subject.

As a branch of the wide-ranging efforts of SHM, many researchers seek to measure the structural vibration behavior (dynamic response of a structure with or without measuring the exerting excitations), and infer from the vibration data the level of structural integrity. Among many nondestructive evaluation methods, vibration monitoring is one that can be implemented continuously on highway bridges without interrupting traffic.

A thorough literature review on vibration-based SHM was first presented by Doebling et al. (1996), summarizing hundreds of publications up to 1995. A four-level hierarchy, namely, (I) detecting the existence of damage, (II) locating damaged portions, (III) evaluating the severity of damage and (IV) predicting its future consequences, proposed by Rytter (1993) and defined as the goals of SHM. Recently, an updated review of the state was presented by Sohn et al. (2003), summarizing publications from 1996 to 2001. This review interprets vibration-based SHM following a statistical pattern recognition paradigm, consisting of a four-part process: (I) operational evaluation, (II) data acquisition, fusion, and cleansing, (III) feature extraction and information condensation, and (IV) statistical model development for feature discrimination. In this paradigm, features that are believed damage sensitive are extracted from vibration data, and a pattern recognition procedure is employed to classify the feature vectors to determine the existence, location and severity of structural damage. While the important role of statistical methods in SHM was recognized, the ultimate goal of SHM is still damage evaluation, as was defined by the four-level hierarchy in the previous review and by Sikorsky (2005). In view of difficulties associated with mathematical models (often referring to finite element models) of structural systems, especially the difficulty in quantifying the modeling uncertainty and the bias due to modeling errors, the reviewers uphold methods that are

not based on such models as more attractive. However, difficulties of non-model-based methods were also recognized, especially in quantifying the severity of damage where a supervised learning mode is usually adopted. Training patterns have to be generated by a mathematical model whose fidelity remains to be verified, because data sets from a damaged structure are seldom obtained and if exist, not adequate to cover all possible damage scenarios. A sufficient coverage on various scenarios by the training patterns, nonetheless, is essential in the supervised learning procedure.

Research in vibration-based SHM has produced substantial literature, with many conferences and journals held for information exchange and demonstration of research results (e.g. Ghanem and Shinozuka, 1995; Safak 1989; Safak 1991; Feng and Kim, 1998, Feng and Bhang,1999; Feng and Kim, 2001, Park, et al, 2001, Feng et al, 2003, Kim, et al, 2003). These methods can be grouped into two depending on whether the identification is carried out in frequency or time domain. If it is in frequency domain, basically the changes in modal values; frequency, damping, shape, are used as an indication of damage. However; if one wants to identify the changes more in detail like changes in elemental stiffness, time domain identification methods might be more appropriate. Time domain methods can be grouped into two depending on whether they are purely data driven or they are incorporating finite element (FE) model. If it is aimed to determine the changes in the stiffness values, FE model must always be used. Within time domain identification methods, the most common one is the least squares estimation (LSE). It is basically performing an optimization for the parameters such as stiffness and damping so that the error between the measured and the simulated responses is minimized. LSE is useful as a system identification technique, when used in combination with a damage detection algorithm (e.g., Stubbs et al, 200). However, there are some drawbacks of LSE. Firstly, physical insight can

be easily lost and a local maximum can be chosen over a global one (Udwadia, 1988). Secondly, LSE is very time consuming and cannot be applied for “on-line” SHM and damage detection. To overcome this difficulty, the recursive least squares (RLS) technique is proposed so that any time varying property in a system caused by damage can be tracked in real time. However in this case incorporation of FE is sacrificed, i.e. it is purely data driven so change in the system parameters can be tracked but it is not possible to link this to the change in structural stiffness and damping. Also, RLS is susceptible to even low level of noise. As can be seen every method has some drawbacks and is not effective for on-line identification of stiffness values under realistic conditions.

Kalman filtering was a break-through in system engineering field when first proposed four decades ago. It not only uses the data in a probabilistic sense but also gets information from structural model (Kalman, 1960). Results obtained by the Extended Kalman Filter (EKF) approach from simulated data and well defined models with known damage scenarios were reported (Yun and Shinozuka, 1980; Hoshiya and Saito, 1984; Yang et al, 2005; Straser and Kiremidjian, 1996; Loh and Chung, 1993; Loh and Tou, 1995, Ghanem and Ferro, 2006). However, applicability of the EKF approach to civil engineering structures involving high uncertainties in structures and loadings under realistic damaging events has not yet been studied.

Evident by these reviews and more recent papers (e.g. Bolton et al., 2001; Hera, 2004; Koh et al., 2003; Lam et al., 2004; Yang and Lin, 2005), despite significant efforts, damage identification by SHM is still a highly challenging problem. When implementing vibration-based SHM to real-life structures, the limitation of sensing capacity (e.g. spatial limitation due to insufficient number of sensors or prohibitive positions of instrumentation, and temporal limitation due to insufficient sensor

frequency range and excitation bandwidth), and the operational and environmental variations of the structures have significantly increased the difficulties.

Nonetheless, it is believed that part of the challenges in SHM can be attributed to a scholars' preference of an inductive, objective and entirely data-driven methodology. A shift of epistemology from a purely inductive to a deductive-inductive hybrid methodology might help to ease the problem and bring forward useful results. In the deductive-inductive methodology, *a priori* knowledge, derived either from established theories, engineering experiences, or even subjective postulations, is incorporated in a probabilistic model of the structural system. In this model, the extent of knowledge limitation is represented by the uncertainty of the model structure and parameters. This model is subjected to correction or refinement based on sensor data, by first deducing the expected vibration behaviors from the *a priori* model, and then comparing them with the sensor observations and updating the model in a systematic induction to reconcile the predicted and observed vibration. The advantage of this approach is that gaps of necessary information not provided by sensor data are filled in with the currently available best understanding of the system. Therefore, SHM is no longer merely a means of nondestructive damage evaluation, but a procedure of information collection to correct/refine the probabilistic model of the structural system so as to gradually diminish the system uncertainty.

The above methodology is essentially a Bayesian approach. This vision of SHM can be traced back to Beck (1989), where a Bayesian framework was laid down for structural system identification that selects the most probable model from a class of models based on input/output measurement. The major usage of this data-improved model is for response prediction for future loads, which was shown asymptotically correct as the sample size of measurement increases. Later in Beck and Katafygiotis

(1998), this vision was formalized to not only update the model, but also assess the uncertainties of the model itself and its predictions. This formulation addresses explicitly the difficult problem in parameter identification: the inherent ill-conditioning and non-uniqueness. If the *a posteriori* probability of the parameters has mono-mode, the system is globally identifiable; or if it has multiple but distinct peaks, the system is locally identifiable; when it has sustained support in a manifold within the parameter space, the system is unidentifiable. In the latter two cases, prediction of structural behaviors is still possible in this framework, using more than one candidate model, but weighting their predictions according to their model *a posteriori* probability. The last case was treated in Beck and Au (2002) using a Markov chain Monte Carlo method. The Bayesian framework was extended in Beck and Yuen (2004) to address the modeling error issue arising when the 'true' system is not within the class of models being examined. Classes of models were compared based on the Bayesian *a posteriori* probability, which was revealed to consist of two parts: one appreciates the fitness of the model to the data, and the other appreciates the model parsimony. The capacity of a data-updated model to predict in a probabilistic sense the structural response to future loads was utilized to make a connection between SHM results and structural reliability evaluation (e.g., Park, et al, 1997, Papadimitriou et al., 2001; Beck and Au, 2002). Solutions to the implemental difficulties in SHM due to operational and environmental variations were suggested also in a Bayesian framework. In Yuen et al. (2002) a time-domain Bayesian updating was proposed when system inputs are not measured, and in Yuen and Beck (2003), the same problem is addressed by a frequency-domain approach. In Vanik et al. (2000) variation of modal parameters (frequencies and mode shapes) was treated in a Bayesian framework to set a probabilistic measure of the significance of modal

feature changes. Although damage identification is not the major concern of the model updating procedure, it is also possible if damage can be defined quantitatively in terms of parameter changes (Yuen et al., 2004).

This approach is certainly model-dependant. However, it can be argued that models are almost inevitable anyway in structural condition assessment (e.g., in training pattern generation) and in evaluation of current and expected future performance of a structure. To minimize the disadvantage caused by modeling errors, one may need to avoid a deterministic perspective of a model, but instead, use a probability measure to represent modeling uncertainty.

Chapter 3

HARDWARE INSTALLATION AND UPGRADES

This chapter reports the upgrades on the monitoring systems at the Jamboree Road Overcrossing (JRO) and the West Street On-Ramp (WSO) that were installed during the Phase-I study, and the instrumentation of the 3rd bridge, the Fairview Road On-Ramp Overcrossing (FROO).

3.1 Upgrades of Phase-I JRO Monitoring System

The monitoring system at the JRO underwent the following major upgrades in Phase II of this research.

3.1.1 Addition of Temporary Sensors

In the spring of 2002, four additional temporary accelerometers were installed on the JRO bridge. The purpose of such additional instrumentation is two-folded: Firstly, analysis of the vibration data obtained from the permanent sensors only shows that the number of sensors is not sufficient for mode shape identification therefore additional sensors are needed; and secondly, it is to obtain data comparable to the initial data sets collected when temporary sensors were on the bridge at the very

beginning of the monitoring project. Channel 13 to 16 are the temporary accelerometers added (Fig. 3.1.1). Channel 16 was later found to be out of order. Therefore, the JRO monitoring system currently has 14 accelerometers and one displacement sensor (Channel 12). Due to the limited funding, we could not install sensors at all the desirable locations such as Abutment 1.

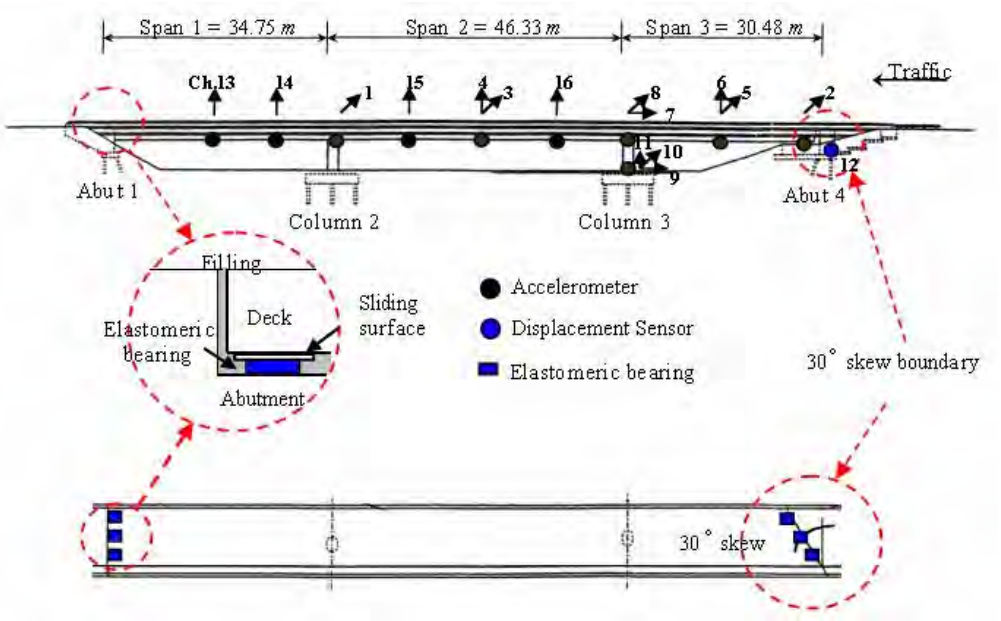

Figure 3.1.1 Sensors on JRO

3.1.2 Installation of Wireless Remote Data Acquisition System

To overcome a distance of 6 miles and remotely access the monitoring system and verify its working conditions, a wireless data acquisition system was installed on the JRO bridge during the first quarter in 2004. The system includes the following acquired hardware and software developed in this project.

Hardware:

(1) A pair of Cisco Aironet 350 Wireless Bridges, working in IEEE 802.11b Network Standard, 2.4 to 2.497 GHz frequency range. One was installed at the bridge site, mounted inside the existing data logger box, configured as the *civil-eng-root* end with IP address 128.200.109.194. The other was installed in the facility room in Engineering Tower at UC Irvine, configured as the *civil-eng-nonroot* end with IP address 128.200.109.195. Figure 3.1.2 shows the web pages where the status of these pair of devices are displayed and their working parameters can be configured by a system administrator.

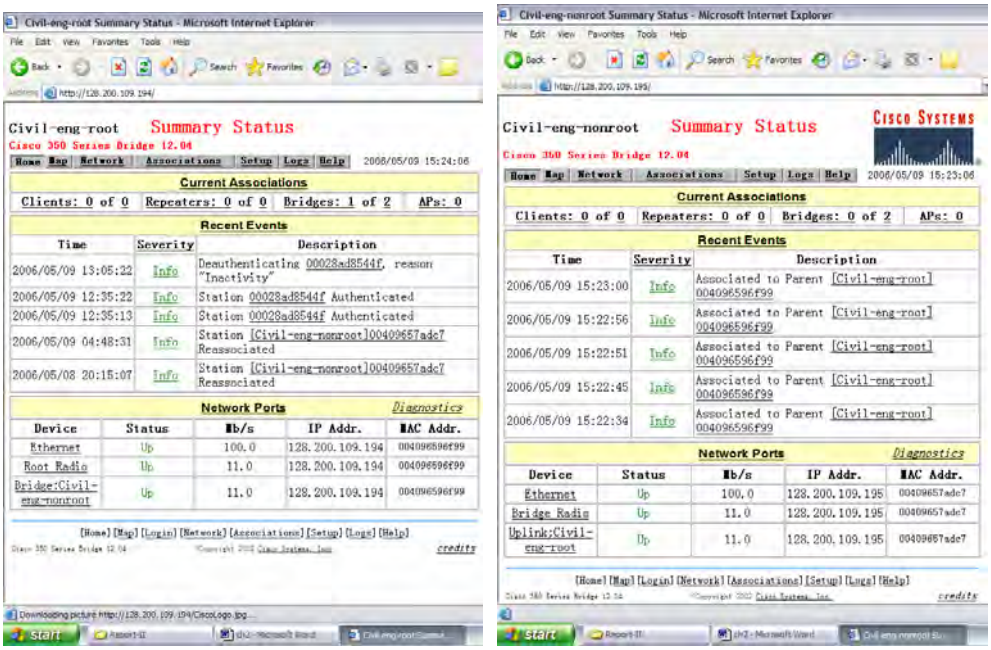

Figure 3.1.2 Web Pages of the Wireless Bridges

(2) A pair of Cisco AIR-ANT3338 Aironet Antennas, with gain 21dBi, capable of approximate range of 25 miles (at 2Mbps) or 11.5 miles (at 11Mbps). One was mounted on top of a steel pole at the bridge site; the other was mounted on top of a pole on the roof of Engineering Tower at UC Irvine (Fig. 3.1.3). The steel pole at the bridge site was designed and constructed by K. A. Wang & Associates. Inc.

(a) Antenna mounted on a steel pole at JRO

(b) Antenna mounted on a pole at Engineering Tower on UC Irvine Campus

Figure 3.1.3 Directional Antennas

(3) A LAN converter provided by Tokyo Sokushin Co., Ltd, the sensor and data logger maker, to connect the data logger to the Internet through it RS 232 series port. The LAN converter is configured to listen on 128.200.109.205:23, and connected to the *civil-eng-root* wireless bridge. This LAN converter converts the data logger to a TCP-IP device enabling the networking.

Software:

The first software used for this remote data acquisition system is TS-Terminal V2.4, a wireless data acquisition software initially by Tokyo Sokushin Co. Ltd. (Fig. 3.1.4). With this software, virtually any computer running TS-Terminal and connected to the Internet can access the data logger remotely. Data can be monitored almost in real time on remote terminals. Data files on the flash memory card at the bridge site data logger can be downloaded to the remote terminal and deleted from the flash memory

card. The remote terminal can send commands to the data logger to trigger the recording (to the flash memory card only), calibrate the sensor and change the data logger's setting.

However, there several fatal problems were discovered in the is project with this software: 1) A remote terminal running the TS-Terminal software cannot record real time data stream on its own hard disk; 2) The stability of the software is not satisfactory: especially, system frequently breaks down during downloading multiple files from the flash memory card; and 3) most importantly, TS-Terminal was developed as a remote terminal, not as a server, therefore, it supports only one online user at one time and it does not support data visualization and distribution on internet.

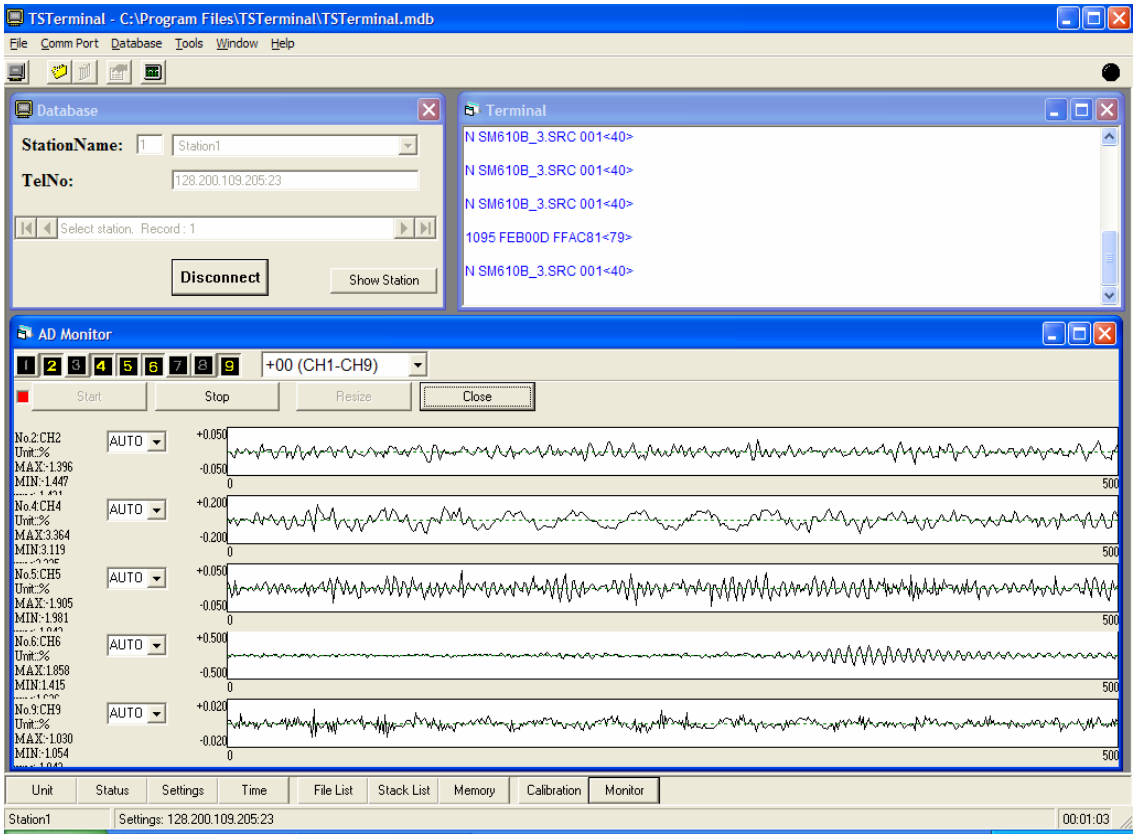

Figure 3.1.4 TS-Terminal Software

3.1.3 Development of Communication Software TS-Terminal

Seeking a solution to the above problems of the TS-Terminal, a new software with a remote data acquisition capability was developed by this team at UC Irvine based on the platform of TS-Terminal. The newly developed software (Fig. 3.1.5) has been installed on a computer on UCI campus, and functions as a server that receives streaming data from the data logger on the remote bridge site, saves them in the local computer and buffers them for Internet publication. The new software has algorithm to accommodate data transmission errors during wireless communication, thus suffering much less interruptions during data transmission.

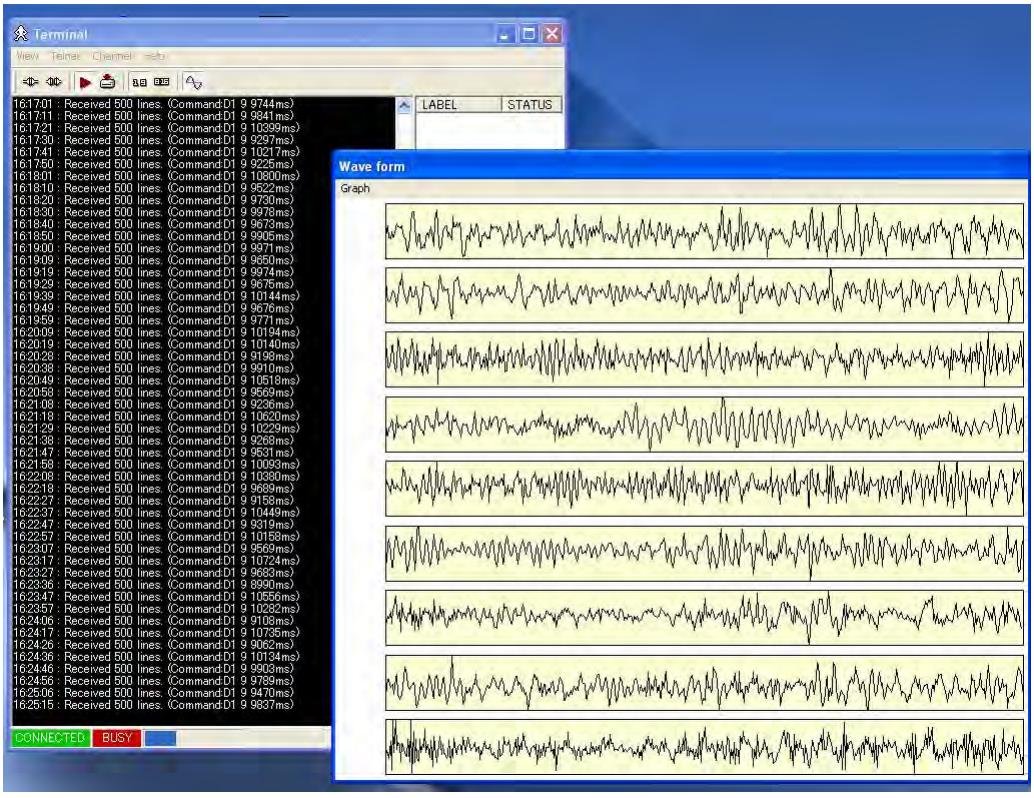

Figure 3.1.5 Server Software

3.1.4 Development of Server/Client Solution for Real-time Internet Waveform Display and Data Acquisition

Besides this server software, a Java applet was further developed in this project for displaying real-time data on Internet. This Java applet is a client agent that displays the waveforms of the data in the buffer of the server (Fig. 3.1.6). This applet provides a way for the public as well as Caltrans to view the real-time data on Internet. It is available at http://mfeng.calit2.uci.edu/ (Special approval from Caltrans is needed for downloading the data). This pair of server/client software also provides a way to verify the working status of the JRO monitoring system.

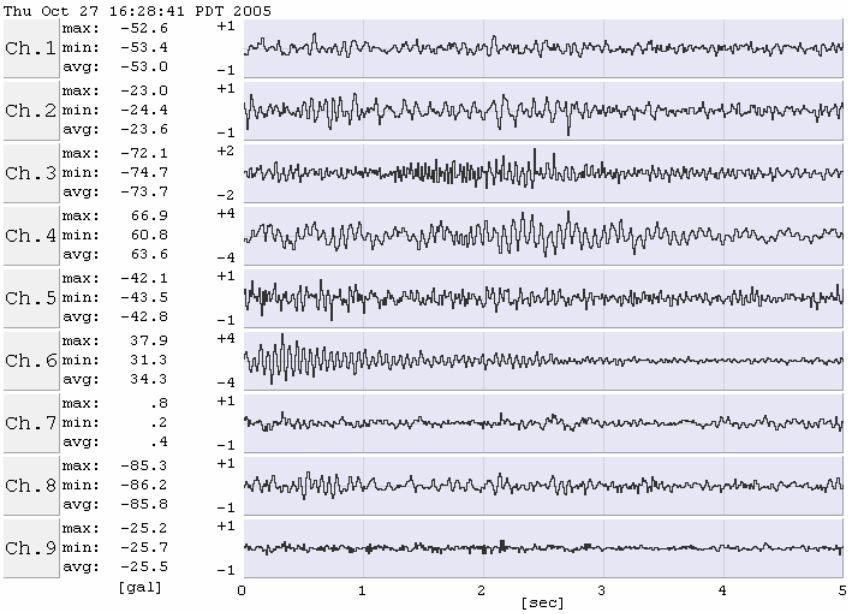

Figure 3.1.6 Java Applet – Client Software

3.1.5 Power System Upgrade

To provide sufficient power for the existing data logger, and also the devices added for the wireless remote data acquisition system, two additional deep-cycle auto rechargeable batteries were installed at JRO in the batteries box (Fig. 3.1.7). A transformer was used to provide DC 38V for the Cisco wireless bridge and the Cisco

AIR-ANT3338 Aironet Antenna by these two additional batteries. Three charging controllers were integrated into the system to protect the batteries from over-charging or discharging (currently, these controllers are configured to auto-reset after several hours if over-charging or discharging is detected).

Figure 3.1.7 Battery Box

3.2 Upgrades of Phase–I WSO Monitoring System

During Phase-II of the research project, data retrieval of the WSO system has been proven very difficult. The major difficulty comes from that fact that the data logger was installed inside the box girder due to the unavailability of an easy-to-access space. To access the data logger or to retrieve the data recorded in the memory card, one needs to climb into the enclosed box-girder through a man hole. Entering such an

enclosure environment requires special training. To access the man hole, one needs a ladder which requires a pick-up truck for its transference. For safety, accessing the man hole is not recommended without proper guidance.

To cope with these problems, a wireless LAN router and a serial to LAN converter were installed inside the box-girder of the WSO. Figure 3.2.1 shows a system configuration of this wireless transmission setup. With this wireless transmission setup, recorded vibration data can be retrieved from the outside box-girder of the WSO.

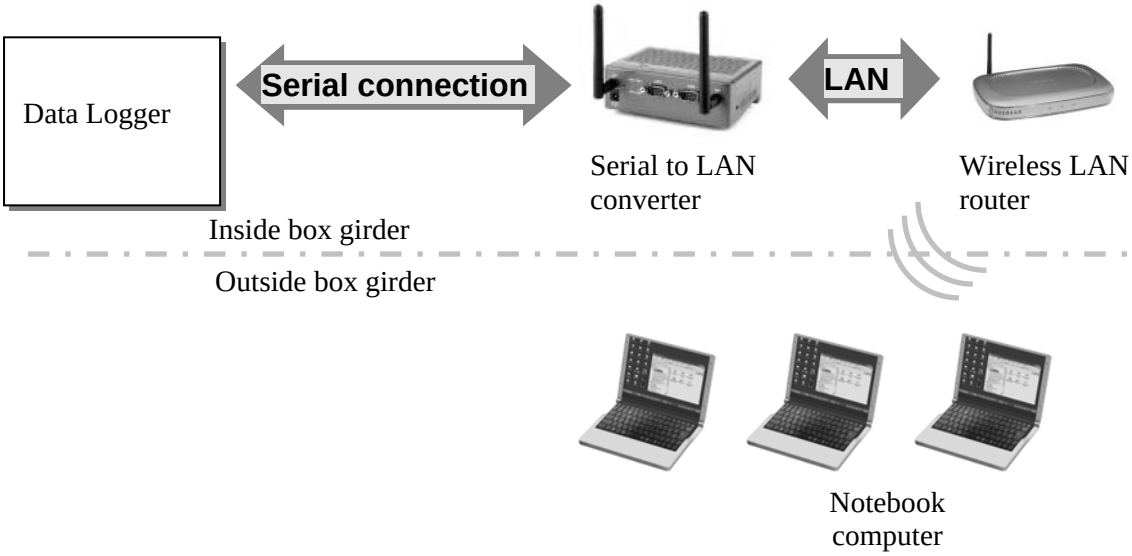

Figure 3.2.1 Configuration of Wireless Transmission

Recorded vibration data is retrieved from the data logger through a serial communication line. The serial to LAN converter, which is connected to the data logger, converts this serial data to TCP/IP format in order to connect to the wireless LAN router. This converted data is transmitted to the commercially available wireless LAN router, which is placed close to the man-hole in the box girder, by wired connection. The wireless LAN router establishes a local area network by using

private IP address and broadcasts the vibration data to the outside box girder. A notebook computer, which has a wireless NIC, can receive the broadcasted vibration data from the wireless LAN router without entering the enclosed box-girder by connecting established local area network. Although limitation of transmission distance of the wireless LAN router is 50 [m] according to its specification, it is possible to extend this distance by installing a wireless access point to provide more convenience.

This wireless transmission setup is working stably, and many vibration data has been collected on the WSO wirelessly.

3.3 Instrumentation of the 3rd Bridge: FROO

During Phase II of the research project, a third bridge is instrumented with a sensor system consisting of accelerometers, LVDT type strain meters and conventional strain gauges, displacement meters, pressure sensors and thermocouples.

3.3.1 Bridge Description

The Fairview Road On-Ramp Overcrossing (FROO), located in Costa Mesa, Orange County, California, is the on-ramp of Fairview Road onto the north bound of I-405 freeway, overcrossing the Harbor Boulevard off-ramp. Figure 3.3.1 is a map from Google Local showing its location.

Figure 3.3.1 Location of the FROO

The FROO is a four-span continuous cast-in-place pre-stressed post-tension box-girder bridge (Fig. 3.3.2). The total length of the bridge is 224.0 m (734.9 ft.), in which the lengths of spans are 52.5, 59.5, 59.5 and 52.5 m (172.2, 195.2, 195.2 and 172.2 ft), from span 1 to span 4 respectively (Fig. 3.3.3). The bridge is supported on three monolithic single columns and sliding bearings on both abutments. The sliding bearings (Fig. 3.3.4) allow creep, shrinkage, and thermal expansion or contraction. The typical cross section of the box-girder is shown in Fig. 3.3.5.

Compared with the other two instrumented and monitored bridges (the JRO and the WSO), the FROO has more and longer spans. It enriches the spectrum of the monitored bridges. Instrumentation of this bridge offers opportunities to study and understand behaviors of longer span RC bridges where the abutments are expected to affect relatively less on the overall bridge dynamic behaviors. It will be of great interest to monitor and evaluate the long-term structural performance of such bridges under not only seismic but also service loads, and to compare their performance with that of the bridges with less and shorter spans.

During Phase II of this research project, the FROO was under going construction. It was completed and opened to the traffic in 2004. Thus it provided excellent opportunity for embedding strain sensors in concrete and pressure sensors in the abutments during the construction. Accelerometers were mounted inside the bridge box-girder for better protection. Based on the experience of data analysis of the other two instrumented bridges, the FROO was instrumented with a denser sensor system with more accelerometers and strain gauges in comparison with the JRO and WSO.

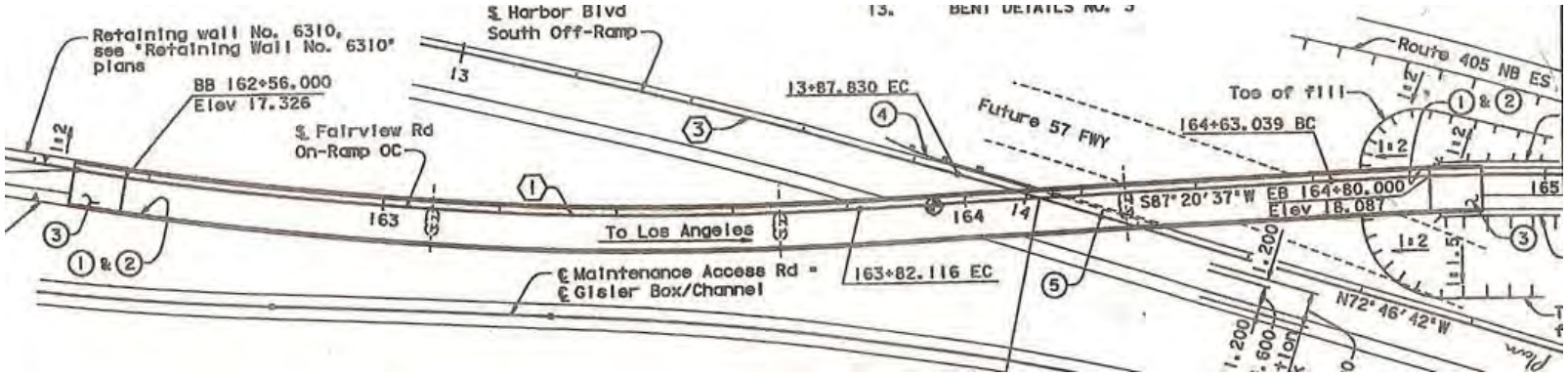

Figure 3.3.2 Plan view of the FROO

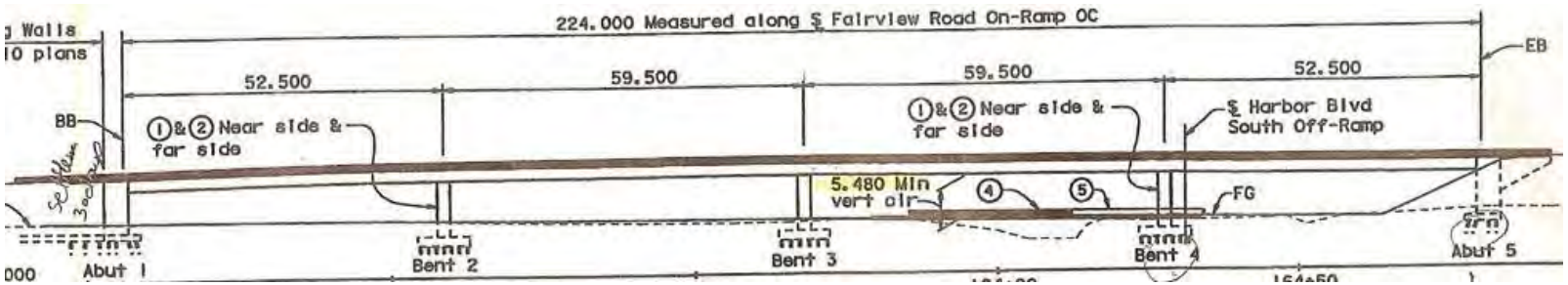

Figure 3.3.3 Elevation of the FROO

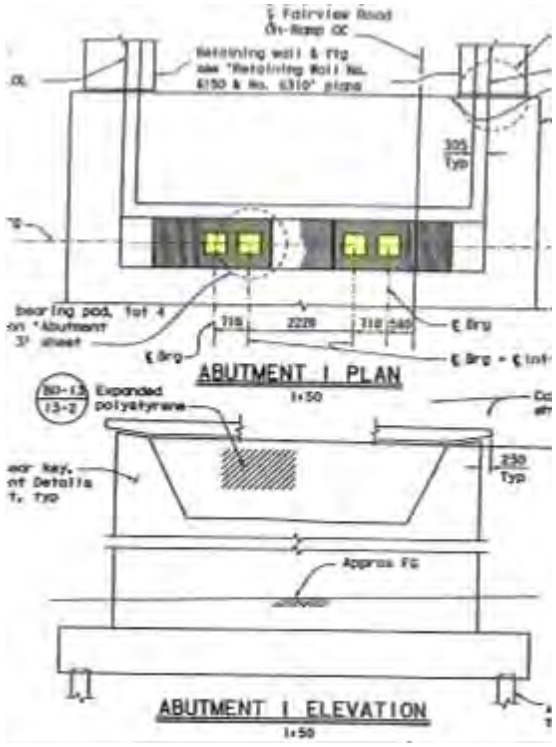

Figure 3.3.4 Bearing at Abutment 1

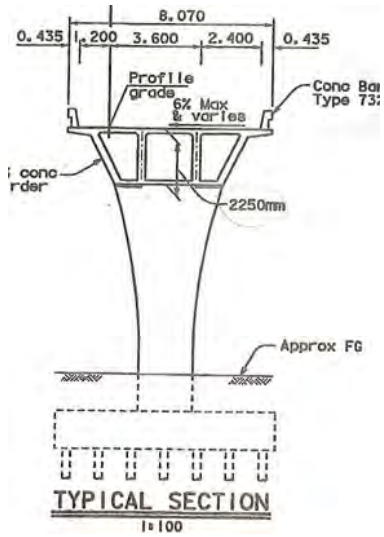

Figure 3.3.5 Typical Cross-section of the Box-girder

3.3.2 Monitoring System Design and Installation

Accelerometers

A total of 21 channels of acceleration sensors were installed both on the bridge super- and substructures. As shown in Table 3.3.1 and Fig. 3.3.6, one tri-axial accelerometer (A0), five bi-axial (A2, A3, A5, A9 and A12), and eight uni-axial (A1, A4, A6, A7, A8, A10, A11 and A13) were installed. Pictures of a uni-axial, a bi-axial and a tri-axial accelerometers are shown in Figures 3.3.7 to 3.3.9. Except for A0, which was installed against the end wall at Abutment 1 to measure the ground motion in the three directions, accelerometers (A1 to A13) were mounted on the floor surface inside the box-girder, by brackets bolted into the concrete (as shown in Fig. 3.3.10), to measure the superstructure vibration at different positions. A1 to A13 were aligned along the longitudinal center line of the box-girder to mitigate the effect of torsional modes. Again due to the limited funding, it was not possible to install additional sensors to measure the torsional modes. We recommend to add more sensors to measure the torsional modes when funding becomes available in the future. The positions of A1 to A13 are in respectively in the middle and quarter points of the spans.

The positive directions follow the sign conventions as noted in Table 3.3.1, which documents the orientations of the accelerometers. The sub-column '*Marked*' in column '*Direction*' documents the assigned directions by the sensor manufacturer that were marked on the enclosure box of each sensor. The sub-column '*Planned*' denotes the installation plan. However, due to the actual difficulties of installation, for example the obstacle during concrete drilling, or the miss-match of the bracket orientation, the actual '*Installed*' orientation can be different from the plan. For example, the row for A0 should be interpreted as: we intended to install the accelerometer marked as (+X) along

the positive longitudinal direction (planned +X), but we ended up with installing it along the negative vertical direction (installed –Z); similarly, we ended up with installing the accelerometer marked with (+Y) and (+Z) along the negative transverse (-Y) and positive longitudinal (+X) directions, respectively.

The cables of the accelerometers (and those of the embedded strain meters) run inside the box-girder and through the cap beams on top of the bents (through pre-installed PVC pipes). After the installation, the ceiling slabs of the box-girder were cast and there is no access to the sensors on span 2 to 4. One accelerometer, A6, on span 2 was found to be shorted somewhere inside the box-girder and thus not functional.

For the convenience of future system maintenance, this report documents the detailed wiring and splicing maps used in the accelerometer installation. Figure 3.3.11 shows the container box on a concrete pad and the junction box mounted on the wall of Abutment 1. The container box houses the data logger, the strain meter conditioner and the uninterrupted power supply (UPS) unit, as in Fig. 3.3.12. The 48-channel 22-bit A/D data logger provides the A/D conversion and controls the triggering, timing, sampling, recording and data streaming for all the sensors in this system. It also supplies DC ±15V power for the accelerometers. The 11-channel strain meter conditioner, on the other hand, is for the strain gauges and the pressure sensors only (this will be discussed in detail later). The strain and pressure signals, conditioned by this device, are further connected to the data logger for A/D.

The cables of the sensors (the accelerometers, strain gauges, pressure sensors, displacement sensor and GPS antenna), going through the conduits, are spliced in the junction box following Table 3.3.2. The spliced cables are then wired to either the data logger or the strain meter conditioner, depending on the sensor types. The DC ±15V

power is spliced inside the junction box to provide power for all the accelerometers. Figure 3.3.13 documents the detail splicing of the accelerometer cables in the junction box.

Strain Meters (LVDT type)

Seven LVDT type strain meters were embedded in the bridge superstructure (Fig. 3.3.14a), and three were embedded in Column 3 (Fig. 3.3.14b). All these strain meters were built on dummy rebars and attached to the steel cage before concrete casting. After the concrete cured, the strain meters are assumed to develop deformations consistent with the concrete surrounding them, thus measuring the strain of the concrete at that position.

Figure 3.3.15 shows the installation positions of the strain meters in the superstructure (denoted as SD1 to SD7) . The purpose of installing these strain meters is to monitor the evolution and the lose of pre-stress in the superstructure. Therefore, they were installed along a pre-stressing tendon and aligned horizontally. The other three strain meters were installed in Column 3 (denoted as SC1 to SC3) at the same elevation, measuring vertical strains at the three equally dividend points of the periphery of a circular cross section. However, one of these three sensors (either SC1 or SC2) was damaged during the construction of the bridge. Nonetheless, the remaining sensors can still serve the major purpose of this instrumentation: to obtain information of the static gravity load on Column 3.

A strain meter conditioner supplies 5V DC power to the strain meters, and at the same time, conditions the strain signals (Channels 1 to 9 of the conditioner) before sampled by a data log (whose channel connection is documented in Table 3.3.2). A detailed cable splicing map is documented in Fig. 3.3.16.

Strain Gauge (Resister type)

In addition to the LVDT type strain meters, conventional resister type strain gauges were also embedded in the substructure (Figures 3.3.17 and 3.3.18). They are used to measure strain distribution in the reinforced concrete footing of the columns (Fig. 3.3.18) and as a comparison to the LVDT strain meters in Column 3 (Fig. 3.3.17). Conventional strain gauges are not expected to last as long as the LVDT type strain meters, therefore not wired to the data logger. A portable strain reader and a temperature compensator can be used to acquire data from these strain gauges. Boxes housing the signal conditioner and the data log were installed at the column surface above the ground (Fig. 3.3.19).

Soil Pressure Sensors

Two soil pressure sensors (P1 and P2, Fig. 3.3.20) were installed between the soil and the end walls of Abutment 1 and Abutment 4, respectively. Sensor installation was performed before the backfill of the soil (Fig. 3.3.21). Pressure sensors are of similar sensing mechanism as the LVDT type strain meters, and thus conditioned by the strain meter conditioner (Channel 10 and 11) and wired to Channel 42 and 43 of the data log (Table 3.3.2).

Displacement Sensor

A displacement sensor (D1, Fig. 3.3.22) was installed at Abutment 1 to measure the relative displacement between the abutment and the superstructure along the longitudinal direction. This sensor requires 5V DC power which is supplied by a converter/transformer installed in the data log housing box. The sensor data are acquired to Channel 44 of the data log (Table 3.3.2).

Thermocouples

Three thermocouples were installed in the superstructure in span 1. One of them measures the outside temperature and the other two the inside temperature of the box girder, with the first one installed near the ceiling and the second one near the floor of the box girder. These thermocouples were connected to a signal conditioner that is located inside the box girder (Figure 3.3.23). The conditioner takes in ±15V DC power from the data log and supplies to the thermocouples, and at the same time, reads the outputs of the thermocouples. Table 3.3.2 and Fig. 3.3.24 show the details of the splicing.

Figure 3.3.25 summarizes the current channel assignment of the data logger (SAMTAC-700). There are some spare channels for further expansion of the instrumentation system.

Table 3.3.1 Installation of Accelerometers

No.	Model No.	Serial No.	Location	Bracket	Direction		
					Marked	Planned	Installed
A0	SV355T	020723	Abutment 1 Ground	No	+X,+Y,+Z	+X,+Y,+Z	-Z, -Y, +X
A1	SV155T	020729	Beginning of span1	No	+X	+Y	-Y
A2	SV255T	020724	Middle of span1	Type2	+X, +Y	+Y, +Z	+Y, +Z
A3	SV255T	020725	End of span1	No	+X, +Y	+X, +Y	-X, +Y
A4	SV155T	020730	1/4 point of span2	Type1	+X	+Z	+Z
A5	SV255T	020726	1/2 point of span2	Type2	+X, +Y	+Y, +Z	+Z, +Y
A6	SV155T	020731	3/4 point of span2	Type1	+X	+Z	+Z
A7	SV155T	020732	End of span2	No	+X	+Y	+Y
A8	SV155T	020733	1/4 point of span3	Type1	+X	+Z	+Z
A9	SV255T	020727	1/2 point of span3	Type2	+X, +Y	+Y, +Z	+Y, +Z
A10	SV155T	020734	3/4 point of span3	Type1	+X	+Z	+Z
A11	SV155T	020735	End of span3	No	+X	+Y	+Y
A12	SV255T	020728	Middle of span4	Type2	+X, +Y	+Y, +Z	+Y, +Z
A13	SV155T	020736	End of span4	No	+X	+Y	+X

Notes: (a) +X: longitudinal, (from abutment 1 to aboutment5), +Y: transverse, from North to South, +Z: vertical, from bottom to top. (b) Bracket Type1 is for uni-directional accelerometer, and Type 2 is for bi-directional accelerometer.

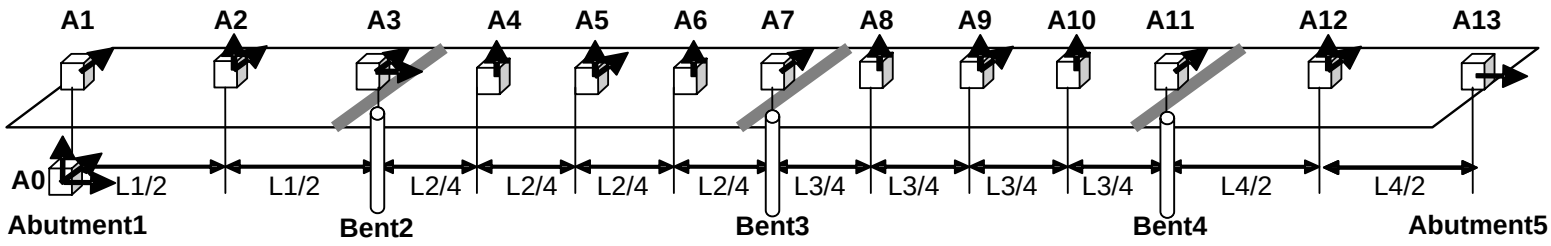

Figure 3.3.6 Schematic Layout of the Accelerometers

Figure 3.3.7 Picture of a Uni-axial Accelerometer

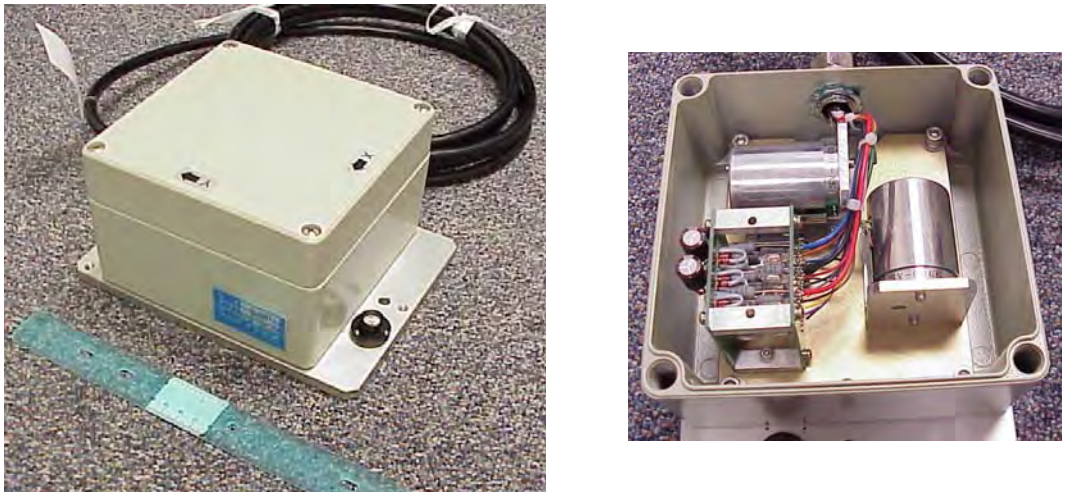

Figure 3.3.8 Pictures of a Bi-axial Accelerometer

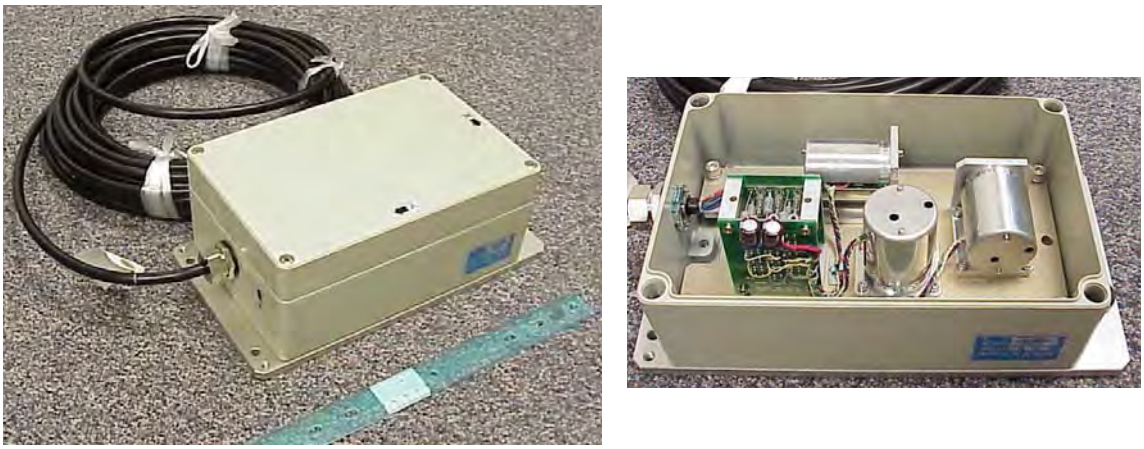

Figure 3.3.9 Pictures of a Tri-axial Accelerometer

(a) A uni-axial accelerometer mounted in box-girder without bracket

(b) A bi-axial accelerometer mounted in box-girder with a bracket to adjust the sensor orientations

Figure 3.3.10 Pictures of Accelerometers Mounted in the Box-girder

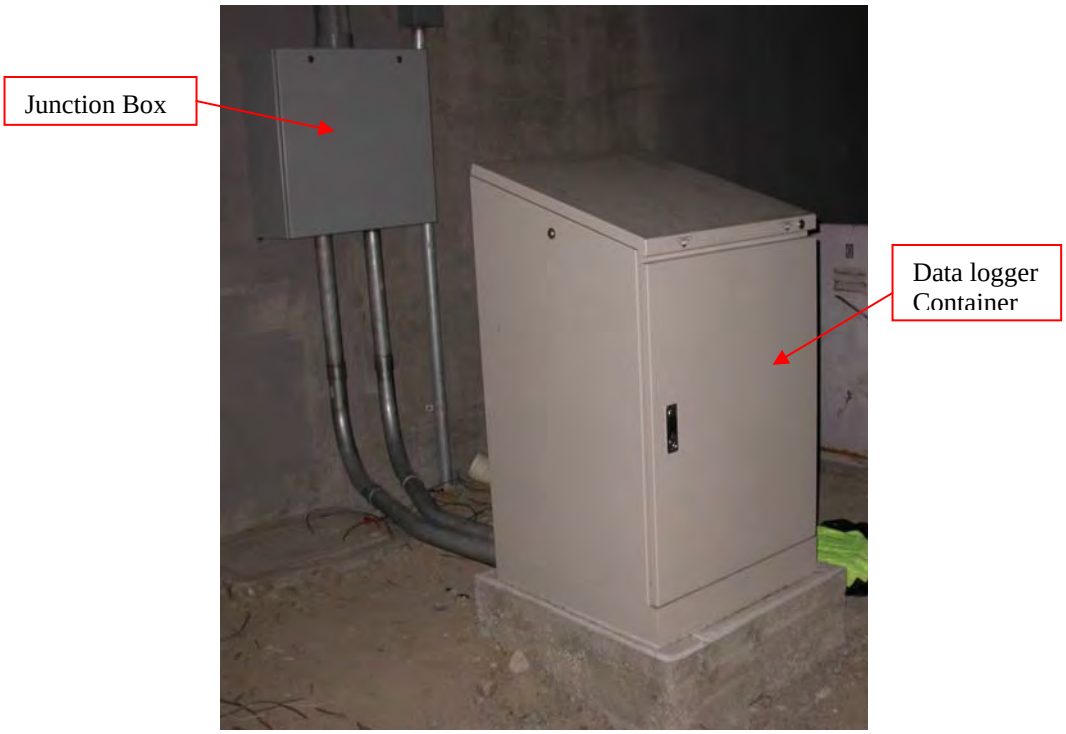

Figure 3.3.11 Picture of the Data-logger Container and the Junction Box

Figure 3.3.12 Data-logger and the Strain Meter Conditioner in the Container

Table 3.3.2 Splicing and Wiring Map

Sensor No. & Dir as Installed	Sensor No. & Dir as Marked	Other Cables	Splicing Cable Tag	Ch. No. in Strain Meter Conditioner	Ch. No. in Data Logger
(-)A0Z	A0X		Thick Cable	-	19
(-)A0Y	A0Y		Thick Cable	-	20
A0X	A0Z		Thick Cable	-	21
(-)A1Y	A1X		A1 blue	-	9
A2Y	A2X		A2 blue	-	10
A2Z	A2Y		8 red	-	1
(-)A3X	A3X		A3 blue	-	17
A3Y	A3Y		4 red	-	11
A4Z	A4X		11 red	-	2
A5Z	A5X		A5 blue	-	3
A5Y	A5Y		7 red	-	12
A6Z	A6X		A6 blue	-	--
A7Y	A7X		A7 blue	-	13
A8Z	A8X		A8 blue	-	5
A9Y	A9X		A9 blue	-	14
A9Z	A9Y		12 red	-	6
A10Z	A10X		A10 blue	-	7
A11Y	A11X		A11 blue	-	15
A12Y	A12X		A12 blue	-	16
A12Z	A12Y		2 red	-	8
A13X	A13X		A13 blue	-	18
		±15V	13 red	-	--
ANT		GPS	9 red	-	ANT
SD1	SD1		SD1 blue	1	33
SD2	SD2		SD2 blue	2	34
SD3	SD3		SD3 blue	3	35
SD4	SD4		SD4 blue	4	36
SD5	SD5		SD5 blue	5	37
SD6	SD6		SD6 blue	6	38
SD7	SD7		SD7 blue	7	39
SC1/2	SC1		SC1/2 blue	8	40
SC3	SC3		SC3 blue	9	41
P1			1 red	10	42
P2			3 red	11	43
T DC IN	T1		T1 blue	-	--
T1/T2/T3 OUT	T2		T2 blue	-	22, 23, 24
D1	D1		6 red	-	44

Notes: **(a)** Symbol (-) marks the sensor with an orientation that is opposite to the assigned positive direction. **(b)** Channel 4 of the datalogger is currently not used, because A6 is found to malfunction. **(c)** Currently, temperature sensors T1 and T2 are not connected to the datalogger. **(d)** The antenna has not received GPS signal up to date. **(e)** Due to the fading of the marks on SC1, SC2, T1 and T2, SC1 is not distinguishable from SC2; to distinguish T1 and T2 it will rely on future data reading and reasonable engineer judgment. **(f)** Channels 22 to 32, and channels 45 to 48 are currently unused.

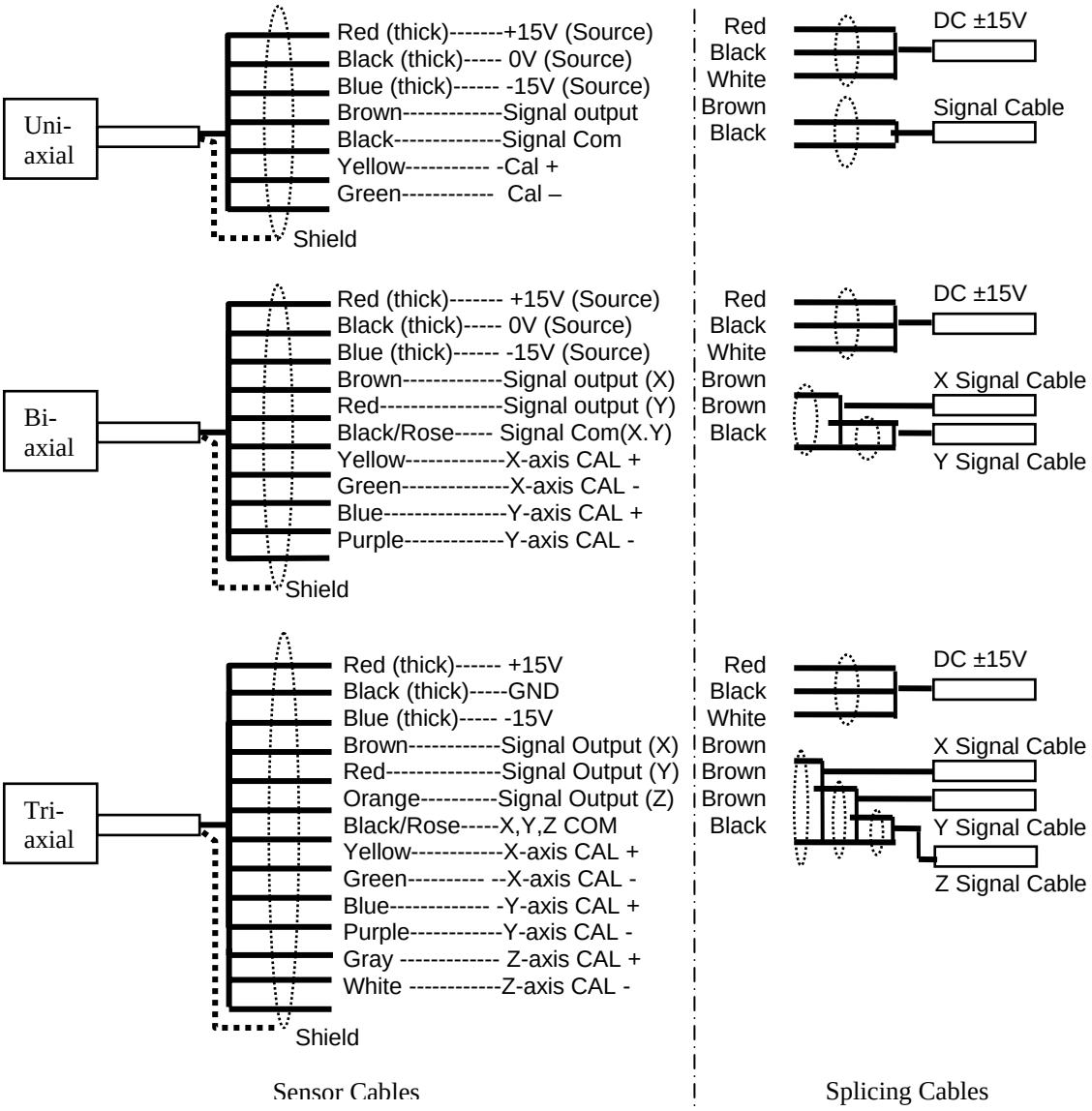

Figure 3.3.13 Accelerometer Splicing in the Junction Box

(a) LVDT Type Strain Meter Installed in the Deck

(b) LVDT Type Strain Meter Installed in the Column

Figure 3.3.14 LVDT Type Strain Meters Installation

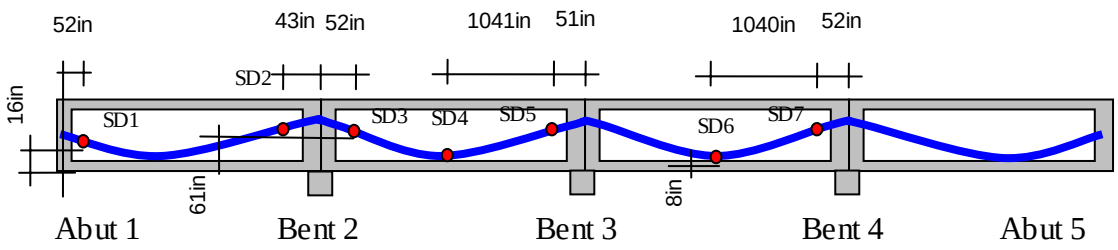

Figure 3.3.15 Position of the Strain Meters on the Deck

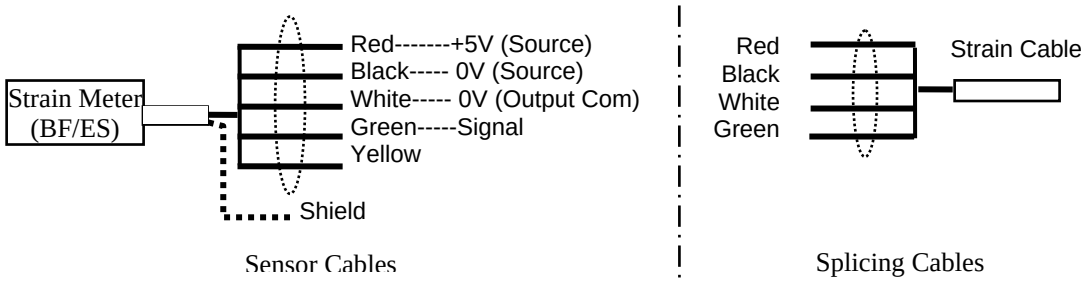

Figure 3.3.16 Strain Meter Splicing in the Junction Box

Figure 3.3.17 Conventional Strain Gauge and LVDT Strain Meter Installed in Column 3

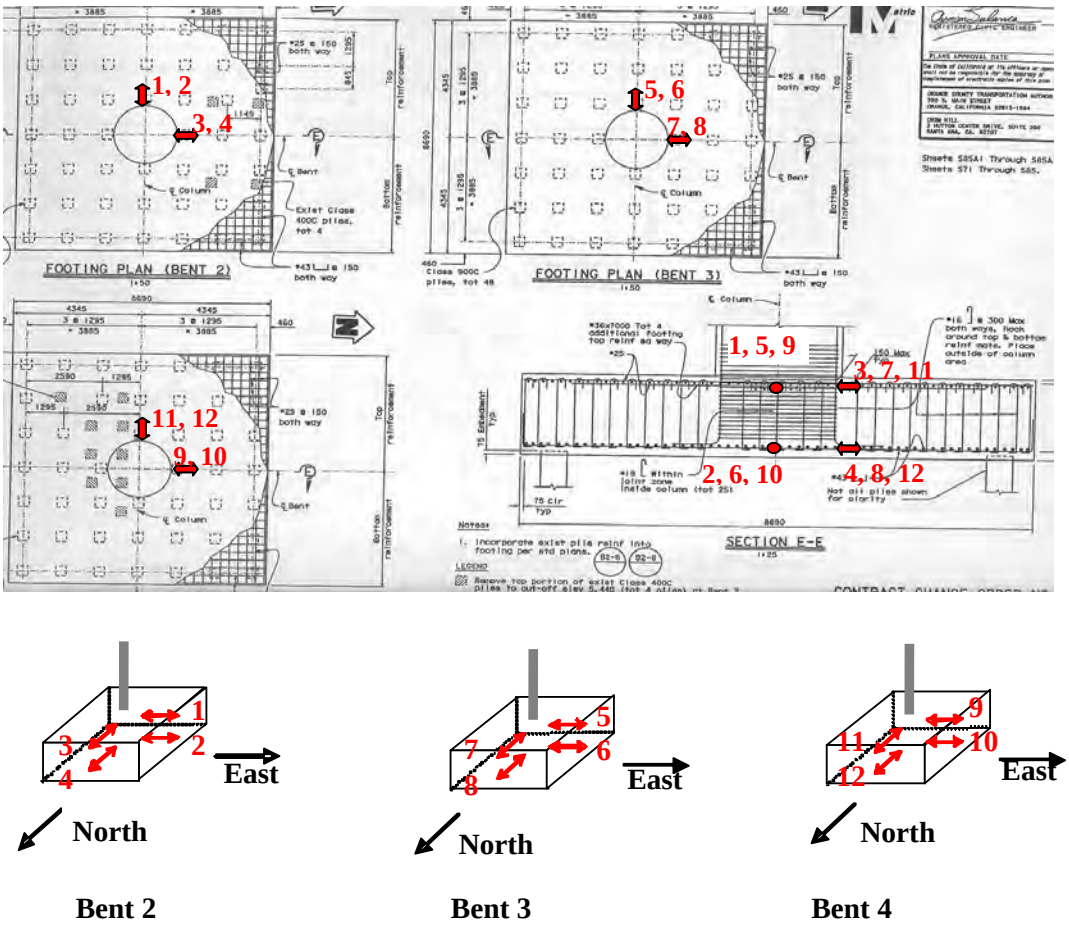

Figure3.3.18 Conventional Strain Gauges Installed in Footings

Figure 3.3.19 Installation of Signal Box for Conventional Strain Gauges

Figure 3.3.20 Soil Pressure Sensor

Figure 3.3.21 Backfilling at Abutment 1

Figure 3.3.22 Displacement Sensor

(a)Thermocouple Sensor head

(b)Signal Conditioner: Front

(c)Signal Conditioner: Back

Figure 3.3.23 Thermocouple and Signal Conditioner

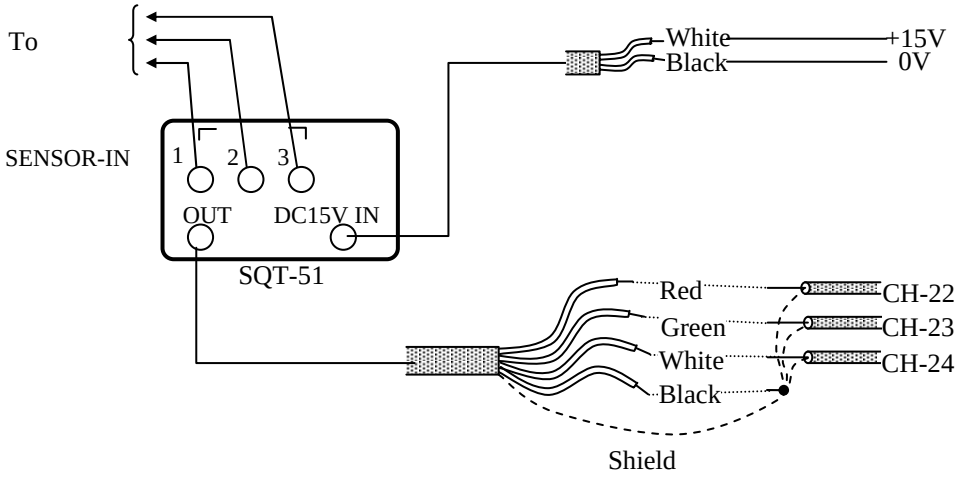

Figure 3.3.24 Thermocouple Wiring Map

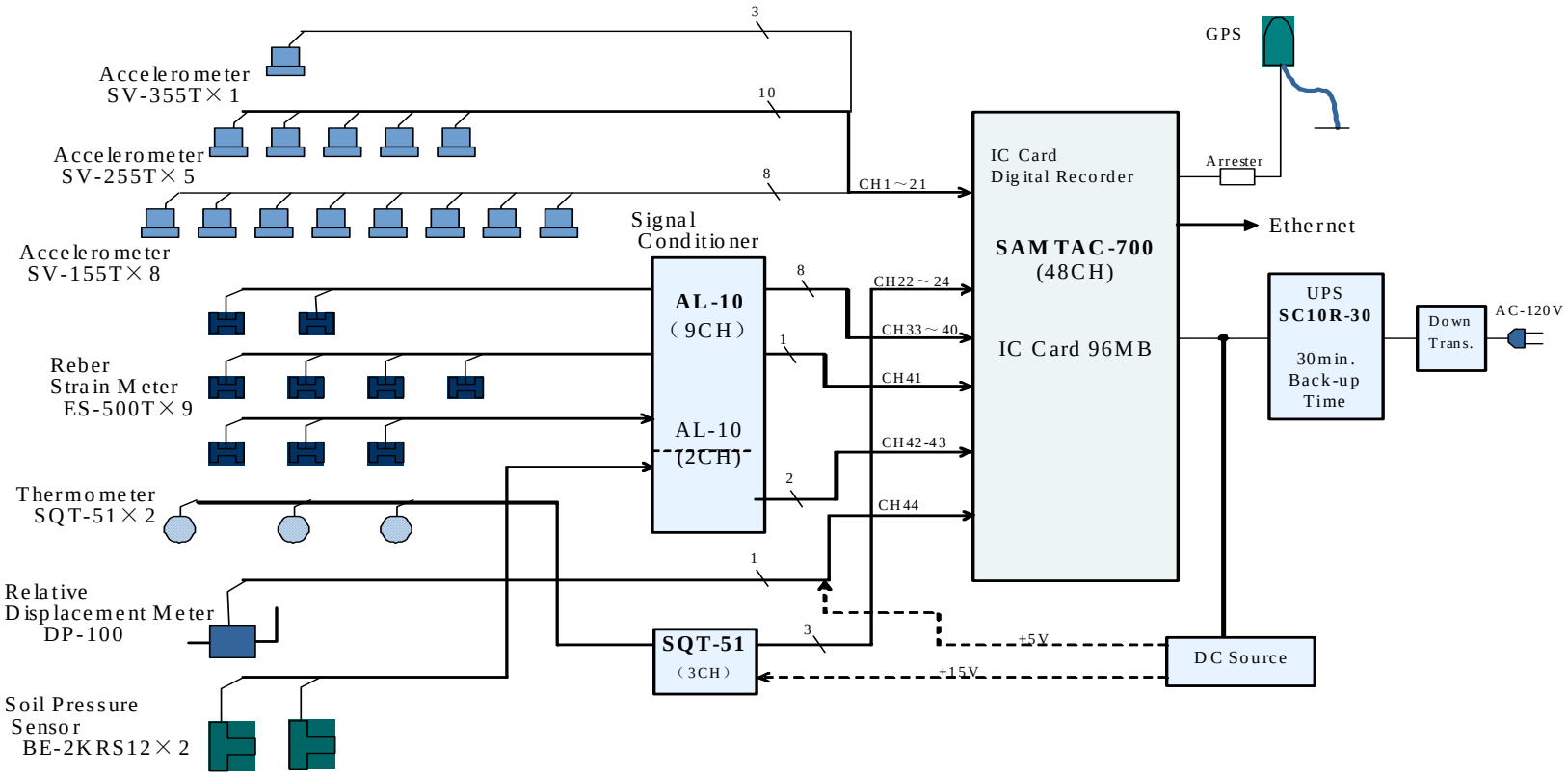

Figure 3.3.25 Map of Channel Assignment of the Data-logger

Chapter 4

VIBRATION DATA

This chapter documents vibration data collected on the three instrumented highway bridges during Phase II of the research project.

Each of the data loggers on the three monitoring systems can be set to continuously monitor 3 channels of accelerometers and if the signals of these three channels meet the selected triggering criteria, the data logger will be automatically triggered to record vibration signals of all sensors. They can also be manually triggered in the control panel to record a 1-minute vibration data file. If a pair of triggering jumper wires is used, the data logger can record continuously as long as the jumper is engaged. In this report, the data files recorded in these 3 modes are cataloged as the 'triggered' data, which are recorded in the compact flash memory cards on the data logs and retrieved and analyzed off-line. On the JRO, however, after the system upgrades, in addition to these 3 modes we are also able to continuously receive 9 channels of the on-line data streamed through the wireless system, and save them on the server computer. Data collected in this mode are the 'streamed' data.

Besides the working modes of the data loggers, vibration data are also cataloged by the different types of excitation sources. The bridge vibrations due to ambient effects (e.g. wind) or traffic loads constitute the majority of the collected data. In this case, the excitation on the bridge structure is not measured, but the bridge response to such excitation is recorded. Usually in such ambient/traffic-induced vibration, the superstructure response exhibits much larger amplitude than the substructure

response, and the vibration is mainly in the vertical direction. Another excitation source is ground motion. During Phase II of the research project, two moderate earthquakes were recorded by the monitoring systems. These ground motion-induced vibrations are both in the transverse and vertical directions. The ground motion sensors pick up considerable vibration at the footing of the substructure, which can be considered as the time-history of the ground motion acceleration that excited the bridge.

4.1 Ambient/Traffic-Induced Vibration on JRO

Since the JRO was instrumented with the monitoring system, total of 1712 data sets have been collected on this bridge.

4.1.1 Triggered Data

After analyzing all the collected data it was observed that the maximum transverse acceleration in the middle of the span is between 2-20 gal; whereas the maximum vertical acceleration ranges between 10-80 gal. Table 4.1.1 documents the triggered vibration data that have been collected.

Table 4.1.1 Summary of Triggered Data on the JRO

Date	Time	$(a_4)_{max}$	Date	Time	$(a_4)_{max}$
05/03/2002	09.29	12	09/10/2004	18.11	21
01/24/2003	08.39	42	05/24/2005	19.07	34
…	…	…	…	…	…

Typical traffic-induced time histories for the vertical and transverse accelerations at middle of Span 2 are shown in Fig 4.1.1.

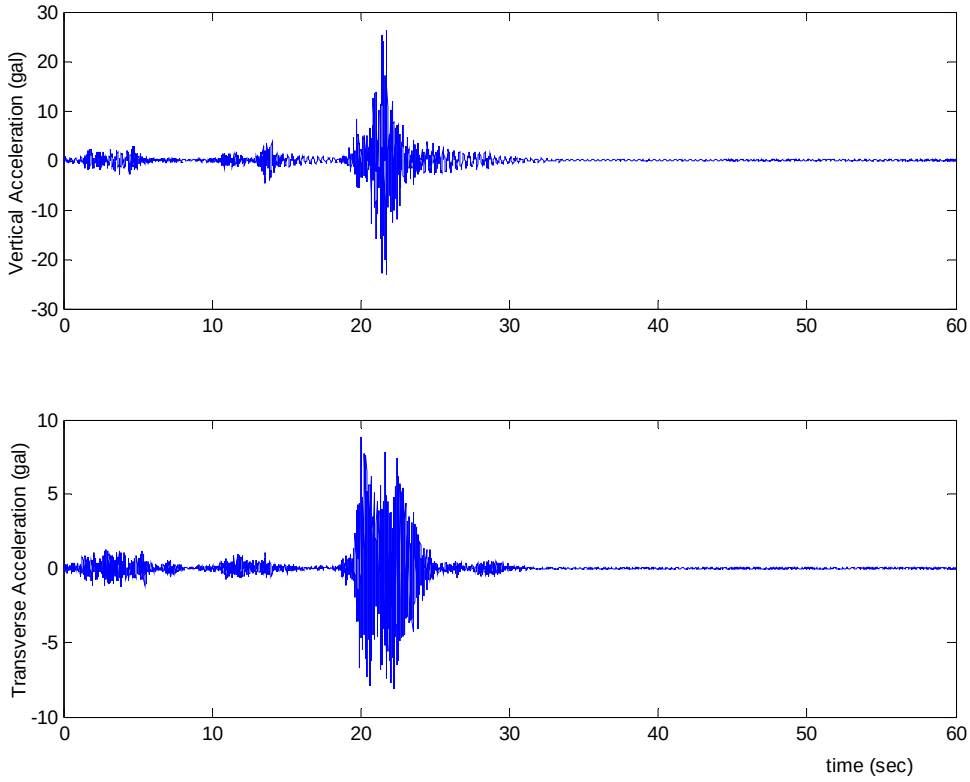

Fig 4.1.1 Saved Traffic-Induced Vibrations at JRO

4.1.2. Streamed Data

Starting August 2006, 5 min long data have been automatically collected every hour. The increase of the data length enabled more precise modal identification results. Table 4.1.2 documents the streamed vibration data that have been collected.

Table 4.1.2 Summary of Streamed Data on the JRO

Date	Time	$(a_4)_{max}$	Date	Time	$(a_4)_{max}$
08/30/2006	11.00	16	09/17/2006	11.00	23
09/02/2006	11.00	22	09/30/2006	11.00	36
…	…	…	…	…	…

Typical traffic-induced time history for the vertical and transverse accelerations at the middle of Span 2 are shown in Fig 4.1.2.

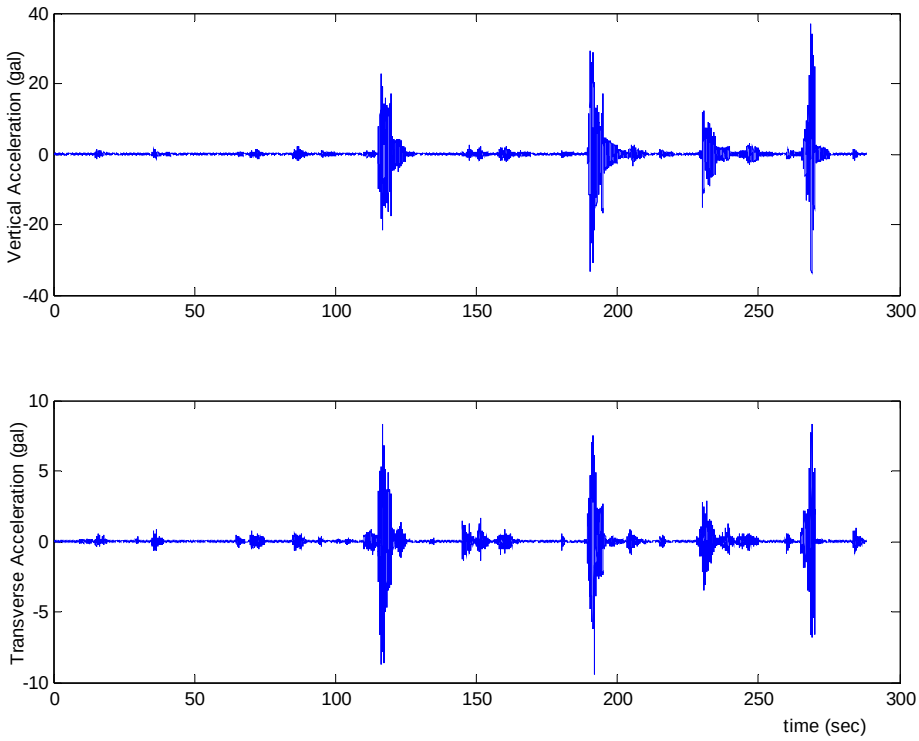

Fig 4.1.2 Scheduled Traffic-Induced Vibrations at JRO

4.2 Moderate Earthquake on JRO

On June 16, 2005, a moderate earthquake occurred at 1:53 pm (PDT) in Yucaipa, CA. The local magnitude is between 4 to 5 MI, and the distance from the epicenter to the JRO is about 105 km (65 miles). The monitoring system at the JRO was triggered by this ground motion and recorded this event. The record shows a peak ground acceleration in North-South of 11.6 gal, in East-West of 13.0 gal and vertical of 3.55 gal. These values are consistent with the Shake-Map instrumental intensity maps (Fig. 4.2.1).

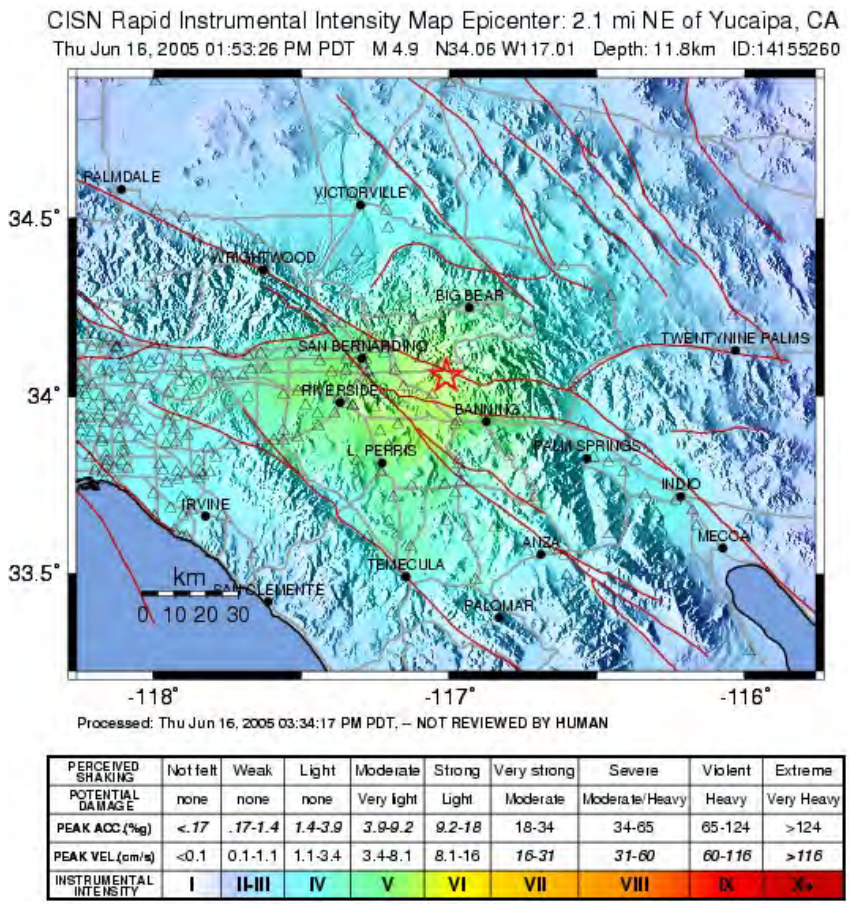

PERCEIVED SHAKING	Not felt	Weak	Light	Moderate	Strong	Very strong	Severe	Violent	Extreme
POTENTIAL DAMAGE	none	none	none	Very light	Light	Moderate	Moderate/Heavy	Heavy	Very Heavy
PEAK ACC.(%g)	<.17	.17-1.4	1.4-3.9	3.9-9.2	9.2-18	18-34	34-65	65-124	>124
PEAK VEL.(cm/s)	<0.1	0.1-1.1	1.1-3.4	3.4-8.1	8.1-16	16-31	31-60	60-116	>116
INSTRUMENTAL INTENSITY	I	II-III	IV	V	VI	VII	VIII	IX	X+

Fig. 4.2.1 Instrumental Intensity Map by Shake-map

The earthquake records of the selected channels are plotted in Fig. 4.2.2. One can observe that the earthquake excited bridge vibration in the transverse direction more than the traffic does. Transverse vibration (Ch-3) in the middle of span 2 has an amplitude of 25 gal, comparable to that of the vertical direction (Ch-4) in the same event, but much larger than the transverse vibration induced by traffic. The bridge vibration near the ground, such as Ch-10, is much stronger than that under traffic excitation. Peak ground accelerations for this event are given in Table 4.4.1. Also note that the vertical vibration remains in the same level for both traffic excited and earthquake excited vibrations. One can see the impulse-like pattern in the vertical vibration record during the event, indicating vehicles passing the bridge during the earthquake event.

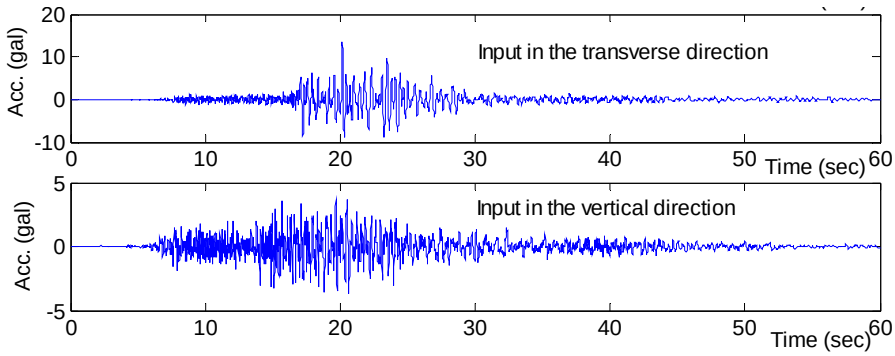

(a) Input Motion

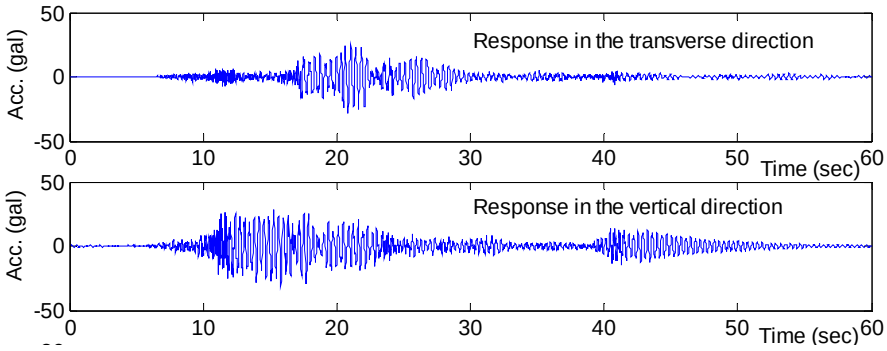

(b)Earthquake Response

Figure 4.2.2 Typical Earthquake Records on JRO

Table 4.4.1 Peak Ground Motion at the JRO

Direction	Longitudinal	Transverse	Vertical
Peak Ground Acceleration (gal)	11.6	13.0	3.6

4.3 Ambient/Traffic-Induced Vibration on WSO

Ever since the WSO bridge was instrumented with a monitoring system, total of 92 data sets have been collected on this bridge. Some examples can be seen in Table 4.3.1.

Table 4.3.1 Summary of Collected Triggered Data on the WSO

Date	Time	$(a_9)_{max}$	File Name	Date	Time	$(a_{10})_{max}$	File Name
5/17/05	1:21:29	0.0256	1D62155D	5/17/05	1:21:29	0.1028	1D62155D
9/26/05	11:31:16	0.0293	1E74B7D0	9/26/05	11:31:16	0.2032	1E74B7D0
…	…	…	…	…	…	…	…

Typical traffic induced time history for the vertical and transverse accelerations recorded at the middle of Span 2 are shown in Fig 4.3.1.

4.4 Moderate Earthquake on WSO

There was a moderate earthquake on 16 July, 2005. The ground motions of the earthquake are shown in Fig. 4.4.1. The peak acceleration of each direction is shown

in Table 4.4.1. Unlike the vibration induced by traffic, the transverse direction is most dominant component.

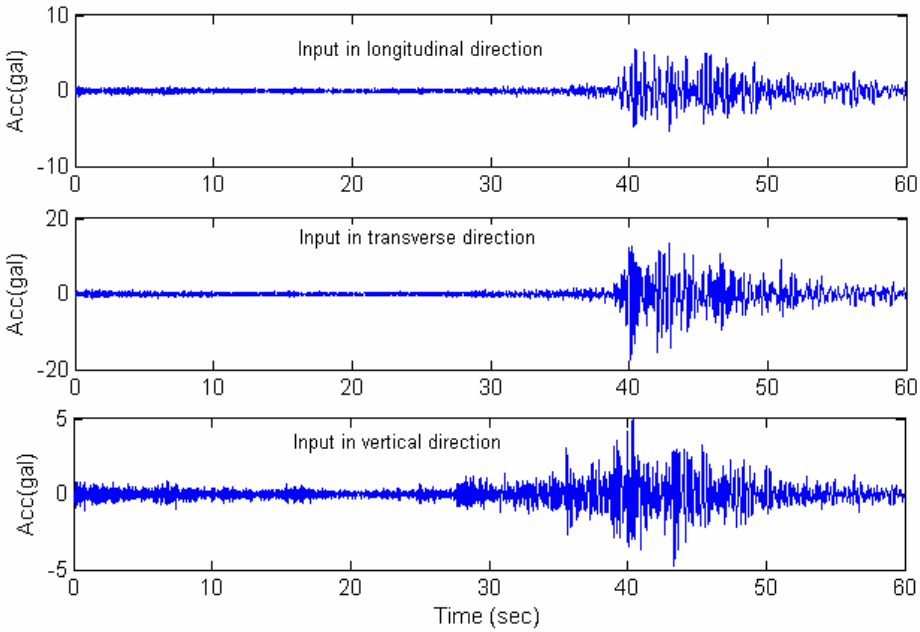

(a) Input ground motion

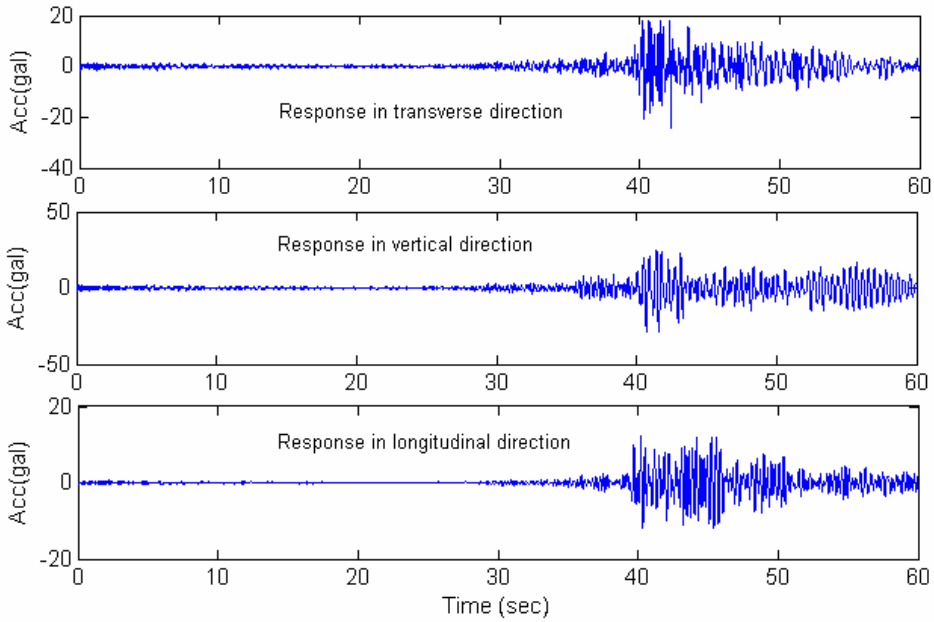

(b) Earthquake response

Figure 4.4.1 Typical Earthquake Records on WSO

Table 4.4.1 Peak Ground Motion at the WSO

Direction	Longitudinal	Transverse	Vertical
Peak Ground Acceleration (gal)	5.6	13.6	5.0

4.5 Ambient Vibration Data on FROO

Figure 4.5.1 shows the typical acceleration time history of the Fairview On Ramp at the middle of span 3. In Table 4.5.1 the examples of monitored peak acceleration values are shown.

Table 4.5.1 Summary of collected data on the FROO

Date	Time	$(a_9)_{max}$ *	File Name	Date	Time	$(a_9)_{max}$ **	File Name
3/20/2006	16:05:35	0.3019	20E90163	3/20/2006	16:05:35	0.1826	20E90163
3/20/2006	16:17:34	0.1755	20E90462	3/20/2006	16:17:34	0.1336	20E90462
…	…	…	…	…	…	…	…

*: Vertical direction, ** : Transverse direction.

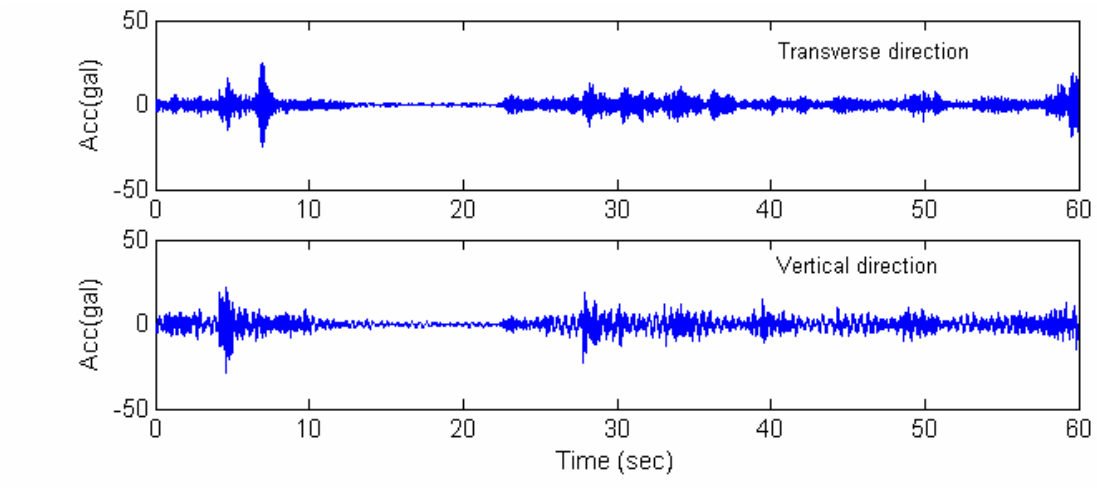

Figure 4.5.1 Time History of FROO (Middle of Span 3)

Chapter 5

STRAIN DATA AND ANALYSIS

In this chapter, dynamic strain data from the West St. On-Ramp (WSO) under traffic loads were analyzed and compared with the those based on moving-load analysis. From the results, it was found that in the WSO the transverse mode was excited by heavy moving vehicle and it caused higher strain in the column than that predicted in the design.

5.1 Strain Sensors and Locations

The strain sensors were permanently embedded in concrete members of the West Street On-Ramp (WSO) during construction. The strain gauges were completely welded to dummy reinforcing bars. The specification of the strain gauges is shown in Table 5.1.1. The sensors were installed to measure the dynamic strains induced by bending moments. The locations of strain gauges are shown in Fig 5.1.1

Table 5.1.1 Strain Gauge Specification

Parameter	Specification
1. Model	ES-500T
2. Strain range	±1000μ Srain
3. Average resolution	0.01μ Srain
4. Average sensitivity	0.55 mV/μStrain
5. Temperature coefficient	0.7×10^{-5}/°C (-20 to +60°C) 85μV/kg
6. Gauge length	500mm
7. Frequency response	DC - 50Hz
8. Cable	4 Conductor, shielded (Extensible length 300m)

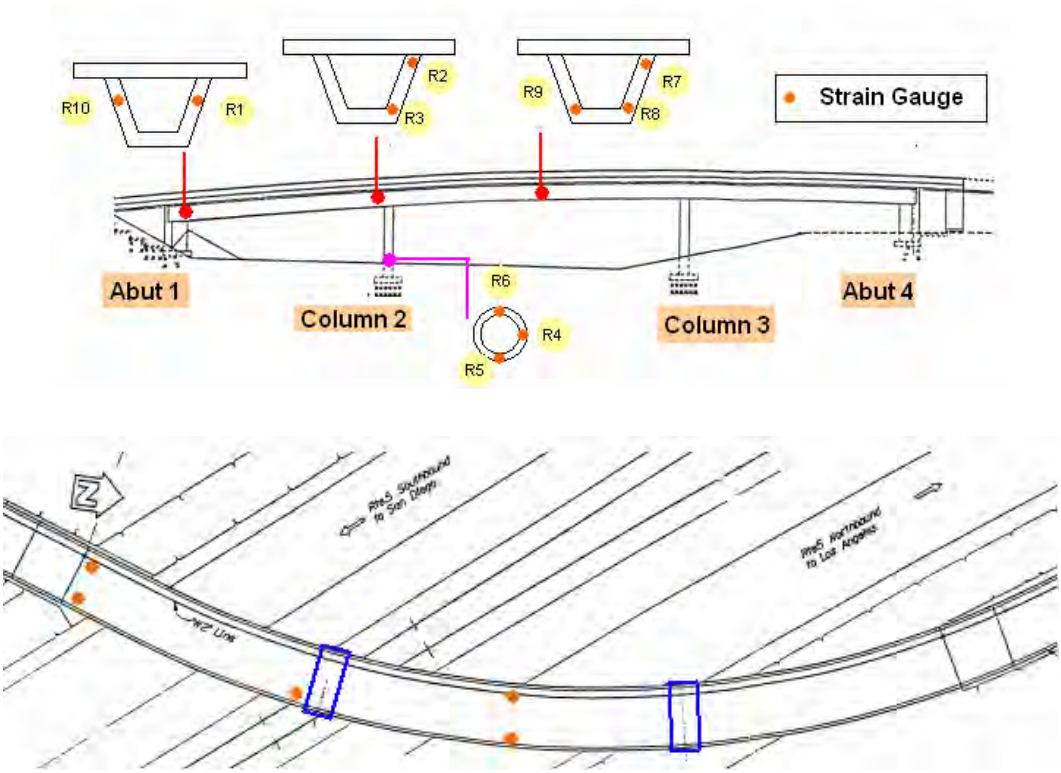

Fig.5.1.1 Strain gauge locations of WSO

5.2 Characteristics of Dynamic Strain Data

The dynamic strain time history of each sensor assembles the moment influence line at the sensor location. In this section, the characteristics of the dynamic strain time history were discussed in comparison with the static moment influence line.

5.2.1 R1 and R10

The strain gauges R1 and R10 are embedded in the girder near Abutment 1 of the bridge. R1 is located in the outer girder while R10 inner girder. As shown in Figure.5.2.1, the influence line of the moment at R1 and R10 shows sharp increase and gradual decrease. The same trend was observed from the recorded data for R1 as shown in Figure 5.2.2. From the influence line and the recorded data, one can observe that when a vehicle enters the bridge the strain at R1 increases abruptly and as the vehicle passes through, the strain decreases gradually. However, as depicted in Figure 5.2.3, R10 does not show the same pattern as R1. It is considered that R10 is not reliable.

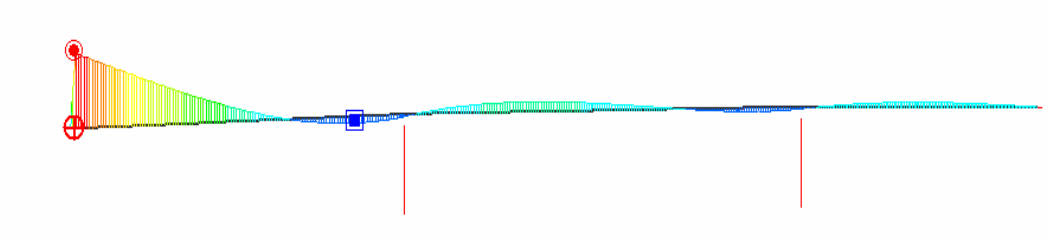

Figure.5.2.1 Influence Line for R1 and R10

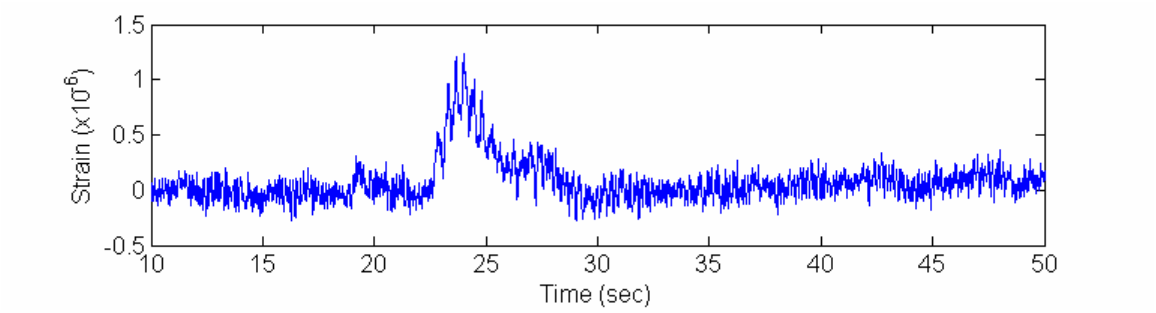

Figure.5.2.2 Strain Time History of R1

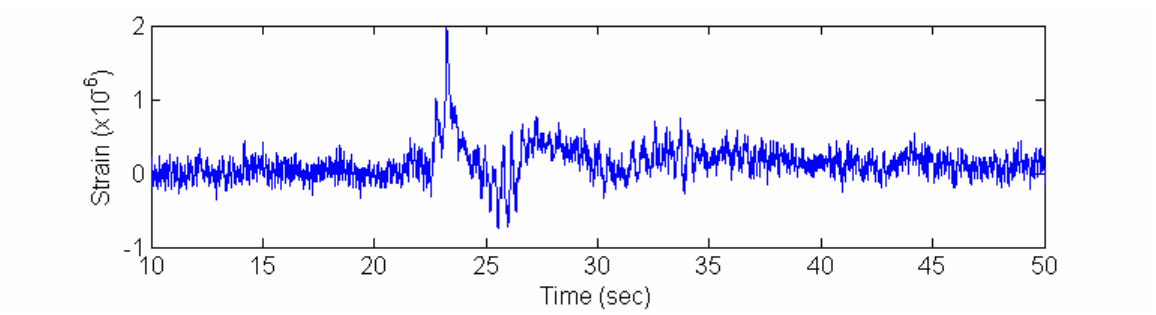

Figure.5.2.3 Strain Time History of R10

5.2.2 R2 and R3

Sensors R2 and R3 are located in the outside girder above column 2 outside of the diaphragm. R2 is embedded in the upper part of the girder while R3 in the lower part of the girder. Influence lines for R2 and R3 are respectively shown in Figures 5.2.4 and 5.2.5. Because these two strain gauges are located in the upper and lower parts of the same cross section, they show opposite strain signs at the same time. From the influence lines, it can be inferred that the strain value is higher when vehicle traverses on span 1 than other spans, and each influence line has two peaks.

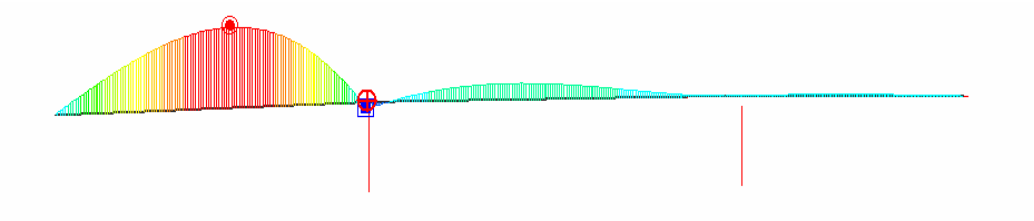

Figure.5.2.4 Influence Line of R2

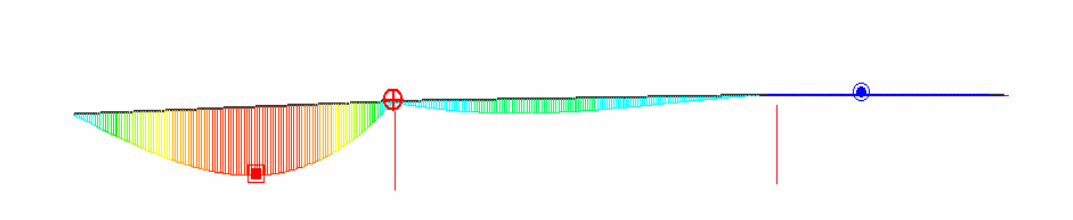

Figure. 5.2.5 Influence Line of R3

Similar trend is observed from the time histories of R2 and R3. The recorded time history of R2 and R3 are shown in Figures 5.2.6 and 5.2.7.

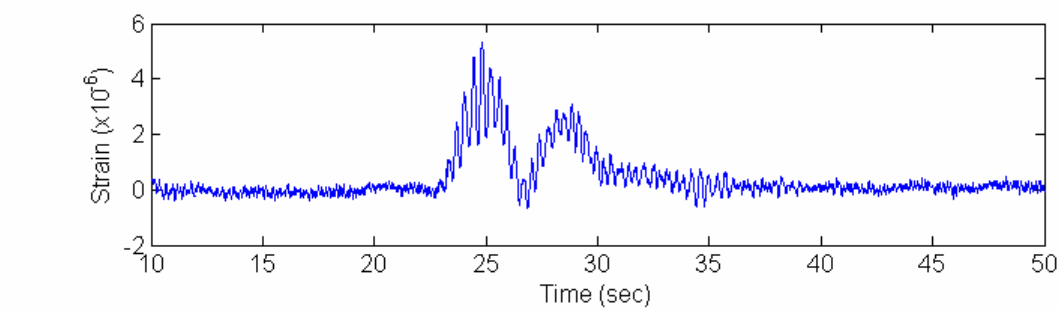

Figure.5.2.6 Strain Time History of R2

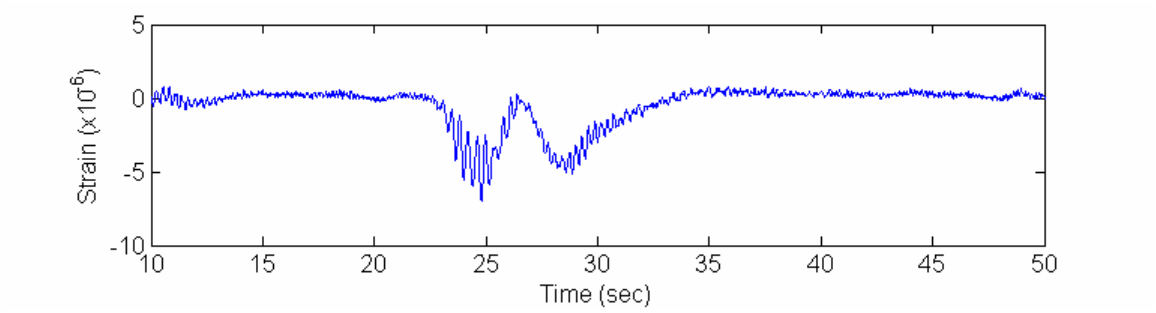

Figure. 5.2.7 Strain Time History of R3

5.2.3 R4, R5, and R6

The strain sensors R4, R5, and R6 are located in the column 2 under the ground level. The location of each sensor can be seen in Figure. 5.1.3. The influence line of R4 in Figure.5.2.8 shows one and half cycle. The same trend can be seen from strain time history of R4 in Figure.5.2.9. It should be noted that the strain sensors located in the column shows both signs with almost the same strain values for both tension and compression. It means that the column experiences both tension and compression when vehicle traverses the bridge.

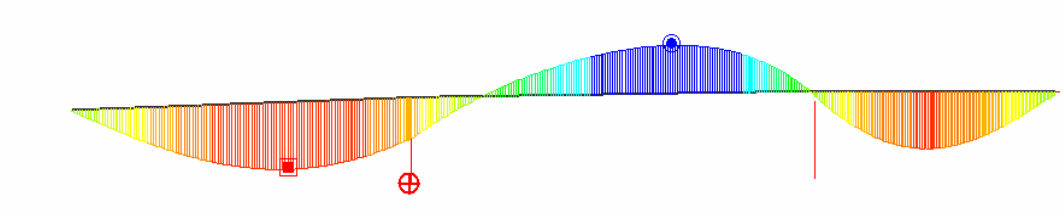

Figure.5.2.8 Influence Line of R4

R5 and R6 are located on the opposite side of the column 2 in the transverse direction. Thus, when R5 is in tension then R6 is in compression and vice versa. Therefore it can be inferred that R5 and R6 show approximately the same strain value with opposite signs. The recorded strain time histories of R5 and R6 are shown in Figures 5.2.10 and 5.2.11.

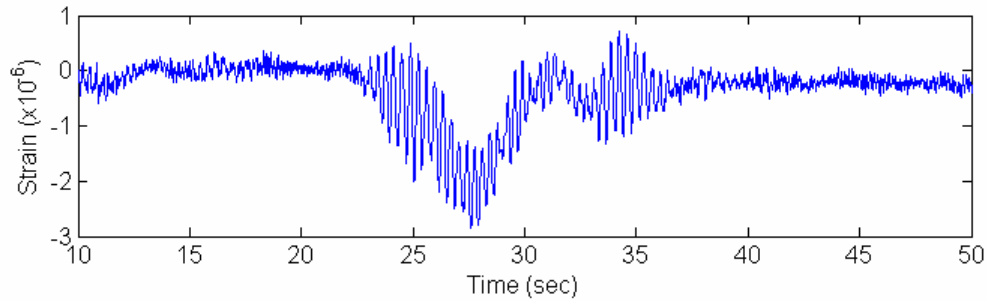

Figure.5.2.9 Strain Time History of R4

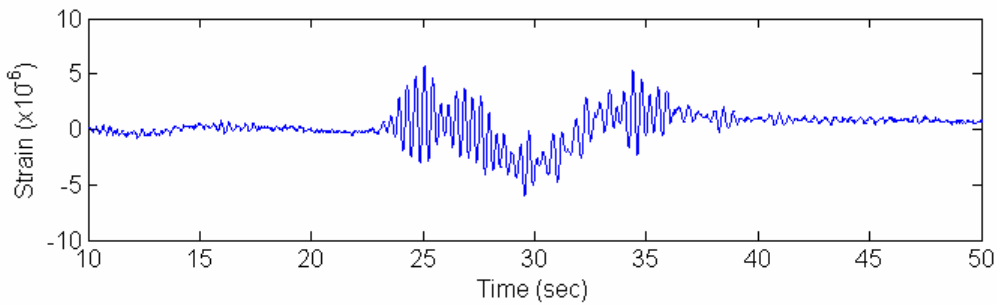

Figure. 5.2.10 Strain Time History of R5

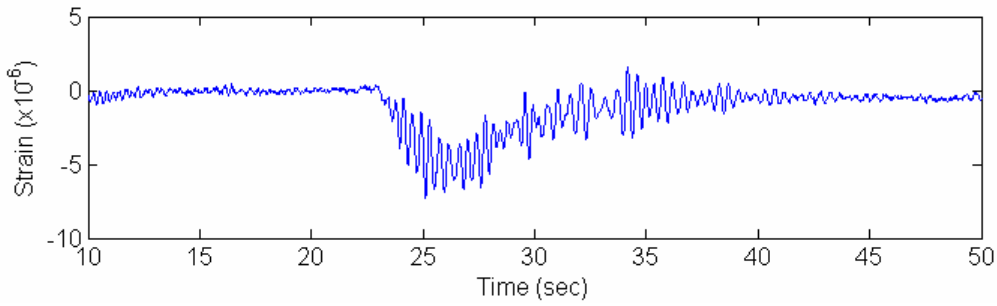

Figure.5.2.11 Strain Time History of R6

5.2.4 R7, R8, and R9

The sensors R7, R8, and R9 are embedded in the middle of span 2. R7 is located at the upper part of the outside girder. R8 and R9 are located at the lower part of the girder. R8 is in the outside girder and R9 in the inside girder. The moment at the middle of span 2 is negative when a moving vehicle is located on the span 1 and 3 but it is positive on the span 2.

Figures 5.2.12 and 5.2.13 show the influence lines of R7 and R8 (R9) respectively. Since R7 is located at the upper part of the girder, the strain data should show the exact opposite sign to R8 and R9. As depicted in Figure 5.2.14, however, the monitored data at R7 did not show the expected trend. The sensor at R7 is believed to be out of order. Figures 5.2.15 and 5.2.16 show the time histories of the strains at R8 and R9. The shape of the time histories is the same as the compressed shape of influence line of R8.

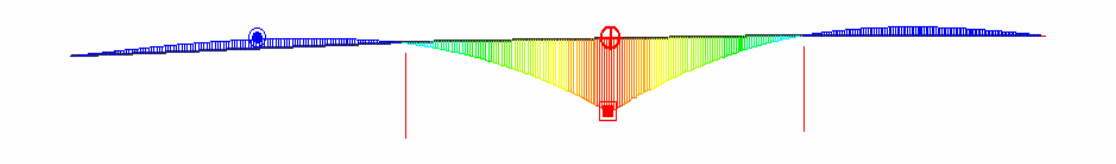

Figure. 5.2.12 Influence Line of R7

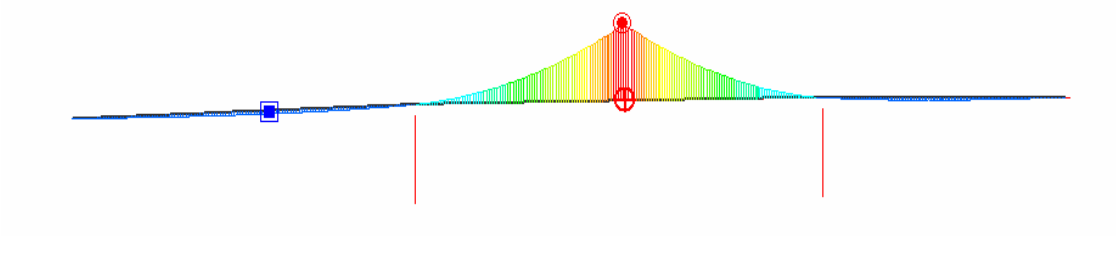

Figure. 5.2.13 Influence Line of R8 and R9

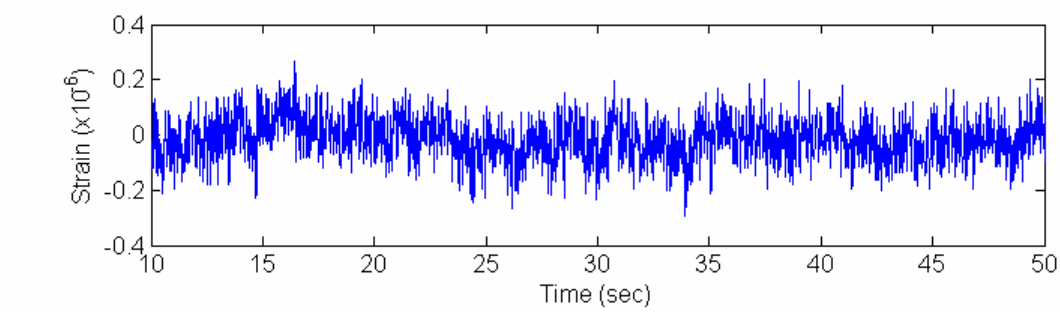

Figure. 5.2.14 Strain Time History of R7

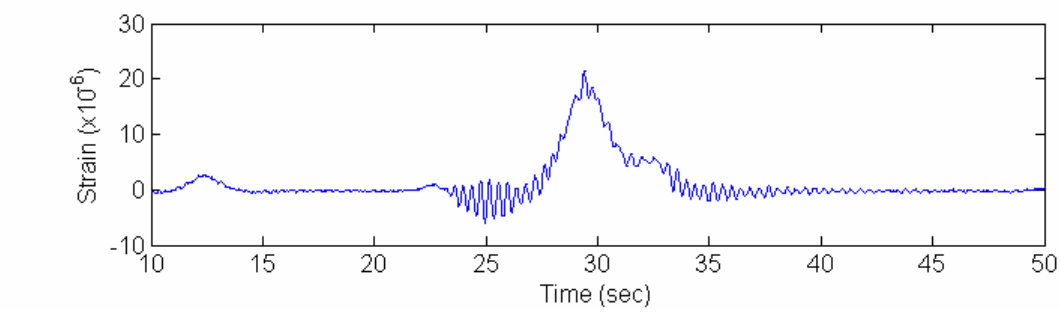

Figure. 5.2.15 Strain Time History of R8

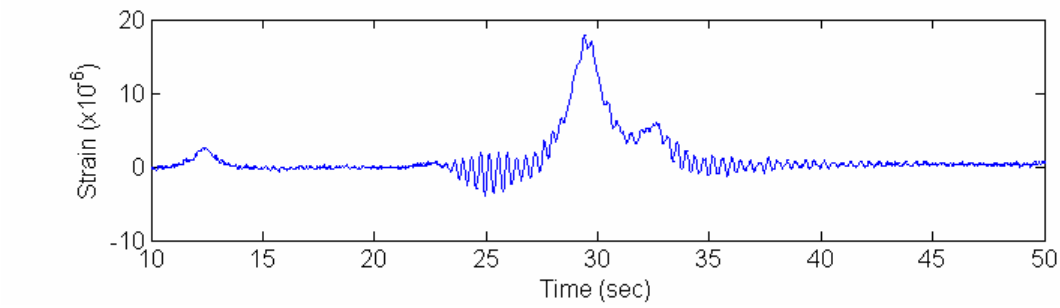

Figure. 5.2.16 Strain Time History of R9

5.3 Comparison of Measured and Computed Strain

The maximum and minimum strains measured by each strain sensor were compared with that computed from the moving load analysis. The dynamic effect of the design live load was represented by employing an impact factor. The centrifugal force due to the curvature of the bridge was also considered in the analysis. The computed maximum strains of in the girder showed higher values than those from the measurement. However, the measured strains of the column were higher than the computed ones. From analysis of the measured strains and accelerations, the high strains at the columns were attributed to the transverse vibration excited by moving vehicles.

5.3.1 Measured Maximum Strain

(1) R1 and R10

The maximum strain of each data sets for R1 and R10 is shown in Figure. 5.3.1. The maximum strain values of R1 and R10 are 2.282μ and 2.246μ respectively. Though the maximum strain of these two strain sensors is nearly the same, the average strain of R10 is much smaller than R1. The average strain of R1 and R10 is 1.047μ and 0.614μ. The maximum values and the average values of all the strain sensors are shown in Table 5.3.1.

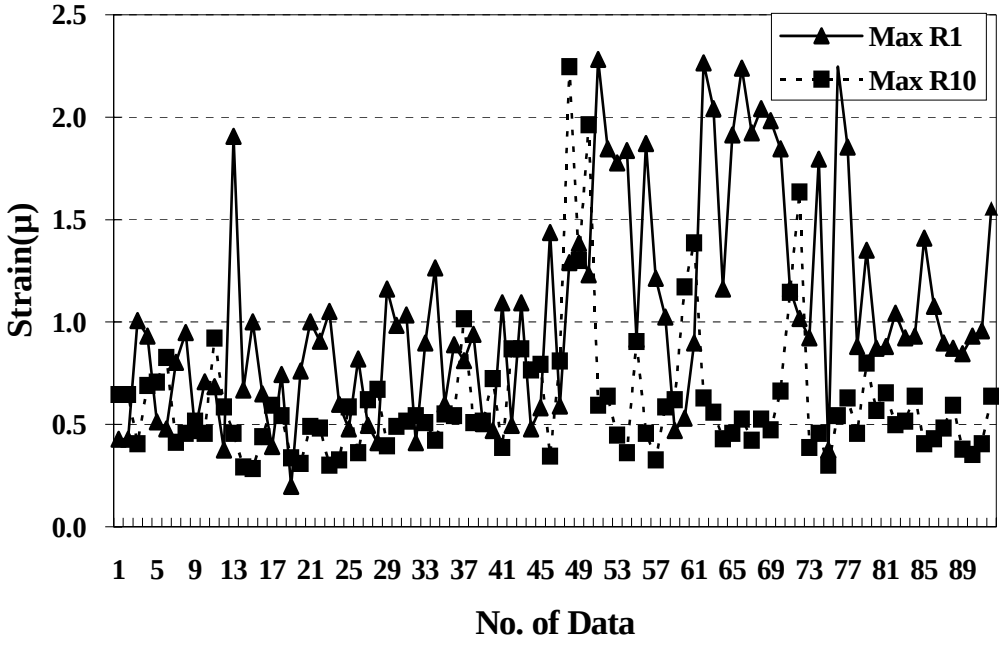

Figure.5.3.1 Maximum Strain of R1 and R10

Table 5.3.1 Measured Strain

Sensor	Maximum (μ)	Max. Average (μ)	Minimum (μ)	Min. Average (μ)
R1	2.282	1.047	-0.641	-0.298
R2	6.686	2.726	-3.222	-0.635
R3	3.312	0.831	-7.751	-3.482
R4	5.364	1.072	-4.138	-1.451
R5	11.132	2.463	-14.828	-4.738
R6	12.745	2.379	-7.326	-2.049
R7	0.440	0.256	-0.399	-0.249
R8	18.513	6.494	-5.204	-1.640
R9	21.471	10.317	-7.035	-2.2132
R10	2.246	0.614	-1.489	-0.505

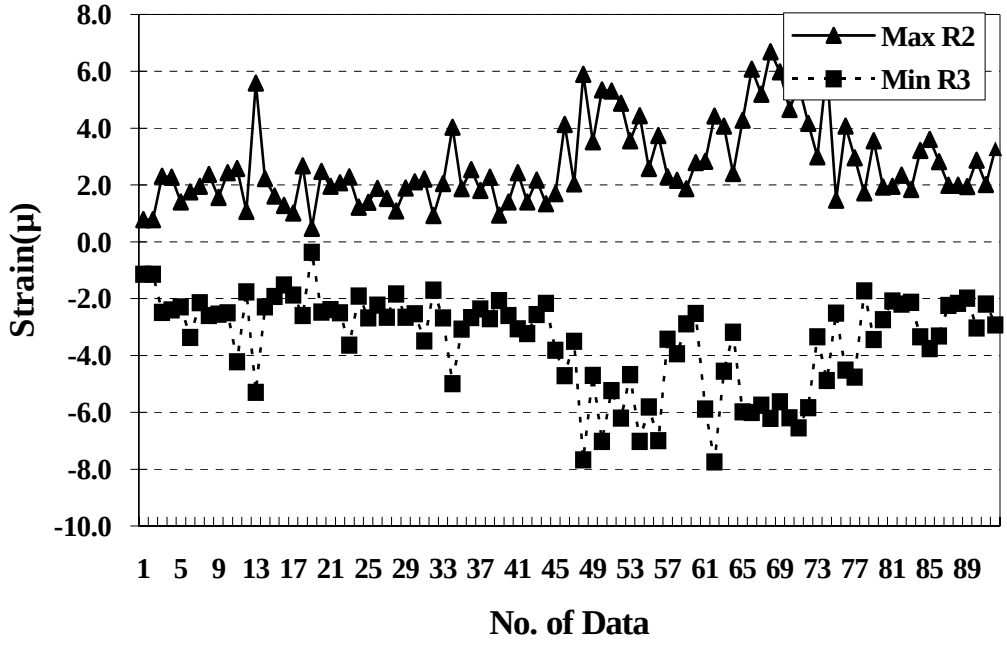

Figure. 5.3.2 Maximum Strain of R2 and R3

(2) R2 and R3

The maximum strain values of R2 and R3 are shown in Figure. 5.3.2. Because of the sensor locations of R2 and R3, the maximum strain at R2 corresponds to the minimum one at R3. The largest strain of R2 is 6.686μ while the smallest value of R3 is –7.751μ. The average strain value of R2 and R3 is 2.726μ and –3.482μ.

(3) R4, R5, and R6

The maximum and minimum strain of R4, R5, and R6 are shown in Figures 5.3.3 through 5.3.5. From Figure 5.3.3 the maximum tensile and compressive strain of R4 are approximately the same. It means that the column experiences the same negative and positive moment in the longitudinal direction. Figures 5.3.4 and 5.3.5 for R5 and

R6 indicate that column 2 is subject to both negative and positive moments in the transverse direction as well.

The maximum tensile and compressive strains of R4 are 5.364μ and –4.138μ respectively. The maximum and minimum strain of R5 are 11.132μ, –14.828μ, and those of R6 are 12.745μ and –7.326μ respectively.

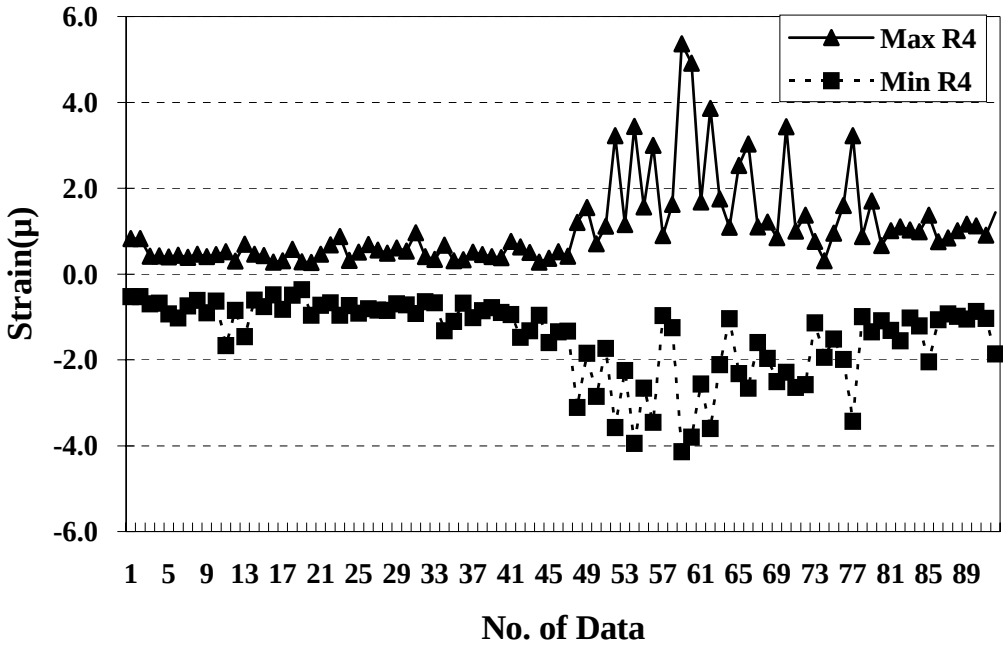

Figure. 5.3.3 Maximum and Minimum Strain of R4

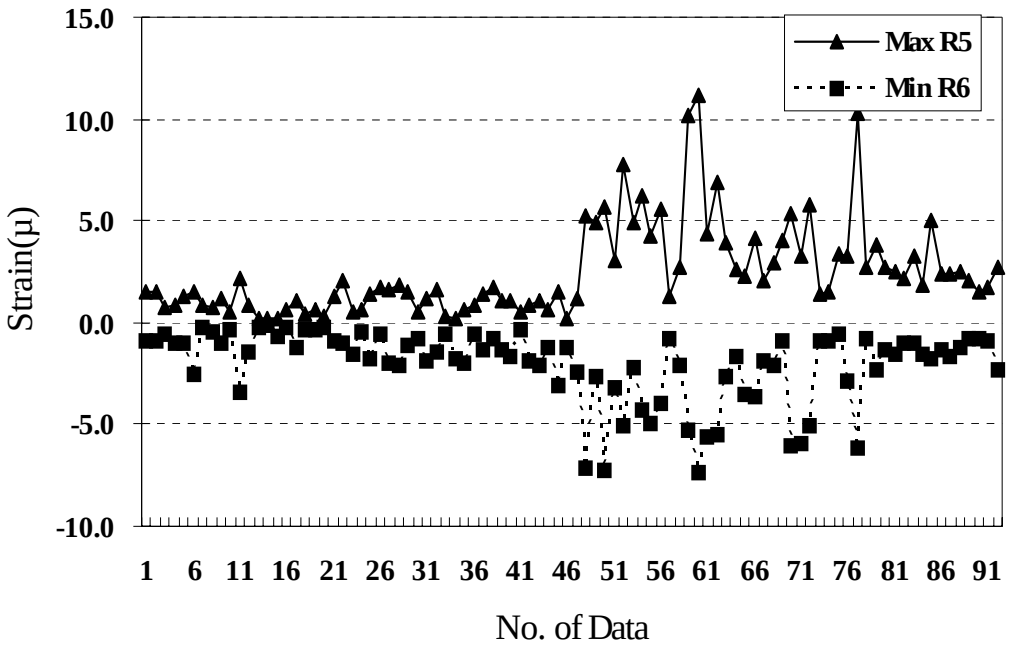

Figure. 5.3.4 Maximum Strain of R5 and Minimum strain of R6

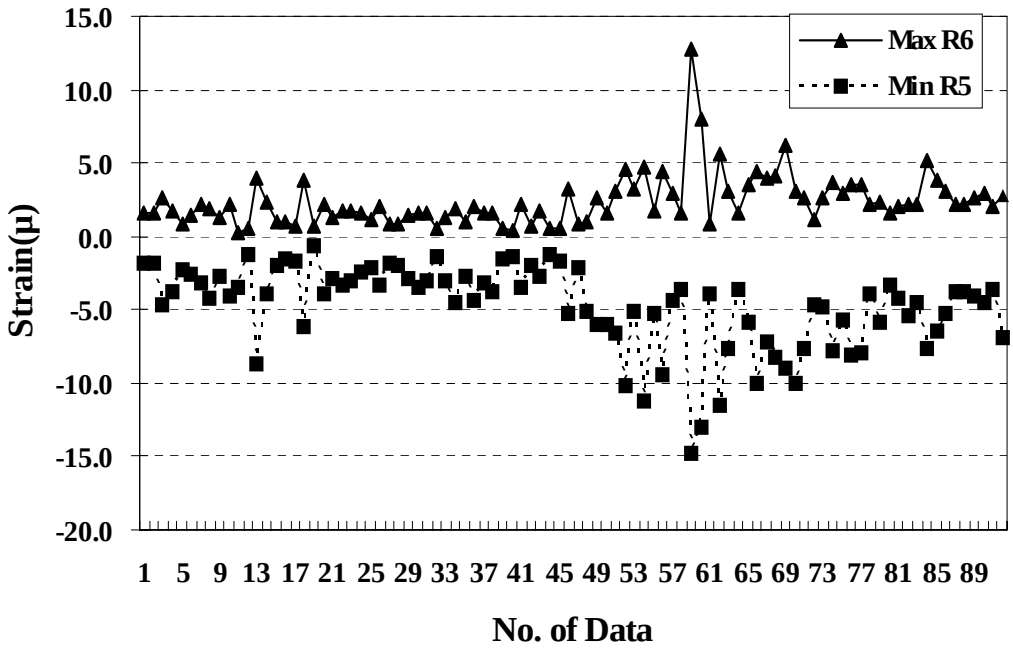

Figure. 5.3.5 Maximum Strain of R6 and Minimum Strain of R5

(4) R7, R8, and R9

Figure 5.3.6 shows the minimum strain at R7 while Figure 5.3.7 the maximum strains at R8 and R9. Considering the locations of R7 and R8 or R9, the absolute strain value of R7 should be similar to that of R8 or R9, but all the strain values of R7 are between 0 and -0.4μ. The strain sensor at R7 is thus considered to be out of order.

The maximum values of strains at R8 and R9 are respectively 18.513μ and 21.471μ. It is found that the strain at R9 is larger than that at R8. The average strain of R8 is 6.494μ and that of R9 is 10.317μ. The strain difference between R8 and R9 is attributed to the their locations; R9 is located in the inside girder while R8 the outside girder.

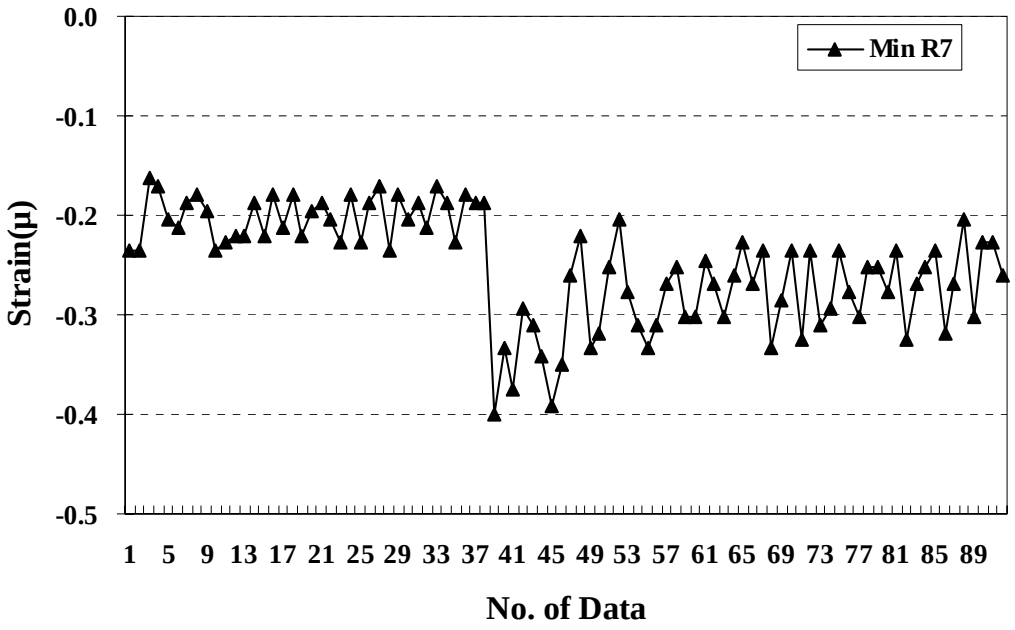

Figure. 5.3.6 Minimum Strain of R7

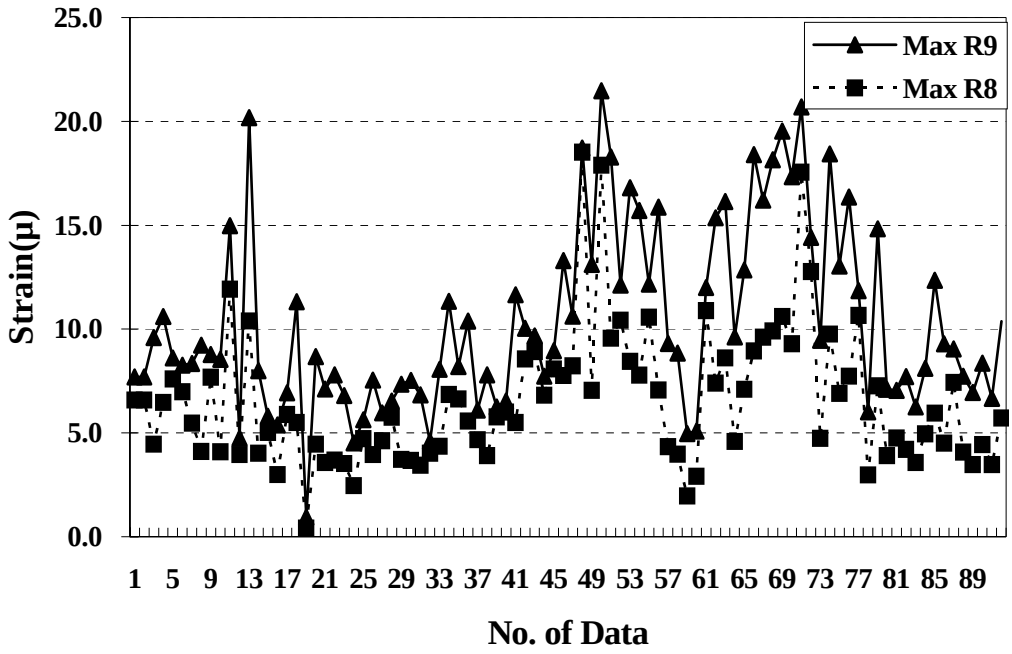

Figure. 5.3.7 Maximum Strain of R8 and R9

5.3.2 Finite Element Analysis under Design Live Load

(1) Finite Element Model

For the comparison of the monitored strain data with analytical one, finite element (FE) analysis was carried out. Three-dimensional beam elements were used for the deck and column components of the bridge. The superstructure has 12% inclination in the transverse direction and it was represented using the angular rotation of the element local axis. The superstructure was modeled with totally 200 beam elements and a column with 16 beam elements. Figure.5.3.8 shows the FE model of the bridge.

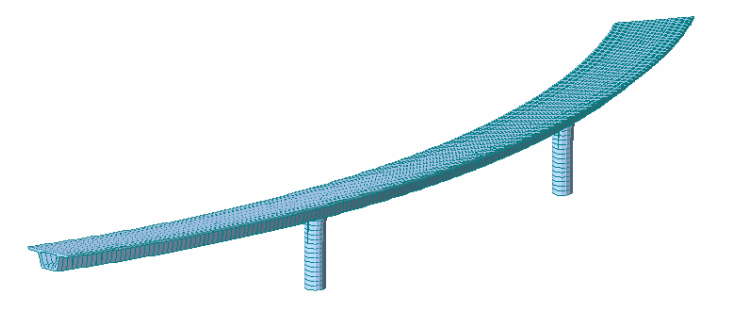

Figure. 5.3.8 Finite Element Model of WSO

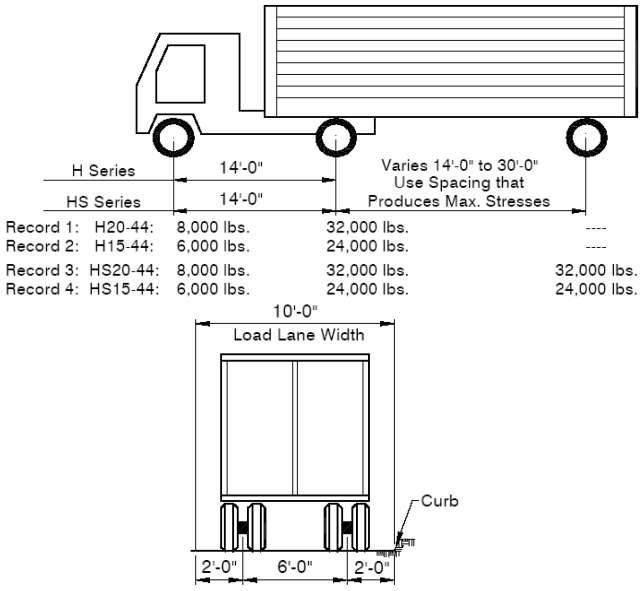

Figure. 5.3.9 HS 20-44 Load

The most difficult aspect is to model the bridge boundary conditions - the column footing and abutments realistically and accurately. Considering that the use of the model is for analyzing the bridge response to operational traffic loads, the abutment bearings of the bridge were modeled as linear horizontal, vertical, and rotational springs, while the footing piles as fixed. The bearing stiffness values at both the abutments were assigned according to FHWA (1996) as 6.58×10^4 kip/ft for the longitudinal springs, and 1.29×10^5 kip/ft and 1.48×10^5 kip/ft for the transverse and vertical springs respectively. The rotational spring stiffness are 6.29×10^7 kip-ft/rad

and 3.5×10^{7} kip-ft/rad for longitudinal and transverse direction axis. It is noted that these values were used for the preliminary finite element analysis. They later were identified and updated by the vibration measurement as shown in Chapter 9.

(2) Moving vehicle load

The design live load HS 20-44 load was used for moving vehicle load analysis. Figure 5.3.9 shows the axial load and spacing of the HS 20-44 load. The total axial load of HS20-44 is 72kips and the width of the truck is 10 feet. The WSO has two traffic lanes of 24 feet but the possible traffic passage lanes were defined based on the width of HS20-44. A total of 12 lanes were defined as shown in Figure5.3.10. The lanes from R3 to R8 are located on the inside of the horizontal curvature of the bridge and the lanes from L3 to L8 on the outside. The number after 'R' and 'L' represents the eccentricity of the lane from the center of the bridge.

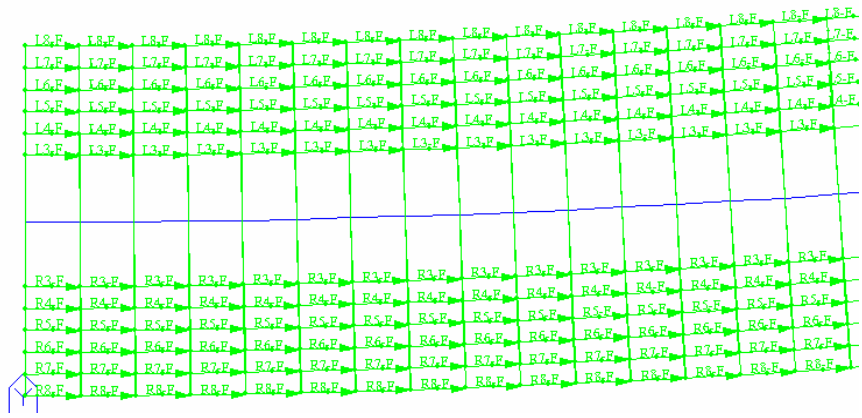

Figure. 5.3.10 Lanes for moving load analysis

(3) Centrifugal Force

Centrifugal force exerted by moving vehicles due to the curvature of the bridge was considered in the finite element model according to the design specification.

Centrifugal force was taken as the product of the axle weights of the design truck and the factor C computed as:

$$C = \frac{4}{3}\frac{V^2}{gR}$$

where:

V= vehicle speed (ft/sec)

g = gravitational acceleration: 32.2 (ft/sec)

R= radius of curvature of traffic lane (ft)

Centrifugal forces were applied horizontally at a distance 6.0 feet above the roadway surface. It was found from the finite element analysis that girder strain under centrifugal forces was less than 1.5 μ but the column strain was more than 6 μ. So the centrifugal forces affected more on the column strain than the girder strain.

(4) Strain sensitivity to lanes

Figure. 5.3.11 to 5.3.16 show the strain at each sensor location from the FE analysis and Table 5.3.2 summarizes the FE analysis results together with the monitored data. From the figures it can be seen that each strain varies according to the vehicle location. Sensitivity coefficient S is defined in Eq. (5-1) in order to compare the sensitivities of each strain sensor to the vehicle location.

$$S(\%) = \frac{\mu_{\max} - \mu_{\min}}{\mu_{\min}} \times 100 \qquad (5\text{-}1)$$

where S : Sensitivity

$\mu_{\max}$: Maximum strain value of FE results

$\mu_{\min}$: Maximum strain value of FE results

The sensitivity coefficients for all the strain sensors are plotted in Figures 5.3.11 through 5.3. 16. The sensitivity of R1 and R10 is 2.82% and that of R2 and R3 is 52.82% while the sensitivity of R7, R8, and R9 is 40.68%. The sensitivity values of R1 and R10 are very low compared with those of other sensors. These two sensors are installed near the abutment (entrance) of the bridge, and thus the moment does not change much due to the different locations of the vehicle. The large sensitivity values for the sensors installed in the girder above the column 2 and at the middle of span 2 imply that the moments at those locations are quite dependent on the location of vehicle load in the transverse direction.

The column, as mentioned earlier, shows both tensile and compressive strains when a vehicle traverses the bridge. The sensitivity values for the column are quite different for tension and compression. For example, the sensitivity value of R4 is 84.51% for tensile strain and 29.51% for compressive strain, and those for R5 (R6) are 226.64% and 4.61%. Though the absolute strain values are not large compared with those of R8 and R9, the sensitivity values of the column are much larger than those of the girder.

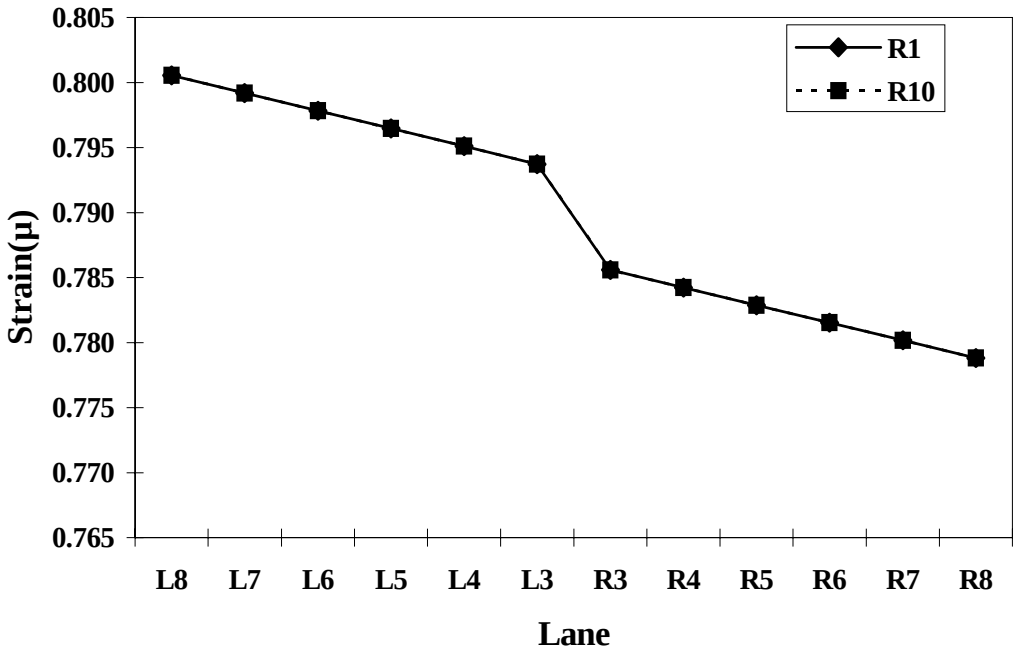

Figure. 5.3.11 Strain R1 and R10 due to Vehicle Locations

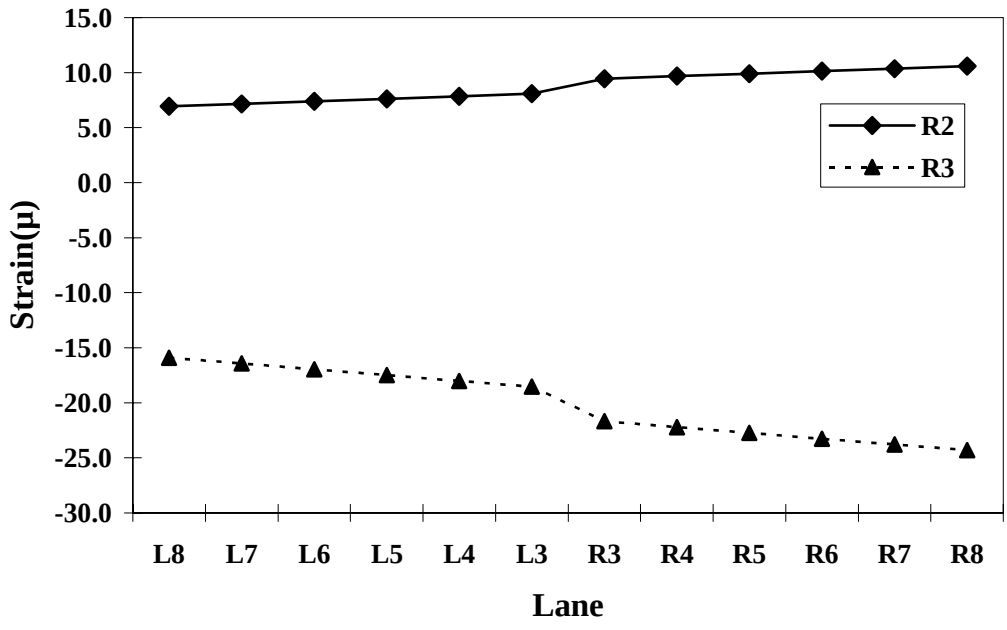

Figure. 5.3.12 Strain R2 and R3 due to Vehicle Locations

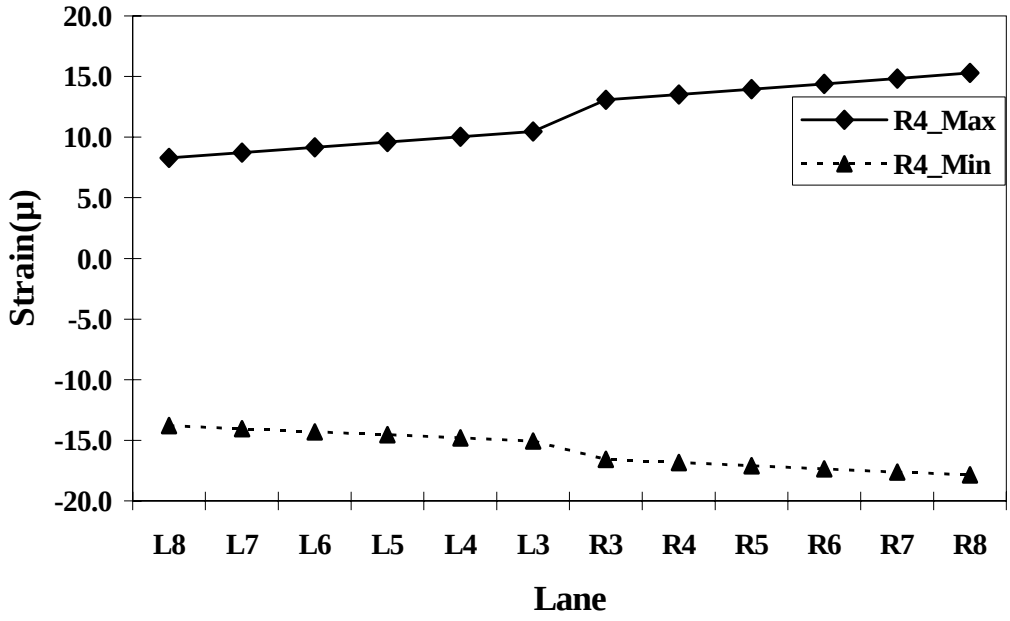

Figure. 5.3.13 Strain R4 due to Vehicle Locations

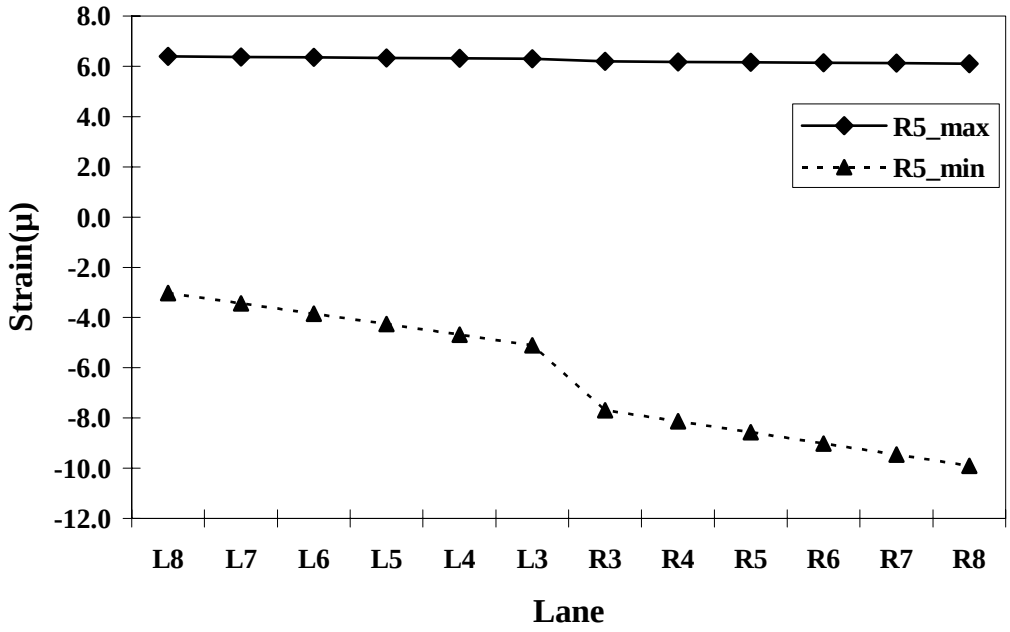

Figure. 5.3.14 Strain R5 due to Vehicle Locations

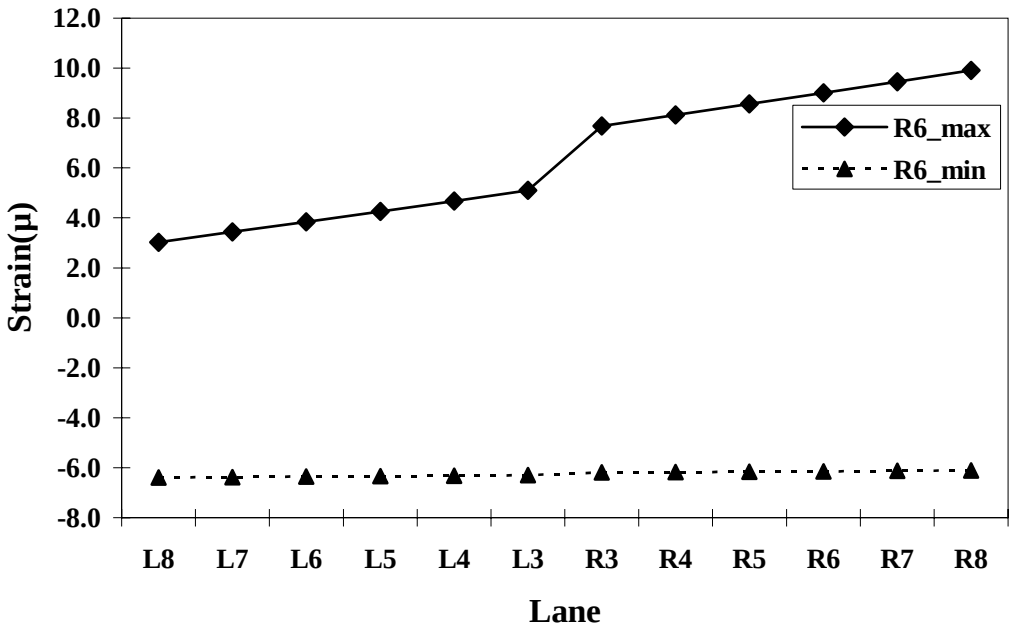

Figure. 5.3.15 Strain R6 due to Vehicle Locations

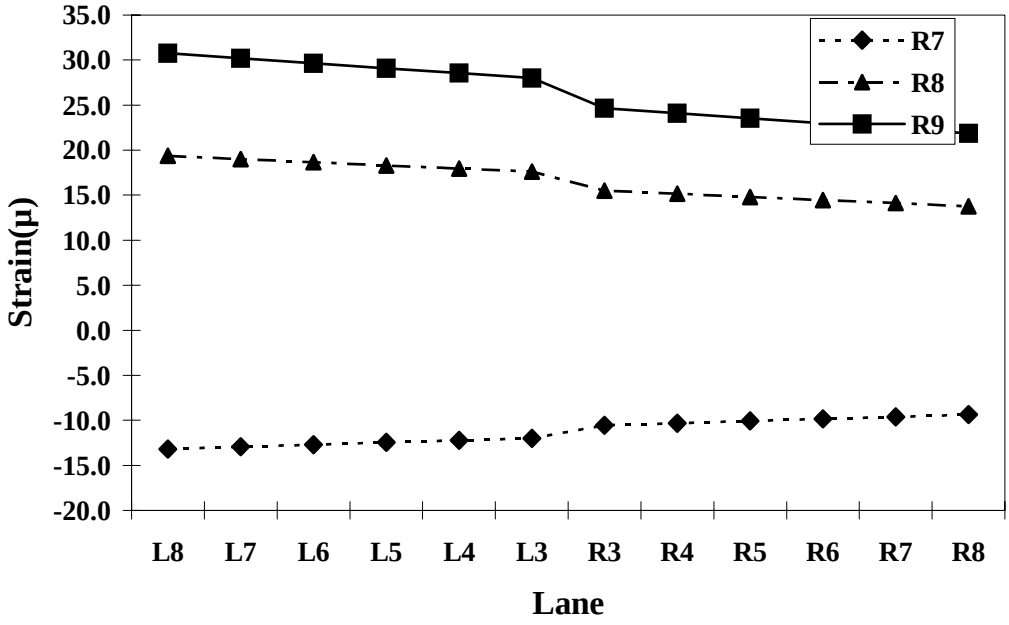

Figure. 5.3.16 Strain R7, R8, and R9 from Finite Element Analysis

5.3.3 Comparison of Strain Data

Table 5.3.2 shows the maximum and minimum strains of each strain sensor extracted from the recorded 92 data sets, in comparison with those from the finite element analysis. Sensors R1 and R10 are located at the girder near the entrance of the bridge. The recorded maximum strains at R1 and R10 are nearly twice higher than those from the analysis. This is due to the impact at the expansion joint of the bridge superstructure at the entrance of the bridge. This impact was not considered in the finite element analysis.

Table 5.3.2 Strain from measurement and analysis

Sensor		Monitored (μ) (1)	Computed (μ) (2)	Difference (%) $\left(=\frac{(2)-(1)}{(2)}\times 100\right)$
R1		2.282	0.801	(185)
R2		6.686	10.595	37
R3		-7.751	-24.307	68
R4	Max	5.364	15.280	65
	Min	-4.138	-17.862	77
R5	Max	11.132	6.391	(74)
	Min	-14.828	-9.905	(50)
R6	Max	12.745	9.905	(29)
	Min	-7.326	-6.391	(15)
R7*		0.440	-13.178	-
R8		18.513	19.360	4
R9		21.471	30.771	30
R10		2.246	0.801	(180)

* : out of order

From Table 5.3.2 the difference between the computed and measured strains at R2 and R3 (on the girder on the top of column 2) are higher than those at R8 and R9 (on the girder in the middle of span 2). The measured maximum strains at the box girder above column 2 are much higher than the computed ones, while the difference is much smaller in the middle of span 2. This implies that the load capacity of the box girder above the column is higher than that of the middle of span 2. On the other hand, the strain difference inside column 2 depends on the direction. At R4 (in the longitudinal direction), the strain difference is 65% but at 5 and R6 (in the transverse direction) they are respectively –74% and 22%. The negative strain difference of R5 means that the recorded maximum strain exceeds the computed maximum strain.

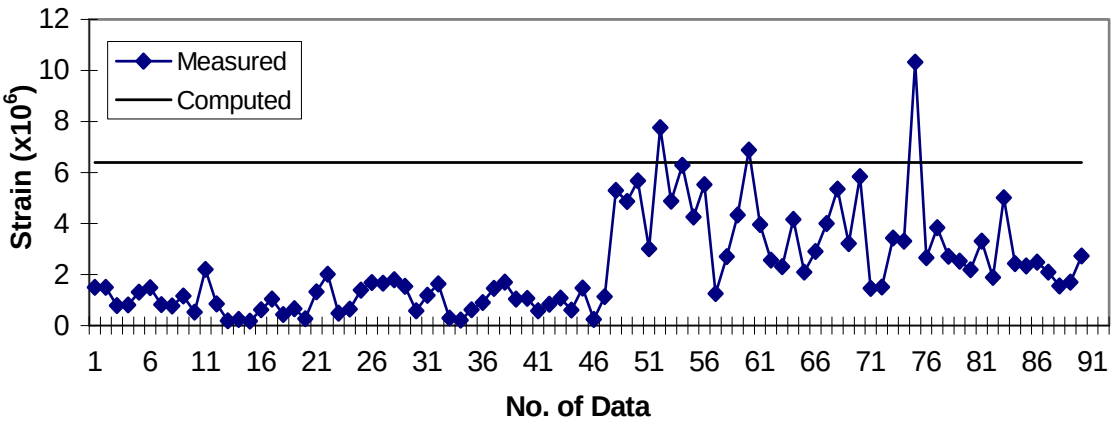

Fig. 5.3.17 Long-term monitored data of R5

Figure 5.3.17 shows the maximum strain envelop of R5 from the monitored data set. The solid line is the strain obtained from the finite element analysis under the HS-20 design load. A typical time history of R5, whose maximum value is near the computed strain, is shown in Figs.5.3.18 (a) and (b), in comparison with acceleration A5 recorded at the same time.

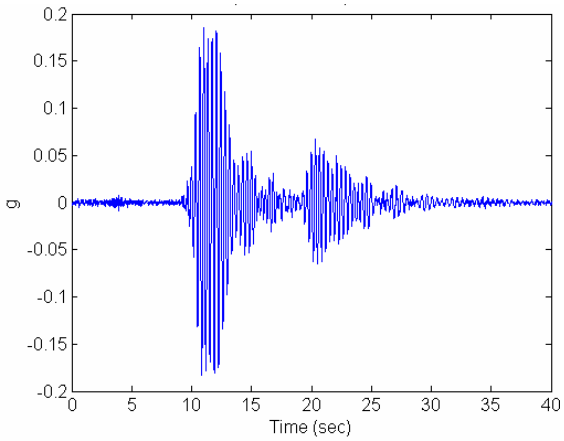

(a) A5 (deck-above column :trans. dir.)

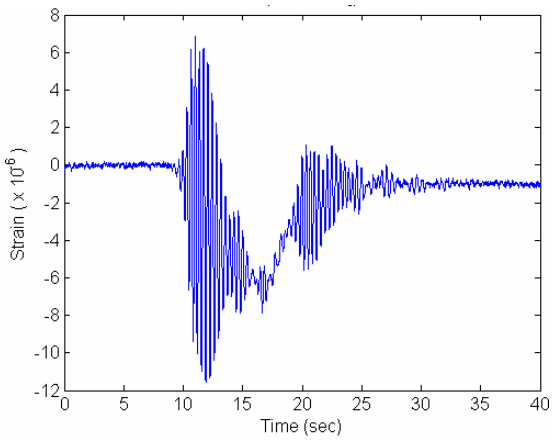

(b) R5 (bottom of column)

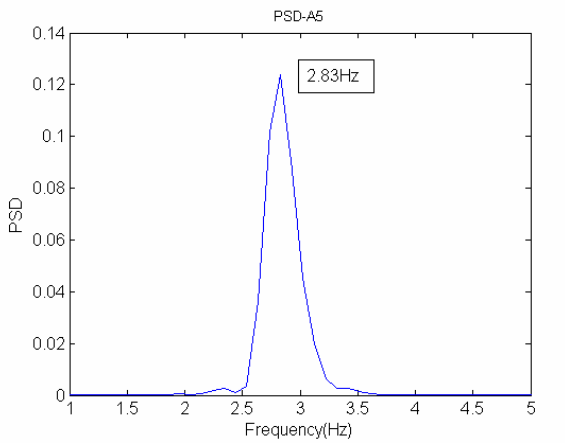

(c) PSD of A5

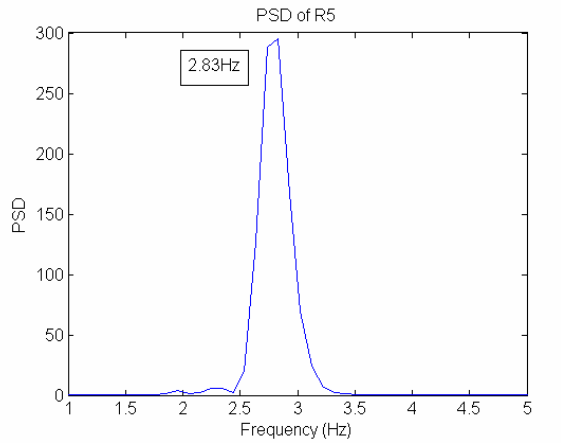

(d) PSD of R5

Fig. 5.3.18 Monitored time histories and their power spectral density (6/28/2006)

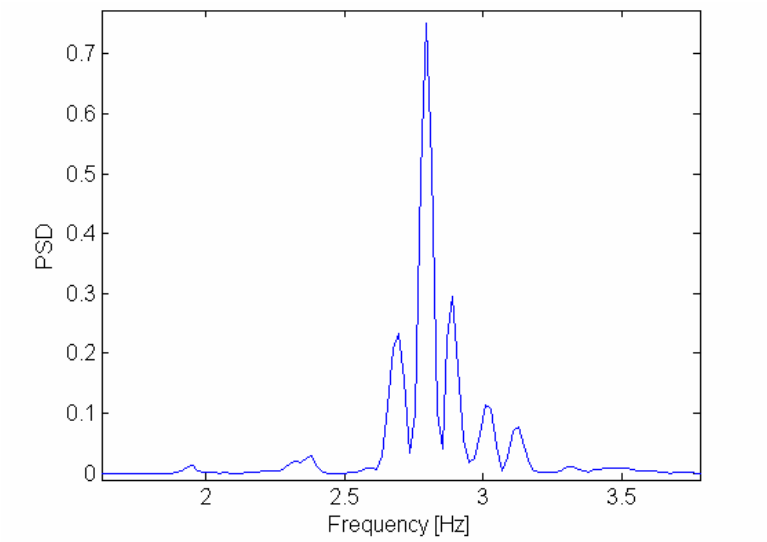

Fig. 5.3.19 Power spectral density of acceleration (transverse direction)

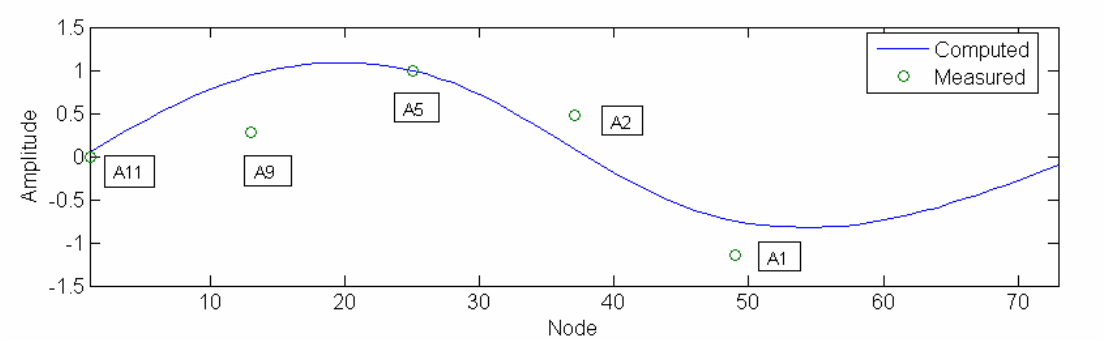

Fig. 5.3.20 The fourth mode shape (transverse direction)

Figures 5.3.18 (c) and (d) plot the power spectral density (PSD) of A5 and R5. The dominant frequencies identified from the acceleration (A5) and strain (R5) time histories are identical and close to the fourth mode frequency of the bridge in Fig. 5.3.19. Figure 5.3.20 shows the fourth mode shape of the bridge in the transverse direction from the analysis and measurement. It is clear that the moving heavy vehicle excited the fourth ode of the bridge, resulting in higher strain in column 2 in the transverse direction, as shown in Fig.5.3.18 (b), than that expected from analysis.

5.3 Summary

In the strain analysis, the measured strain from the WSO was compared with computed one. Because input vehicle loads could not be measured, the results of strain analysis can be interpreted only in a qualitative way. From the comparison of the measured and computed strain, it is found that generally the bridge superstructure was more conservatively designed than the column under moving vehicle load. It is also noted that the column of the WSO was more affected by heavy moving vehicles than the superstructure. From the frequency analysis of the acceleration and strain measured column, it was found that some vehicles excited the transverse mode of the bridge resulting in higher strain in the column than that expected from analysis. The design based on the dynamic factor underestimate the strain in the column.

Chapter 6

DEVELOPMENT OF STRUCTURAL HEALTH MONITORING METHODOLOGIES

This chapter presents methodologies developed for identifying the structural "health" conditions of highway bridges.

6.1 Definition of Structural Health and Damage

Structural elemental stiffness is proposed to be an indicator of the structural "health". As a structure deteriorates due to aging or suffers from damage by extreme events such as earthquakes, the structural stiffness will degrade, and as a result, the global dynamic characteristics of the structure will change. Therefore, by measuring the structural vibration, it is possible to identify the change in structural dynamic characteristics, and furthermore change in structural stiffness. When the reduction in structural stiffness exceeds a certain threshold, the structure is defined as damaged. The use of structural stiffness enables assessment of not only extent but also locations of damage.

6.2 System Identification Methodologies

In this project, a number of system identification methods were developed for identifying structural elemental stiffness based on structural vibration responses to traffic or earthquake excitations. For assessing the bridge superstructure health, it is proposed to use traffic-induced vibration as the moving vehicle induces high-amplitude vertical vibrations. For this purpose, a unique traffic excitation model was developed that incorporates partial traffic information based on video monitoring, and as a result it is more realistic than the conventional assumption of white noise. Bayesian updating and neural network system identification methods were developed for identification of bridge structures based on traffic excitations.

For assessing seismic damage that usually occurs in bridge columns, it is proposed to use seismic-induced vibrations. Because the damaged structure is a nonlinear system while most of the available system identification methods are for linear systems, the project developed a special system identification method based on the extended Kalman filtering that can deal with nonlinear systems.

The following provides a literature review of related system identification methods. System identification methods for structures based on vibration measurement can be grouped into two depending on whether the identification is carried out in frequency or time domain, as shown in Figure 6.2.1. If it is in frequency domain, basically the changes in modal values; frequency, damping, shape, are used as an indication of damage. However; if one wants to identify the changes more in detail like changes in elemental stiffness, time domain identification methods might be more appropriate. Time domain methods can be grouped into two depending on whether they are purely data driven or they are incorporating FE model. If it is aimed to determine the changes in the stiffness values, FE model must always be used. Within time domain identification methods, the most common one is the least squares estimation (LSE). It is basically performing an optimization for the parameters such as stiffness and

damping so that the error between the measured and the simulated responses is minimized. LSE is useful as a system identification technique, when used in combination with a damage detection algorithm (Stubbs et al, 2000). However, there are some drawbacks of LSE. Firstly, physical insight can be easily lost and a local maximum can be chosen over a global one. Secondly, LSE is very time consuming and cannot be applied for "on-line" structural health monitoring and damage detection. To overcome this difficulty, the recursive least squares (RLS) technique is proposed so that any time varying property in a system caused by damage can be tracked in real time. However in this case incorporation of FE is sacrificed, i.e. it is purely data driven so change in the system parameters can be tracked but it is not possible to link this to the change in structural stiffness and damping. Also, RLS is susceptible to even low level of noise. As can be seen every method has some drawbacks and is not effective for on-line identification of stiffness values under realistic conditions.

Kalman filtering was a break-through in system engineering field when first proposed four decades ago. It not only uses the data in a probabilistic sense but also gets information from structural model (Kalman, 1960). Results obtained by the Extended Kalman Filter (EKF) approach from simulated data and well defined models with known damage scenarios were reported (Yun and Shinozuka, 1980; Hoshiya and Saito, 1984; Yang et al, 2005; Straser and Kiremidjian, 1996; Loh and Chung, 1993; Loh and Tou, 1995, Ghanem and Ferro, 2006). However, applicability of the EKF approach to civil engineering structures involving high uncertainties in structures and loadings under realistic damaging events has not yet been studied. This research effort can be seen within this report.

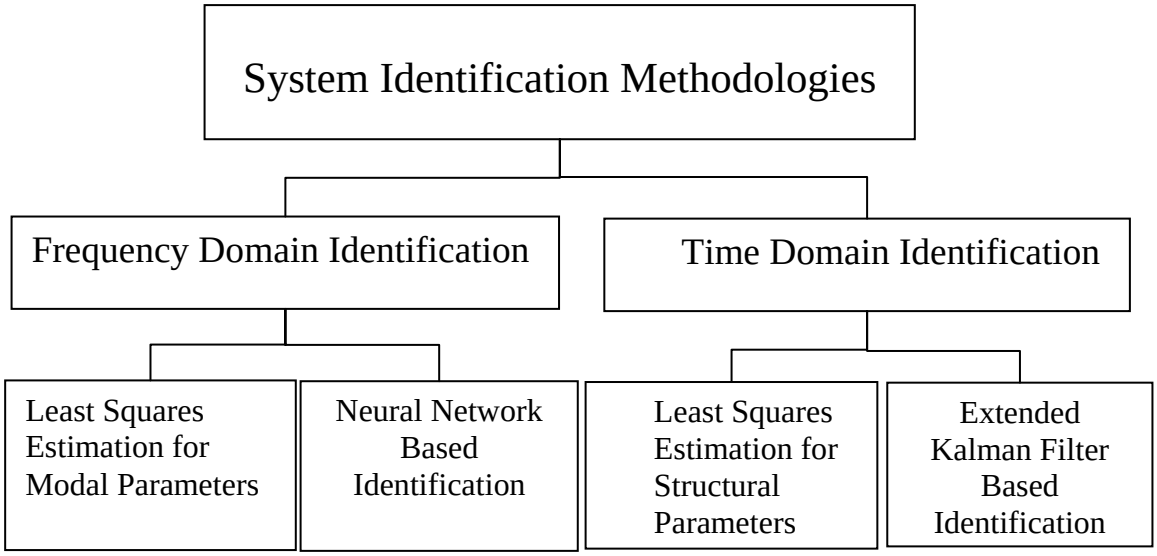

Figure 6.2.1 System Identification Methodologies

6.3 Traffic Excitation Modeling and Super-Structure Condition Assessment

Since it is impossible to measure the input traffic excitation on a bridge, a stochastic model of traffic excitation on bridges is developed in this project, by assuming that vehicles traversing a bridge (modeled as an elastic beam) arrive in accordance with a Poisson process, and that the contact force of a vehicle on the bridge deck can be converted to equivalent dynamic loads at the nodes of the beam elements. The parameters in this model, such as the Poisson arrival rate and the stochastic distribution of vehicle speeds, are obtained by image processing of the traffic video. The model reveals that traffic excitation on bridges is spatially correlated. Partial traffic information expressed by the stochastic model is incorporated in a Bayesian framework to evaluate the structural properties and update their uncertainty for condition assessment of the bridge superstructure. The vehicle weights are also estimated simultaneously in this procedure. This method is validated in the testbed.

6.3.1 Output-Only System Identification

The desirableness of measuring vibration responses of an instrumented highway bridge to traffic excitations for a long-term SHM purpose has been addressed by many authors. To list a few of its practical advantages over other bridge structural condition assessment methods: (I) It does not interrupt traffics; (II) It captures the *in-situ* dynamic behavior of the bridge undergoing its normal service; (III) It can be performed continuously, scheduled periodically or triggered automatically and (IV) It requires no special experimental arrangement or a heavy shaker/hammer. During such measurements, however, the excitation loads are neither controllable nor (easily) measurable. Thus, to extract the structural properties of the bridge from the vibration data, system identification is performed based only on the measured time histories of the bridge responses (system output) without measuring the traffic excitations (system

input). As a result, to facilitate such output-only identification of structural properties, models or assumptions representing the stochastic characteristics of the input must be established *a priori*, otherwise there can be various combinations between bridge structural properties and excitation loads that might have resulted in the same measured vibration responses.

In recent years, several output-only identification techniques have been developed. These include the natural excitation technique (Caicedo et al., 2004; James et al., 1996; Shen et al., 2003), the frequency domain decomposition (Brincker et al., 2001; Feng et al. 2004), the subspace decomposition (Peeters et al., 2001), the random decrement technique (Asmussen and Brincker, 1996; Feng and Kim, 1998) and various types of ARMA model fitting techniques (Garibaldi et al., 1998; Huang, 2001; Jensen et al., 1992). A common assumption in these output-only techniques is the spatially uncorrelated white noise input model (referred to hereafter as the conventional excitation model). In mathematical terms, the conventional model has an input covariance matrix that conforms to $\mathrm{cov}[\mathbf{F}(t),\mathbf{F}(t+\Delta t)] = \delta(\Delta t)\cdot\mathbf{\Sigma}$, where $\mathbf{\Sigma}$ is a matrix constant and the Dirac's delta function $\delta(\Delta t)$ is non-zero only when $\Delta t = 0$. Note that $\mathbf{F}(t)$ is the input vector at time t, a multivariate random process with its i-th component $F_i(t)$ being the random input at the i-th spatial location (or degree-of-freedom, DOF). Despite its mathematical attractiveness, the conventional excitation model can be inadequate to account for the operational variations of the excitation on a bridge, and moreover, it incorrectly excludes the correlation between excitation processes at different spatial points when $\Delta t \neq 0$, which indeed, is an intrinsic characteristic of the traffic excitation.

In this section, a stochastic model of traffic excitation on bridges is developed based on the physics of moving loads traversing a beam, taking into account various sources of randomness, to accommodate the operational variation of the traffic on a bridge.

6.3.2 Physical Formulation of Traffic Loads on a Bridge

When a vehicle traverses a short- to medium-span highway bridge, which is usually rather rigid with, for example, concrete box-girders, the bridge-vehicle system can be sufficiently decoupled to a beam-moving force model (Cebon, 1999; Pan and Li, 2002; Pesterev et al., 2003; Pesterev et al., 2004; Schenk and Bergman, 2003; Yang et al., 2000), i.e., the bridge (modeled as an elastic beam) is subjected to a time-variant tire force $P(t)$ moving across it. In this study, $P(t)$ is taken as a constant P for each of the passing vehicles, which can account for the static tire force, or the weight of the vehicle. The dynamic variation of tire force is considered either (I) having a higher frequency than the interested bridge frequency, or (II) having a broad-band contain, so that the dynamic vehicle-bridge interaction can be ignored in the bridge frequency bandwidth. This assumption applies to most of the vehicles, which have a natural frequency between 10 to 15Hz, higher than the bridge frequency (usually 1-5Hz), except for very heavy trucks whose frequency can be as low as 2-10 Hz (Cebon, 1999). This formulation is schematically shown in Figure. 6.3.1, where $\overline{m}$, $\overline{c}$, $\overline{E}$ and $\overline{I}$ are the mass per unit length, the damping coefficient, the Young's modulus and the cross-sectional moment of inertial of the bridge girder, respectively, v is the speed of the vehicle, and y_b is the vertical deflection of the bridge with respect to the equilibrium position. The governing equation of motion for $y_b(t)$ is

$$\bar{m}\frac{\partial^2}{\partial t^2}y_b(x,t)+\bar{c}\frac{\partial}{\partial t}y_b(x,t)+\overline{EI}\frac{\partial^4}{\partial x^4}y_b(x,t)=-\delta(x-vt)P \tag{6.1}$$

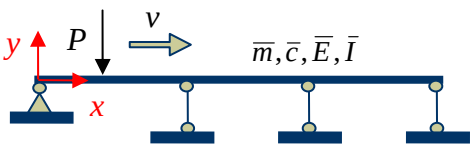

Figure 6.3.1 Beam-moving Force Model

When multiple vehicles move across the bridge, the vehicle arrival can be assumed to follow a Poisson process with mean rate γ (Shinozuka and Kobori, 1972; Turner and Pretlove, 1988). Assuming that the *i*-th vehicle traverses the bridge with a constant speed v_i, the right hand side of Eq. (6.1) can be replaced by

$$F_x(t)=-\sum_{i=1}^{N(t)}P_i\delta[x-v_i(t-\tau_i)] \tag{6.2}$$

where, $F_x(t)$ is the time history of traffic force at location x on the bridge; $N(t)$ is the number of vehicle arrivals during time interval $[0,t)$, and τ_1, τ_2, ···, τ_i, ···, $\tau_{N(t)}$ are the sequence of arrival times. P_i is the weight of the *i*-th vehicle. $\{P_i\}$ ($i=1$ to $N(t)$) are independent random variables identically distributed as a random variable P, independent to the Poisson process, with second order statistic $E(P^2) = S_P$. v_i is the speed of the *i*-th vehicle. $\{v_i\}$ ($i=1$ to $N(t)$) are independent random variables identically distributed as a random variable v, normally distributed with mean μ_v and standard deviation σ_v, independent to $\{P_i\}$ and the Poisson process as well.

Note that in this formulation, each vehicle has its own weight and traveling speed, which allows for accounting the stochastic distributions of these traffic properties in the excitation model.

Equation (6.2) defines a filtered Poisson process $F_x(t)$. See e.g. Parzen (1962) for a formal definition, terminology and account of the properties of a filtered Poisson Process.

For computing the bridge response to moving vehicles, Pan and Li (2002) proposed the dynamic nodal loading (DNL) method. In the DNL method, the time-variant moving force is converted into load histories at each of the nodes in the finite element (FE) model based on the equivalent nodal forces (ENFs) concept.

Let the bridge girders be modeled by beam elements with 2 DOFs at each node, namely, the vertical displacement y_i and the in-plane rotation θ_i at node i. It has been established that a vertical force P applied within the beam element is equivalent to the combined action of a nodal shear Q_i and a nodal moment M_i (the ENFs) acting at the nodes (Hibbeler, 2002). When the force moves across the beam elements, the ENFs are functions of the position of the moving force (Figure. 6.3.2).

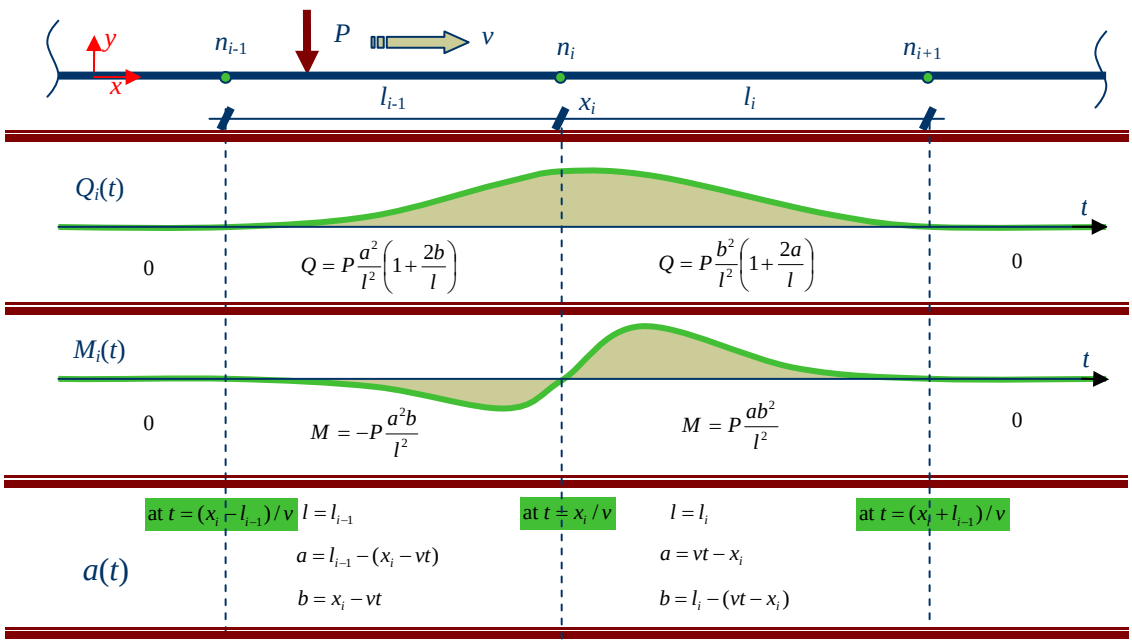

Figure 6.3.2 ENFs at Node i.

When the moving force P is a unit constant, and its speed v also constant, the ENFs are

$$Q_i(t) = W_i^Q(t,v) = \begin{cases} 0 & (t \le \frac{x_i - l_{i-1}}{v}) \\ \frac{(l_{i-1} - x_i + vt)^2}{l_{i-1}^{\ 2}}\left[1 + \frac{2(x_i - vt)}{l_{i-1}}\right] & (\frac{x_i - l_{i-1}}{v} < t \le \frac{x_i}{v}) \\ \frac{(l_i + x_i - vt)^2}{l_i^2}\left[1 + \frac{2(vt - x_i)}{l_i}\right] & (\frac{x_i}{v} < t \le \frac{x_i + l_i}{v}) \\ 0 & (\frac{x_i + l_i}{v} < t) \end{cases} \tag{6.3}$$

$$M_i(t) = W_i^M(t,v) = \begin{cases} 0 & (t \le \frac{x_i - l_{i-1}}{v}) \\ -\frac{(l_{i-1} - x_i + vt)^2}{l_{i-1}^{\ 2}}(x_i - vt) & (\frac{x_i - l_{i-1}}{v} < t \le \frac{x_i}{v}) \\ \frac{(l_i + x_i - vt)^2}{l_i^2}(vt - x_i) & (\frac{x_i}{v} < t \le \frac{x_i + l_i}{v}) \\ 0 & (\frac{x_i + l_i}{v} < t) \end{cases} \tag{6.4}$$

where, l_i and l_{i-1} are depicted in Figure. 6.3.2, representing the lengths of elements on the right and left of node *i*, respectively; x_i is the coordinate of node *i*; while $W_i^Q(t,v)$ and $W_i^M(t,v)$ are defined as the 'ENF functions' for the shear and moment at node *i*, with the superscripts *Q* and *M* corresponding to shear and moment, respectively.

By establishing an FE model of the bridge girder and converting the moving force into the ENFs on all the nodes, the moving force problem is converted to a classical time-history analysis problem with a random excitation history at each node, e.g., the equivalent forces at node *i* are now

$$F_i^Q(t) = -\sum_{j=1}^{N(t)} P_j W_i^Q(t - \tau_j, v_j) \tag{6.5}$$

$$F_i^M(t) = -\sum_{j=1}^{N(t)} P_j W_i^M(t-\tau_j, v_j) \tag{6.6}$$

Equations (6.5) and (6.6) indicate that $F_i^Q(t)$ and $F_i^M(t)$ are both filtered Poisson processes, in which, P_j and v_j are both characteristic variables independent to the driving Poisson process and independent to each other. This is slightly different than the classical definition of a filtered Poison process, where there is only one independent characteristic variable. However, multiple characteristic variables, or represented by a random vector, can be accommodated in the extended Campbell's theorem, as long as their joint distribution is given. The response function, either $PW_i^Q(t,v)$ or $PW_i^M(t,v)$, is argumented by random variables *P* and *v*, and by deterministic { x_i, l_i, l_{i-1} } for a given node *i*.

6.3.3 Traffic Excitation Covariance Model

Now, consider two ENFs, either of the two types at the same node: $F_i^Q(t)$ and $F_i^M(t)$, or of same or different types at different locations, i.e.: $F_i^Q(t)$ and $F_j^Q(t)$, $F_i^M(t)$ and $F_j^M(t)$, or $F_i^Q(t)$ and $F_j^M(t)$. They are different filtered Poisson processes driven by the same underlying Poisson process {*N*(*t*)}. Covariance between them is, for example,

$$\mathrm{cov}[F_i^Q(t), F_j^M(s)] = \gamma E(P^2) \int_{-\infty}^{\infty} \int_{-\infty}^{\infty} W_i^Q(t-\tau, v) W_j^M(s-\tau, v) f_v(v) dv d\tau \tag{6.7}$$

where, $f_v(v)$ is the probability density function of vehicle speed *v*. Assuming normal distribution with mean μ_v and standard deviation σ_v,

$$f_v(v) = \frac{1}{\sigma_v \sqrt{2\pi}} \exp\left[-\frac{(v-\mu_v)^2}{2\sigma_v^2} \right] \tag{6.8}$$

Equation (6.7) is a model of traffic excitation on a bridge, representing its stochastic characteristics. The model parameters include: (I) the geometry of a FE model of a bridge, which is deterministic for a specific problem; and the stochastic distribution of the traffic characteristics, namely, (II) the mean rate of vehicle arrivals, γ, (III) the second order statistic of vehicle weights, $E(P^2) = S_P$, and (IV) statistics of the vehicle speed μ_v and σ_v. Parameters γ, μ_v and σ_v are obtainable from traffic video, as to be shown later; S_P is considered time-variant, $S_P = A^2(t)$, to account for the variation of the traffic condition. Therefore, even in the case that the underlining Poisson process of vehicle arrivals and the vehicle speed distribution are stationary, the traffic excitation processes could still be non-stationary.

Equation (6.7) can be numerically evaluated by double quadrature, given the geometry and the parameters. A numerical example is given to demonstrate this procedure and some important natures of traffic excitation.

In this example, a segment of a bridge deck is modeled as beam elements with various lengths, as depicted in Figure. 6.3.3. Covariances of ENFs at various nodes against ENFs at the first node n_1 are computed, according to Eq. (6.7). Mean rate of vehicle arrivals γ is taken to be 2 per second. S_P is taken to be unit, because this will only affect the scale of covariance amplitude. Two cases of vehicle speed distribution are assigned and the results are compared. In Case 1, μ_v = 20 m/s (45 mile/h, the normal traffic speed on a typical highway bridge), σ_v = 5 m/s (11.3 mile/h); while in Case 2, μ_v = 30 m/s (67.5 mile/h, relative high speed) and σ_v = 5 m/s. In the numerical double quadrature, the upper and lower limits of integration for variable v are taken to be $\mu_v \pm 3\sigma_v$ to account for the major portion of the distribution of v. The upper limit for variable τ is the larger between t and s, while the lower limit is sufficiently small to account for the vehicles that arrive before counting start. Typical results are graphed in 3D plots (Figures 6.3.4 to 6.3.7) showing covariance as a function of (s-t), for ENFs at different nodes at spatial coordinate (x_i-x_1). Note that the dependence of

the spatial coordinate (x_i-x_1) on a specific point (n_1) is due only to the unequal element lengths; otherwise, the processes are both temporally stationary and spatially homogeneous.

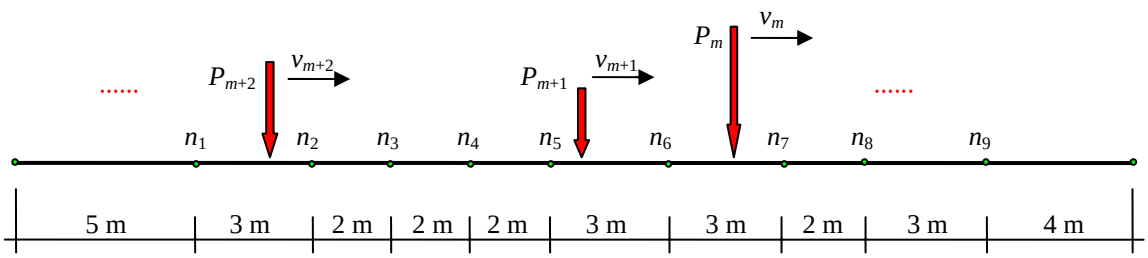

Figure 6.3.3 Geometry of a Finite Element Model

Figures 6.3.4 and 6.3.5 show $\mathrm{cov}[F_1^Q(t), F_i^Q(s)]$ for Cases 1 and 2 respectively, while Figures. 6.3.6 and 6.3.7 show $\mathrm{cov}[F_1^M(t), F_i^Q(s)]$ for Cases 1 and 2 respectively. From these figures, one can observe the following interesting phenomena.

I) Covariances as temporal functions of (s-t) of the same types of ENFs (either *QQ*, *MM*, *MQ* or *QM*) are of similar shapes for different nodes at various spatial coordinates. The shape is determined by the shapes of the ENF functions involved in the covariance, as can be seen from these figures, *QQ* type covariance has a different shape from *MQ* type covariance.

II) All types of covariances have an impulse-like temporal pattern. The wave length of the impulse is related to vehicle speed μ_v and the lengths of the adjacent beam elements. The larger μ_v the shorter the wave length is, and the longer element length the longer wave length.

III) Examining the spatial behavior of the covariance, a similar shape of covariance propagates along the spatial axis, with time delays proportional to the distance between two nodes. Since the covariances are non-zero functions between any pair of nodes, the exciting force processes are certainly spatially correlated.

IV) Comparing Figure. 6.3.4 with Figure. 6.3.5 (or similarly Figure. 6.3.6 with Figure. 6.3.7), the line connecting the peaks of the covariance functions, when projected to the (s-t)-(x_i-x_1) plane, has a slope consistent with μ_v. It is of interest to examine the following two extremes, where when taking the covariance to frequency domain by Fourier transform, the spectrum density matrix has constant (frequency independent) elements:

IV.1) The first extreme is when $\mu_v = 0$. One can conjecture that all the impulses shall reach their peaks along the line of x_i-x_1 = 0, leaving other portion of the surface essentially zero. This implies that the excitation processes at various spatial nodes are not correlated, to which the conventional excitation model applies. This extreme takes place when a bridge carries two-way traffic and the traffics on both directions are exactly symmetric.

IV.2) The second extreme is when $\mu_v = \infty$. One can similarly conjecture that the peaks of the impulses lie along the line of s-t = 0. This implies that the excitation processes at all the spatial nodes are perfectly correlated without time delay.

From these observations, it is concluded that: (I) The traffic excitation process at a spatial point can be assumed to be temporally white due to the temporal impulse-like covariance functions, which is asymptotically correct as the average vehicle speed increases or the element length is shortened; (II) The spatial correlation is an intrinsic nature of traffic excitation, with only an exception when the bridge carries symmetric two-way traffic. This intrinsic nature is not surprising, because same train of vehicles traverse different nodes on the beam, so that the excitation load one node experiences will be essentially a delayed process of the excitation experienced by a preceding node.

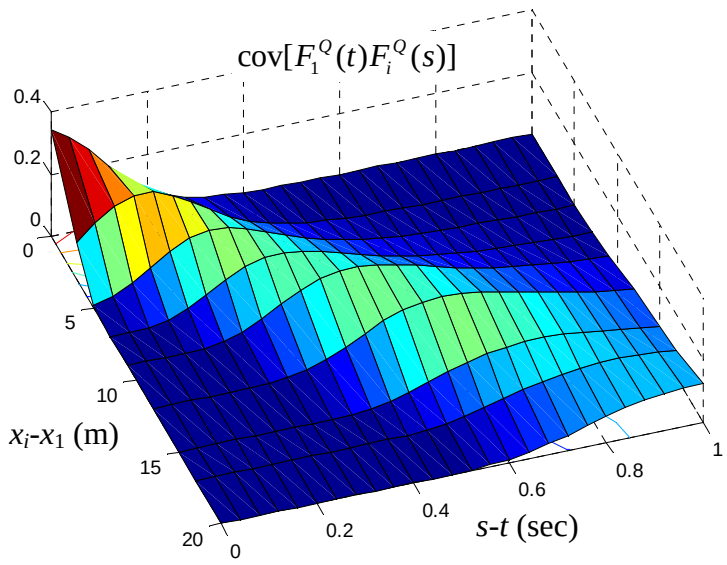

Figure 6.3.4 cov[$F_1^Q(t)F_i^Q(s)$] for Case 1: γ =2 /s, S_P = 1, μ_v = 20 m/s, σ_v = 5 m/s

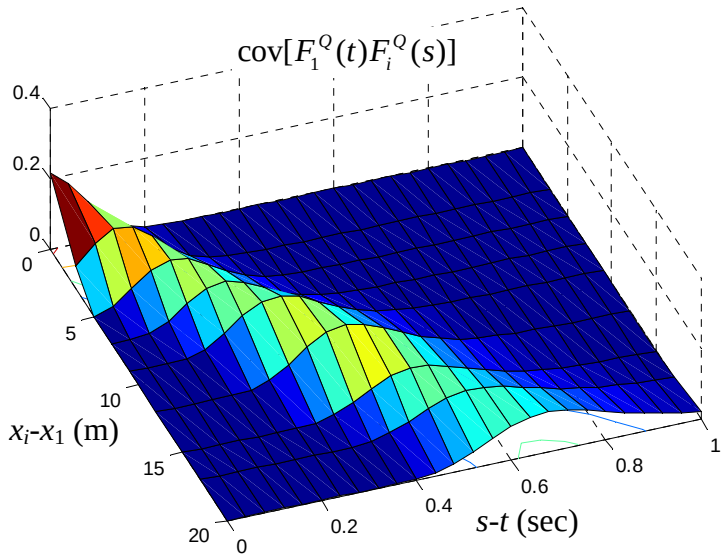

Figure 6.3.5 cov[$F_1^Q(t)F_i^Q(s)$] for Case 2: γ =2 /s, S_P = 1, μ_v = 30 m/s, σ_v = 5 m/s

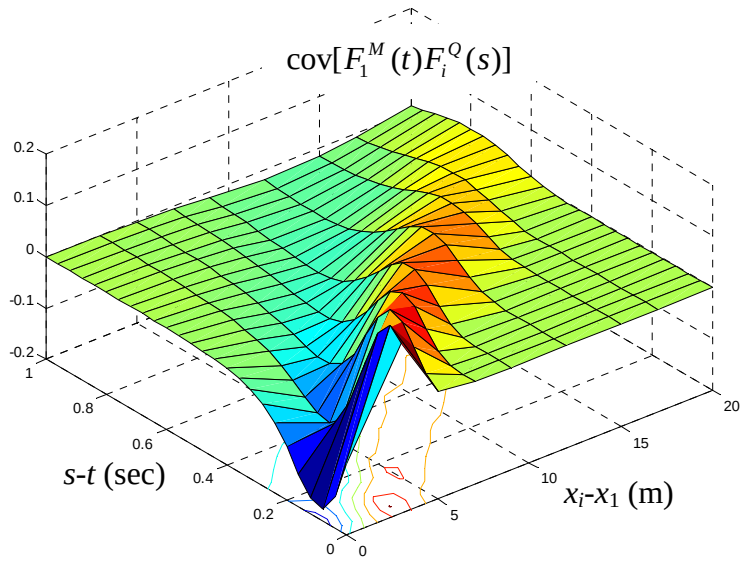

Figure 6.3.6 cov[$F_1^M(t)F_i^Q(s)$] for Case 1: γ =2 /s, S_P = 1, μ_v = 20 m/s, σ_v = 5 m/s

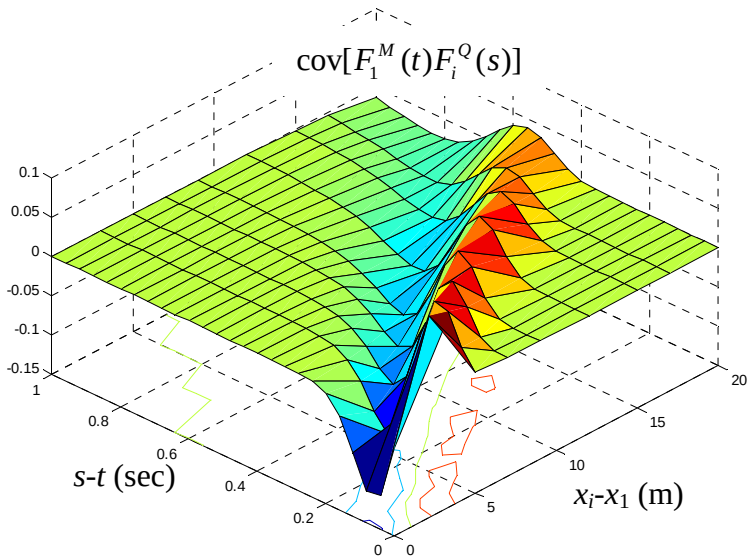

Figure 6.3.7 cov[$F_1^M(t)F_i^Q(s)$] for Case 2: γ =2 /s, S_P = 1, μ_v = 30 m/s, σ_v = 5 m/s

6.3.4 Distortion on the Response Spectrum due to Spatially Correlated Excitation

Most of the conventional response-only modal extraction methods (including FDD, PP and many other techniques) rely on two stochastic characteristics of the excitation: spatial un-correlation and broad-band frequency contents, to obtain reasonable estimation of the structural properties when only the structural responses are available. The physical significance of these excitation characteristics is that, they render the input spectrum $\mathbf{S_{FF}}(\omega)$ almost frequency independent, so that within the frequency range of interest, the input $\mathbf{S_{FF}}(\omega)$ causes neither significant amplitude variation nor substantial phase shifting that overlays the structural frequency response. Otherwise, variation of $\mathbf{S_{FF}}(\omega)$ can cause $\mathbf{S_{YY}}(\omega)$ to differ significantly from the structural frequency response functions, depressing a peak at the resonant frequency, or distorting the relative vibration amplitudes at various spatial points. Since it is discovered in the previous sections that traffic excitation on a bridge is intrinsically spatially correlated, it will be investigated how this spatial correlation distort the response spectrum.

To simplify the consideration and gain insight of the physics of the excitation, consider a case where the nodes of the beam elements are equally spaced in the finite element model of a bridge. According to Eq. (6.3), $W_i^Q(t,v)$ and $W_j^Q(t,v)$ have exactly the same shape (provided that i or j is not the end node of the bridge), and $W_j^Q(t,v)$ is the delayed version of $W_i^Q(t,v)$ with time lag $\Delta = (x_j - x_i)/v$, i.e., $W_j^Q(t,v) = W_i^Q(t-\Delta,v)$. Therefore, by Fourier transform of $\mathrm{cov}[F_i^Q(t), F_j^Q(s)]$, which has an expression similar to Eq. (6.7), one obtains the relation between an off-diagonal element and a diagonal element in the excitation spectrum density matrix,

$$\left[\mathbf{S_{FF}}\right]_{ij}^{QQ}(\omega) = e^{-i\omega\Delta}\left[\mathbf{S_{FF}}\right]_{ii}^{QQ}(\omega)\,. \tag{6.9}$$

As has been concluded in the last section, the diagonal element $\left[\mathbf{S_{FF}}\right]_{ii}^{QQ}(\omega)$ can be approximated by a constant *c*, because it is temporally white. The off-diagonal terms, however, contain phase shift $e^{-i\omega\Delta}$, which is frequency dependent.

A simple analogue to this situation is an *n*-DOF system subjected to inputs with inter-channel delays:

$$\mathbf{M}\ddot{\mathbf{Y}} + \mathbf{C}\dot{\mathbf{Y}} + \mathbf{K}\mathbf{Y} = \mathbf{F} \tag{6.10}$$

where the *k*-th channel of the input vector **F**, is related to the first channel in frequency domain by:

$$F_k(\omega) = e^{-i\omega(k-1)\Delta} F_1(\omega) \tag{6.11}$$

This input possesses similar correlation nature as the traffic excitation on a bridge does. By modal decomposition of Eq. (6.10), the response **Y** in frequency domain is,

$$\mathbf{Y}(\omega) = \mathbf{\Phi}\mathbf{\Lambda}(\omega)\mathbf{\Phi}^T\mathbf{F}(\omega) \tag{6.12}$$

where diagonal matrix $\mathbf{\Lambda}(\omega)$ is comprised of elements $\Lambda_{ii}(\omega)$,

$$\Lambda_{ii}(\omega) = \frac{1}{-\omega^2 m_i + j\omega c_i + k_i} \tag{6.13}$$

with m_i, c_i and k_i being the modal mass, damping and stiffness of the *i*-th mode. The *i*-th channel of response is, by Eq. (6.12),

$$Y_i(\omega) = \sum_{j=1}^{n} \varphi_{ij}\Lambda_{jj}(\omega) \sum_{k=1}^{n} \varphi_{kj} F_k(\omega) \tag{6.14}$$

In the vicinity of a lightly damped mode, say the *j*-th mode,

$$\left|\Lambda_{jj}(\omega)\right| >> \left|\Lambda_{ii}(\omega)\right| \quad (\text{for } j \neq i) \tag{6.15}$$

Therefore Eq. (6.14) in this vicinity becomes,

$$Y_i(\omega) \approx \varphi_{ij}\Lambda_{jj}(\omega)\sum_{k=1}^{N}\varphi_{kj}F_k(\omega) \tag{6.16}$$

If the excitation is frequency independent, $Y_i(\omega)$ in the vicinity of the j-th mode has the same mode as $\Lambda_{jj}(\omega)$ and a magnitude proportional to the j-th mode shape φ_{ij}. However, upon incorporating the frequency dependent input in Eq. (6.11),

$$Y_i(\omega) \approx \varphi_{ij}\Lambda_{jj}(\omega)\sum_{k=1}^{N}\varphi_{kj}e^{-i\omega(k-1)\Delta}F_1(\omega) \tag{6.17}$$

Let $F_1(\omega) = c$ and define a function $g_j(\omega)$,

$$g_j(\omega) = \sum_{k=1}^{N}\varphi_{kj}e^{-i\omega(k-1)\Delta} \tag{6.18}$$

Assuming that the j-th mode takes a sine shape, calculate $g_j(\omega)$ and graph it together with $Y_i(\omega)$ and $\Lambda_{jj}(\omega)$ in Figure. 6.3.8, which illustrates the distortion effect of correlated excitation. The true peak is depressed and a misidentified frequency can further leads to error in mode shape reconstruction.

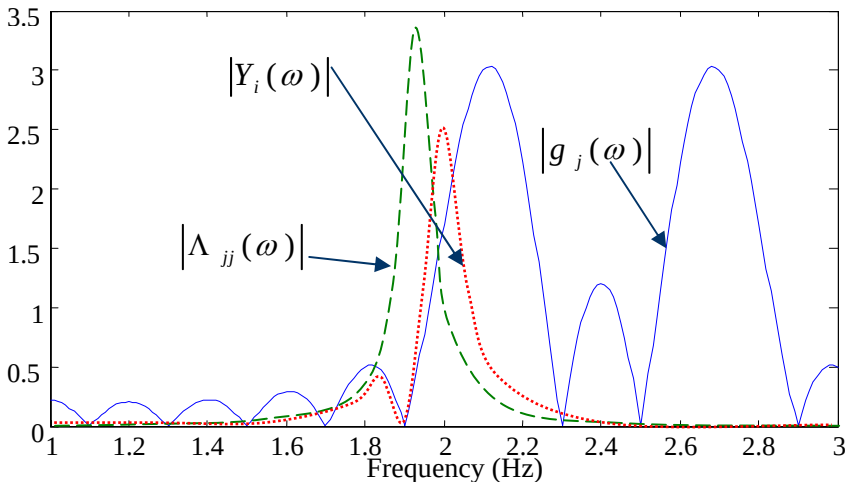

Figure 6.3.8 Distortion of the Response Spectrum

6.3.5 Video-based Traffic Monitoring and Processing

It can be seen from the above discussion that, to characterize the traffic excitation, traffic information such as the arrival times and the speeds of the vehicles is crucial, and should be somehow measured. Thanks to the prevailing digital image capturing and processing technology, traffic can be monitored by camcorders, and vehicle arrival times and speeds can be extracted from digital video.

Figure 6.3.9 shows how such information is extracted from the digital video of a pickup truck. For each vehicle, two frames are selected that show the instants when the vehicle first enters and eventually exits the coverage zone of the camcorder. From these two frames, the instantaneous positions of the vehicle and the time stamps of the frames are read. The speed of the vehicle is then deduced assuming that the speed remains approximately constant during this interval. This procedure can be automated by image processing based on a moving object identification technique. Traffic on a bridge was videotaped for 360 seconds, when a total of 128 vehicles passed the site. For brevity, Table 6.3.1 tabulates the information of the first ten vehicles extracted from the video images.

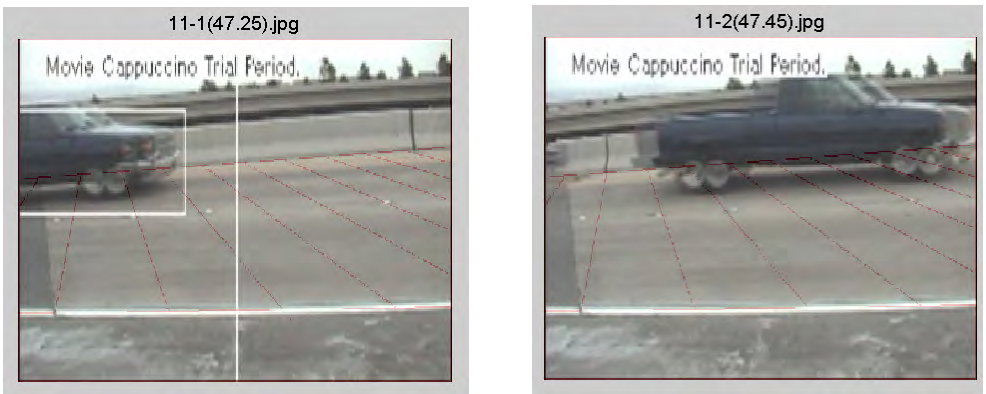

Figure 6.3.9 Captured Video Images of a Vehicle Traveling on the Bridge

Table 6.3.1 Traffic Information Extracted from the Video Images

No.	Type	Arrival Time (sec)	First Position (m)	Second Position (m)	Time Interval (sec)	Speed (m/s)
1	SUV	4.61	2.44	8.53	0.27	22.58
2	CAR	6.34	2.13	9.14	0.27	25.96
3	PICKUP	7.61	8.53	11.43	0.13	22.27
4	CAR	8.18	4.57	9.14	0.20	22.86
5	CAR	8.21	8.53	12.19	0.20	18.29
6	CAR	9.48	9.14	11.89	0.13	21.10
7	CAR	10.68	8.99	11.28	0.13	17.58
8	SUV	11.41	3.66	9.14	0.20	27.43
9	SUV	12.08	9.45	11.58	0.13	16.41
10	VAN	14.72	3.66	9.14	0.29	18.92

Note: The vehicle types were classified into five different categories, namely: CAR (passenger cars), SUV (sport utility vehicles), VAN, PICKUP, and TRUCK (large cargo trucks).

One can employ statistical inference to obtain parameters γ, μ_v and σ_v of the traffic excitation model based on such data extracted from the traffic video. Parameter γ is obtained by fitting an exponential distribution to the inter-arrival time between two successive vehicle arrivals, listed as the time intervals in Table 6.3.1. It is found γ = 2.34 per second (maximum likelihood estimation) for this period. Figure 6.3.10(a) shows the fitness of the distribution function to the histogram of the time intervals. Mean and standard deviation of vehicle speeds are also easily obtained from data in Table 6.3.1, μ_v = 21.45 m/s and σ_v =3.26 m/s. It is found that its distribution is approximately normal as shown in Figure. 6.3.10(b).

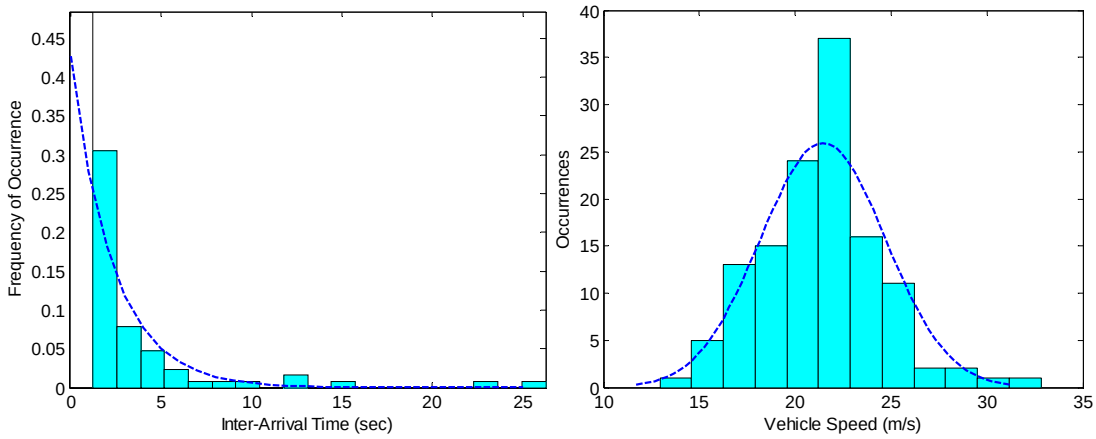

(a) (b)

Figure 6.3.10 Infer Parameters from Traffic Video Information

The statistics of the vehicle weight S_P is hard to estimate from traffic video, and it is fluctuating due to the time-variation of traffic condition. Therefore, it is modeled as a modulating intensity $S_P = A^2(t)$ and will be identified from the bridge response amplitude.

6.3.6 Structural Condition Assessment

To assess the structural condition of a bridge, vertical vibration of its superstructure is measured by accelerometers simultaneously while traffic video is taken. Element stiffness is identified from the vibration data in a Bayesian framework, using the traffic excitation model developed above as the stochastic description of the system input.

6.3.6.1 Bayesian Updating

In Yuen et al. (2002), a structural model identification method has been developed in a Bayesian framework, given a stochastic description of the non-stationary excitation. In the foregoing sections, such a description of the traffic excitation on bridges has been fully developed, as in Eq. (6.3.7). Therefore, the Bayesian estimation can be employed to identify θ. The Bayesian method will first be summarized and in view of the nature of the traffic excitation model, the method is simplified for better computational efficiency.

The Bayesian theorem gives the updated probability distribution of the parameters θ, given measured response $\mathbf{Y}_{1,N}$,

$$p(\theta \mid \mathbf{Y}_{1,N}) = c \cdot p(\theta)\, p(\mathbf{Y}_{1,N} \mid \theta) \tag{6.19}$$

where c is a normalizing constant. $\mathbf{Y}_{m,p}$ is a vector comprising the zero-mean response measurements $\mathbf{y}_k$ from time $m\Delta t$ to $p\Delta t$, $m \le k \le p$, and Δt is the sampling interval:

$$\mathbf{Y}_{m,p} = \left[\mathbf{y}_m^T \cdots \mathbf{y}_k^T \cdots \mathbf{y}_p^T\right]^T \tag{6.20}$$

$p(\theta)$ is the *a priori* probability density function (PDF) of θ, which can be assumed uniformly distributed lacking knowledge about it. To efficiently evaluate $p(\mathbf{Y}_{1,N} \mid \theta)$, an approximation was introduced.

$$p(\mathbf{Y}_{1,N} \mid \theta) \approx p(\mathbf{Y}_{1,N_p} \mid \theta) \prod_{k=N_p+1}^{N} p(\mathbf{y}_k \mid \theta; \mathbf{Y}_{k-N_p,k-1}) \tag{6.21}$$

This approximation is in the sense that information of response earlier than $N_p\Delta t$ before step k is not very helpful to better estimate $\mathbf{y}_k$, or formally $p(\mathbf{y}_k \mid \theta; \mathbf{Y}_{k-N_p,k-1}) \approx p(\mathbf{y}_k \mid \theta; \mathbf{Y}_{1,k-1})$. It is suggested in Yuen et al. (2002) that $N_p\Delta t$ shall be taken no shorter than the fundamental period of the structure.

If the excitation is Gaussian, the response will be Gaussian and the distribution is fully described by its mean (assuming zero-mean) and covariance matrix $\mathbf{\Sigma}^{Y}_{1:N,1:N}$:

$$\mathbf{\Sigma}^{Y}_{1:N,1:N} = E\left[\mathbf{Y}_{1,N}\mathbf{Y}^{T}_{1,N}\right] = \begin{bmatrix} \mathbf{\Gamma}_{1,1} & \cdots & \mathbf{\Gamma}_{1,N} \\ \vdots & \ddots & \vdots \\ \mathbf{\Gamma}_{N,1} & \cdots & \mathbf{\Gamma}_{N,N} \end{bmatrix} \tag{6.22}$$

where, each sub-matrix $\mathbf{\Gamma}_{m,p} = E\left[\mathbf{y}_m \mathbf{y}^{T}_{p}\right]$, is an N_o-by-N_o covariance matrix between observations at m-th and p-th steps; N_o is the dimension of the observation vector, or the number of sensors. Given a structural system parameterized by a certain vector θ, subjected to traffic excitation with a covariance matrix $\mathbf{\Sigma}^{F}_{1:N,1:N}$, whose elements are given by Eq. (6.7), its structural response covariance $\mathbf{\Sigma}^{Y}_{1:N,1:N}$ can be evaluated in a close form, which will be discussed later.

We now focus on evaluating each term in the right hand side of Eq. (6.21). The first term,

$$p(\mathbf{Y}_{1,N_P} \mid \theta) = \frac{1}{(2\pi)^{N_o N_P/2}\left|\mathbf{\Sigma}^{Y}_{1:N_P,1:N_P}\right|^{1/2}} \exp\left(-\frac{1}{2}\mathbf{Y}^{T}_{1,N_P}\left(\mathbf{\Sigma}^{Y}_{1:N_P,1:N_P}\right)^{-1}\mathbf{Y}_{1,N_P}\right) \tag{6.23}$$

The following terms, $p(\mathbf{y}_k \mid \theta; \mathbf{Y}_{k-N_P,k-1})$, $k = N_p+1$ to N, are estimated assuming $\mathbf{y}_k$ can be linearly predicted by observations $\mathbf{Y}_{k-N_P,k-1}$ (Yuen et al., 2002):

$$\bar{\mathbf{y}}_k = E(\mathbf{y}_k \mid \theta; \mathbf{Y}_{k-N_P,k-1}) = \mathbf{\Sigma}^{Y}_{k,(k-N_P):(k-1)}\left(\mathbf{\Sigma}^{Y}_{(k-N_P):(k-1),(k-N_P):(k-1)}\right)^{-1}\mathbf{Y}_{k-N_P,k-1} \tag{6.24}$$

with covariance matrix:

$$\bar{\mathbf{\Sigma}}^{Y}_{k,k} = E\left((\mathbf{y}_k - \bar{\mathbf{y}}_k)(\mathbf{y}_k - \bar{\mathbf{y}}_k)^T \mid \theta; \mathbf{Y}_{k-N_P,k-1}\right)$$

$$= \mathbf{\Gamma}_{k,k} - \mathbf{\Sigma}^{Y}_{k,(k-N_P):(k-1)}\left(\mathbf{\Sigma}^{Y}_{(k-N_P):(k-1),(k-N_P):(k-1)}\right)^{-1}\left(\mathbf{\Sigma}^{Y}_{k,(k-N_P):(k-1)}\right)^{T} \tag{6.25}$$

where $\mathbf{\Sigma}^{Y}_{k,(k-N_P):(k-1)} = \left[\mathbf{\Gamma}_{k,k-N_P} \quad \cdots \quad \mathbf{\Gamma}_{k,k-1}\right]$, while $\mathbf{\Sigma}^{Y}_{(k-N_P):(k-1),(k-N_P):(k-1)}$ follows the definition in eq. (6.22). So that,

$$p(\mathbf{y}_k \mid \theta; \mathbf{Y}_{k-N_P,k-1}) = \frac{1}{(2\pi)^{N_o/2}\left|\bar{\mathbf{\Sigma}}^{Y}_{k,k}\right|^{1/2}} \exp\left(-\frac{1}{2}(\mathbf{y}_k - \bar{\mathbf{y}}_k)^T \left(\bar{\mathbf{\Sigma}}^{Y}_{k,k}\right)^{-1} (\mathbf{y}_k - \bar{\mathbf{y}}_k)\right) \tag{6.26}$$

Note that evaluation of Eq. (6.19) through approximation in Eq. (6.21), or specifically by Eqs. (6.23) and (6.26), involves inverting (N-N_P+1) covariance matrices of dimension N_oN_P-by-N_oN_P; while directly evaluating eq. (6.19) through Eq. (6.22) will involve inverting an N_oN-by-N_oN covariance matrix. When $N >> N_P$, the approximation is not only computationally more efficient, but also necessary for a computer with limited memory for matrix storage; in the example to be presented, N_P = 50 while N = 300 for a segment of data of 3 seconds.

We also note two technical problems involved in this updating procedure and the solutions devised in this study. The first one is the ill-conditioned response covariance matrix $\mathbf{\Sigma}^{Y}_{1:Np,1:Np}$ due to linearly correlated observations. When the bridge is excited to vibrate only in a few of its dominating lower modes, the sensor readings are linearly correlated, proportional to each other according to the mode shapes. This results in a singular covariance $\mathbf{\Sigma}^{Y}_{1:Np,1:Np}$, and obviously by Eq. (6.23) leads to an un-operational updating algorithm. In this study, principle component analysis (PCA) is adopted to condense the responses into a few linearly uncorrelated principle components, thus $\mathbf{\Sigma}^{Y}_{1:Np,1:Np}$ contains only the covariance of these principle components. The second problem is associated with PDF updating. Equations (6.23) and (6.26) give the joint PDFs evaluated at the observed data instead of the probability of obtaining the data. To evaluate the probability from the PDF, integration over a high-dimensional vicinity of the data point must be applied. When more data are measured, in Eq. (6.19), N takes a larger number, and the joint PDF $p(\mathbf{Y}_{1,N} \mid \theta)$ is in a higher dimensional field, so that not comparable to, say, $p(\mathbf{Y}_{1,N-1} \mid \theta)$. To avoid this difficulty,

in this study, the conditional probability is normalized by $p'(\mathbf{Y}_{1,N} \mid \theta) = \sqrt[n]{p(\mathbf{Y}_{1,N} \mid \theta)}$ to make sure it is not mis-scaled for different *N*s.

Bayesian probability updating as in Eq. (6.19) can be recursively applied when new data are available from the monitoring system. Given a uniformly distributed initial *a priori* $p(\theta)$, Eq. (6.19) is employed to obtained the *a posteriori* $p(\theta \mid \mathbf{Y}_{1,N})$, utilizing data $\mathbf{Y}_{1,N}$. Similarly, when a new set of data is available, e.g., $\mathbf{Y}_{N+1,2N+1}$, $p(\theta \mid \mathbf{Y}_{1,N})$ is adopted as the *a priori*, and Eq. (6.19) repeated to update the *a posteriori*, $p(\theta \mid \mathbf{Y}_{1,2N+1})$, and so forth. The probability density of θ is sharpened by updating. This methodology will be verified on an instrumented highway bridge of the testbed in the next section. For the time being, to complete the description of the algorithm, we shall discuss a method for the efficient estimation of the response covariance matrix in Eq. (6.22).

6.3.6.2 Estimation of Response Covariance Matrix

When the Poisson vehicle arrival is stationary and the speed distribution is not time variant, note from Eq. (6.7) that the traffic excitation is a uniformly modulated random process, such that

$$\mathrm{cov}[\mathbf{F}(t),\mathbf{F}(s)] = E\left(\mathbf{F}(t),\mathbf{F}^T(s)\right) = \gamma A^2(t)\mathbf{\Sigma}^F(t-s) \tag{6.27}$$

This non-stationary process is separable into a time-variant but frequency independent modulating function $A^2(t)$ and a stationary process with a covariance function $\mathbf{\Sigma}^F(t-s)$. In frequency domain, the stationary process has a spectrum density $\mathbf{S}_s^F(\omega)$ such that

$$\mathbf{S}_s^F(\omega) = \int_{-\infty}^{\infty} \mathbf{\Sigma}^F(t)e^{-i\omega t}dt \tag{6.28}$$

The response covariance of a linear time-invariant system to such a uniformly modulated excitation is (Ou and Wang, 1998),

$$\mathbf{\Sigma}^Y(t,s) = \frac{\gamma}{2\pi}\int_{-\infty}^{\infty} \mathbf{J}(\omega,t)\mathbf{S}_s^F(\omega)\mathbf{J}^T(\omega,s)d\omega \tag{6.29}$$

where,

$$\mathbf{J}(\omega,t) = \int_0^t \mathbf{\Lambda}(t-\tau)A(\tau)e^{i\omega\tau}d\tau \tag{6.30}$$

with $\mathbf{\Lambda}(t)$ being the impulse response of the system; and the superscript T denotes the conjugate transpose. To simplify the calculation, we further assume that the modulation function $A(t)$ varies much slower than $\mathbf{\Lambda}(t)$, which is a reasonable assumption, considering that it usually takes a vehicle several seconds to traverse a bridge, much longer than the fundamental period of the bridge (usually 0.1 to 0.5 second). In view of this assumption,

$$\mathbf{J}(\omega,t) \approx A(t)\int_{-\infty}^{\infty} \mathbf{\Lambda}(t-\tau)e^{i\omega\tau}d\tau = A(t)\mathbf{H}(\omega)e^{i\omega t} \tag{6.31}$$

where $\mathbf{H}(\omega)$ is the frequency response of the system. Now eq. (6.29) is simplified as:

$$\mathbf{\Sigma}^{Y}(t,s) \approx \gamma A(t)A(s)\frac{1}{2\pi}\int_{-\infty}^{\infty} \mathbf{H}(\omega)\mathbf{S}_s^F(\omega)\mathbf{H}^T(\omega)e^{i\omega(t-s)}d\omega \tag{6.32}$$

The integration with respect to ω is indeed the inverse Fourier transform, which, independent to the modulation function, can be performed separately. In discrete time,

$$\mathbf{\Sigma}_{m,p}^{Y} = \mathbf{\Gamma}_{m,p}^{Y} = \mathbf{\Sigma}^{Y}(m\Delta t, p\Delta t) \tag{6.33}$$

To avoid too many unknowns, the modulation function is assumed to be piece-wise constant: $A(k) = A_i$ for $m_i \le k < p_i$.

6.3.6.3 Validation on a Test-bed Bridge

The bridge structural condition assessment procedure based on vibration and traffic monitoring, as described above, has been validated on an instrumented bridge from the testbed, the JRO.

Figure 6.3.11 shows an FE model of this bridge. The columns and the deck girder are modeled by beam-column elements. When the vertical vibration of the deck is of interest, it is modeled to be simply supported at both ends on the abutments. Columns are fixed on the ground. The connections between the column top and the deck are considered rigid. Each node on the deck has 3 DOFs, namely: vertical translation along Z axis, in-plane bending (rotation about Y axis), and torsion (rotation about X axis). The nodes on the columns are allowed 4 DOFs, namely: horizontal translations (along X and Y axes), in-plane bending (rotation about Y axis) and out-of-plane bending (rotation about X axis). Measured data from the five vertical accelerometers,

Channel 4, 6, 13, 14 and 15, as in Figure. 6.3.10, are considered as observation in this study, because of the fact that traffic mainly induces vertical vibration of the deck.

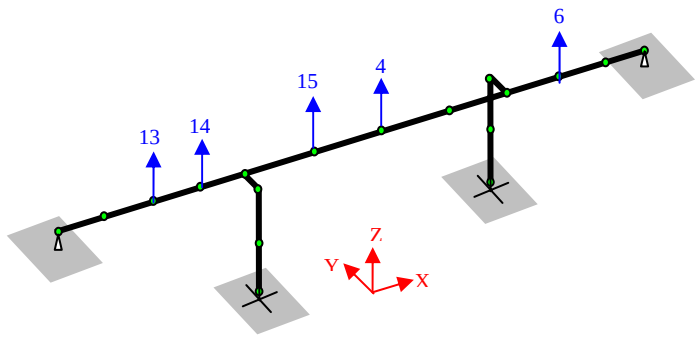

Figure 6.3.11 Sensor System and Finite Element Model of JRO

For the purpose of superstructure condition assessment, only the cross-sectional stiffness, $\overline{EI}$, of the elements of the deck is parameterized with a correction coefficient β for identification and probability updating. The deck has a uniform cross-section box-girder in all the 3 spans; a single β is applied to all the deck elements. However, note that the Bayesian updating procedure presented here is not limited to identifying only one parameter. One can parameterized different β's for different elements if the location of structural damage/degradation is also of interest, which involves no fundamental change in the algorithm except more demanding computation. As in Deotatis et al. (1992) and Ito et al. (1992), only the probabilities associated with a discrete set of parameters are updated. In this study, the range of β is selected from 0.7 to 1.2, and the grid increment is 0.05.

The computation is in the following steps:

Step 1: By Eq. (6.7), compute the traffic excitation covariance matrix $\mathbf{\Sigma}^F(t)$ given the geometry of the FE model and the traffic parameters. The traffic parameters γ , μ_v and σ_v are obtained based on traffic monitoring and video processing, as previously

described. Vehicle weight statistic $E(P^2) = S_P$ is set to 1 and its true value is to be identified in the next steps. Figure 6.3.12 plots a few elements in the resulted $\mathbf{\Sigma}^F(t)$ as examples. Note that $\mathbf{\Sigma}^F(t)$ is the covariance of a stationary multivariate process, and s is arbitrary in Figure 6.3.12.

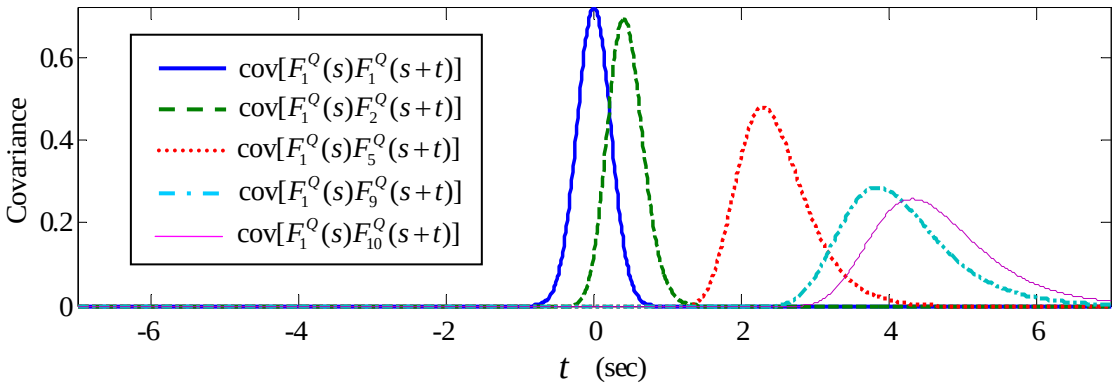

Figure 6.3.12 Elements from Excitation Covariance $\mathbf{\Sigma}^F(t)$

Step 2: Given the *a priori* probability associated with the parameters in the grid, (before the first updating, the *a priori* is set uniform, i.e. 1/11 for all the 11 parameters in the grid), find the most likely parameter β^{ml}, and assemble the system mass, damping and stiffness, the [**M**, **C**, **K**] triple of the FE model parameterized by β^{ml}, so as to compute the frequency response $\mathbf{H}(\omega)$ of the system with parameter β^{ml}. Now calculate the response covariance matrix by eq. (6.32), with $A(t)=A(s)=1$, and denote the result as $\mathbf{\Sigma}_1^Y(t-s)$. Figure. 6.3.13 depicts an element in $\mathbf{\Sigma}_1^Y(t-s)$. The JRO Bridge has a fundamental period of about 0.37 second, so $N_p\Delta t$=0.5 second is taken with sampling interval Δt=0.01 second.

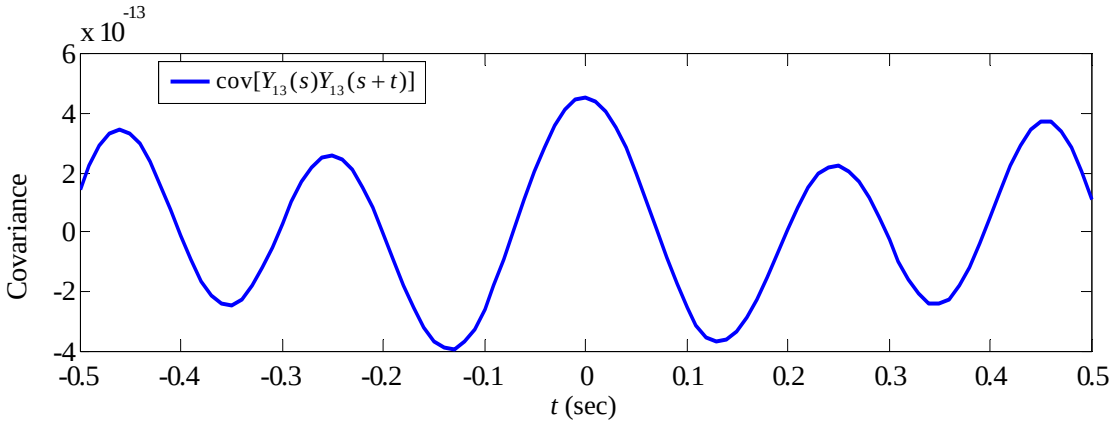

Figure 6.3.13 Element of Predicted Response Covariance $\mathbf{\Sigma}_1^Y(t-s)$

Step 3: The total 360 second acceleration response data measured simultaneously with the traffic video are divided into 120 3-second-long segments; N=300 in each of the segment for an epoch of updating. Load the first segment of data and computer the covariance matrix of the measured data, denoted as experimental $\mathbf{\Sigma}_{ex}^Y(t-s)$, an element of which is depicted in Figure. 6.3.14.

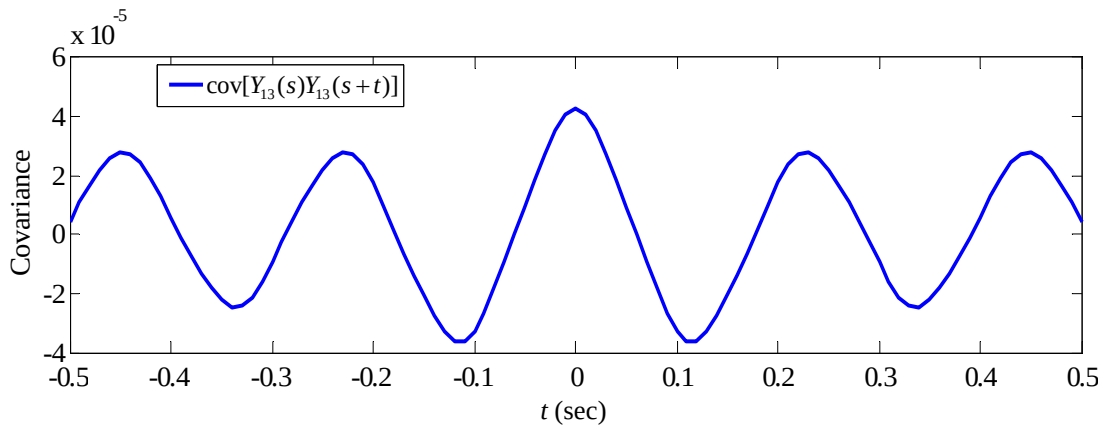

Figure 6.3.14 Element of Experimental Response Covariance $\mathbf{\Sigma}_{ex}^Y(t-s)$

If vehicle statistic $S_P(s)$ is assumed constant in this 3-second segment, there shall be

$$\mathbf{\Sigma}_1^Y(t-s)S_p(s)+\varepsilon=\mathbf{\Sigma}_{ex}^Y(t-s) \tag{6.34}$$

where, ε is the error residue. A least-square routine is adopted to estimate $S_P(s)$ from Eq. (6.34). So, the vehicle weight $P(s)$ is simply the square root of $S_P(s)$.

Step 4: For each of the β in the parameter grid, similarly by Eq. (6.32), calculate the conditional response covariance: $\mathbf{\Sigma}^{Y}(t,s\,|\,\beta)$, with now $A(t)A(s) = S_P(s)$. And further, the conditional probability density $p(\mathbf{Y}_{1,N}\,|\,\beta)$ by eq. (6.42) through the approximation in Eqs. (6.23) and (6.26).

Step 5: Combine the results in Step 4 with the *a priori* parameter probability, normalize to obtain the *a posteriori* by Eq. (6.19).

Now apply the updating procedure recursively. In the next epoch of updating, first set the *a priori* equal to the *a posteriori* resulted in Step 5 in the previous epoch, load the next segment of measured data, and repeat Steps 2 to 5. During this updating procedure, the parameter probability distribution evolves from the uniform distribution to a distribution with the most probable parameter singled out possessing dominating probability.

The updating result using the first 60 second data (consisting of 20 updating epochs) is plotted in Figure. 6.3.15(a). The identified vehicle weight traversing the bridge at each instant is plotted in Figure. 6.3.15(b) companioned with the plot, Figure. 6.3.15(c), of the accelerometer reading at Channel 4. One can see that the identified vehicle weight is consistent with the vibration amplitude. We also note that it is consistent with the traffic flow captured in the video as well. The probability of the deck stiffness is also updated. Note that data between 5 to 15 second have low amplitude comparable to the measurement noise level, and therefore do not provide much information to sharpen the deck stiffness distribution during that period of time. Note also that at the time instant slightly later than 20 second, when a truck traverses the bridge arousing bridge vibration with a larger amplitude, the probability of a lower stiffness β =0.85 surges, signaling the nonlinear behavior of the bridge structure. Overall, after updating using this 60-second record, the probability distribution of deck stiffness is gradually sharpened, resulting in that the stiffness correction

coefficient of the deck element with maximum probability is β =0.95, while another β =0.85 is still with considerable probability.

Recall that the dynamic vehicle-bridge interaction is not considered in the formulation of the stochastic model of traffic excitations; however, when extremely heavy cargo trucks pass over, such interaction is significant and can lead to unreliable identification results. Taking advantage of simultaneously estimated vehicle weights, vibration data during such events can be excluded from the updating procedure, by setting an upper limit on the vehicle weight. In this study, the limit is set to 80 kN, which is estimated based on the specification of a fully loaded large pick-up with a fully loaded trailer (e.g., http://www.automotive.com/2005/12/chevrolet/silverado/specifications/). Vehicles heavier than that are mostly heavy cargo trucks with a different suspension device that have low fundamental frequencies and interact considerably with the bridge.

To visualize the results of this Bayesian updating procedure, Figure.6.3.16 (a) and (b) graph the evolution of the probability distribution over the entire 360-second period and the simultaneously identified vehicle weight history, respectively. Figure 6.3.17 graphs the resulted distribution of β at several selected instants to reveal the effect of Bayesian updating. It is illustrated that in this updating procedure, using the information obtained by vibration sensors and also that from traffic video, the deck sectional stiffness is pin-pointed to 95% of the $\overline{EI}$ value calculated from design drawings, with a probability of 92.2%, which indicates that the superstructure of the JRO possesses a stiffness close to its design value and therefore is in its normal integrity condition.

6.3.7 Summary

A stochastic model of traffic excitation on bridges is developed assuming that vehicles traversing a bridge arrive in accordance with a Poisson process, and that the contact force of a vehicle on the bridge deck can be converted to equivalent dynamic loads at the nodes of the beam elements. Random vehicle arrivals, speeds and weights are considered. The traffic excitation process is formulated as a filter Poisson process with a generalized definition. The Campbell's theorem is extended to apply to random process of this type. The covariance model of traffic excitations on bridges is derived and found conforming to a uniformly modulated non-stationary process. The model reveals that traffic excitation on a bridge is intrinsically spatially correlated in most cases, with only one exception where a bridge carries symmetric two-way traffic. This study demonstrates that the parameters in this model, such as the Poisson arrival rate and the stochastic distribution of vehicle speeds, can be obtained by processing the traffic video images and adopting simple statistical inference techniques. Partial traffic information expressed by this stochastic model is incorporated in a Bayesian framework to evaluate the structural properties and update their uncertainty for condition assessment of the bridge superstructure. It is validated on a monitored real-life highway bridge that the information collected, both by bridge vibration measurement and video-based traffic monitoring, sharpens the probability distribution of the structural element stiffness, pin-points the element properties that serve as the indicators of structural integrity. The vehicle weights are also estimated simultaneously in this procedure.

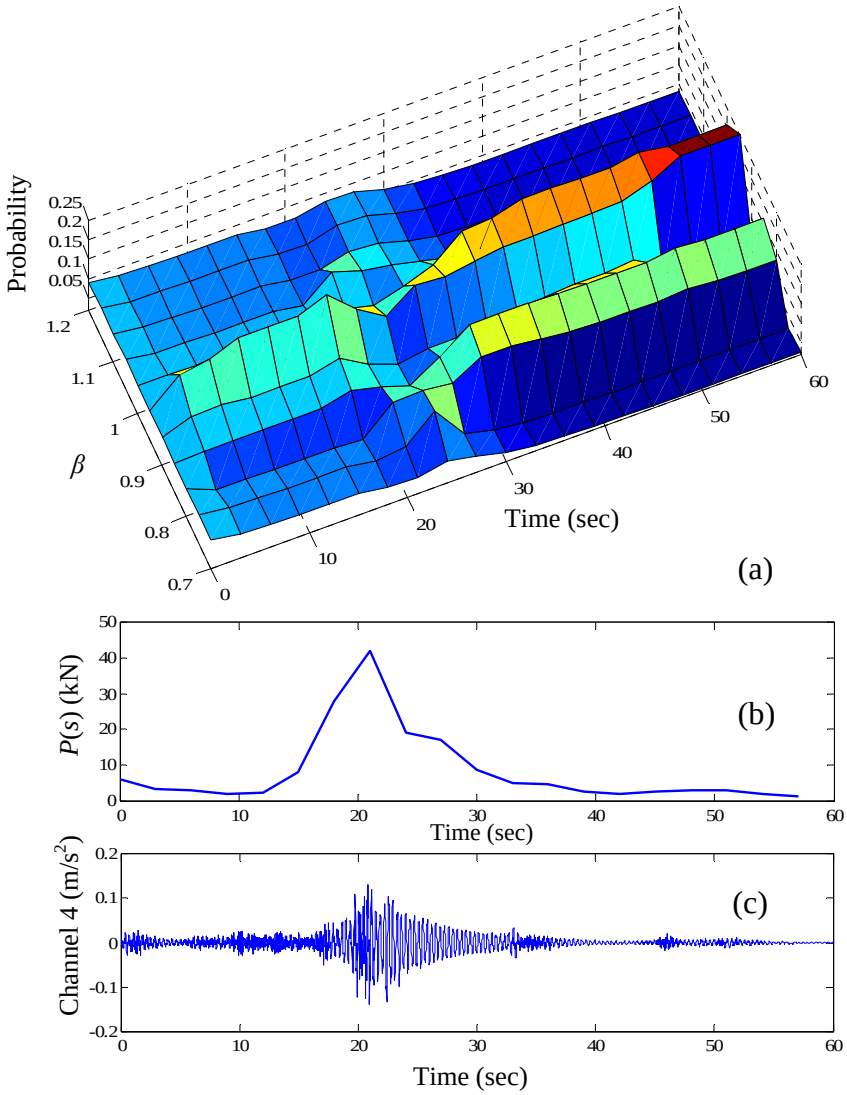

Figure 6.3.15 Results Using 0-60 Second Data

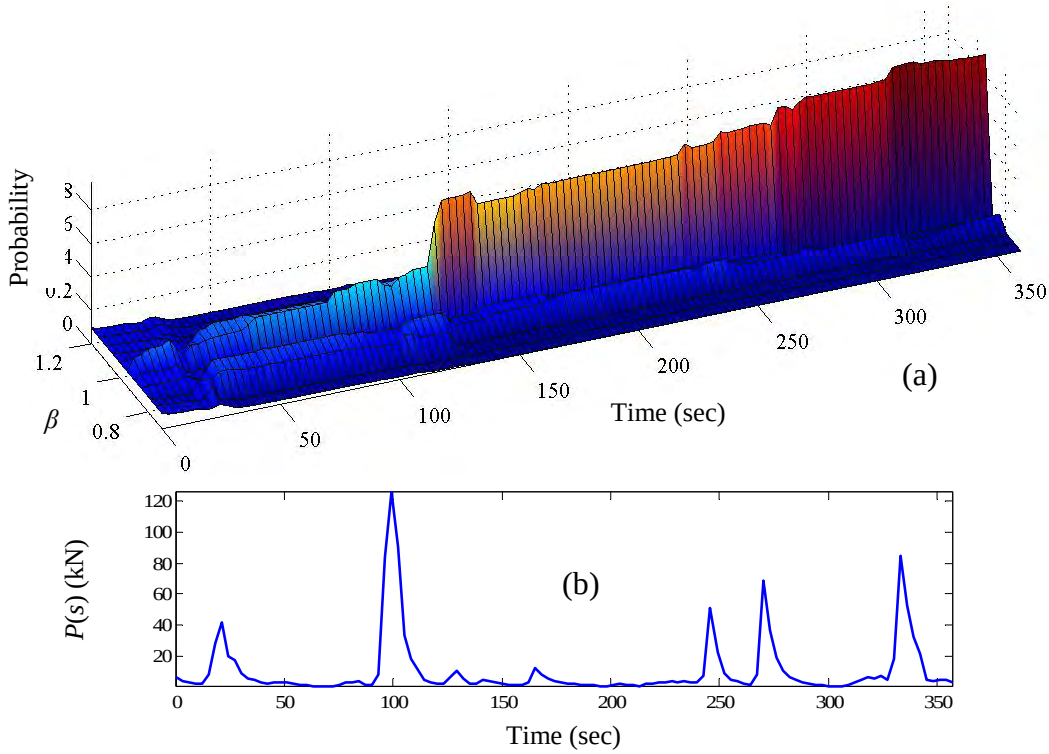

Figure 6.3.16 Results Using Entire 0-360 Second Data

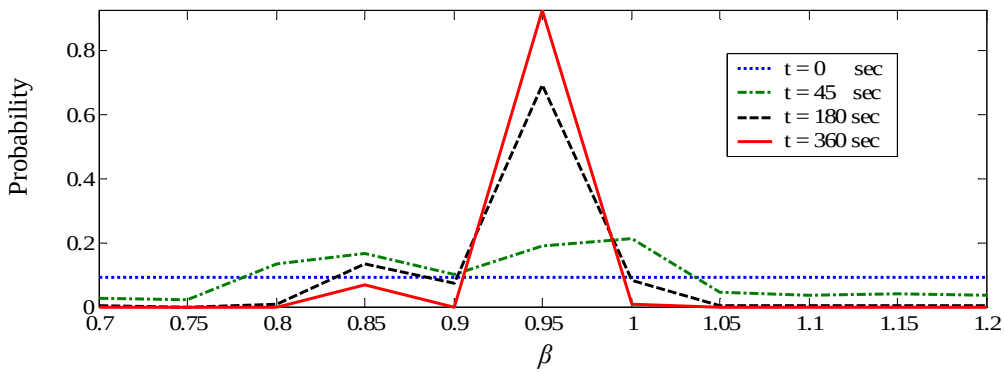

Figure 6.3.17 Distribution of β at Selected Instants

6.4 Sub-Structure Condition Assessment

6.4.1 Frequency Domain Identification

In this section the two system identification methods used in this chapter are outlined. They are model-based parametric methods that utilize global optimization to identify the model parameters that reconcile the predicted and measured vibration characteristics. The system model is assumed LTI, and the identification method is relatively easy to implement by optimization routines.

6.4.1.1 Least Squares Estimation for Modal Parameters

Model parameterization: sectional stiffness reduction coefficients

Actual sectional stiffness is represented by a set of correction coefficients, β_i's , being a fraction of the sectional stiffness calculated from drawings. To be specific,

$$\beta_i = \frac{(k)_A^i}{(k)_D^i}, \tag{6.35}$$

where $(k)_A^i$ is the actual (subscript A) sectional stiffness of Element i (superscript i), and $(k)_D^i$ is the sectional stiffness of the same element calculated from drawings (subscript D). Sectional stiffness k can be either EI for bending stiffness or EA for axial stiffness of an element, depending on the applications.

Rayleigh type damping was assumed in this study for all the models. A Rayleigh damping matrix C is a linear combination of the mass and stiffness matrices M and K, by

$$C = aM + bK . \tag{6.36}$$

Two correction coefficients, α_i (i = 1, 2), quantifying the damping characteristics of the specimens are defined as

$$\alpha_1 = \frac{(a)_A}{(a)_D} \text{ and } \alpha_2 = \frac{(b)_A}{(b)_D}, \tag{6.37}$$

where $(a)_A$ is the actual (subscript A) Rayleigh coefficient a, and $(a)_D$ is the Rayleigh coefficient a assumed for design purpose (subscript D); while $(b)_A$ is the actual (subscript A) Rayleigh coefficient b and $(b)_D$ is that for design purpose (subscript D). $(a)_D$ and $(b)_D$ are obtained by assigning a 5% damping for both the first and the second modes for the finite element model derived from design drawings.

With a finite element model of the specimen parameterized by β_i's and α_i's, collectively denoted as

$$\theta = \{\beta_1, \cdots, \beta_n, \alpha_1, \alpha_2\}^T, \tag{6.38}$$

the analytical natural frequencies, mode shapes, and modal damping ratios are all readily obtained by eigen analysis.

A weighted-nonlinear-least-square procedure was used to identify α_i's and β_i's (i.e., θ) for the specimen in the first experiment, based on the modal characteristics. The following object function is employed:

$$\begin{aligned} Obj(\theta) &= (1000 \cdot \Delta f_1)^2 + (500 \cdot \Delta f_2)^2 \\ &+ (10 \cdot MAC_1)^2 + (MAC_2)^2 + (10 \cdot \Delta\zeta_1)^2 + (\Delta\zeta_2)^2 \end{aligned} \tag{6.39}$$

where, $\Delta f_i = \dfrac{f_i^M - f_i(\theta)}{f_i^M}$, $(i = 1,\ 2)$; $MAC_i = \dfrac{[(\phi_i^M)^T \cdot \phi_i^A]^2}{[(\phi_i^M)^T \cdot (\phi_i^M)][(\phi_i^A)^T \cdot \phi_i^A]}$, $(i = 1,\ 2;$ and $\phi_i^A = \phi_i(\theta)$); and $\Delta\zeta_i = \dfrac{\zeta_i^M - \zeta_i(\theta)}{\zeta_i^M}$, $(i = 1,\ 2)$.

f_i^M, ϕ_i^M and ζ_i^M are natural frequency, mode shape and damping ratio of the *i*-th mode extracted from vibration measurements, respectively; $f_i(\theta)$, $\phi_i(\theta)$ and $\zeta_i(\theta)$ are the analytical frequency, mode shape and damping ratio of the *i*-th mode associated with a correction coefficient set θ. *MAC* values so defined are indicators of the similarity between two shapes. And different weight, such as 1000, 500, 10 and 1, are adopted to emphasize the relative significance among the vibration characteristics and the various confidence levels when they are obtained from the measured data. Parameters in θ, $(\beta_1, \beta_2, \alpha_1, \alpha_2)$, are each confined to a lower bound 0.001 and an upper bound 4, based on a priori knowledge of the structural system. To solve the weighted-nonlinear-least-square problems, a minimization with linear constrains by quasi-Newton method (Polak, 1997) is employed.

6.4.1.2 Neural Network Based Identification

The neural network technique (e.g., Feng and Bahng 1999; Masri et al. 2000; Yun et al. 2001) can be used to obtain the elemental stiffness values based on the measured dynamic characteristics of a structure. The neural network-based system identification method has several advantages compared with conventional system identification methods. The neural network approach is more capable of obtaining elemental stiffness values based on the partially and incompletely measured components of the mode shapes due to the limited sensor number, and on only a few lower modes extractable from the vibration signals. Furthermore, it is very convenient to use the neural network to parameterize any properties of the structures, such as the effective shear area, as the unknowns to be identified. In contrast to many system identification

methods in which the sensitivity matrix may become unstable especially for complex structural systems, the neural network approach does not require calculation of the sensitivity matrix, and thus can be applied to the complex civil engineering structures avoiding the numerical difficulty.

As shown in Figure. 6.4.1, the neural network consists of an input layer, hidden layers, and an output layer. The relationship between input and output of a neural network can be nonlinear or linear, and its characteristics are determined by the weights assigned to the connections between the neurons in two adjacent layers. Changing these weights will change the input/output relationship of the network. A systematic way of determining the weights of the network to achieve a desired input/output relationship is referred to as a training or learning algorithm. The standard back propagation algorithm and radial basis networks were used in this study, for training the neural network to identify structural parameters (the stiffness and the mass matrices of the bridge, and the spring stiffness at the abutments) from measured natural frequencies and mode shapes. The procedure of the neural network-based identification involves the following steps: (1) determining the types of input and output patterns; (2) preparing the training and testing patterns through FE analyses; (3) training the neural network using the back propagation algorithm; and finally (4) estimating the structural parameters of the baseline FE model by inputting the measured natural frequencies and mode shapes to the well trained neural network.

In the present study, the input pattern consists of the natural frequencies and the mode shapes. The output pattern consists of correction coefficients of structural parameters Training input–output data sets were obtained by extensive FE analyses with different sets of correction coefficients.

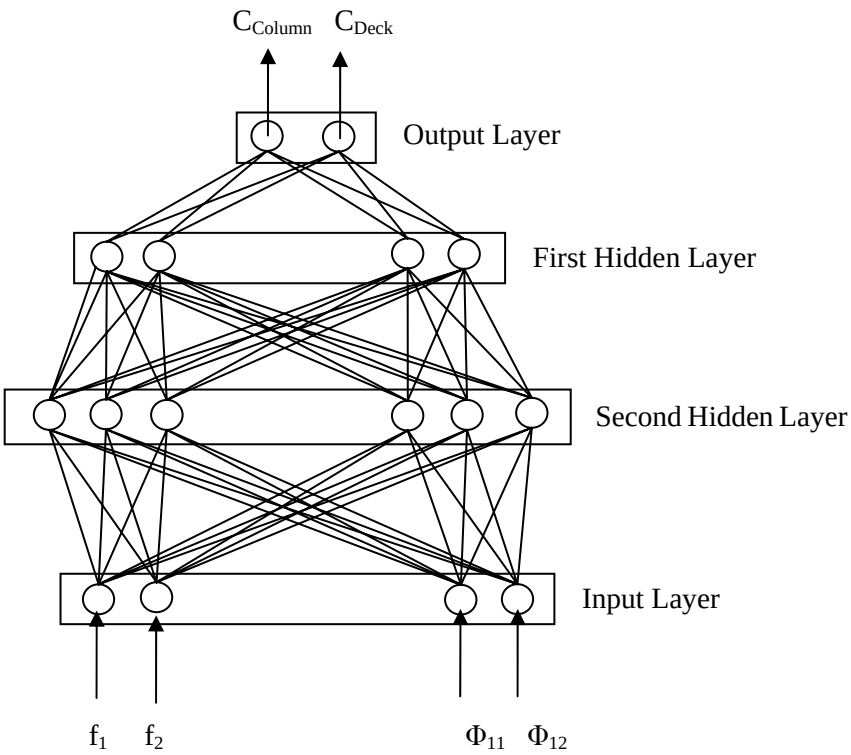

Figure 6.4.1 Architecture of the Neural Network

6.4.2 Time Domain Identification

In this chapter two time domain based system identification methods are discussed. The first one is least squares estimation for structural parameters in an off-line fashion. The second one is extended Kalman filter based identification which is an on - line methodology.

6.4.2.1 Least Squares Estimation for Structural Parameters

Least squares estimation for structural parameters to predict the response time - histories and compare to the measured signals, so as to avoid possible errors when extracting the modal characteristics (frequencies, mode shapes and damping) from vibration data.

A similar weighted-nonlinear-least-square procedure like in section 6.4.1.1 was used to identify α_i's and β_i's (i.e., θ). The object function is:

$$Obj(\theta) = (\Delta\mathbf{Z})^{\mathbf{T}}\mathbf{W}(\Delta\mathbf{Z}) \tag{6.40}$$

where, $\Delta\mathbf{Z} = \mathbf{Z}^M - \mathbf{Z}(\theta)$. $\mathbf{Z}^M$ is a matrix containing the measured time histories of the acceleration responses at the sensor locations, arranged in such a way that its columns are associated with different channels and rows are associated with increasing time. $\mathbf{Z}(\theta)$ is a matrix of predicted acceleration responses using the MIMO state-space model parameterized by θ, arranged in the same manner as $\mathbf{Z}^M$. $\mathbf{W}$ is the inverse matrix of the covariance of the noises in different channels, so that the channels with lower noise level are trusted more than those with higher noise level. The identification of sectional stiffness reduction is now optimizing θ to get a minimum of the object function. Parameters in θ, $(\beta_1, \beta_2, \beta_3, \alpha_1, \alpha_2)$, are each confined to a lower bound 0.001 and an upper bound 4, based on a priori knowledge of the structural system. To reduce the risk of converging to a local minimum, 500 to 1000 times of random searches are performed to get a globally plausible initial set of θ^0. In each of the random search, β_i^0's and α_i^0's are randomly picked from uniform distributions between their lower and upper bounds. The smallest $Obj(\cdot)$ is registered and the associated combination of $(\beta_1^0, \beta_2^0, \beta_3^0, \alpha_1^0, \alpha_2^0)$ is adopted as the initial values for quasi-Newton optimization. The quasi-Newton optimization further refines the parameters, and obtains the parameters that best reconcile the predicted and measured responses.

6.3.2.2 Extended Kalman Filter Based Identification

This study applies the the extended Kalman filter (EKF) approach to identify different levels of damage on a large-scale three-bent bridge model caused by earthquake motions, by defining the damage as structural stiffness degradations. Stiffness values

at the lower and upper portions of each column were selected as unknown physical parameters. The stiffness values were identified even when the structure entered a nonlinear range. Also the change in their values caused by seismic damage was identified on-line.

Proposed Damage Detection Method and EKF Formulation

The well-known EKF equations can be summarized, together with the proposed damage detection method, as follows.

A second order equation of motion for a multi degree of freedom system can be written

$$M.\ddot{u}(t) + C(t).\dot{u}(t) + K(t).u(t) = -M.I.\ddot{u}_g \tag{6.41}$$

where *M* is mass matrix, *C(t)* is time varying damping matrix, *K(t)* is time varying stiffness matrix, *u* is the relative displacement vector, *I* is the influence vector and $\ddot{u}_g$ is the input ground acceleration. $\ddot{u} + \ddot{u}_g$ and $\ddot{u}_g$ are measured, M is calculated from design drawings, *C* is considered to be of Rayleigh type damping, i.e. linear combination of *K* and *M* matrices. The objective is to identify *K(t)* which can be directly used as damage indicator.

An extended state vector can be defined as: $x(t) = [u(t), \dot{u}(t), \Psi(t)]^T$ (6.42)

;where $\Psi(t)$ is the extended state which can be assigned as any physical value such as stiffness, damping or hysteretic parameters.

The EKF determines the optimal estimate of the state $\hat{x}_{k|k}$ that minimizes the trace of the error covariance

$$P_{k|k} = E\left[\left(x_k - \hat{x}_{k|k}\right)\left(x_k - \hat{x}_{k|k}\right)^T\right] \tag{6.43}$$

;where ^ denotes estimation.

There are mainly two conceptual phases in EKF namely prediction and correction phases. In prediction phase, state estimate $\hat{x}_{k-1|k-1}$ and the error covariance $P_{k-1|k-1}$ are projected ahead in time resulting in a priori estimates of $\hat{x}_{k|k-1}$ and $P_{k|k-1}$. In the correction phase these a priori estimates are filtered using the information from the new measurements resulting in a posteriori estimate $\hat{x}_{k|k}$ and $P_{k|k}$.

The system can be defined as:

$$\dot{x}(t) = f(x,t) + w(t) \tag{6.44}$$

;where *w(t)* is process noise.

$$y(t) = h(x,t) + v(t) \tag{6.45}$$

;where *y(t)* is the measurement and *v(t)* is the measurement noise.

The system is supposed to meet the conditions below:

$$E[w(t)] = 0 \tag{6.46}$$

$$E[v_k] = 0 \tag{6.47}$$

$$E[w(t)v_k^T] = 0 \tag{6.48}$$

;where subscript *k* indicates discrete time.

Then the values: Q, R, x_0, P_0 can be defined as:

$$E[w(t)w^T(t)] = Q_c(t) \tag{6.49}$$

$$E[v_j v_k^T] = R_k \delta_{jk} \tag{6.50}$$

$$E[x(t_0)] = x_0 \tag{6.51}$$

$$E[(x(t_0) - x_0)(x(t_0) - x_0)^T] = P_0 \tag{6.52}$$

;where subscript *c* indicates continuous time and *j* indicates discrete time.

Linearized Measurement Matrix H_k (for steps 3, 4 & 5 below) can be obtained as:

$$H(x,t) = \frac{\partial h(x,t)}{\partial x} \tag{6.53}$$

$$H_k = H(\hat{x}_{k|k-1}, t_k) \tag{6.54}$$

Linearized State Matrix F_k (for calculating State Transition Matrix) can be obtained as:

$$F(x,t) = \frac{\partial f(x,t)}{\partial x} \tag{6.55}$$

$$F_k = F(\hat{x}_{k|k-1}, t_k) \tag{6.56}$$

State Transition Matrix Φ_{k-1} can be obtained as (for step 1):

$$\Phi_{k-1} = I + \int_{t_{k-1}}^{t_k} F(\hat{x}_{t|k-1}, t)\Phi(t, t_{k-1})dt \tag{6.57}$$

The last equation can be written as:

$$\Phi(t_k, t_{k-1}) = \exp(\Delta t.F_{k-1}) \qquad \text{Constant F}\forall \text{t} \in [\text{t}_{\text{k-1}}, t_k) \tag{6.58}$$

This can be approximated as:

$$\Phi(t_k, t_{k-1}) = I + \Delta t.F_{k-1} \tag{6.59}$$

Also process noise can be discretized as:

$$Q_{k-1} = \Delta t.Q_c(t_{k-1}) \tag{6.60}$$

After initializing Q, R, x_0, P_0, five steps of Kalman Filtering can be performed as follows:

Kalman Filter Equations:

Step 1: Predicted Covariance:

$$P_{k|k-1} = \Phi_{k-1} P_{k-1|k-1} \Phi_{k-1}^T + Q_{k-1} \tag{6.61}$$

Step 2: Predicted State:

$$\hat{x}_{k|k-1} = \Phi_{k-1} \hat{x}_{k-1|k-1} \tag{6.62}$$

Step 3: Kalman Gain:

$$G_k = P_{k|k-1} H_k^T (H_k P_{k|k-1} H_k^T + R_k)^{-1} \tag{6.63}$$

Step 4: Corrected Covariance:

$$P_{k|k} = (I - G_k H_k) P_{k|k-1} \tag{6.64}$$

Step 5: Corrected State:

$$\hat{x}_{k|k} = \hat{x}_{k|k-1} + G_k [y_k - H_k \hat{x}_{k|k-1}] \tag{6.65}$$

So the state vector x is obtained at each time step. As described in (2) state vector contains information of not only displacement and velocity but also of stiffness value. This means that stiffness value is identified for each time step.

Some observations can be made on the Kalman gain: G_k in (6.63):

As the measurement error covariance R_k approaches zero, the gain G_k weights the residual (difference between the measurement and estimation) more heavily:

$$\lim_{R_k \to 0} G_k = H^{-1} \tag{6.66}$$

On the other hand as the a priori estimate error covariance $P_{k|k-1}$ approaches to zero, the gain G_k weights the residual less heavily:

$$\lim_{P_{k|k-1} \to 0} G_k = 0 \tag{6.67}$$

As the measurement error covariance R_k approaches zero, actual measurement is trusted more. On the other hand, as a priori estimate error covariance $P_{k|k-1}$ approaches zero, the predicted measurement is trusted more.

Chapter 7

EXPERIMENTAL VERIFICATION OF METHODOLOGIES

This chapter documents the experimental verification of the methodologies developed in this research for interpreting the vibration sensor data into the bridge structural integrity. Large-scale shaking table tests were carried out on two realistic bridges models by progressively damaging the models. The structural damage of different extents was then identified based on the structural vibrations measured on the models.

7.1. Large Scale Shake Table Test Verification

The experimental setup, test procedures and damage observed in the two experiments conducted at University of Nevada, Reno (UNR) are described in this section. The data analysis and damage identification will be presented in the next section.

7.1.1. Two Column Bent Test (Experiment 1)

Experiment 1 was performed on a flared 2-column reinforced concrete bent specimen (Figures 7.1.1 and 7.1.2). As sketched in Figure. 7.1.3, two compensative masses were added to simulate the mass of the superstructure; one weighs 60 kips composed of lead placed on the bent beam, and another 40 kips composed of the concrete block

set aside but linked to the beam by a steel rod. Acceleration signals from the five sensors, whose locations are shown in Figure. 7.1.3, were recorded.

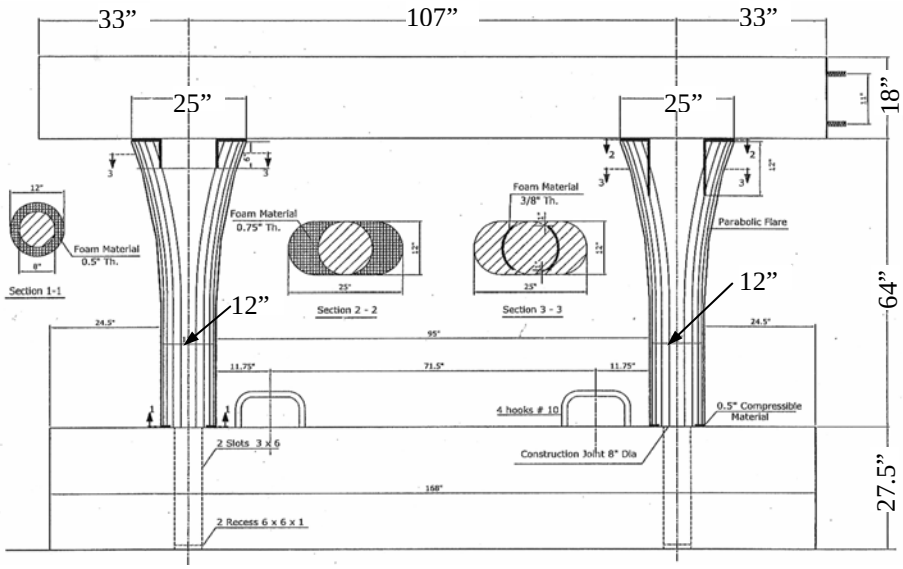

Figure 7.1.1 Layout of the Specimen in Experiment 1
(This drawing is provided by Prof. Sanders at UNR)

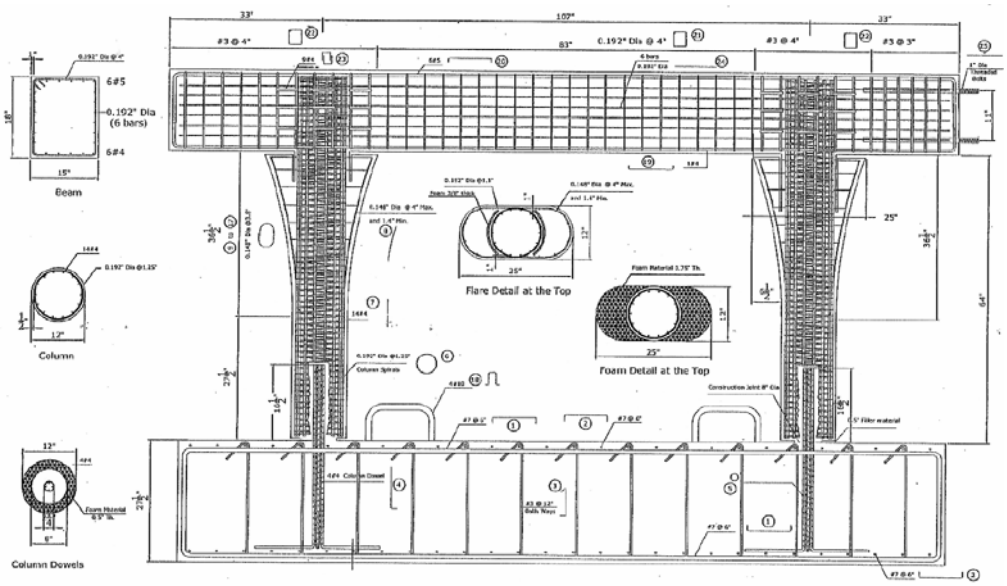

Figure 7.1.2 Reinforcement Details of the Specimen in Experiment 1
(This drawing is provided by Prof. Sanders at UNR)

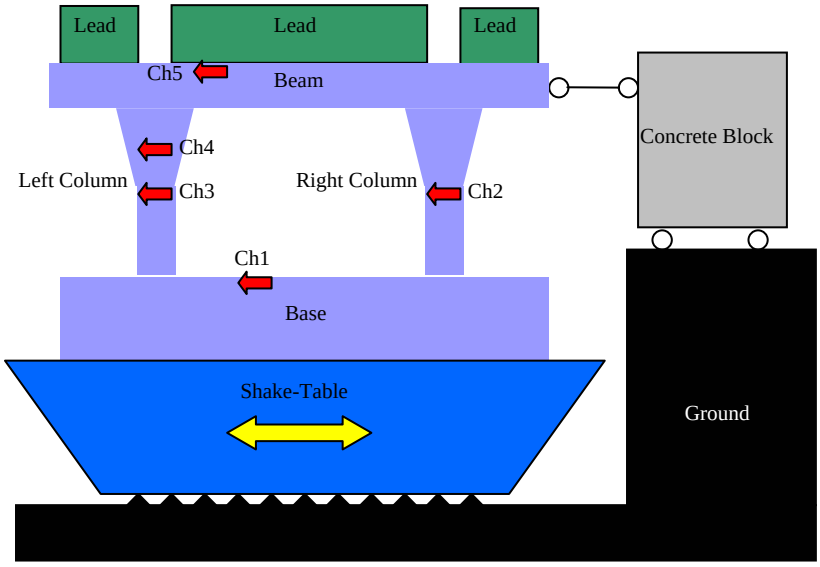

Figure 7.1.3 Schematic Plot of Experiment 1

The ground motion record at the Sylmar station in the 1994 Northridge Earthquake was used as the driving signal of the shaking table to simulation strong motion. Its amplitude was scaled with different scaling factors, namely 0.15, 0.25, 0.50, 0.75, 1.00, 1.25, 1.50, 1.75, 2.00, 2.50, 2.75, sequentially, in different tests to progressively introduce different levels of damage. Before and after each of the strong motions, an ambient input measured at a real bridge, amplified by 50 times just to overcome the friction of the shaking table, drove the shaking table to perturb the bent specimen in the corresponding damage level. In between, four small amplitude free vibrations were also performed to provide another mechanism for identifying the system characteristics at different damage levels.

During the test, after each level of the strong motions, cracks were marked and photos were taken to document the damage. Figure 7.1.4 shows the damage observed in the flared portion of the columns. As the damage accumulated, more and more cracks were observed. However, by looking only at the crack distribution, it is hard to quantify the damage. It is also hard to correlate the crack patterns with the strength or deformation reservation the bent still has before the onset of a catastrophic collapse.

Figure 7.1.4 Damage at Flared Portion of Columns

7.1.2. Full Bridge Test (Experiment 2)

Experiment 2 was performed on a 2-span 3-bent reinforced concrete bridge specimen (Figures 7.1.5 to 7.1.7). As shown in Figure. 7.1.8, each of the three bents is supported individually on a shaking table. The bents are linked by the bridge deck, which consists of three post-tensioned beams. Each of the bents has two columns, having the same design cross sections. But the bents are of different heights (72 in, 96 in and 60 in for Bents 1, 2 and 3, respectively), so that they process significantly different transverse stiffness. To resemble the inertia of other parts of the superstructure not built into this specimen, two compensative masses were added. The shaking tables were driven by input acceleration signals in the transverse direction of the bridge. Eleven accelerometers were installed on the specimen to obtain the acceleration inputs and responses of the bridge, as illustrated in Figure. 7.1.9. Note that the deck is divided into two simply supported spans in the vertical

bending direction. However, in the transverse direction, the existence of the post-tension tendons and the pre-stressed strain warrant a continuous bending moment transmission.

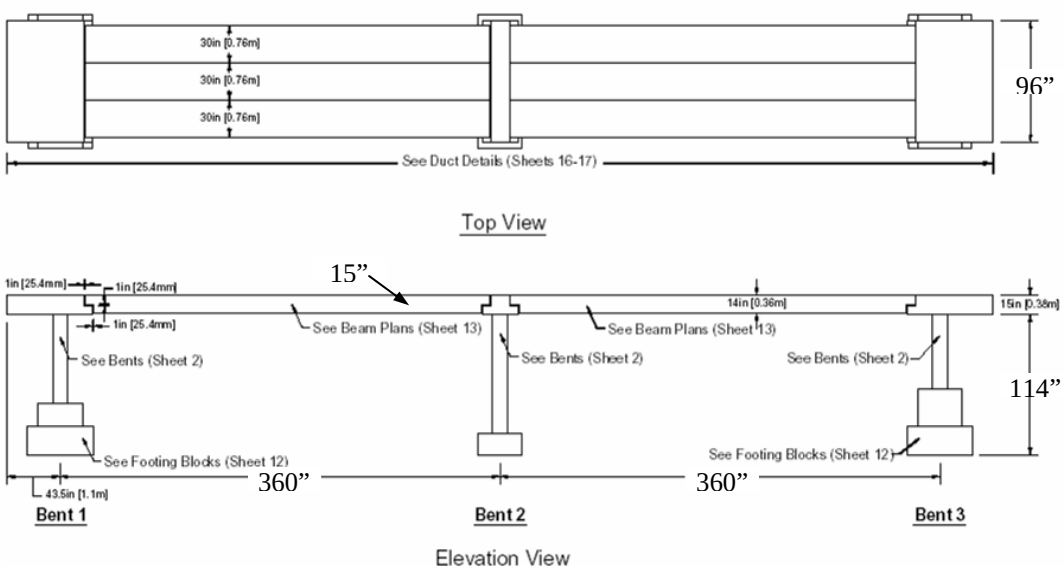

Figure 7.1.5 Design of the Bridge Specimen in Experiment 2
(This drawing is provided by Prof. Saiidi at UNR)

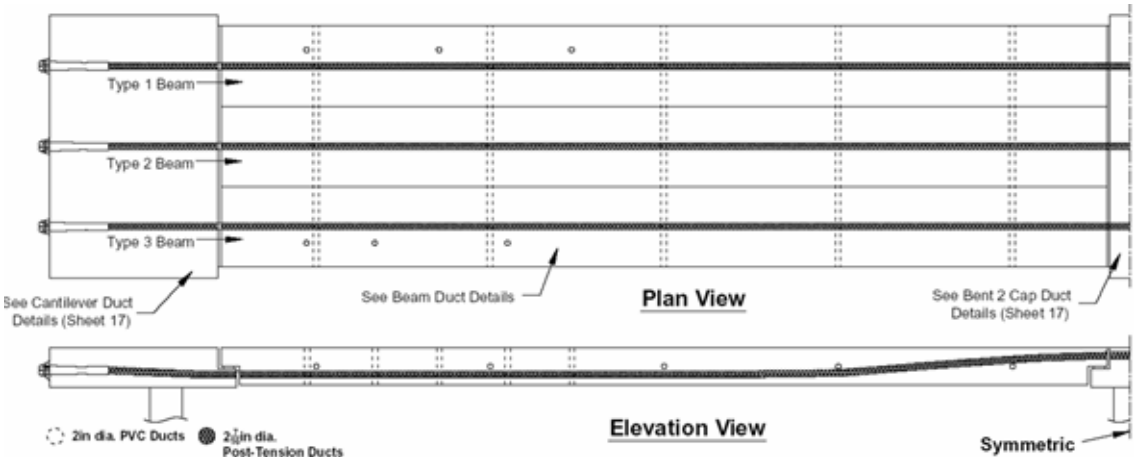

Figure 7.1.6 Design of the Post-tension Ducts in Experiment 2
(This drawing is provided by Prof. Saiidi at UNR)

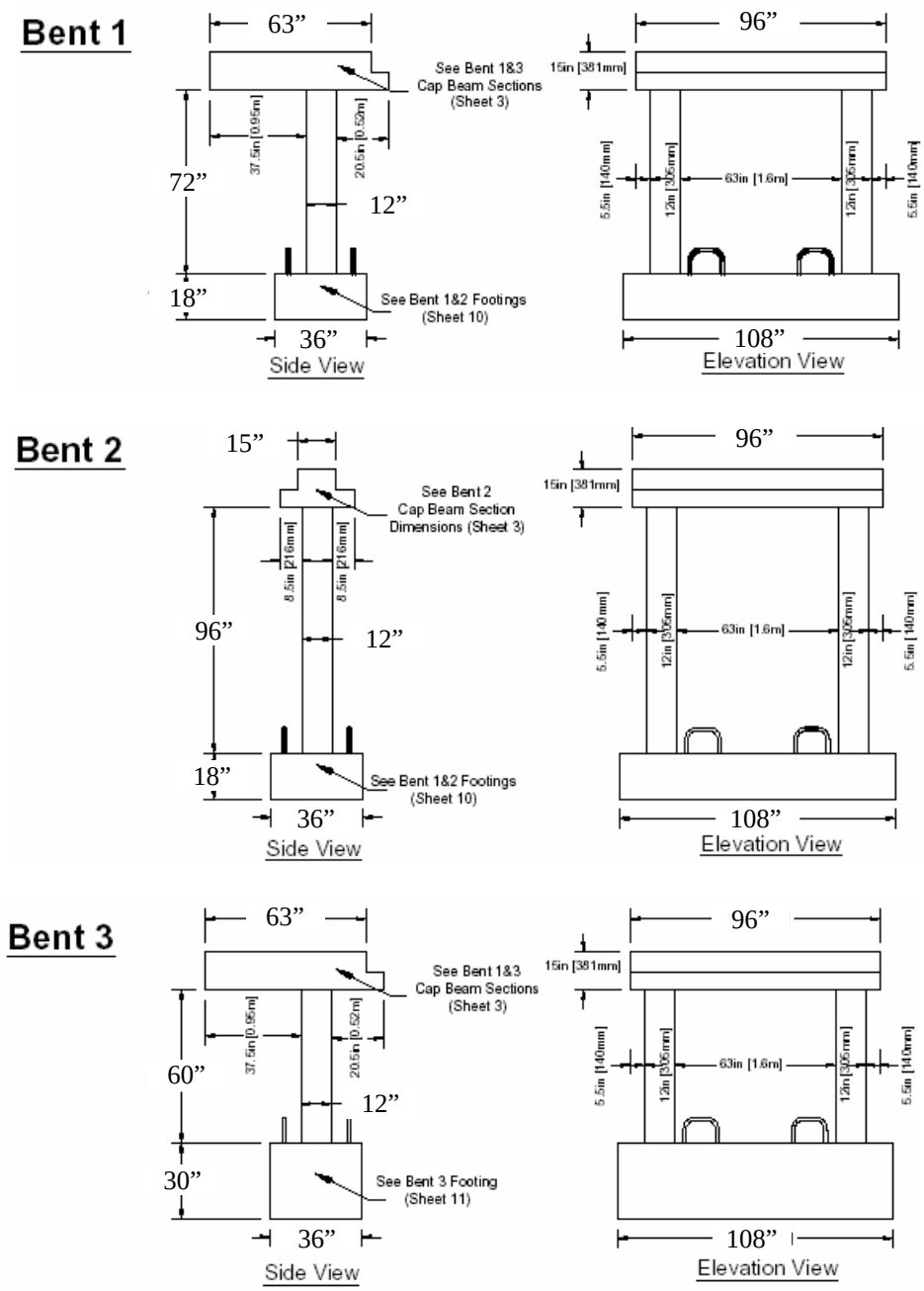

Figure 7.1.7 Design of the Three Bents in Experiment 2
(This drawing is provided by Prof. Saiidi at UNR)

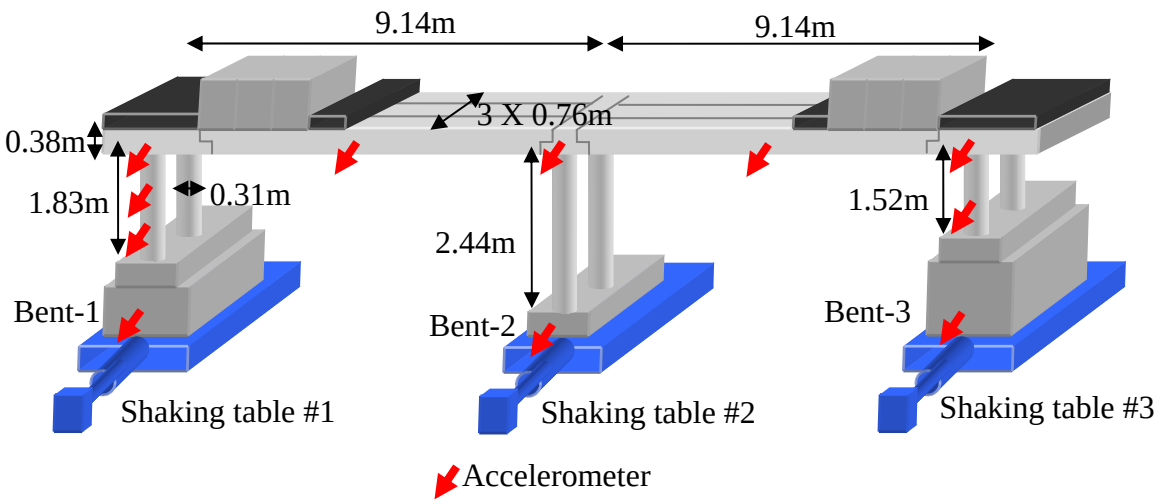

Figure 7.1.8 Illustration of Experiment 2

During the tests, various earthquake ground motions tailored to various soil-foundation scenarios were used as the driving signals of the shaking tables to simulation strong motions. By their demands to the bridge structure, ground motions were classified into different levels, such as low, moderate, high, severe and extreme levels. After the most strong ground motion, a smaller motion was input to mimic an aftershock earthquake. In Table 7.1.1, the sequence of the tests (denoted in Table 7.1.1 by 'T-#') and their input peak ground accelerations (PGA) are listed. Different levels of damage were introduced to the bridge specimen by these strong motions. In between of the strong motions, low amplitude white noise (PGA is approximately 0.05g) drove the shaking tables to perturb the specimen in the corresponding damage level (denoted by 'WN-X-#' or 'WN-Y-#' in Table 7.1.1, where 'X' denotes the excitations along the transverse direction of the bridge, and 'Y' denotes those in the longitudinal direction). Free vibrations were also aroused by inputting a snap wave (denoted by 'S-#' in the table).

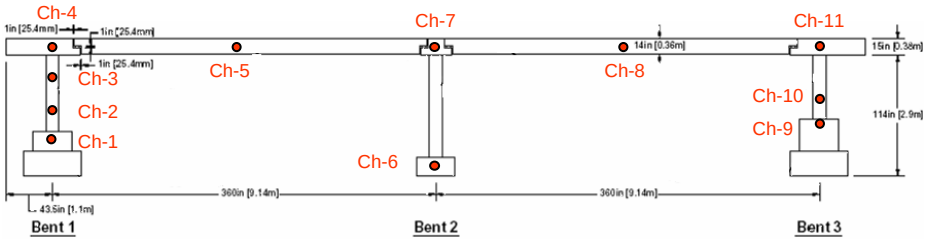

Figure 7.1.9 Schematic Plot of the Sensor Layout in Experiment 2

Table 7.1.1 Test Procedure

Tests	Ground Motion Description	PGA (g)	Damage Description
S-1	Snap (Arouse Free Vibration).		
WN-X-1	White Noise in Transverse.		
WN-Y-1	White Noise in Longitudinal.		
T-12	Low Earthquake in Transverse.	0.0851	
T-13	Low Earthquake in Transverse.	0.1729	Bent 1 yields.
T-14	Moderate Earthquake in Transverse.	0.3193	Bent 3 yields.
S-2	Snap (Arouse Free Vibration).		
WN-X-2	White Noise in Transverse.		
WN-Y-2	White Noise in Longitudinal.		
T-15	High Earthquake in Transverse.	0.6272	Bent 2 yields.
T-16	Severe Earthquake in Transverse.	n.a.	
T-17	Extreme Earthquake in Transverse.	1.135	
S-3	Snap (Arouse Free Vibration).		
WN-X-3	White Noise in Transverse.		
WN-Y-3	White Noise in Longitudinal.		
T-18	Extreme Earthquake in Transverse.	1.3975	
T-19	Extreme Earthquake in Transverse.	1.7033	Bent 3 steel buckles.
S-4	Snap (Arouse Free Vibration).		
WN-X-4	White Noise in Transverse.		
WN-Y-4	White Noise in Longitudinal.		
T-20	After Shot in Transverse.	1.2861	
S-5	Snap (Arouse Free Vibration).		
WN-X-5	White Noise in Transverse.		
WN-Y-5	White Noise in Longitudinal.		

Figure 7.1.10 shows the crack propagation at the lower portion of a column of Bent 1. As the damage accumulated, more and more cracks were observed, and finally concrete spallings were seen at the bottom of the column.

It is observed that cracks are not clear indication of the formation of a plastic hinge. In this experiment, advantages were taken of the densely instrumented strain gauges on the steel rebars embedded before concrete casting to read the deformation of the

steels, based on which yielding of the bents was found. As indicated in Table 7.1.1, the damage procedure observed can be outlined as: Bent 1 yields → Bent 3 yields → Bent 2 yields → Bent 3 steel buckles. This procedure is largely determined by the relative heights of the bents. The onset of Bent 1 yielding is due to the fact that the first mode of this bridge specimen (at its undamaged stage) has the largest displacement demand on Bent 1. After the yielding of Bent 1, Bent 3 attracts most the seismic force and yields, and then so happens to Bent 2 after the yielding of Bents 1 and 3. The final collapse (in the test, the specimen was protected to avoid actual collapse) is associated with the steel buckling at Bent 3, which has the smallest ductility capacity among the three.

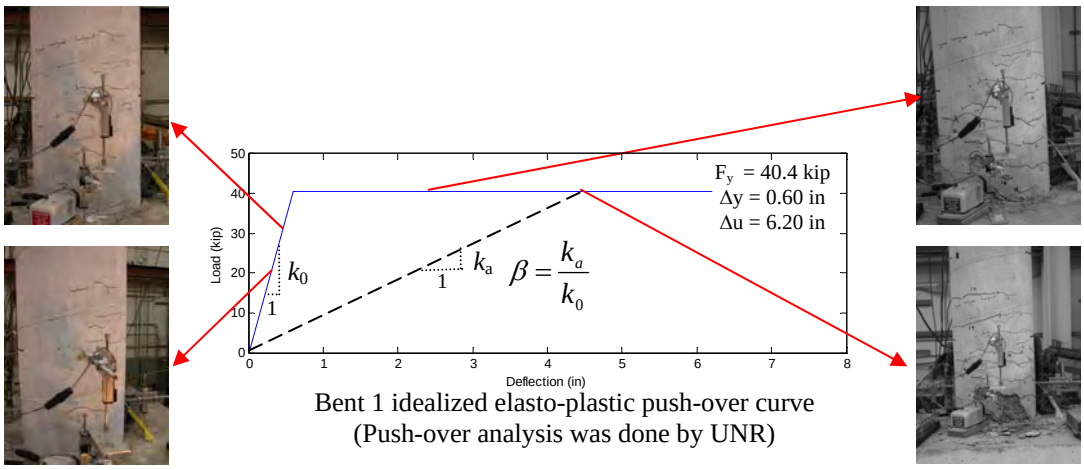

Figure 7.1.10 Damage Observed at a Column of Bent 1

To further confirm the observed damage strain measurements were analyzed. The strain sensors were embedded in the rebars at the locations shown in Figure 7.1.11. In the same figure, strain time history measured during Test-14 at Bent-3 is shown. If the average yielding value of steel, $\varepsilon_y = 0.002$, is taken as a guide; it can be seen that around 4 sec yielding occurs after which the vibration continues around a shifted axis.

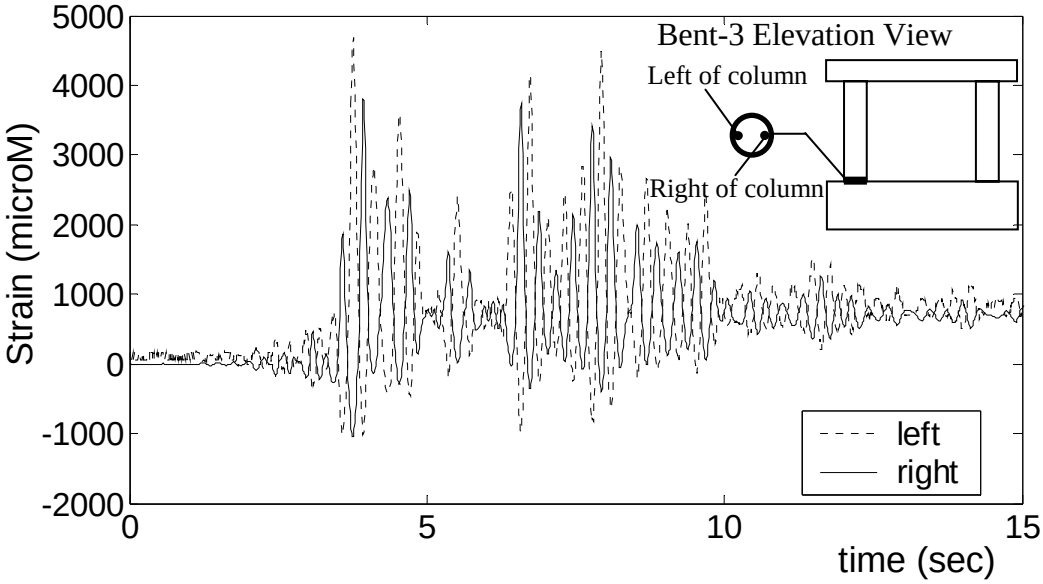

Figure.7.1.11 Strain Measurements at Bent-3 During Test 14

On an existing bridges, however, such strain gauge embedment is hardly possible. Therefore, the objective of this research is to identify such seismic damage using the acceleration measurement, rather than strain measurement. Compared with strain gauges, accelerometers can be much more easily installed on existing structures.

7.2. Damage Identification Based on Low-Level Excitation

The damage detection methods/algorithms developed in Chapter 6 were tested, in which the sectional stiffness reduction, an indicator of damage, is identified based on acceleration measurement. Compared to strain sensors, accelerometers are much easier to install on an existing structure. Therefore, identification of damage based only on acceleration measurement is highly desirable.

7.2.1. Frequency Domain Identification

The ambient perturbations at the base of the bent were scaled from a record on an instrumented highway bridge, the JRO. It has dominating energy in the range between 5 to 10Hz. The specimen varied its responses to this ambient input at different damage stages, as shown by a portion of the response time-histories depicted in Figure. 7.2.1. The specimen behaved linearly before damage occurred (after 15% and 25% Sylmar motions), while the amplitudes and the frequencies were reducing as damage occurred and accumulated.

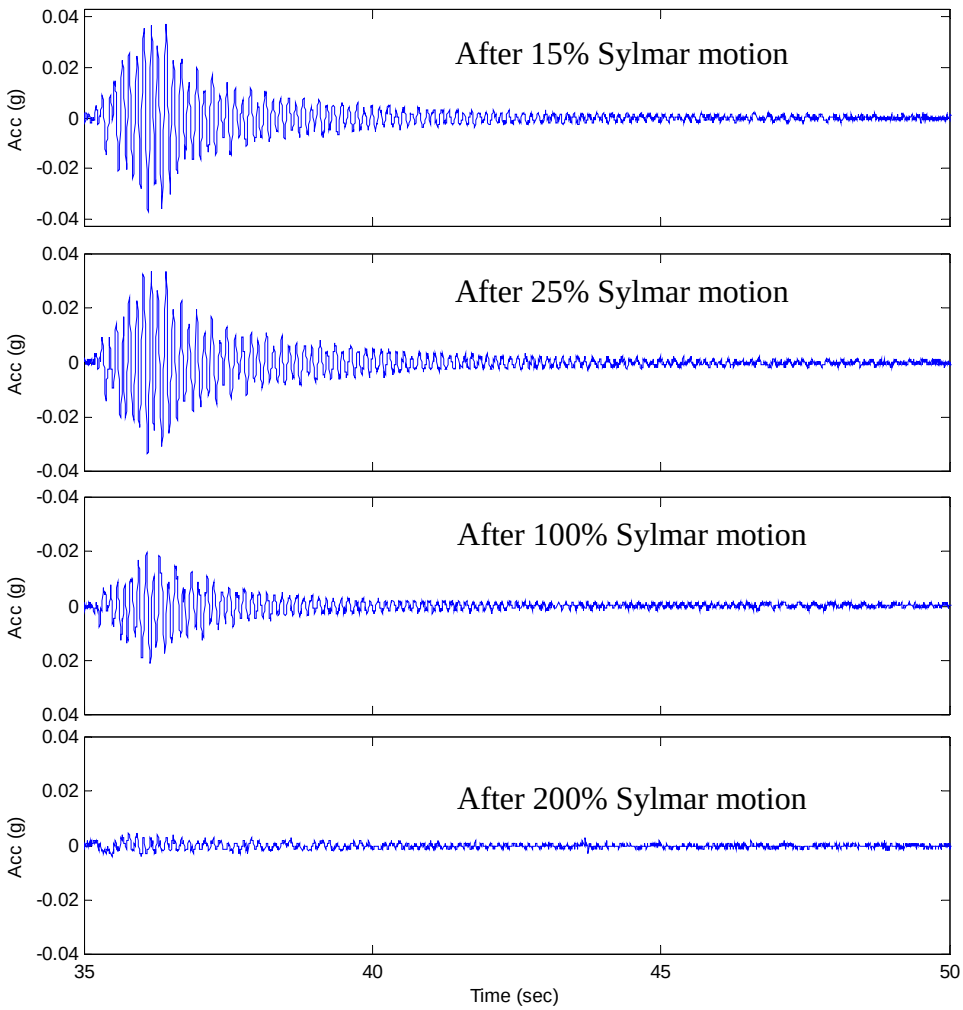

Figure 7.2.1 Measured Acceleration Responses at Ch-5 to Ambient Excitations

Natural frequencies, mode shapes (Table 7.2.3, marked as measured) and damping ratios (Table 7.2.1) for the first two modes are obtained based on the measured

ambient vibration by peak-picking the power spectrum curves (Figure. 7.2.2) and the conventional half-power method. Note that the identification of damping characteristics is not reliable, because viscous damping can not fully represent the nature of hysteretic behaviors.

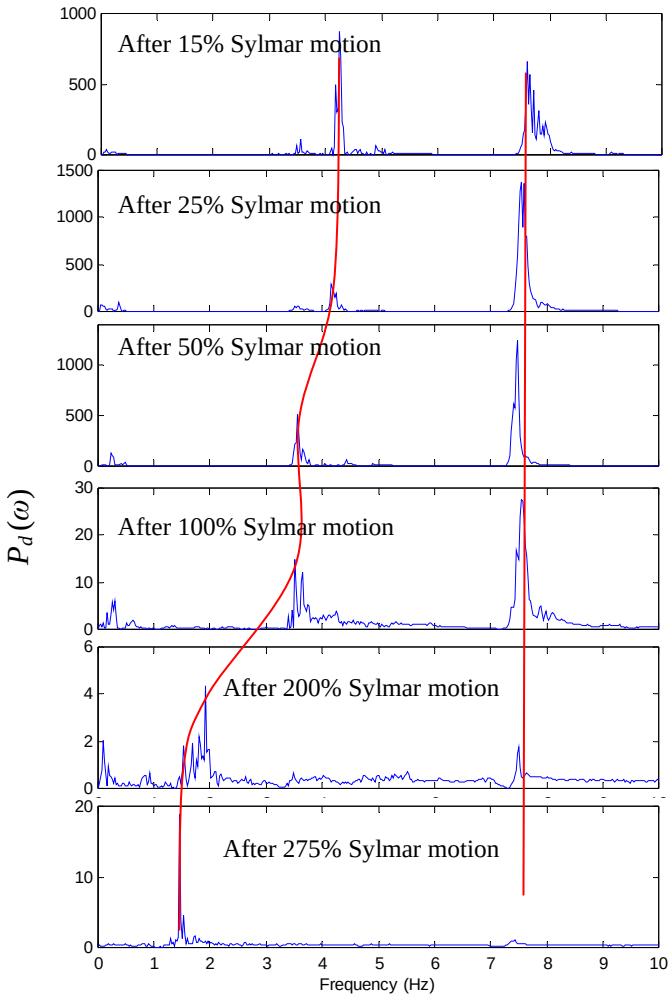

Figure 7.2.2 Peak-Picking of Power Spectrum Density Functions

Table 7.2.1 Damping Ratios ζ

	After 15% Sylmar	After 25% Sylmar	After 50% Sylmar	After 100% Sylmar	After 200% Sylmar	After 275% Sylmar
Mode 1	1.77%	3.43%	2.10%	9.30%	3.29%	2.05%
Mode 2	2.12%	1.15%	1.34%	1.92%	10.43%	15.3%

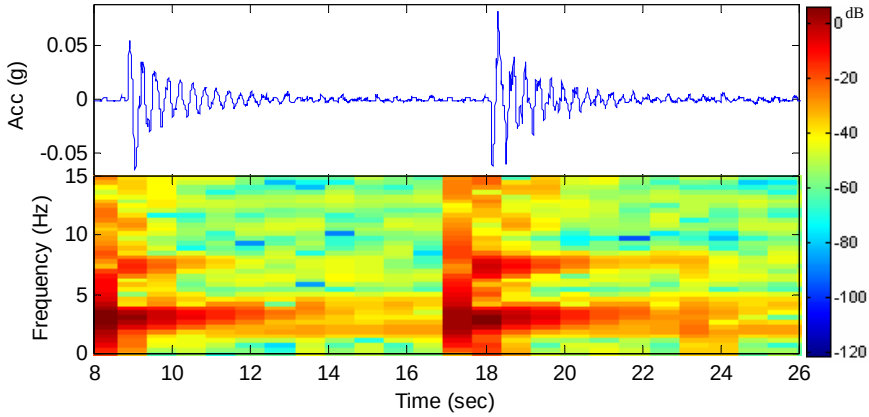

Figure 7.2.3 Free Vibration II (after 100% Sylmar) and Its Time-frequency Plot

Figure 7.2.3 shows the time-frequency plots by short-time Fourier transform of the free vibration response at Ch-5 after 100% Sylmar motion. It illustrates, to some extent, the intrinsic difficulty of time-frequency analysis which intents to trace the structure changes at every instance, i.e., either the frequency resolution or the time resolution have to be compromised.

7.2.2. Time Domain Identification

7.2.2.1. Experiment 1

Using Least Squares Estimation in Frequency Domain outlined previously, the stiffness correction coefficients for the column bending stiffness and the Rayleigh damping coefficients at each damage stage are obtained as in Table 7.2.2.

Table 7.2.2 Identified Correction Coefficients

	After 15% Sylmar	After 25% Sylmar	After 50% Sylmar	After 100% Sylmar	After 200% Sylmar	After 275% Sylmar
β_1	0.9120	0.8651	0.7600	0.5096	0.1035	0.0710
α_1	0.2632	0.9249	0.4874	2.1275	0.1004	0.0027
α_2	0.5561	0.0100	0.1569	0.0001	3.8730	3.8413

Note that the sectional stiffness drops dramatically as damage accumulated, as indicated by β_1 decreasing from 0.91 all the way to 0.07. Therefore, β_1 is a sufficient quantitative indicator of the bent specimen's structural condition and can be plausibly postulated as the secant sectional stiffness at the associated damage stage normalized by the initial sectional stiffness. Table 7.2.3 compares the empirical and analytical modal characteristics using the corrected model.

Table 7.2.3 Comparison of the Modal Characteristics

	After 15% Sylmar		After 25% Sylmar		After 50% Sylmar	
	Measured	Analytical	Measured	Analytical	Measured	Analytical
f_1 (Hz)	4.25	4.11	4.15	4.0329	3.88	3.82
f_2 (Hz)	7.59	8.46	7.54	8.2981	7.47	7.86
ϕ_1	-0.5000	-0.0163	-0.5214	-0.0166	-0.5523	-0.0170
	-0.3587	-0.0167	-0.3633	-0.0170	-0.3372	-0.0175
	-0.4919	-0.0269	-0.4794	-0.0274	-0.4621	-0.0282
	-0.6152	-0.0331	-0.6024	-0.0337	-0.6010	-0.0345
ϕ_2	-0.5722	0.0339	-0.5738	0.0337	-0.5625	0.0336
	-0.3371	0.0356	-0.3389	0.0355	-0.3402	0.0353
	-0.4521	0.0573	-0.4510	0.0571	-0.4537	0.0568
	-0.5952	0.0699	-0.5924	0.0696	-0.6016	0.0692
ζ_1 (%)	1.77	1.77	3.43	3.40	2.10	2.10
ζ_2 (%)	2.12	2.15	1.15	1.68	1.34	1.36
	After 100% Sylmar		After 200% Sylmar		After 275% Sylmar	
	Measured	Analytical	Measured	Analytical	Measured	Analytical
f_1 (Hz)	3.47	3.47	1.76	1.76	1.46	1.47
f_2 (Hz)	7.57	7.57	7.50	7.52	7.42	7.42
ϕ_1	-0.5649	-0.0220	-0.4063	-0.0288	-0.4060	0.0292
	-0.3443	-0.0228	-0.3715	-0.0301	-0.3882	0.0304
	-0.4642	-0.0366	-0.5526	-0.0482	-0.5320	0.0488
	-0.5885	-0.0447	-0.6253	-0.0584	-0.6286	0.0591
ϕ_2	-0.5616	-0.0307	-0.3892	-0.0248	-0.3860	0.0245
	-0.3380	-0.0324	-0.3779	-0.0265	-0.3767	0.0261
	-0.4493	-0.0521	-0.5042	-0.0423	-0.4961	0.0417
	-0.5918	-0.0631	-0.6709	-0.0507	-0.6804	0.0498
ζ_1 (%)	9.30	9.07	3.29	3.29	2.05	2.05
ζ_2 (%)	1.92	4.15	10.43	10.66	15.30	10.24

To further verify the identified results, a finite element model with proper corrections made according to the identified $(\beta_1, \alpha_1, \alpha_2)$ is used to simulate the bent response to ground motions in time domain (Figure. 7.2.4).

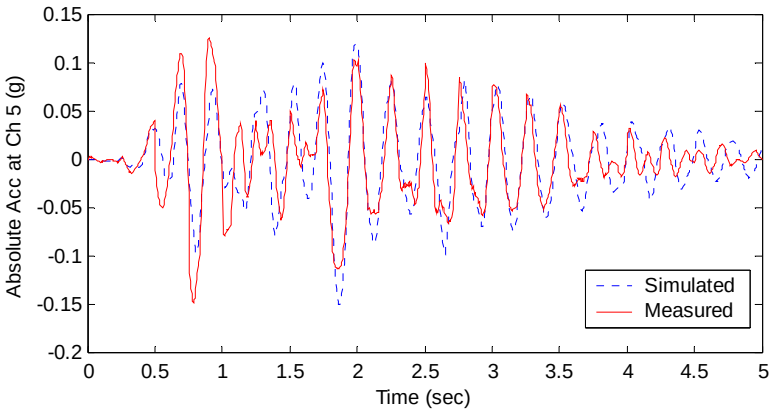

Figure 7.2.4 Simulated and Measured Responses for 15% Sylmar Motion

7.2.2.2. Experiment 2

To lessen the effect of noise, signals were band-pass filtered in frequency range from 1 to 15 Hz. Figure 7.2.5 shows the filtered acceleration at Ch-4 during low-amplitude transverse white noise tests.

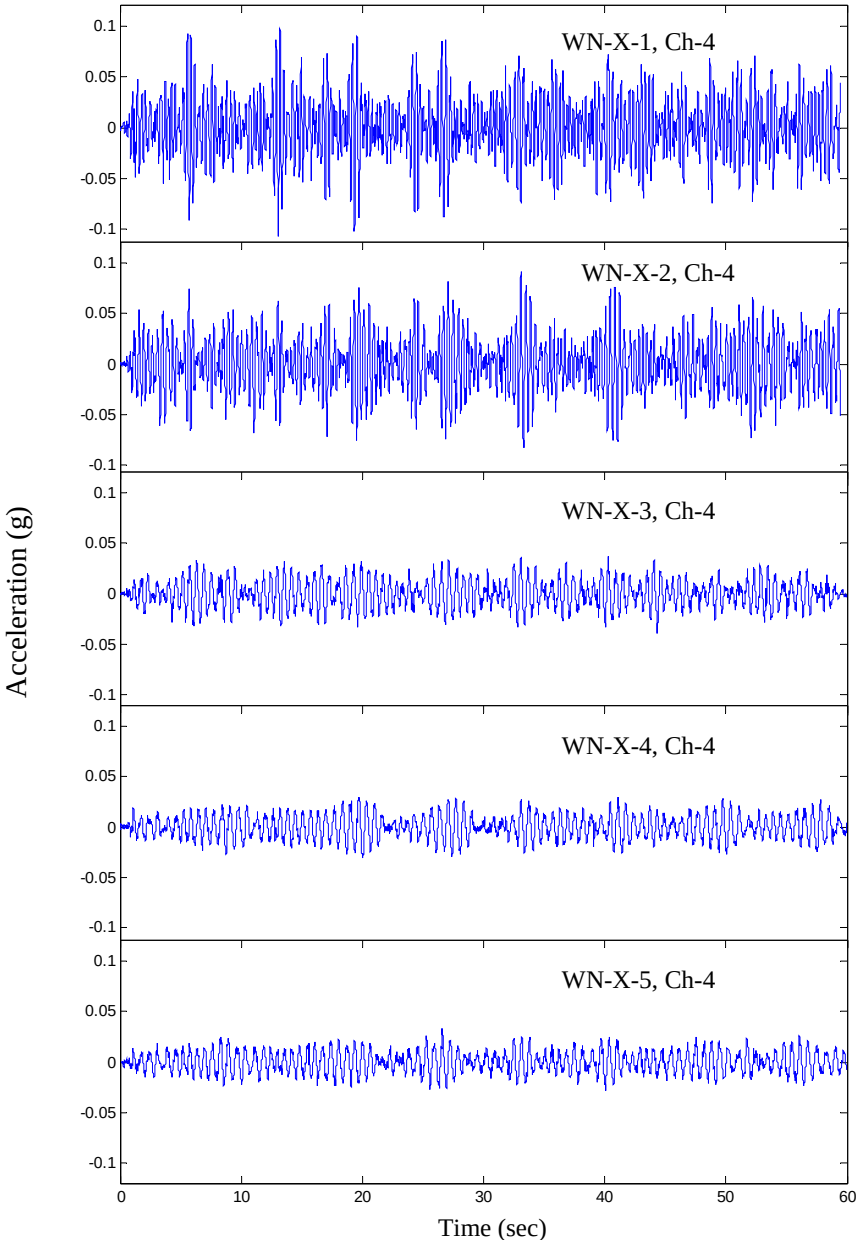

Figure 7.2.5 Acceleration Responses at Ch-4 to White Noise Disturbances at Various Damage Stages

Following the Least Squares Estimation Time Domain outlined above, the correction coefficients were identified at different damage stages using the acceleration measurements obtained in the low amplitude white noise tests. The results are listed in Table 7.2.4. Note that the identified sectional stiffness coefficients clearly indicate the same damage procedure as observed in the experiment. Bent 1 yields → Bent 3

yields → Bent 2 yields → Bent 3 steel buckles. Between WN-X-1 and WN-X-2, β_1 and β_3 drop from 0.78 to 0.53 and from 0.85 to 0.61 respectively, while β_2 remains same level, indicating in a quantitative manner the yielding of Bent 1 and Bent 3 between these two tests. Then between WN-X-2 and WN-X-3, the decrements in all β_1, β_2 and β_3 signal that not only Bent 2 yielded, but also the damage in Bent 1 and Bent 3 further developed. In WN-X-4, β_3 touches down to a very low value, 0.11, associating with the severe damage in Bent 3 (steel buckling). And the results of WN-X-5 are comparable to those in WN-X-4, which is consistent with the observation that the after-shot earthquake actually had not further destroyed the bridge specimen significantly.

Therefore, β_i is a sufficient quantitative indicator of the bridge specimen's structural condition. Based on the previous discussion on post-event low amplitude hysteresis, β_i can be plausibly postulated as the secant sectional stiffness at the associated damage stage normalized by the initial sectional stiffness. If a push-over analysis is performed and a capacity curve of the specimen is obtained, β_i can further be correlated to the deformation capacity reservation the specimen/element still has at this damage stage.

Table 7.2.4 Identified Correction Coefficients

Tests	β_1	β_2	β_3	α_1	α_2
WN-X-1	0.78	0.79	0.85	1.02	2.05
WN-X-2	0.53	0.80	0.61	0.33	6.24
WN-X-3	0.19	0.31	0.18	0.82	3.52
WN-X-4	0.20	0.16	0.11	2.12	1.28
WN-X-5	0.17	0.13	0.13	0.85	4.21

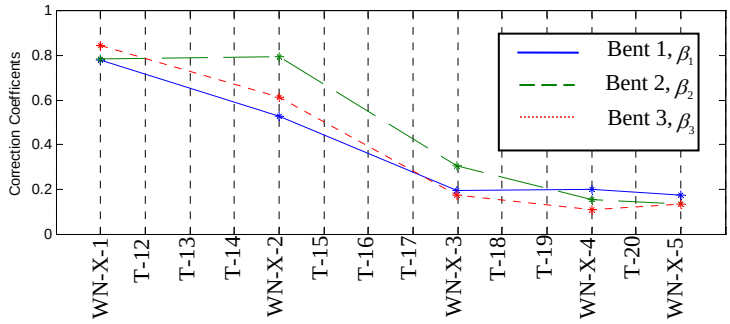

To further verify the identified results, a MIMO model with proper corrections made according to the identified $(\beta_1, \beta_2, \beta_3, \alpha_1, \alpha_2)$ were used to simulate the specimen responses to WN-X-2 and WN-X-5 ground motions in time domain. They capture the primary characteristics of the bridge specimen response, as evident in the time-history simulation results shown in Figures. 7.2.6 and 7.2.7.

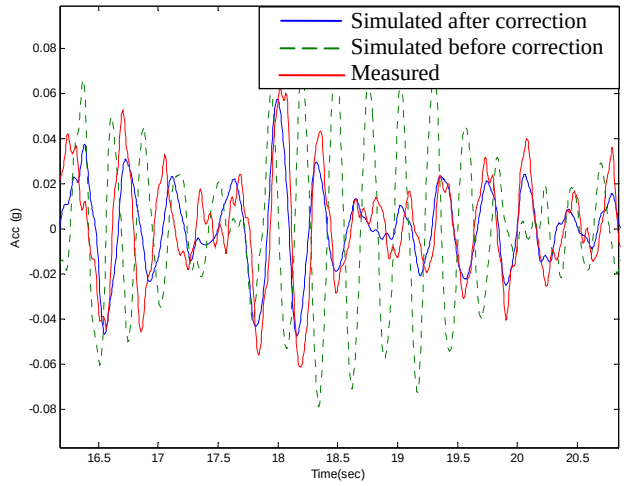

Figure 7.2.6 Simulated and Measured Ch-4 Responses for WN-X-2 Motion

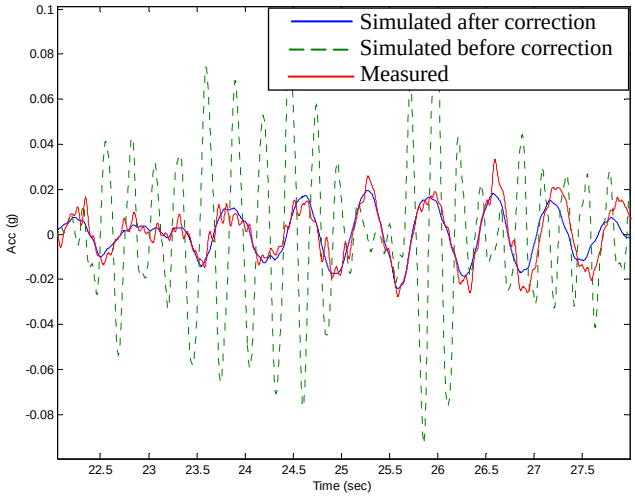

Figure 7.2.7 Simulated and Measured Ch-4 Responses for WN-X-5 Motion

7.3. Damage Identification Based on Earthquake Excitations

In this section, firstly identification of modal parameters of the bridge model from white noise inputs is presented. Because the level of shaking is low, classical frequency domain based approaches can be used. Afterwards structural stiffness values at selected locations are determined using EKF. Lastly, comparison of the results is presented.

7.3.1. Frequency Domain Identification

7.3.1.1. Frequency Domain Identification Using White Noise Input

Because of its level of shaking the white noise input will cause no further damage to structure. So the Fourier Transform can be used to obtain the modal frequencies of the bridge model at that damage level, these results are also used for verification of the EKF results afterwards. In Figure.7.3.1 effect of yielding can be clearly seen from the lengthening of the first modal period. Another observation would be after T-14,

the second mode (3.7 Hz) and third mode (13.7 Hz) are no more visible. The modal shapes indicated by circles for the WN-1 can also be seen (top view of deck).

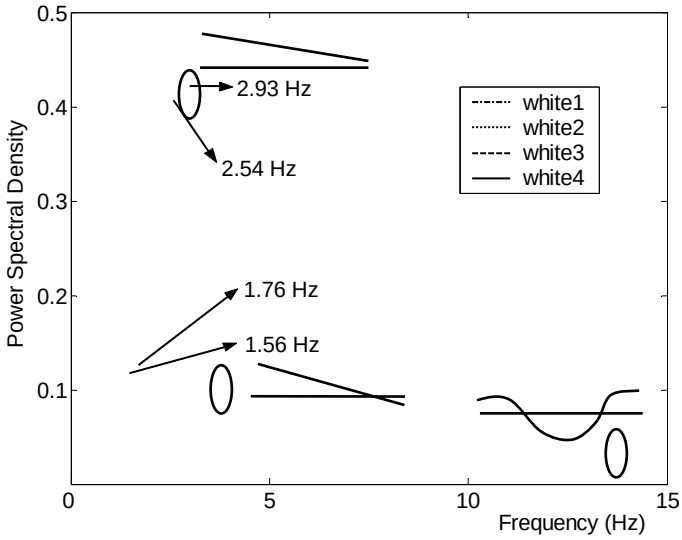

Figure.7.3.1 Fourier Spectral Results Obtained from White Noise Input

7.3.1.2. Frequency Domain Identification Using Ending Portions of Earthquake Motions

The strong input motions cause damages in the structure and results in non-linear system behavior. So the Fourier transform cannot be performed over the whole time history. One way is to use short time frequency transform in which the whole time history is divided into segments and it is assumed that the system performs linear within these segments. Afterwards the change in natural frequency can be tracked and attributed to damage. What is done in this study is just to focus on the ending portions of the response (Figure 7.3.3). In this part of the response because the input level is low, system behaves in the linear range. The only problem is that identified modal frequency is dependent where the ending portion is taken. This effect can be seen in Figure 7.3.4. The identified natural frequency represents the condition of the system after the damaging event. The change of the dynamic characteristics over the four tests can be tracked in Figure 7.3.5. This value can be compared to the one obtained before the event and a conclusion can be made. To represent the system one input

and one output channels are chosen for which the ratio of them stands for the system, structure.

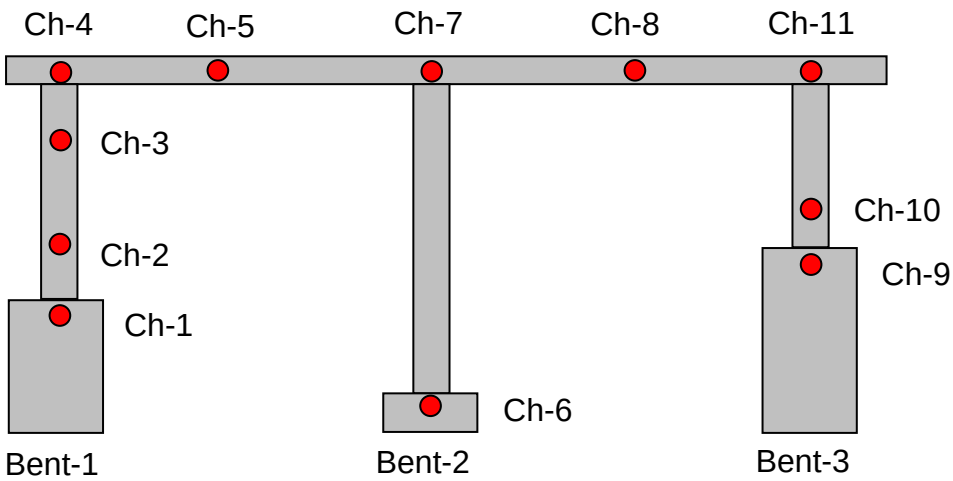

$$H(w) = \frac{Y(w) \quad \rightarrow \text{Ch-7}}{X(w) \quad \rightarrow \text{Ch-6}}$$

Figure 7.3.2 Sensor Locations and System Identification Methodology

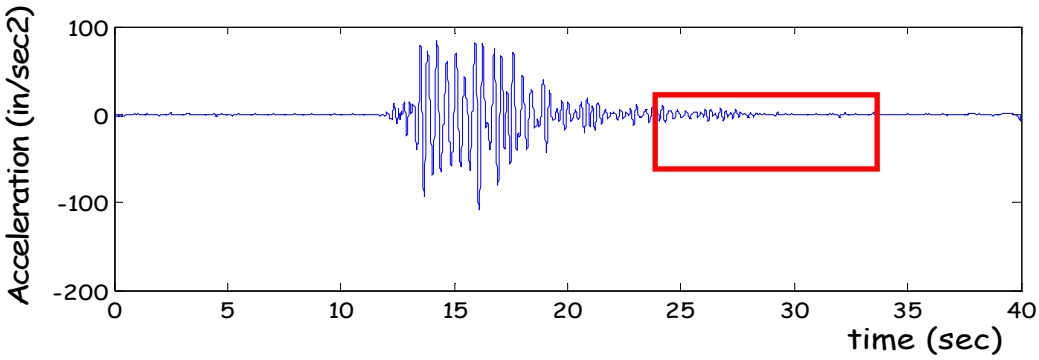

Figure 7.3.3 Time History Portion Used for the Identification

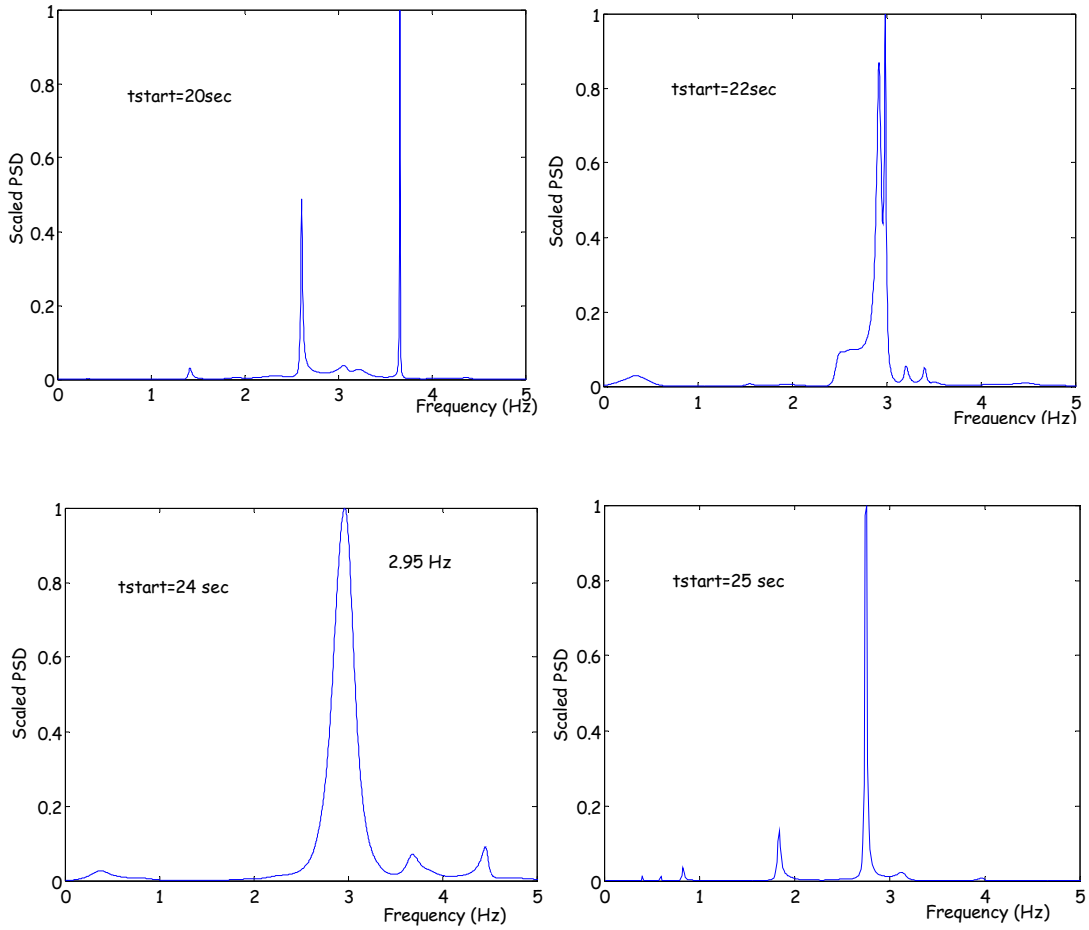

Figure 7.3.4 Identified Natural Frequency with Different Starting Points of the Ending Portion

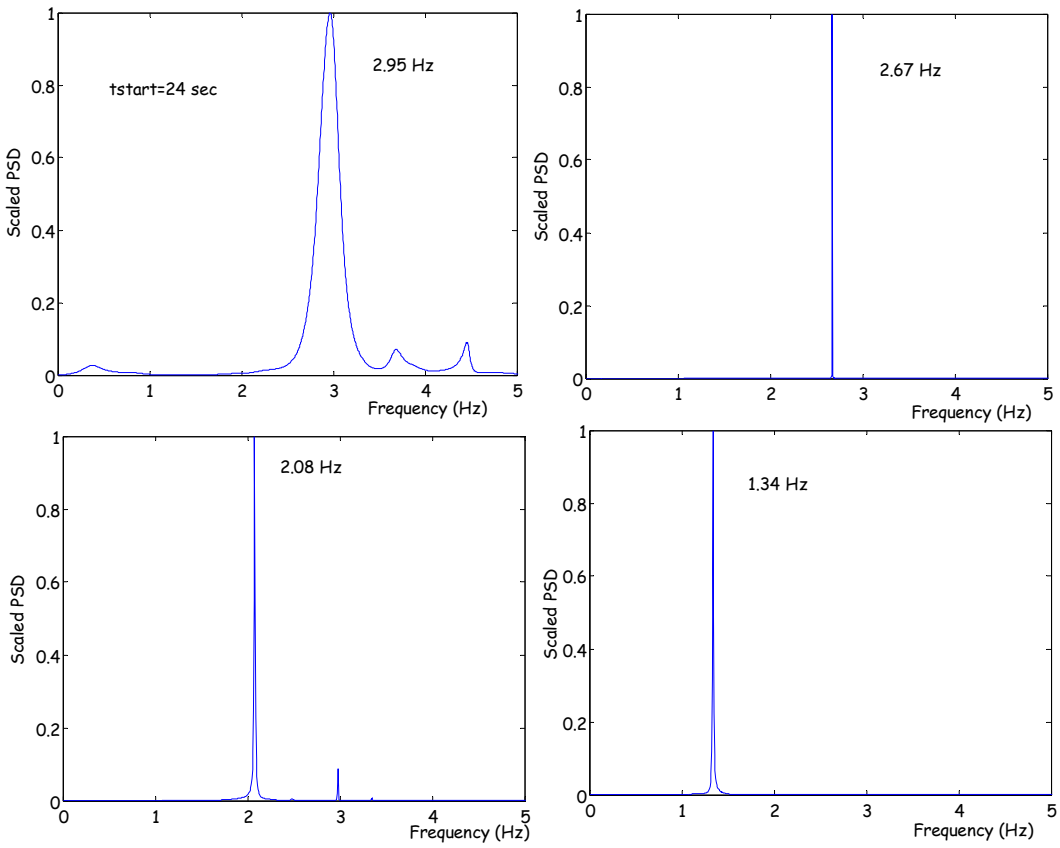

Figure 7.3.5 Identified Natural Frequencies Using End Portions

In Table 7.3.1, identified frequencies obtained from the white noise and ending portions of the strong motion input are compared. The percent change in the identified frequencies obtained from the ending portions are calculated based on the reference identification. In parenthesis max value of the input motion is given.

Table 7.3.1 Comparison of Identified Natural Frequency Using White Noise and End Portions

	T13	T14	T15	T19
End Portions	2.95 Hz (0.02g) (1%)	2.67 Hz (0.03g) (5%)	2.08 Hz (0.04g) (15%)	1.34 Hz (0.08g) (14%)
Reference (White Noise)	<2.93 Hz (0.1g)	2.54 Hz (0.1g)	1.76 Hz (0.05g)	1.56 Hz (0.05g)

7.3.2. Time Domain Identification

Finite Element Model and Calibration

An FE model was generated in MATLAB, which is afterwards used as embedded in the EKF code itself. Figure.7.3.6 shows the degree of freedom (DOF) assigned to the model; each node has both translational and rotational DOF. During the analyses rotational DOF are condensed (Transformation going back and forth between the true and condensed model is performed when needed). The DOF 1-2-7-9-10-11-13-5 are the same as the sensor locations; DOF 8-12 are created so that additional mass could be assigned; DOF 3-4-6 were assigned so that the lower and upper portions of each column could be treated as an extended state for the EKF.

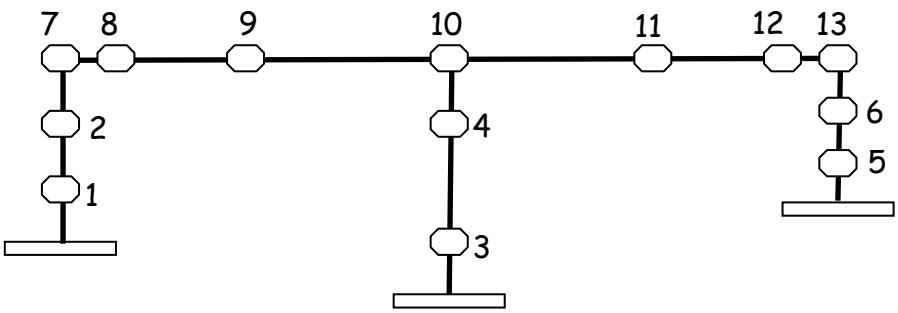

Figure.7.3.6 Schematic View of Finite Element Model

As a first step, FE model was calibrated using the WN-1 input so that the characteristics of the undamaged model could be matched. Modal frequencies and shapes were used for stiffness calibration, mass was thought be calculated pretty much perfectly. Afterwards response was simulated by this calibrated model and the white noise measurement was used to check the damping level. Although any kind could be used, it was seen that Rayleigh Damping was satisfactory. In Table 7.3.2, modal frequencies and shapes obtained from FE model and white noise analysis can be seen.

Table 7.3.2 Finite Element Model Calibration

Mode1	Frequency (Hz)	Shape (DOF)				
		7	9	10	11	13
WN-1	2.93	1	0.83	0.68	0.53	0.34
FE Model	2.95	1	0.85	0.67	0.51	0.31
Mode2	Frequency (Hz)	Shape				
		7	9	10	11	13
WN-1	3.70	1	0.61	0.30	-0.05	-0.43
FE Model	3.69	1	0.62	0.31	-0.08	-0.40
Mode3	Frequency (Hz)	Shape				
		7	9	10	11	13
WN-1	13.70	-0.79	0.61	1	0.61	-0.79
FE Model	12.29	-0.72	0.55	1	0.55	-0.72

Damage Detection Results Based on EKF

Using this calibrated model, EKF was run for each of the strong ground motions one after another. At each time step the state transition matrix is obtained analytically from the FE model already embedded into the code and each five steps of EKF are implemented, the structural stiffness is corrected after and the new Jacobian matrix which is used for state transition matrix, is calculated again. So at the end of the strong input motion, the structural stiffness value at any assigned portion Figure.7.3.7 and the estimation of the response Figure.7.3.8 are obtained.

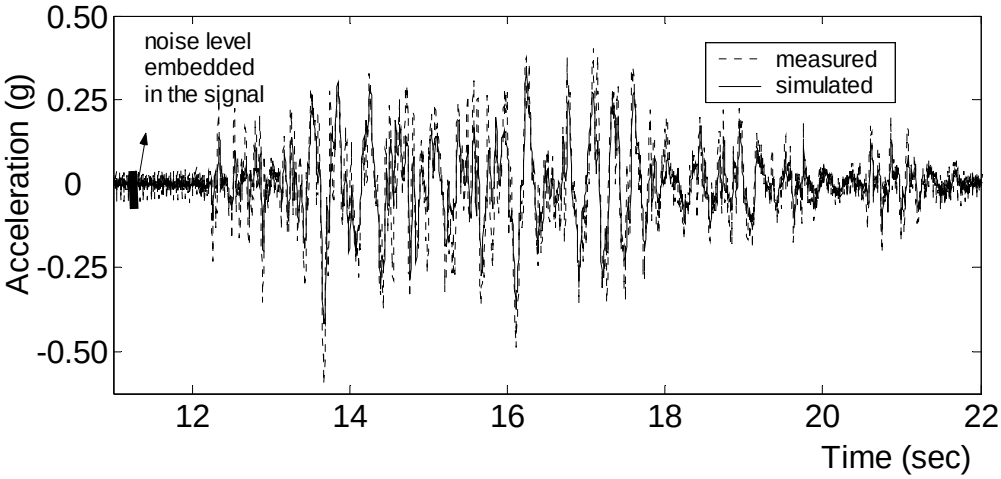

Figure.7.3.7 Comparison of Responses at DOF 10 for T-13

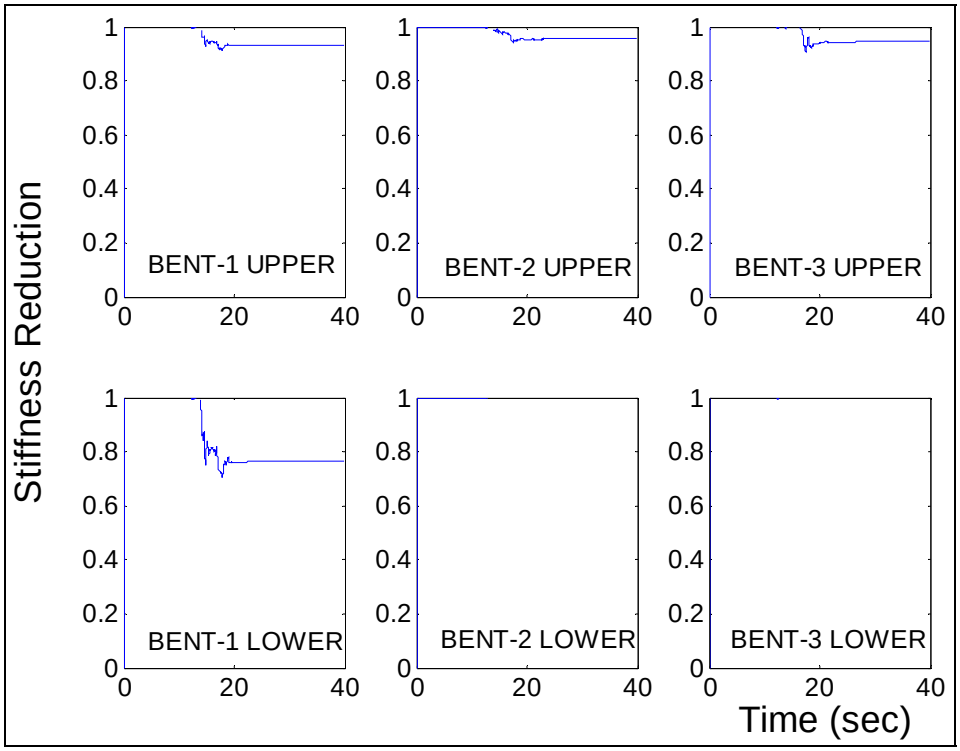

Figure.7.3.8 Stiffness Reduction During T-13

The level of noise in the data is quite high. Figure 7.3.9 shows an example where the measurement obtained in T-13 is filtered with a low pass of 20 Hz, and the filtered data matches the simulated one better.

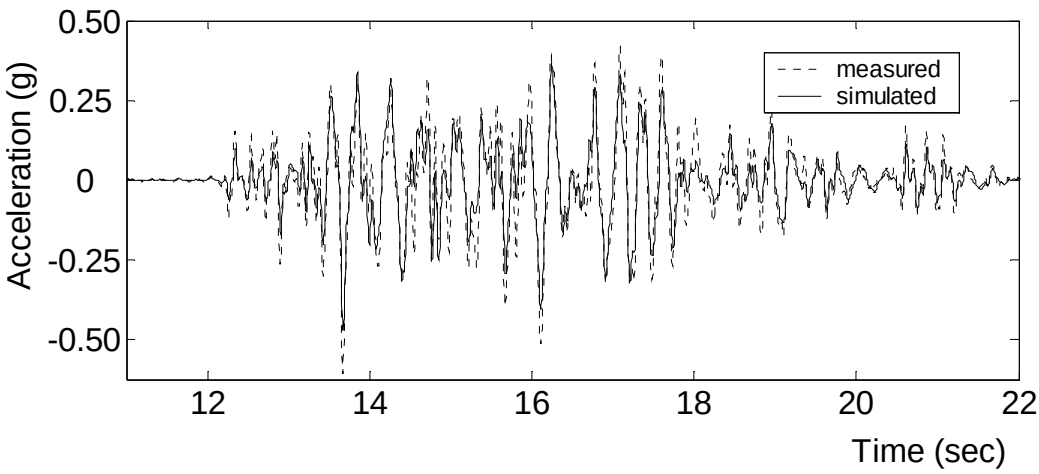

Figure.7.3.9 Comparison of Responses at DOF 10 for T-13 (Filtered)

There is a trade-off between the performance of tracking of any change in extended states and the estimation of measurement. The P_0, x_0 values turn out to be detrimental: assigning a very different initial value to x_0 than its true value might result in a wrong value. However in structural identification problems, almost always we have a rough estimate for the initial value. For this test it was seen that up to around 20% fluctuation of the initial guess could be compensated. On the other hand the P_0 value determines how much we allow the EKF to trace the changes, i.e. we can choose P_0 such that all the importance is given to the measurement so the data can be fitted perfectly. In this case, however, the extended states stay unchanged. If we give too much importance to the model, the changes in the extended states might be dramatic. A true region for P_0, which gives the same results for the extended states, can be figured out after several trials. It was also observed that the results obtained are prone to the number of extended states. Assigning all the portions which are thought to be susceptible to any change as an extended state is observed to be effective, e.g. assigning just the lower portions of the bents as extended states would give different results. Figures 7.3.10 - 7.3.12 show the identified reduction in structural elemental stiffness during the earthquake shaking. Figure 7.3.13 shows the comparison of the measured acceleration response with the simulated one using the identified elemental stiffness during T-19. The good agreement demonstrates the effectiveness and accuracy of the stiffness identification algorithms developed in this study.

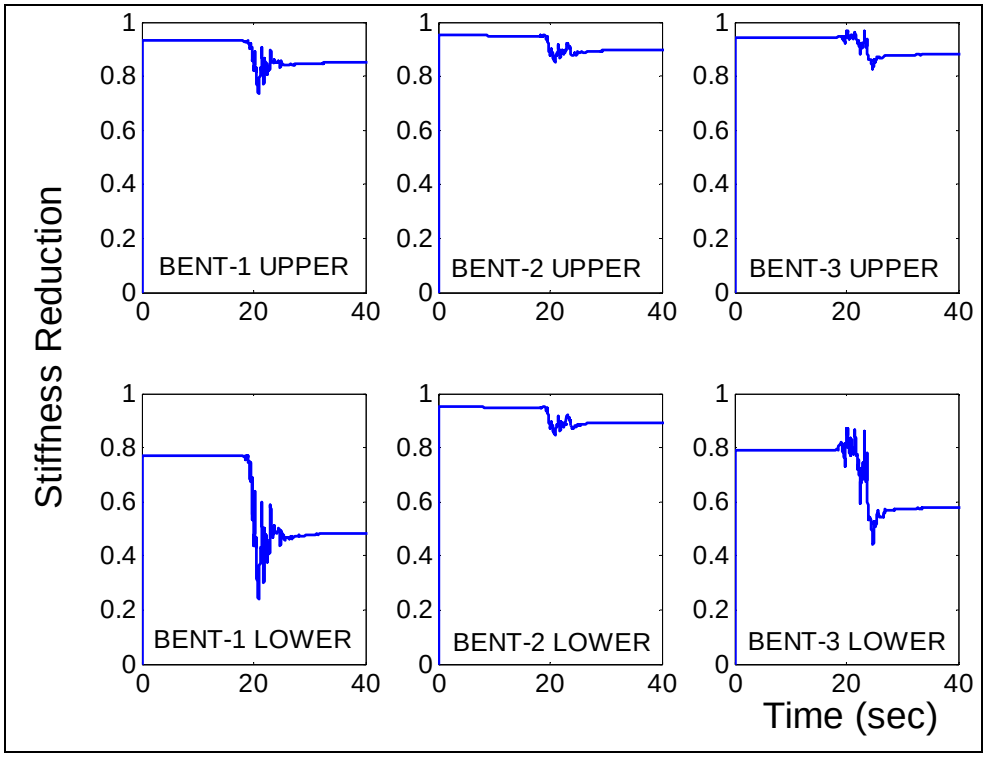

Figure.7.3.10 Stiffness Reduction During T-14

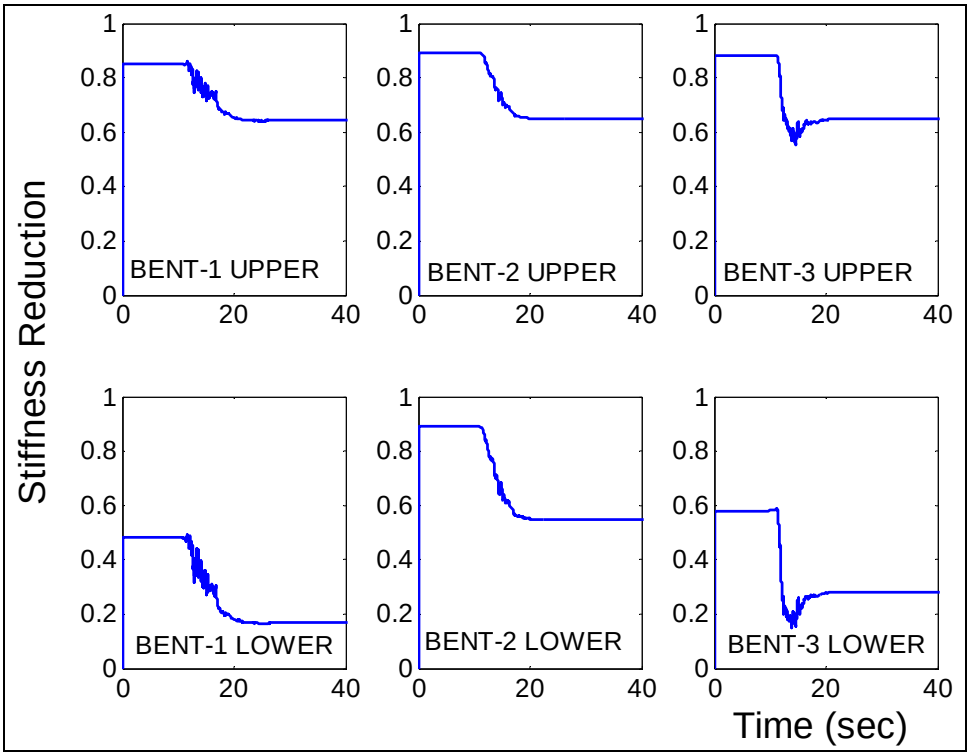

Figure.7.3.11 Stiffness Reduction During T-15

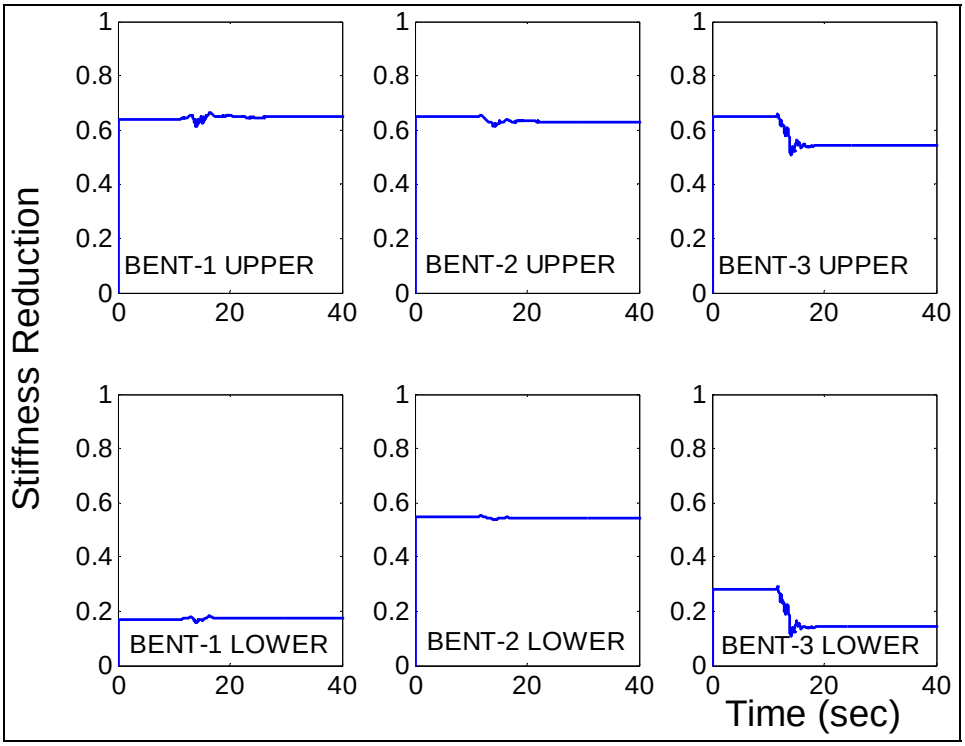

Figure.7.3.12 Stiffness Reduction During T-19

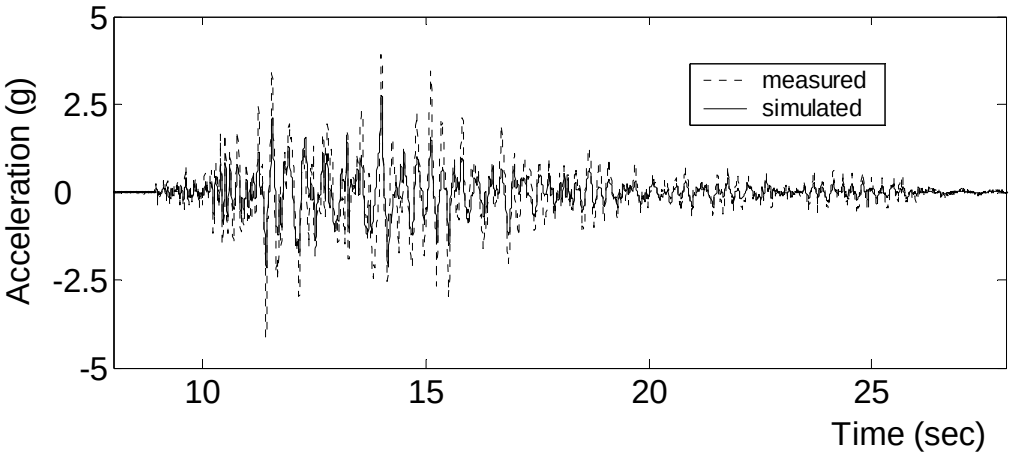

Figure.7.3.13 Comparison of Responses at DOF 10 for Test-19

In Table 7.3.3 the frequencies obtained from the measurement under the low-level white noise input is compared with those obtained from FE model with the stiffness values identified from the EKF (estimated). It can be seen that modal frequencies are quite close to each other. The possible reason for slight discrepancy in the latter earthquake motions might be due to some cracking on the bridge model (other than the plastic hinges) which was not taken into account in the EKF formulation.

Table.7.3.3 Comparison of First Modal Frequency

Input	Measured (Hz)	Estimated (Hz)
WN-1	2.93	2.94
T-13		2.74
T-14		2.55
WN-2	2.54	
T-15		1.82
WN-3	1.76	
T-19		1.64
WN-4	1.56	

Chapter 8

FIELD TEST ON WEST ST. ON-RAMP

For the West St. On-Ramp (WSO), two field tests have been carried out under a controlled environment using a test vehicle (a water truck). The first one was right after the completion of the bridge construction in 2001, while the second one was in 2006. Both braking and bumping tests were carried out, based on which the dynamic characteristics of the bridge were identified and compared. The second test also included a static load test.

8.1 Static Load Test

The purpose of the static load test was to verify the FE model of the WSO. The test was carried out on September 8, 2006, by parking a test vehicle at various locations of the bridge and measuring the strain responses using the embedded strain sensors. Then the measured strains were compared with those computed from the FE model.

8.1.1 Load Cases

The static test was carried out by parking the test vehicle in various locations. Figure 8.1.1 shows the test vehicle location in the transverse direction. The test vehicle was driven along path T-1 which is 2’ away from the left guide wall of the bridge and then

parked at the selected locations along the longitudinal direction, as shown in Table 8.1.1 and Fig. 8.1.2. Each load case is chosen to produce the maximum strain for each of the embedded strain sensors, whose locations are shown in Fig. 5.1.1.

Table 8.1.1 Test Vehicle Locations in Longitudinal Direction

Load Case	L-1	L-2	L-3	L-4	L-5
Distance	2.50’	77.60’	135.16’	238.93’	277.05’

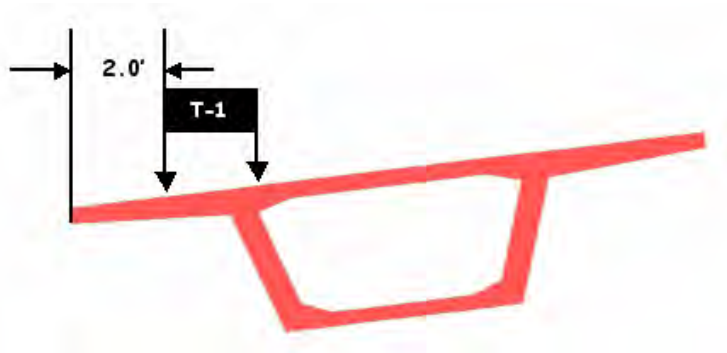

Fig. 8.1.1 Test Vehicle Locations in Transverse Direction

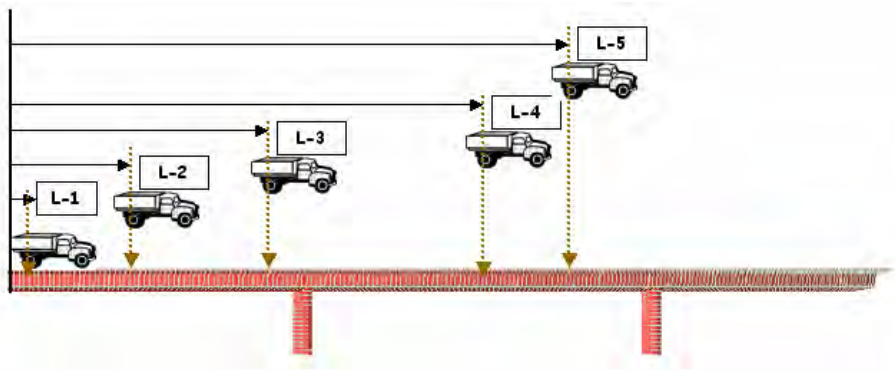

Figure 8.1.2 Test Vehicle Locations in Longitudinal Direction

8.1.2 Test Vehicle

Fig. 8.1.3 shows the axle loads and distances between axels of the test vehicle used for the field test. It has 3 axles, and the distance between the first and second axle is 16’ and the second and third axle is 4’. The distance between tires is 6’-8”. The axle load is 16 kips for front axle and 19 kips for each rear axle.

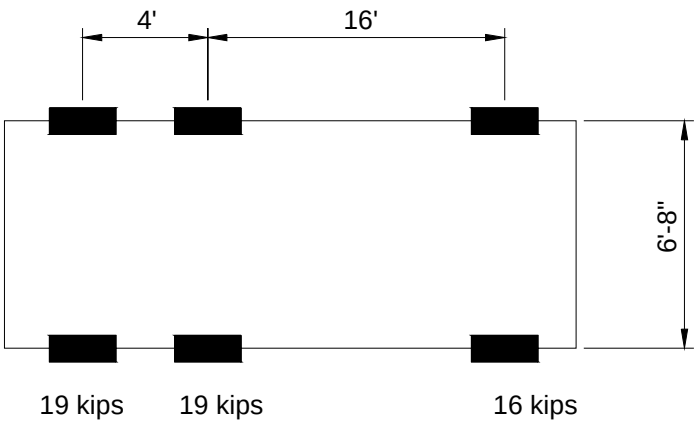

Figure 8.1.3 Axle Load of the Test Vehicle

8.1.3 Static Test Results and Comparison with Analysis

The strain time histories of all the embedded strain sensors recorded during the static load test (case T-1) are plotted together in Fig. 8.1.4. The test vehicle was driven along the path and parked at each location for about 20 seconds. Table 8.1.2 summarizes the strain from each static load case. The shaded values are the maximum or minimum strains.

The strains under the same vehicle load was analyzed using the finite element (FE) model. The stiffness values in the FE model were computed based on the design drawing. Table 8.1.3 shows the computed maximum strain at the sensor locations under the test vehicle load. The values in parenthesis indicate the difference between

the measured and computed strains. Except R10, all measured strains are smaller than the computed ones, indicating the stiffness of the actual bridge structure is higher than the one designed for. In addition, the computed strains of R2 and R3 are higher than those of R8 and R9, implying that the girder members above the bent are designed more conservatively than those in the middle of the span.

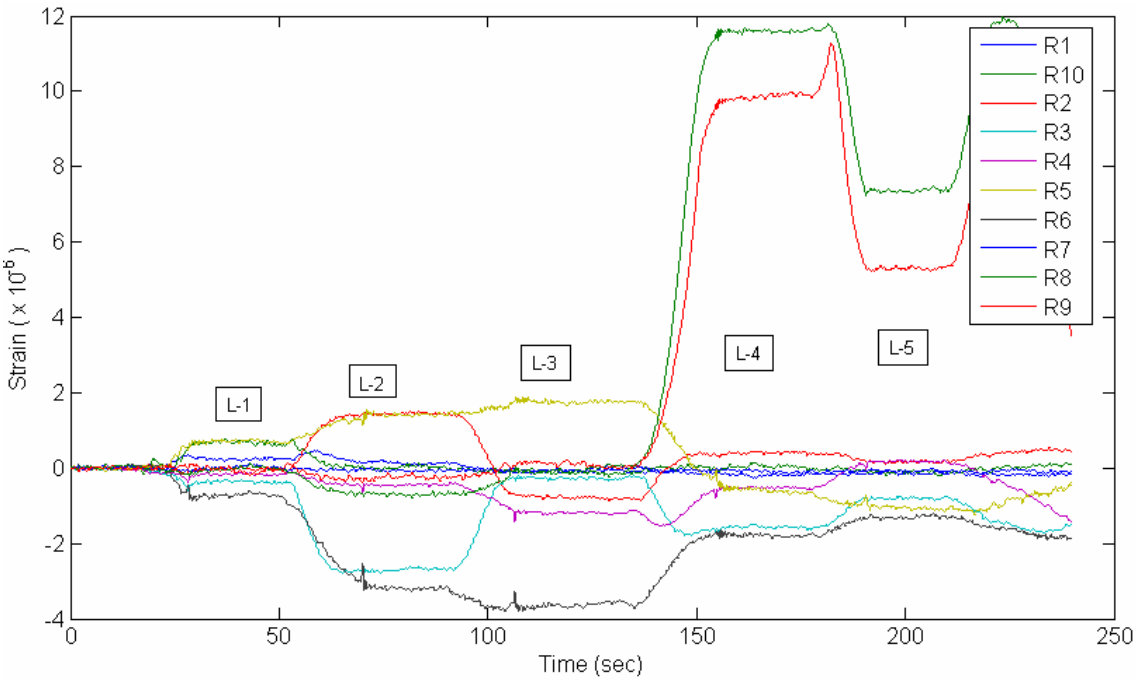

Figure 8.1.4 Strain Time History of All Sensors

Table 8.1.2 Measured Strain from Static Test

Sensor	L-1	L-2	L-3	L-4	L-5
R-1	0.243	0.126	-0.065	-0.196	-0.139
R-2	-0.033	1.456	-0.789	0.408	0.167
R-3	-0.358	-2.682	-0.275	-1.555	-0.797
R-4	-0.162	-0.445	-1.188	-0.521	0.176
R-5	0.710	1.410	1.757	-0.577	-1.081
R-6	-0.739	-3.196	-3.610	-1.777	-1.282
R-7*	-0.002	-0.075	-0.016	-0.078	-0.096
R-8	-0.053	-0.705	-0.005	11.599	7.381
R-9	-0.006	-0.218	0.070	9.850	5.304
R-10	0.688	0.038	-0.126	0.058	0.167

* : out of order

Table 8.1.3 Computed Maximum Strain

R1	R2	R3	R4	R5	R6	R7	R8	R9	R10
0.595	5.370	-12.320	-5.398	4.110	-4.110	-9.753	22.772	14.327	0.595
(1.44)	(2.69)	(3.59)	(3.54)	(1.34)	(0.14)	(-)*	(0.96)	(0.45)	(-0.14)

* : out of order, values in parenthesis : $\dfrac{\mu_{computed} - \mu_{measured}}{\mu_{measured}}$

8.2 Braking and Bumping Tests

The braking and bumping tests were carried out twice over a period of five years. The first one was carried out in 2001 when the bridge construction was completed (Feng and Kim, 2001). The second braking and bumping test took place in 2006 at the same time when the state test was performed. The same test vehicle was used. The purpose of the breaking and bumping test was to identified the dynamic characteristics of the bridge and their change over the five years. The details of the first test were documented in the Caltrans report by Feng and Kim (2002). This report focuses on the second test.

8.2.1 Test Procedure

The test procedures for both tests were identical. In the braking test, the excitation force was applied to the bridge by suddenly applying a break to the test vehicle at the middle of span 2. Although the applied breaking force was not high enough to excite higher vibration modes of the bridge, the first three modes were identified from the bridge acceleration responses to the braking test. In the bumping test, the test vehicle was driven over a wooden block at the middle of span 2.

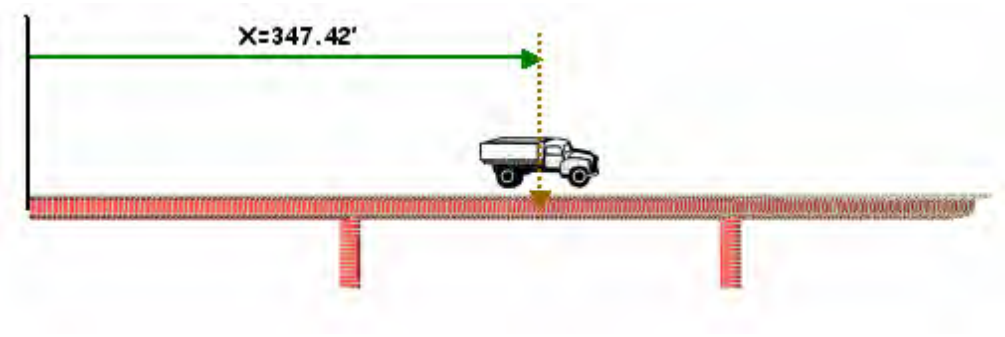

Figure 8.2.1 Exciting Force Location of Braking and Bumping Test

8.2.2 Braking Test Results

Locations of accelerometers

To improve the accuracy of the mode shape identification, six fiber optic accelerometers (FOA) developed by the first author were temporarily installed on the WSO, in addition to those permanently installed conventional force-balance accelerometers. Fig. 8.2.2 shows the locations of the both types of the accelerometers, in which the conventional accelerometers are marked with “A”.

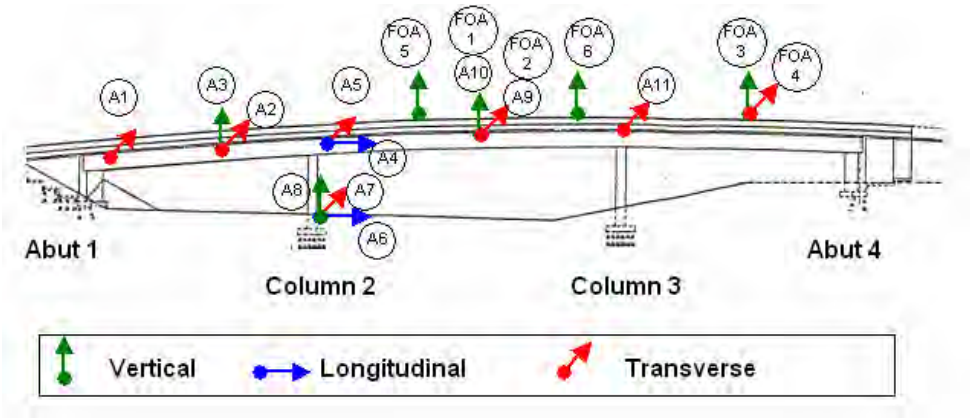

Figure 8.2.2 Locations of Fiber Optic Accelerometers

Mode frequency and mode shape

Figure 8.2.3 shows example acceleration time histories from both the conventional force-balance type accelerometer and fiber optic accelerometer.

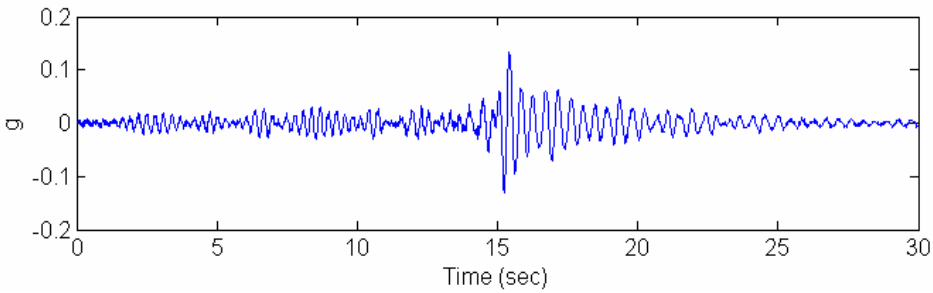

(a) Force-balanced Type Accelerometer (A10)

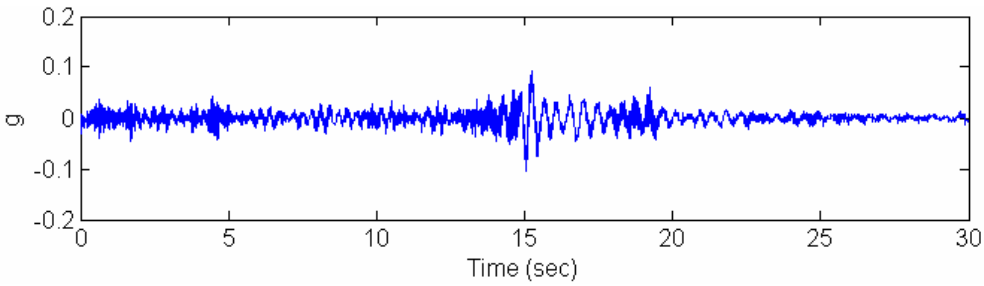

(b) Fiber Optic Accelerometer (FOA1)

Figure 8.2.3 Acceleration Time History from Braking Test

The power spectral density (PSD) functions from the time histories are shown in Fig. 8.2.4 and Fig. 8.2.5, respectively for those measured by the conventional accelerometers and the fiber optic accelerometers. The mode frequencies measured by the both types of the accelerometers are very close to each other. From the PSD's, mode frequencies of bridge were identified, as shown in Table 8.2.1. The frequencies identified from the 2001 bumping test were also listed for comparison purposes. The first and second mode frequencies identified from the 2006 bumping test have decreased by approximately 12% and 7% respectively in comparison with those identified from the 2001 bumping test. It is noted that after the 2001 test, a sound wall was constructed on the WSO. Taking into consideration of the weight of the sound wall, it is found from analysis that each of the first and second mode frequencies reduces by approximately 5%. Therefore, 7% and 2% reductions respectively in the first and second mode frequencies are observed during this five year period.

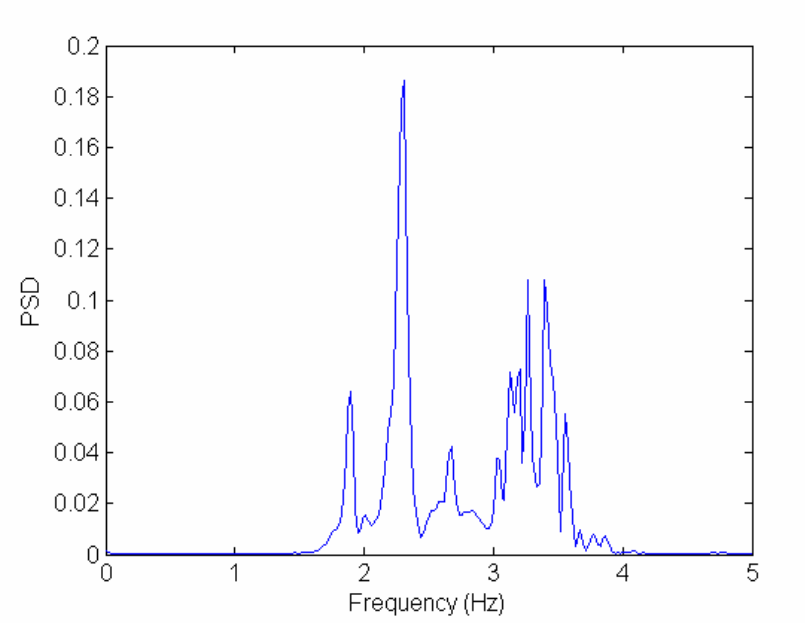

Figure 8.2.4 PSD from Conventional Accelerometer

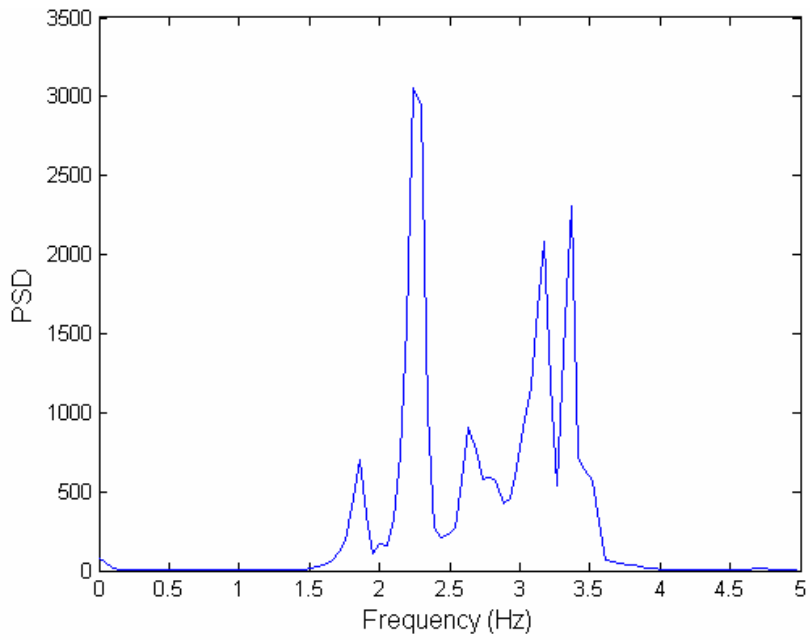

Figure 8.2.5 PSD from Fiber Optic Accelerometer

Table 8.2.1 Mode Frequency from Braking Test

Mode		First (Hz)	Second (Hz)	Third (Hz)
2001		2.148	2.465	-
2006	Conventional	1.895(-11.8%)	2.305(-6.5%)	2.676
	FOA	1.856(-13.6%)	2.265(-8.1%)	2.637

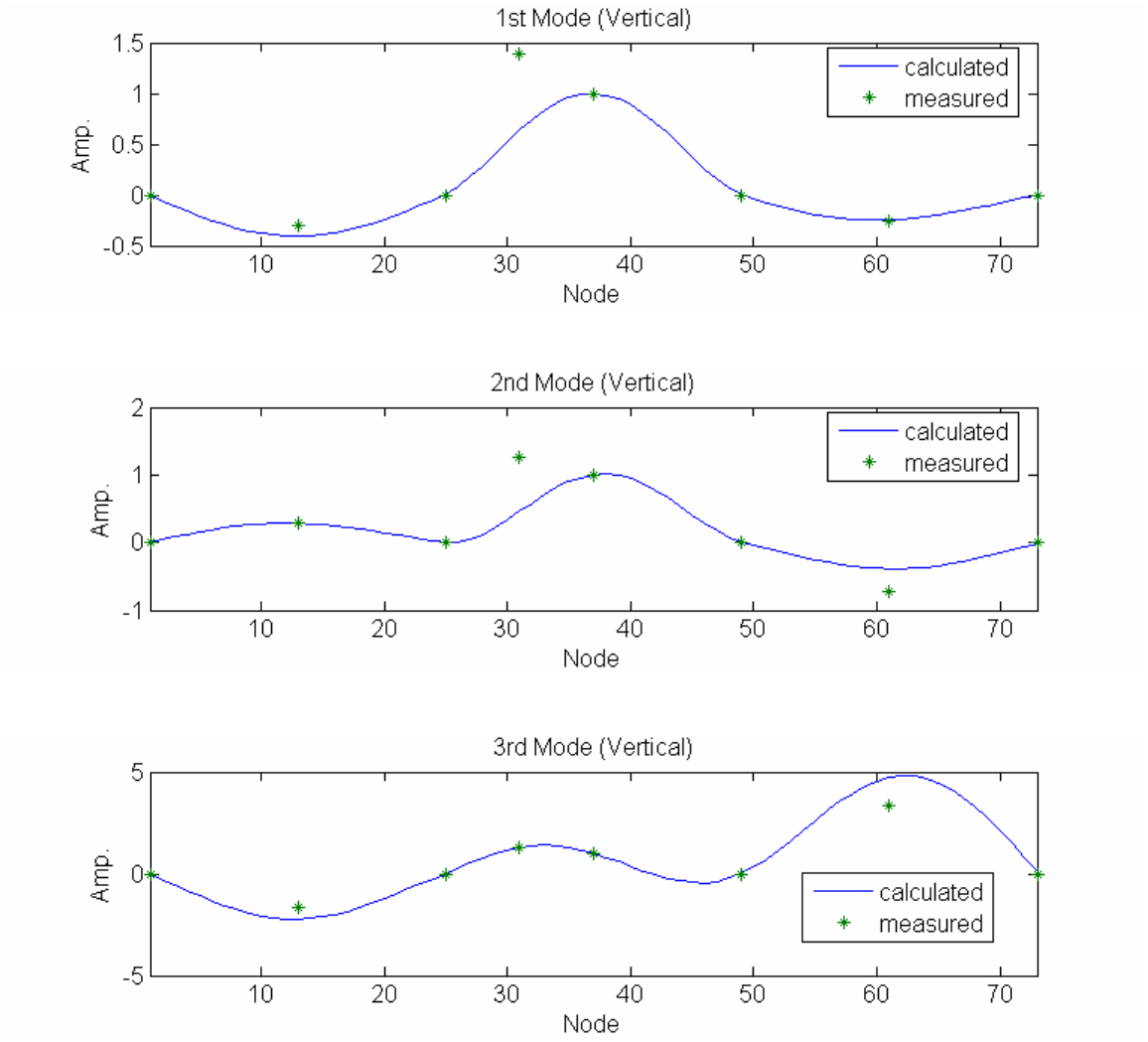

Figure 8.2.6 Mode Shape from Braking Test (Vertical Direction)

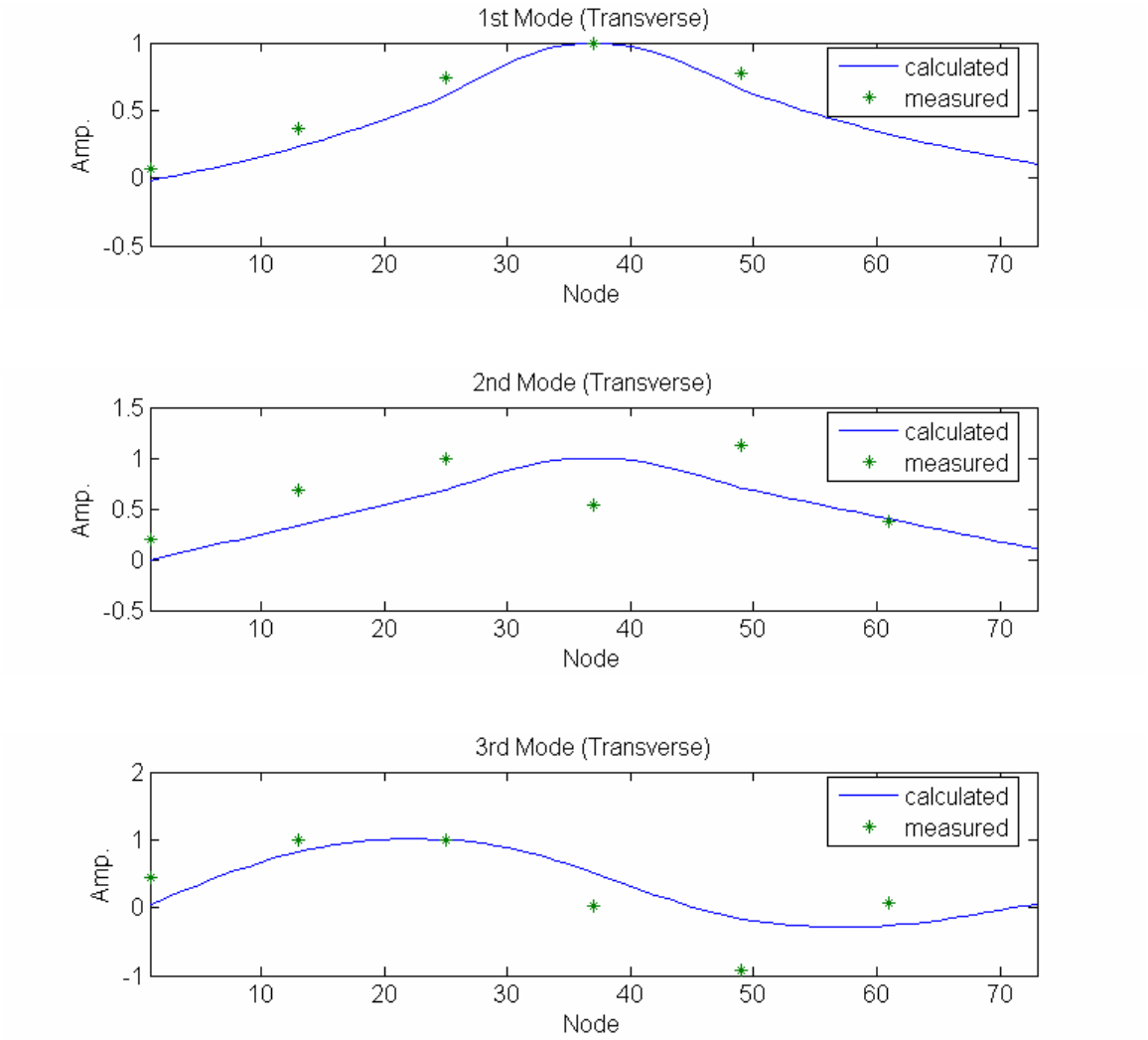

Figure 8.2.7 Mode Shape from Braking Test (Transverse Direction)

Figures 8.2.6 and 8.2.7 show the mode shapes of the bridge identified from the measurement and analysis in the vertical and transverse directions. The measured mode shapes match well with computed ones. The first three mode shapes are coupled with the vertical and transverse modes. The first and second mode shapes in the vertical directions are different, but those in the transverse mode are quite similar.

8.2.3 Bumping Test Results

In the bumping test, the excitation force was applied by driving the test vehicle over a 4X4 wooden block at the middle of span 2. Figures. 8.2.8 through 8.2.10 show the time histories of acceleration measured at different locations .

Figure 8.2.11 shows the PSD of the acceleration from bumping test. The comparison of the mode frequencies between the previous and present tests are given in Table 8.2.2. The first and second mode frequencies identified from the present test are respectively reduced by 4.2% and 3.2% from the previous ones.

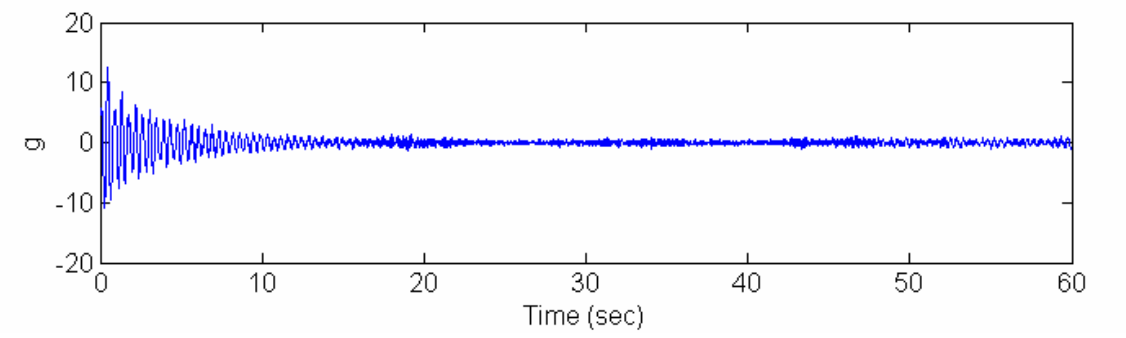

Fig. 8.2.8 Time History of Acceleration at A10

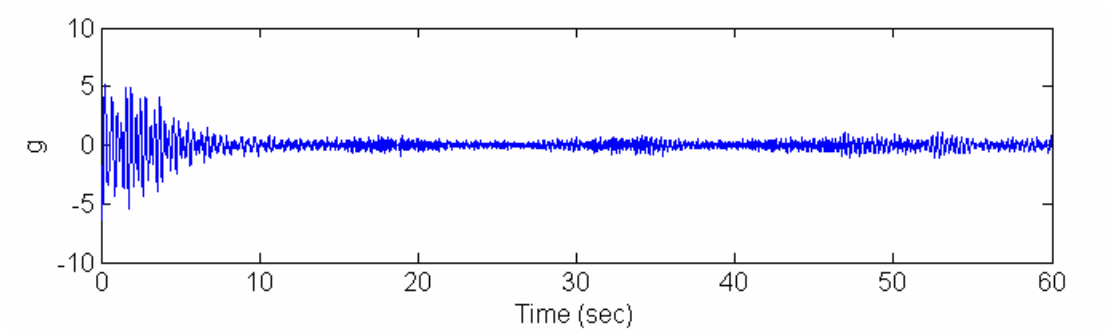

Fig. 8.2.9 Time History of Acceleration at A3

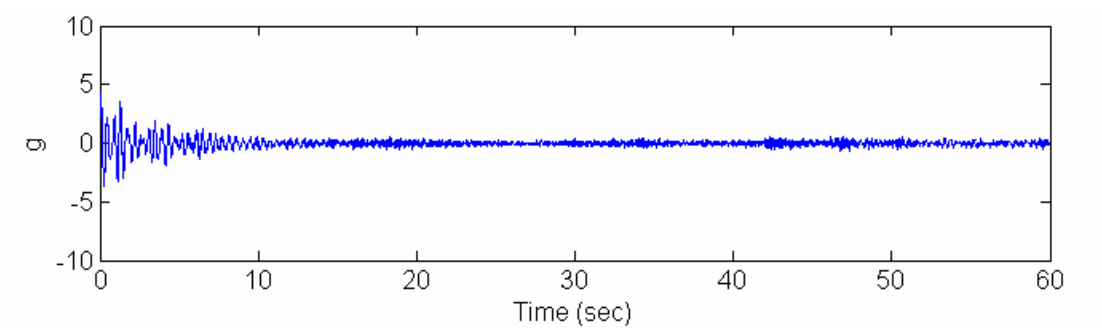

Fig. 8.2.10 Time History of Acceleration at A5

Table 8.2.2 Mode Frequency from Bumping Test

Test Year	First mode (Hz)	Second mode (Hz)	Third mode (Hz)
2001	2.100	2.441	-
2006	2.012 (-4.2%)	2.363 (-3.2%)	2.656

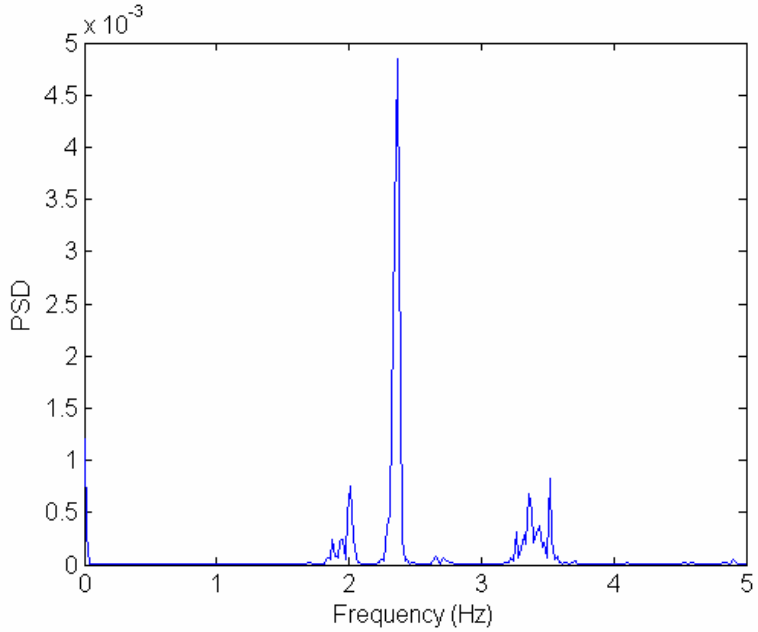

Figure 8.2.11 PSD from Bumping Test

8. 3 Dynamic Load Test

8.3.1 Dynamic Load Cases

The test vehicle was driven two times on the each lane. Because of the limited length of the approach road to WSO, vehicle speed was limited to about 10-20mph. Table 8.3.1 summarize the dynamic load cases

Table 8.3.1 Dynamic Load Cases

Load cases	Description
RL-1	First driving on right lane
RL-2	Second driving on right lane
LL-1	First driving on left lane
LL-2	Second driving on left lane

8.3.2 Dynamic Strain Results

Figures 8.3.1 through 8.3.3 show the strain time histories of R3, R5, and R8 as the test vehicle travels through the left lane of the WSO (under load case LL-1). Table 8.3.2 shows the measured maximum dynamic strain values from each sensor and Table 8.3.3 shows comparison of the maximum strains from the moving load analysis, static load test, and dynamic load test.

In Table 8.3.3 the difference between the static and dynamic strains varies at different sensor locations. The high dynamic strains at R1 and R10 show the impact effect from the expansion joint at the beginning of the bridge. It is noted that the differences between the dynamic and static strains at R2 and R3 are higher than those at R8 and R9. This indicates that the bridge superstructure elements above the column are more affected by the dynamic moving vehicle than those in the middle of the span.

In the column the difference between the static and dynamic strains varies in different directions. It is found that the strain in the longitudinal direction (R4) is more affected by the moving vehicle than that in the transverse direction (R5 or R6).

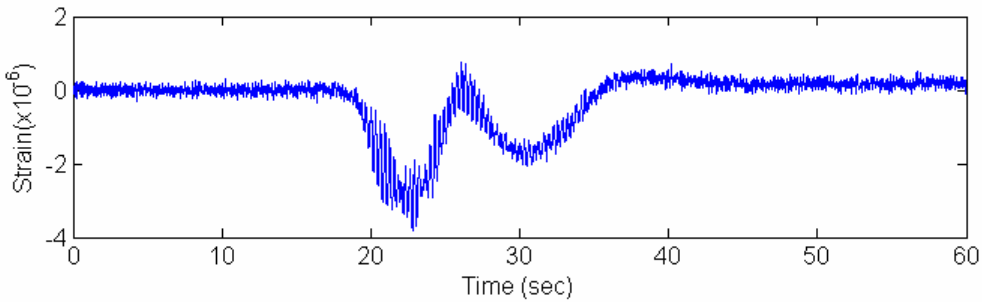

Figure 8.3.1 Time History of Strain at R3

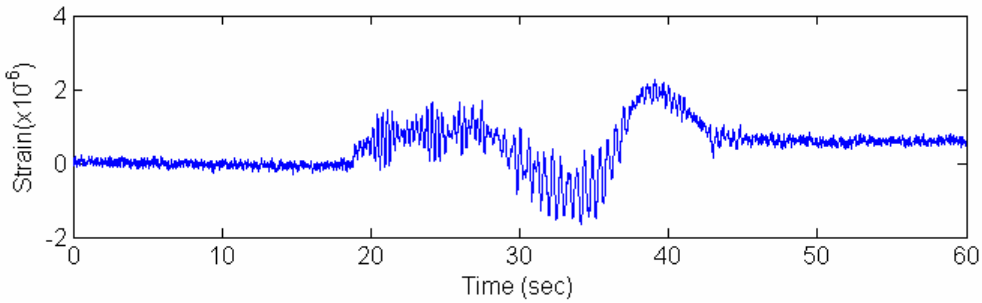

Figure 8.3.2 Time History of Strain at R5

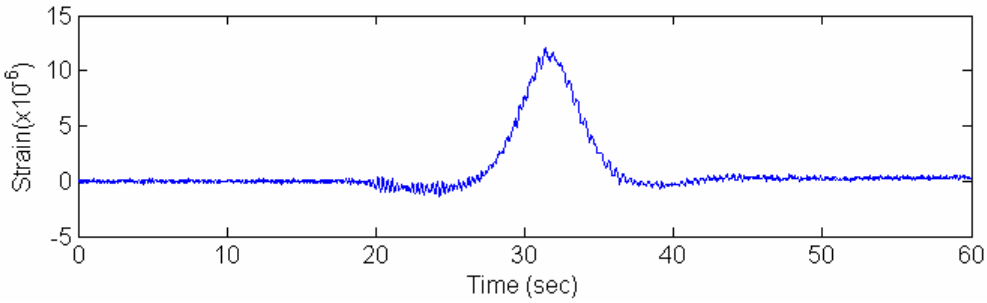

Figure 8.3.3 Time History of Strain at R8

Table 8.3.2 Measured Dynamic Strain

Sensor		RL-1	RL-2	LL-1	LL-2
R-1		1.966	1.692	0.769	0.709
R-2		4.180	4.224	2.436	2.436
R-3		-0.778	-4.066	-3.797	-3.693
R-4	Min	-4.880	-1.235	-1.667	-1.399
	Max	1.019	0.570	0.674	0.959
R-5	Min	-2.121	-4.279	-1.818	-1.672
	Max	1.878	2.109	1.681	2.264
R-6	Min	-0.245	-1.800	-3.717	-4.465
	Max	1.524	1.533	0.615	0.258
R-7*		-1.177	-0.285	-0.302	-0.228
R-8		16.397	15.987	12.091	11.550
R-9		8.353	8.274	12.054	11.574
R-10		0.654	0.559	1.300	1.317

Table 8.3.3 Comparison of Strain

Sensor	Analysis	Static test (1)	Dynamic test (2)	Difference $= \frac{(2)-(1)}{(1)}$
R-1	0.595	0.243	1.966	7.090
R-2	5.370	1.456	4.224	1.901
R-3	-12.320	-2.682	-4.066	0.516
R-4	-5.398	-1.188	-4.880	3.108
R-5	4.110	1.757	2.264	0.288
R-6	-4.110	-3.610	-4.465	0.236
R-7*	-9.753	-	-	-
R-8	22.772	11.599	16.397	0.414
R-9	14.327	9.850	12.054	0.224
R-10	0.595	0.688	1.317	0.914

* : out of order

8.3.3 Mode Frequency

Figures 8.3.4 through 8.3.6 show the acceleration time histories of A3, A5, and A10 under the dynamic load case LL-1. Table 8.3.4 shows the extracted mode frequency from the measured acceleration time histories. Compared with the previous braking test results in 2001, the first and second mode frequencies are reduced by 14.1% and 6.3% respectively. However, considering the weight of the sound wall (that was built on the bridge after the first breaking test in 2001), the frequencies of the first and second modes are each reduced by 5%. Therefore, it is reasonable to state that 9.1% and 1.3% change in the first and second mode frequencies are observed between the first and second vehicle breaking tests.

Table 8.3.4 Mode Frequency from Dynamic Load Test

Mode	RL-1 (Hz)	RL-2 (Hz)	LL-1 (Hz)	LL-2 (Hz)	Average
1st	1.895	1.758	1.895	1.836	1.846 (-14.1%)*
2nd	2.324	2.305	2.305	2.305	2.309(-6.3%)*
3rd	2.636	2.695	2.715	2.676	2.681

* : The values in parenthesis are the difference from the results of braking test in 2001

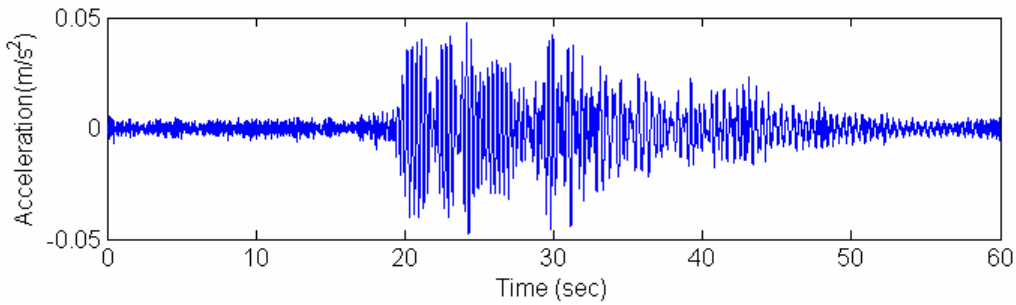

Figure 8.3.4 Time History of Acceleration at A10

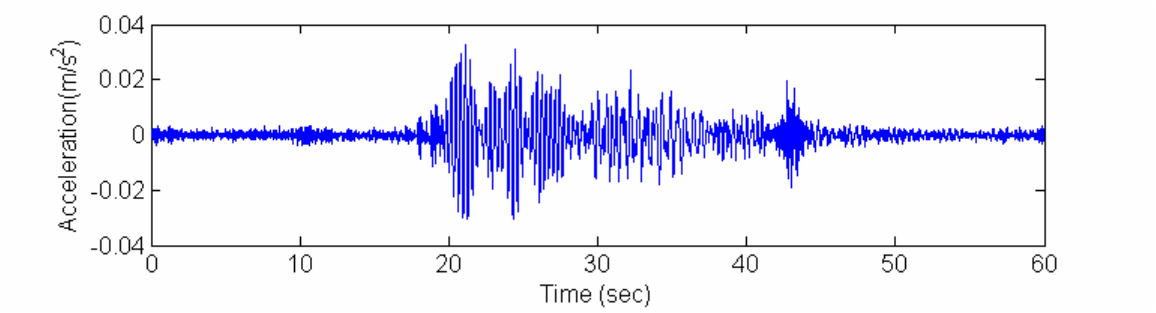

Figure 8.3.5 Time History of Acceleration at A5

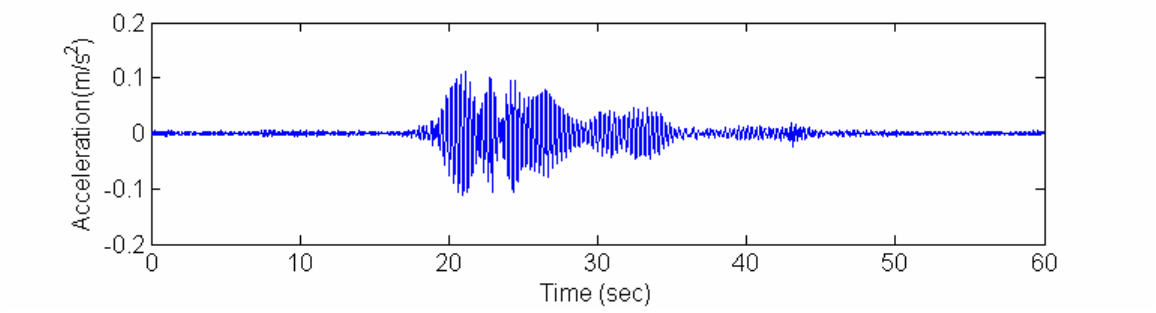

Figure 8.3.6 Time History of Acceleration at A3

Chapter 9

DEVELOPMENT OF DATABASE

In this chapter, development of database for the modal frequency values is first presented for all the three instrumented bridges. A large amount of data has been collected for the Jamboree Road Overcrossing (JRO) and the database reveals the scattering of frequency values over a long period of time. In the second part of the chapter, a database for structural element stiffness values is presented. The stiffness values were identified using the neural network-based identification method developed in this project.

9.1 Database for Modal Parameters

From the traffic-induced ambient vibration data sets the mode frequencies were derived using the frequency domain decomposition (FDD) method. A database of the modal frequencies has been developed for each of the three instrumented bridges.

9.1.1 JRO

As discussed in Chapter 4, 1707 traffic-induced vibration data sets have been manually since 2002. For the last two months five-minute long data are retrieved wirelessly every hour. Based on these measured acceleration time histories, modal frequencies of the bridge were identified. The variations of the first four modal frequencies are shown in Figure 9.1.1-9.1.4 throughout a four-year period from 2002 to 2006. As seen in the figures, the change in the identified modal frequencies is in

the order of +/-10%. Whether this change is due to the change in the environment or in structure is under investigation.

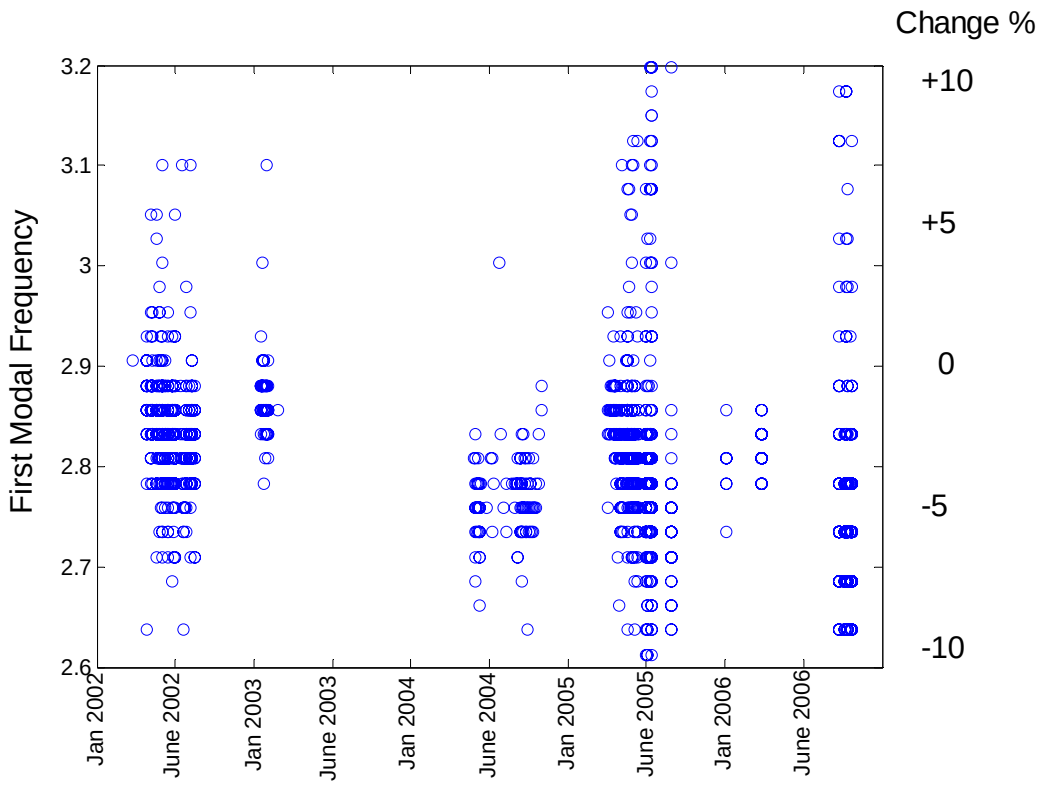

Figure 9.1.1 First Modal Identification Results

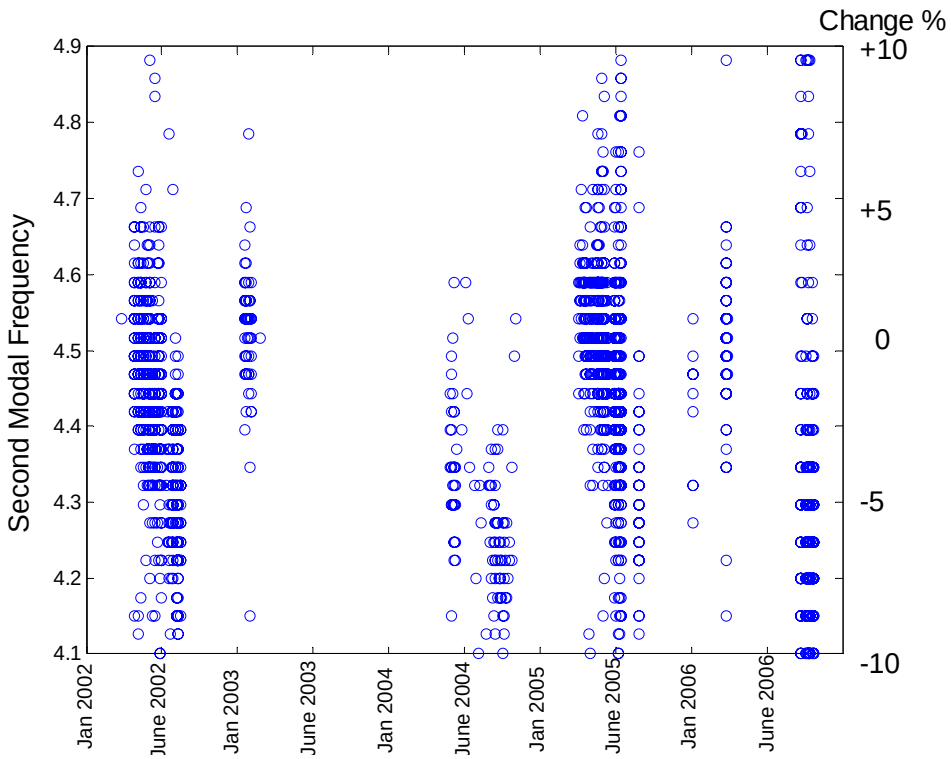

Figure 9.1.2 Second Modal Identification Results

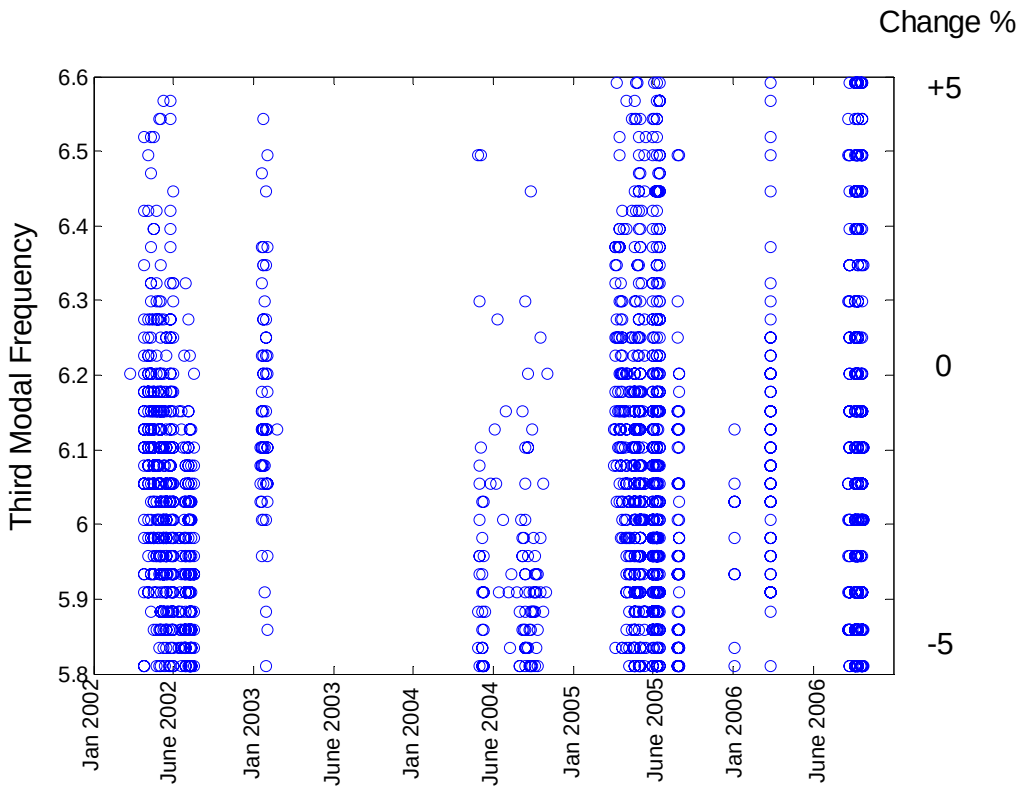

Figure 9.1.3 Third Modal Identification Results

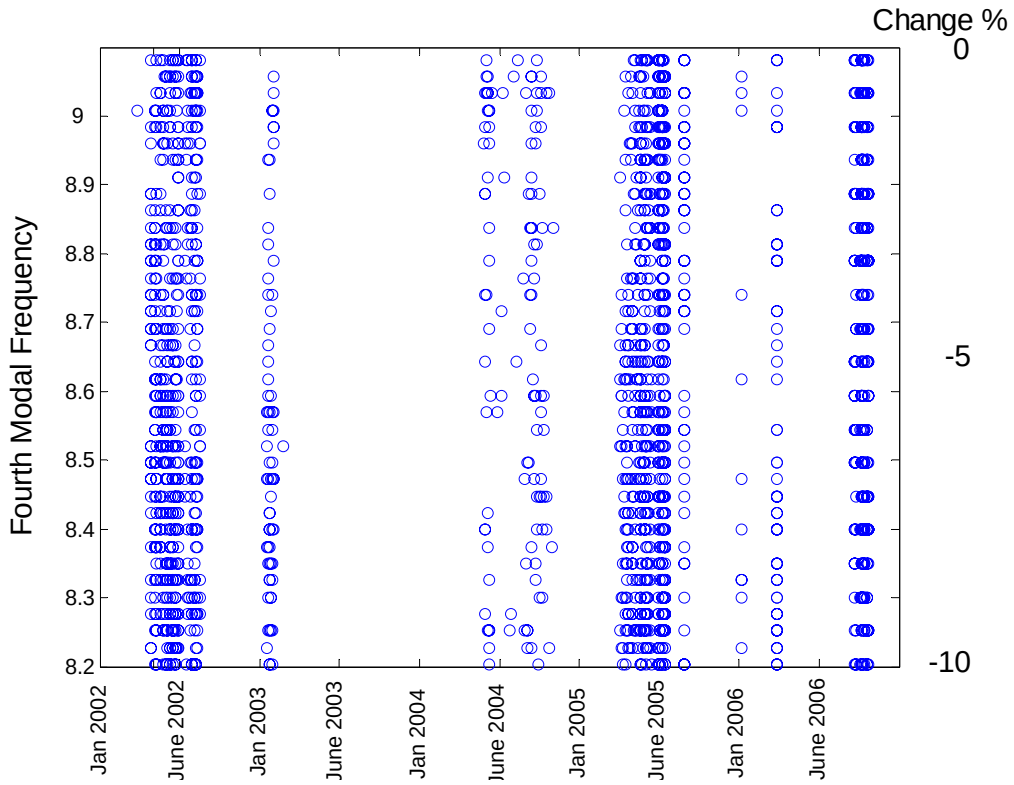

Figure 9.1.4 Fourth Modal Identification Results

9.1.2 WSO

Controlled Vibration Test

As described earlier, a controlled vibration test was performed using a fully loaded water truck in 2001 before the bridge opened to traffic. The test included braking (suddenly applying brake) and bumping (driving over a block) test. Table 9.1.1 shows the identified modal frequencies from the vibration response data collected at the braking and bumping tests, together with those computed from the finite element analytical model. It is noted that the modal frequencies identified from the bumping test are lower than those from the braking test. This is because the bumping test caused more intense vibration to the bridge than the braking test.

Table 9.1.1 Modal frequencies from controlled vibration test (Hz)

Mode	FE	Braking vibration test	Bumping vibration test
1	2.12	2.15	2.10 (-2.33)
2	2.70	2.47	2.44 (-0.97)
3	2.72	-	-

Note: The values in the parentheses are the differences (%) between braking and bumping results

Ambient Vibration

During a two-year period of monitoring from January, 2004 through January, 2006, totally 92 traffic-induced vibration data sets were recorded from at WSO. The triggering threshold was set at 0.002g, in order to record the bridge responses to only heavy vehicles. Figure. 9.1.5 shows the distribution of the 92 data sets according to the triggered time, from which it is observed that most of the data sets were recorded between 4 A.M. and 8 A.M..

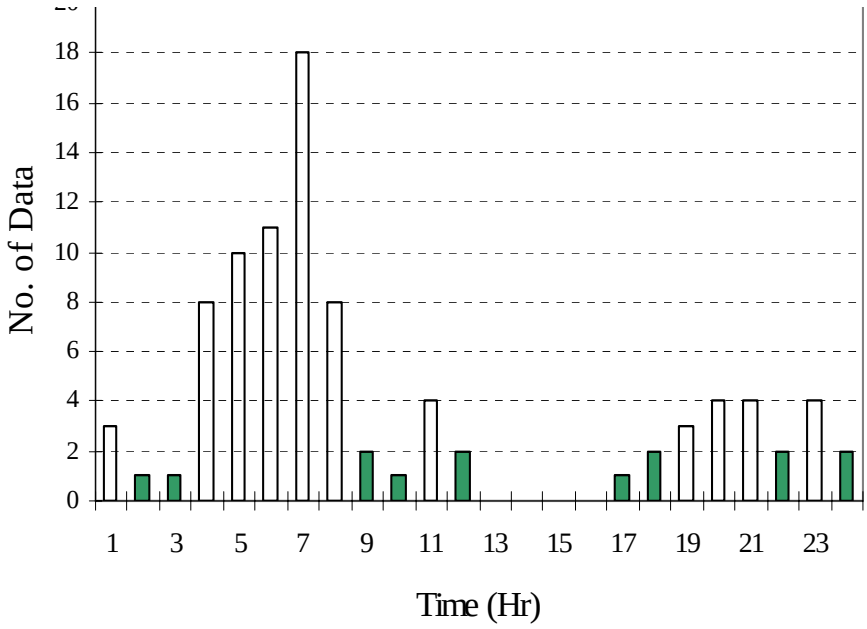

Figure 9.1.5 Distribution of Data Recording Time

Figure. 9.1.6 shows typical acceleration time histories under vehicle excitations. Figure. 9.1.6 (a) and (b) are the transverse accelerations at the middle of span 1 and 2, while (c) and (d) are the vertical accelerations at the same locations. It is observed from these figures that the magnitude of the vertical acceleration is higher than that of the transverse one under traffic excitations.

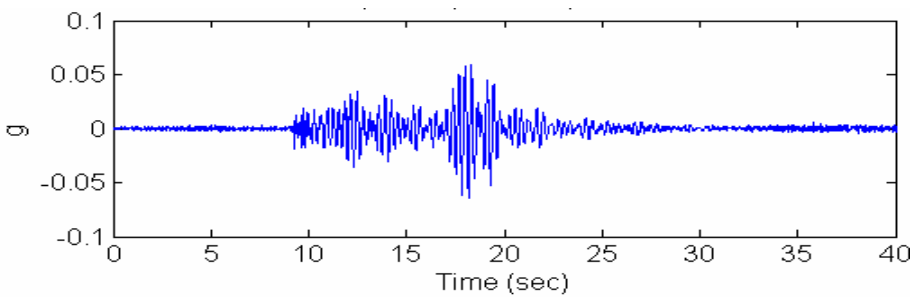

(a) Transverse (A2)

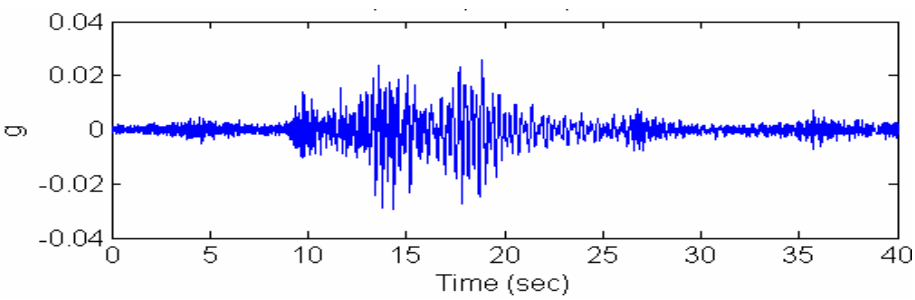

(b) Transverse (A9)

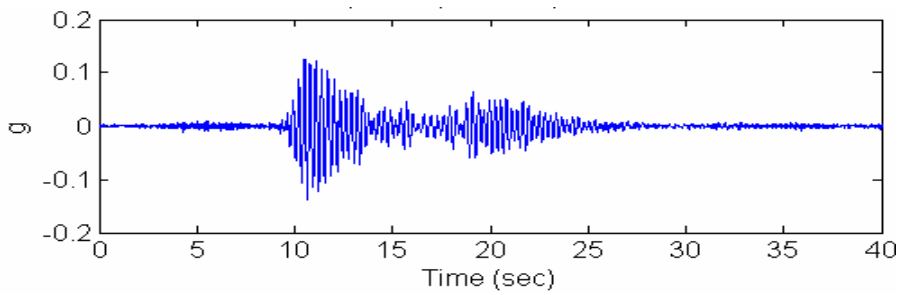

(c) Vertical (A3)

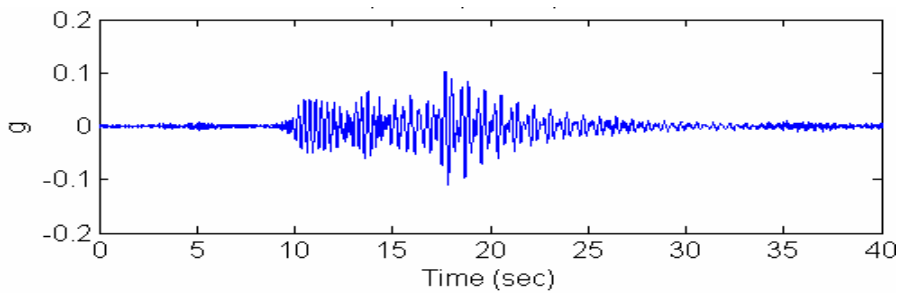

(d) Vertical (A10)

Figure 9.1.6 Typical Traffic-Induced Accelerations in Middle of Spans 1 and 2

From the ambient vibration data sets the mode frequencies were derived using the frequency domain decomposition (FDD) method. Table 9.1.2 shows the modal frequencies extracted from the recorded ambient vibration data. It is noted that the first or second mode frequency was not found from some of the data sets in the table. Even during the same day, for example, January 30, 2004, the first modal frequency was not found from the data recorded at 7:23 A.M., though it was identified from the other three data sets. Considering that the recorded data were under heavy vehicles, the lack of the first or second mode vibration can be attributed to the effect of the dynamic characteristics of the moving vehicles.

Table 9.1.2 Modal Frequencies Identified from Ambient Vibration Records

Mode	2004						2005			
	01/30				03/30		04/06	05/17	09/21	09/23
	6:40	6:43	7:23	7:33	4:03	4:27				
1 (Hz)	1.99 (-7.4)	1.99 (-7.4)	-	1.99 (-7.4)	-	-	1.94 (-9.7)	-	1.95 (-9.2)	1.90 (-11.5)
2 (Hz)	2.42 (-1.8)	2.42 (-1.8)	2.44 (-1.0)	2.42 (-1.8)	2.41 (-2.2)	2.41 (-2.2)	-	2.40 (-2.6)	2.40 (-2.6)	2.35 (-4.7)
3 (Hz)	2.79	2.83	2.81	2.83	2.77	-	2.81	2.74	2.79	2.72
4 (Hz)	3.49	3.48	3.45	3.43	3.47	3.49	-	-	-	3.44

Note: The values in the parentheses are the differences (%) between the ambient and 2001 braking test results

The numbers in parentheses in Table 9.1.2 indicate the differences between the frequencies identified from the ambient vibration data and those from the 2001 braking test. Compared with the 2001 braking test results in Table 9.1.1, the first and second mode frequencies were respectively reduced by 8.8% and 2.5%. However, the frequency reduction cannot be wholly attributed to the stiffness reduction of the bridge because the mode frequencies from ambient vibration are compared with the

results from braking test. The existence of the sound wall on the bridge is another reason. When the braking test was conducted in 2001, there was no sound wall on the bridge. From the finite element analysis the effect of the sound wall on the first three mode frequencies was found as nearly 5%. So the frequency reduction is 2-4% for the first mode.

Scattering of the identified modal frequencies over the two-year monitoring period is shown in Figure 9.1.7

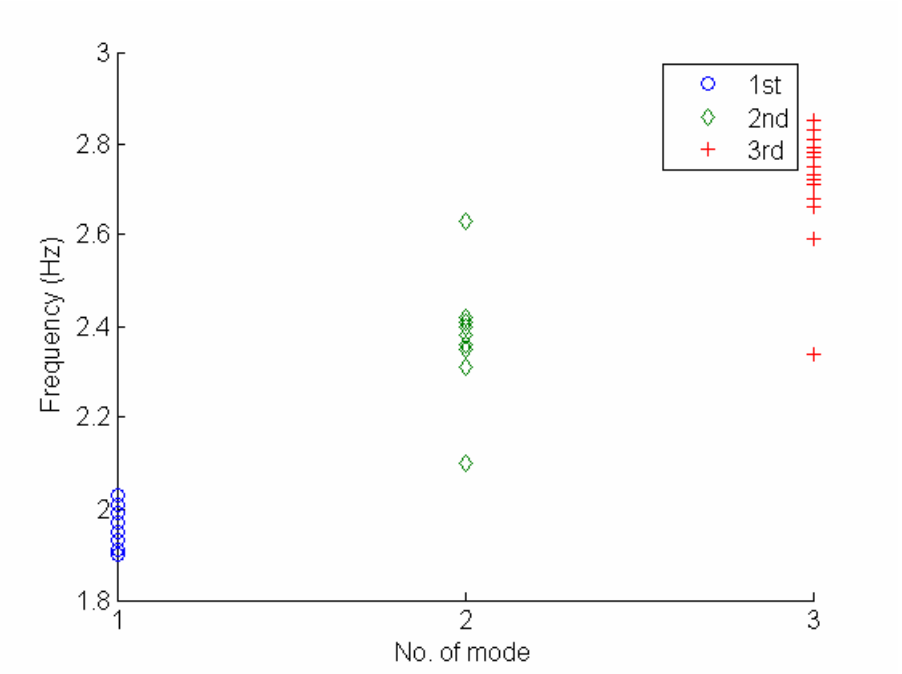

Figure 9.1.7 Mode Frequency Change at WSO

Earthquake Vibration

One earthquake was recorded during the two-year monitoring of the WSO. It was the Yucaipa earthquake on June 16, 2005 with a magnitude 4.9. The accelerations at the bottom of column 2, as shown in Figure 9.1.8, can be considered as the input ground motion to the bridge. The dominant ground motion component is in the transverse direction with a peak ground acceleration 0.173g.

Using the ground motion input and the superstructure response output, the frequency response function (FRF) can be obtained as

$$H(\omega) = \frac{X(\omega)}{F(\omega)} \tag{9-1}$$

where $X(\omega)$ = power spectral density function of the response acceleration at the superstructure; $F(\omega)$ = power spectral density function of the input motion.

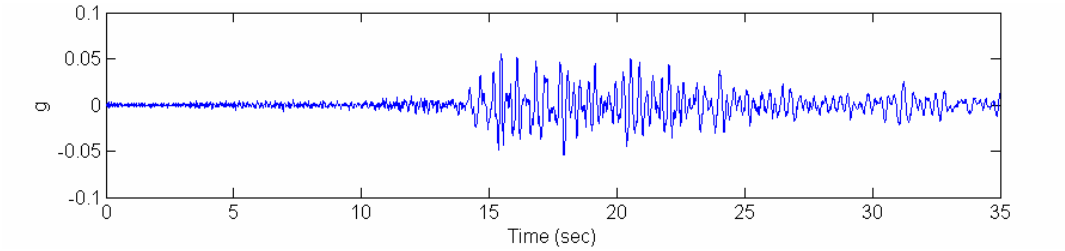

(a) Longitudinal direction (A6)

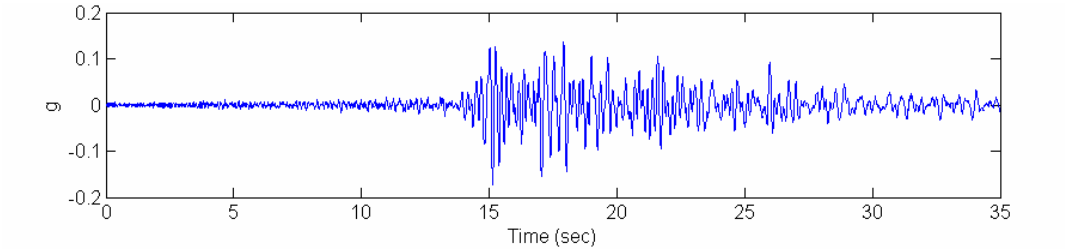

(b) Transverse direction (A7)

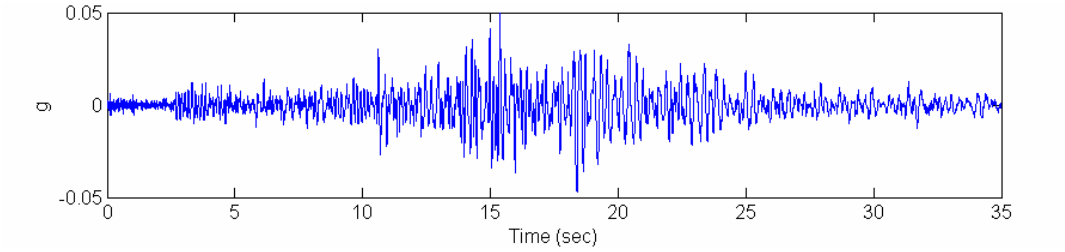

(c) Vertical direction (A8)

Figure 9.1.8 Ground Motion of the Yucaipa Earthquake

Figures 9.1.9 (a) and (b) plot FRF's when the transverse acceleration at the bottom of column 2 is used as the input motion and transverse accelerations at different locations of the superstructure as the output motion. The first three modal frequencies can be clearly identified and their values are shown in Table 9.1.3. The first and

second modal frequencies are 1.95 and 2.34 Hz respectively. The numbers in parentheses indicate the frequency reduction from the 2001 braking test results in Table 9.1.1. The first and second modal frequencies decreased by 9.1% and 4.9% respectively from the initial braking test results. The amount of reduction in the modal frequencies is very similar to those in Table 9.1.2 identified from the ambient vibration tests. During the earthquake, heavy vehicles were not found on the bridge from the strain monitoring records. Therefore, the identified modal frequencies are not affected by moving vehicles.

Table 9.1.3 Modal Frequencies Identified from the Yucaipa Earthquake

Mode	Transverse (Hz)	Vertical Dir (Hz)
1	1.95 (-9.1%)	1.95 (-9.1%)
2	2.10	2.10
3	2.34 (-4.9%)	2.34 (-4.9%)
4	2.54	2.54

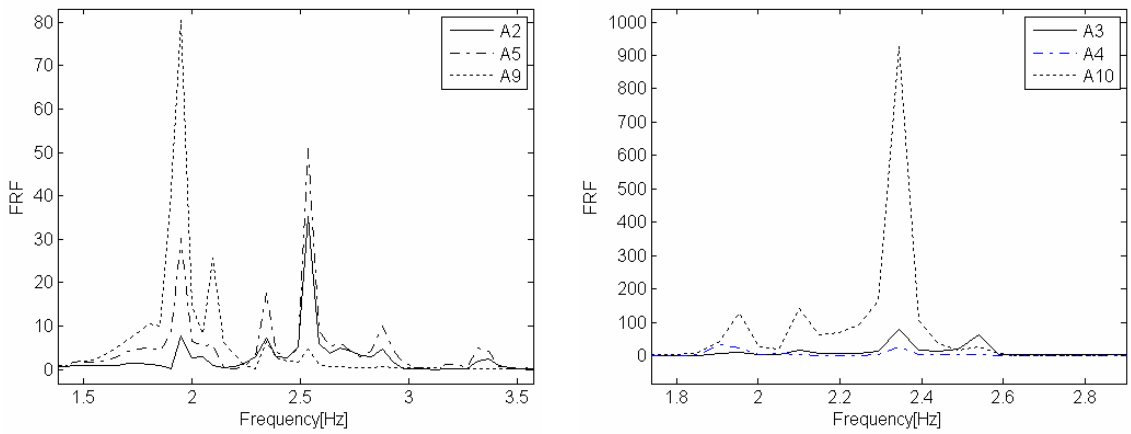

(a) Output motion- Transverse (b) Output motion-Vert. & long.

Figure 9.1.9 Frequency Response Functions of WSO under Earthquake

9.1.3 FROO

This subsection first develops a finite element (FE) model of the Fairview Rd. On-Ramp Over-crossing (FROO), and then identifies modal frequencies of the bridge based on measured ambient vibration data in comparison with the analytical ones.

9.1.3.1 Preliminary Finite Element Model

Finite element modeling

Finite element analysis of the FROO was carried out using the commercial structural analysis program Midas ver.6.3. The 3-dimensional beam element was used for the superstructure and columns. The superstructure component was modeled with a total of 80 beam elements and each column with 4 beam elements. Figure 9.1.10 shows the finite element model of the bridge.

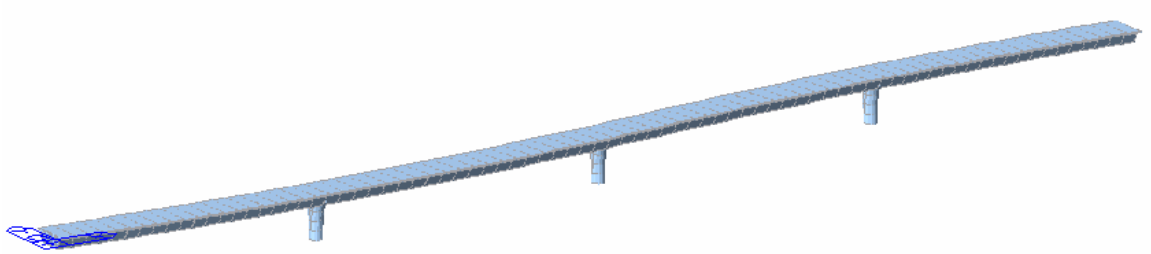

Figure 9.1.10 Finite Element Model of FROO

The boundary conditions of the columns were assumed as fixed, while the bearings at the abutments of the bridge were modeled as linear horizontal, vertical, and rotational springs. The bearing stiffness values at both ends of the deck were assigned as 6.58×10^4 kip/ft for the longitudinal springs, and 1.29×10^5 kip/ft and 1.48×10^5 kip/ft for the transverse and vertical springs respectively. The rotational spring stiffness is

6.29×10^7 kip-ft/rad in the longitudinal direction and 3.5×10^7 kip-ft/rad in the transverse direction.

Analytical Modal Frequencies and Shapes

The first three mode shapes are shown in Figure 9.1.11 and the mode frequencies of the bridges are shown in Table 3.3.1. The first six mode frequencies of the FROO are very closely spaced between 2 ~ 2.6 Hz. The first three vibration modes are vertical modes and the fourth mode is the first transverse mode.

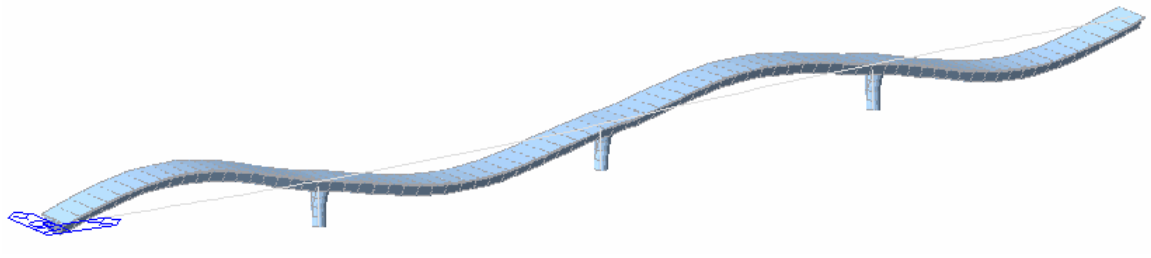

(a) The first mode shape (frequency : 2.085 Hz)

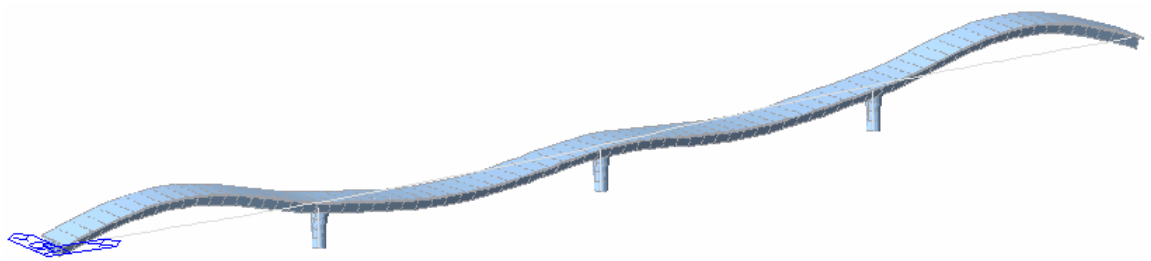

(b) The second mode shape (frequency : 2.168Hz)

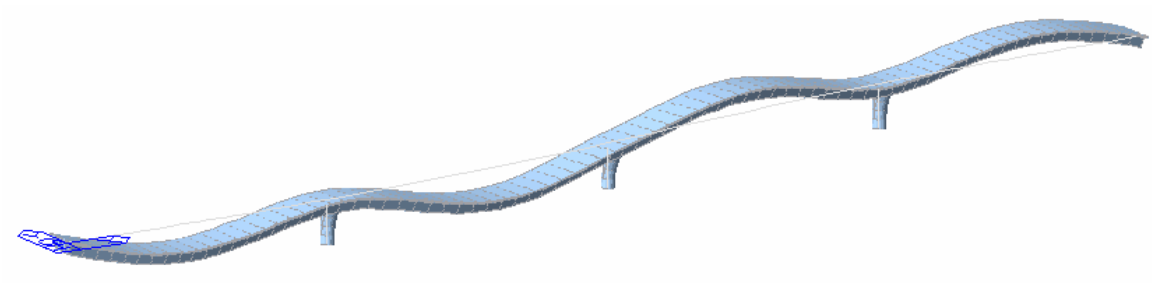

(c) The third mode shape (frequency : 2.348Hz)

Figure 9.1.11 Mode shapes of FROO

Table 9.1.4 Modal Frequencies of FROO

Mode	Period (sec)	Frequency (Hz)
1	0.479	2.085
2	0.461	2.168
3	0.426	2.348
4	0.404	2.473
5	0.382	2.618
6	0.375	2.665
7	0.320	3.126
8	0.306	3.270
9	0.203	4.925
10	0.183	5.453

9.1.3.2 Ambient Vibration Data and Modal Frequency Identification

Some traffic-induced ambient vibration data have been collected at FROO. Figure 9.1.12 shows typical acceleration time histories at the middle of span 2 under traffic excitations.

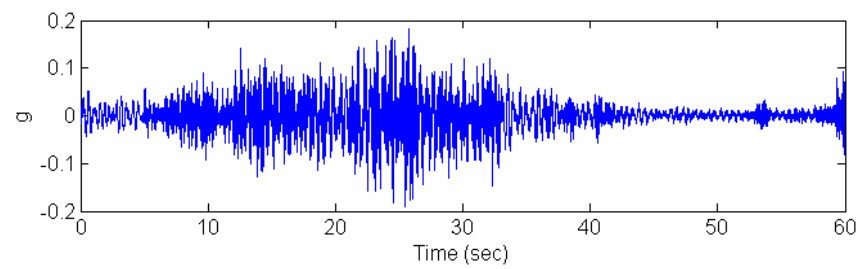

(a) Middle of span 2 (A5-vertical direction)

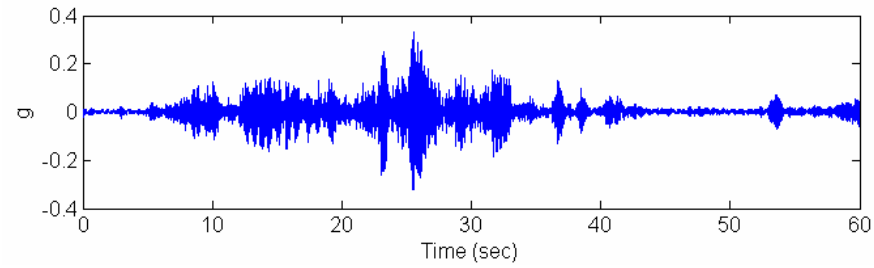

(b) Middle of span 2 (A5-transverse direction)

Figure 9.1.12 Typical Traffic-Induced Accelerations

From the ambient vibration data sets the mode frequencies were derived using the frequency domain decomposition method. Table 9.1.5 shows the modal frequencies extracted from the recorded ambient vibration on March 20, 2006. Small variations in the identified modal frequencies were observed in the table.

Table 9.1.5 Mode Frequencies Identified from Ambient Vibration Records

Mode	3:48 P.M.	3:52 P.M.	3:54 P.M.	3:56 P.M.	3:58 P.M.	4:05 P.M.	4:07 P.M.	4:09 P.M.
1 (Hz)	1.51	1.51	1.51	1.51	1.51	1.51	1.51	1.51
2 (Hz)	2.05	2.05	2.03	2.00	2.00	2.05	2.00	2.02
3 (Hz)	2.32	2.29	2.32	2.29	2.29	2.29	2.29	2.29

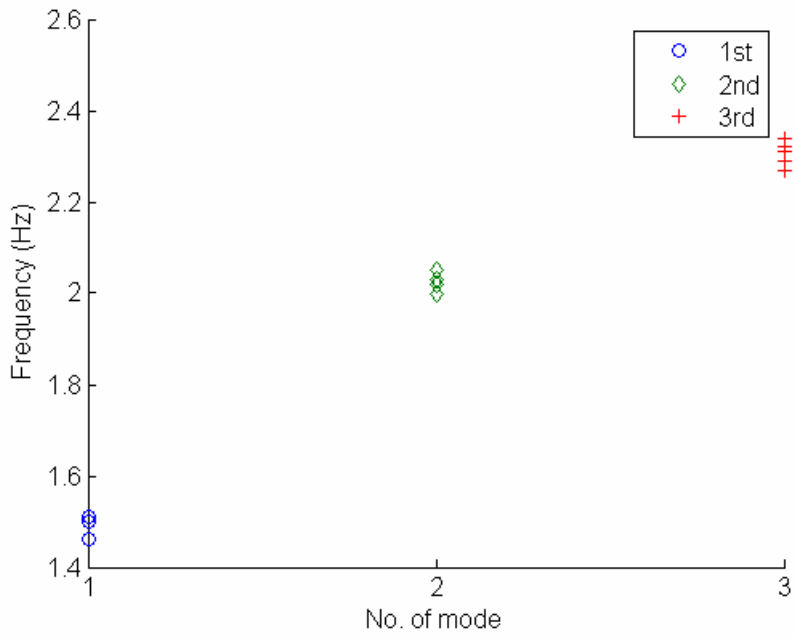

Figure 9.1.13 Mode Frequency Changes of the FROO

In order to obtain more accurate mode frequencies of the bridge, 10-minute acceleration data measured on March 20 were used for modal identification again. Figure. 9.1.14 shows the 10 minutes acceleration time histories. Figures 9.1.15 through 9.1.17 show the PSD's from the measured acceleration data. From the PSD of the vertical acceleration data, it was difficult to identify a peak around 1.5Hz. However, PSD from the transverse acceleration clearly shows a peak at 1.489Hz. From these results, the first three mode frequencies of the FROO were found to be 1.489 Hz, 2.026 Hz, and 2.295Hz.

From the FE analysis presented earlier, the first three modal frequencies were 2.085 Hz, 2.168 Hz, and 2.348 Hz. However the first modal frequency identified from the ambient vibration data is much lower than the computed one. The analytical model of the FROO is being updated to a baseline based on the measured vibration data.

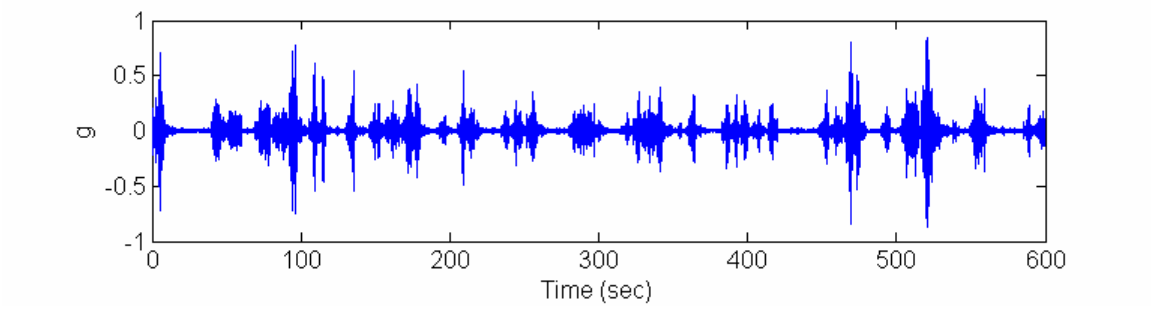

(a) A-5 (transverse direction)

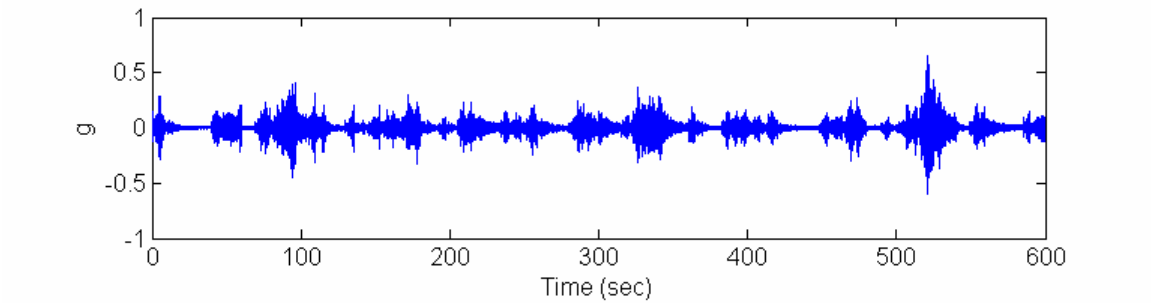

(b) A-5 (vertical direction)

Figure. 9.1.14 Acceleration Time History of the FROO

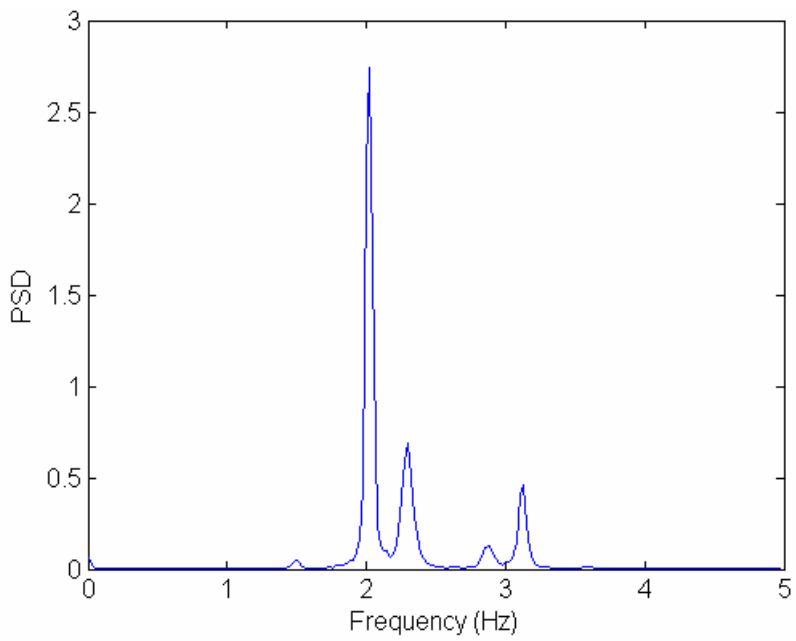

Figure 9.1.15 PSD from All Acceleration Channels

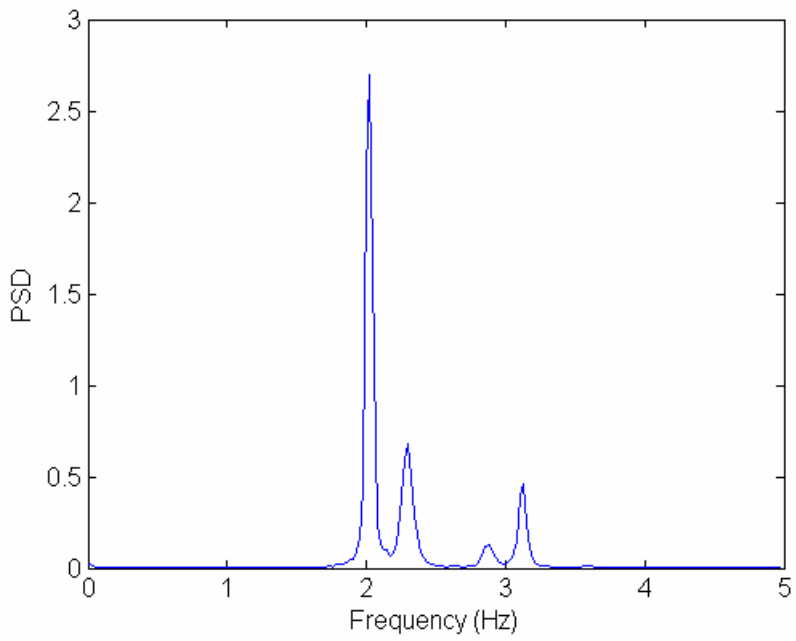

Figure 9.1.16 PSD from Vertical Acceleration Channels

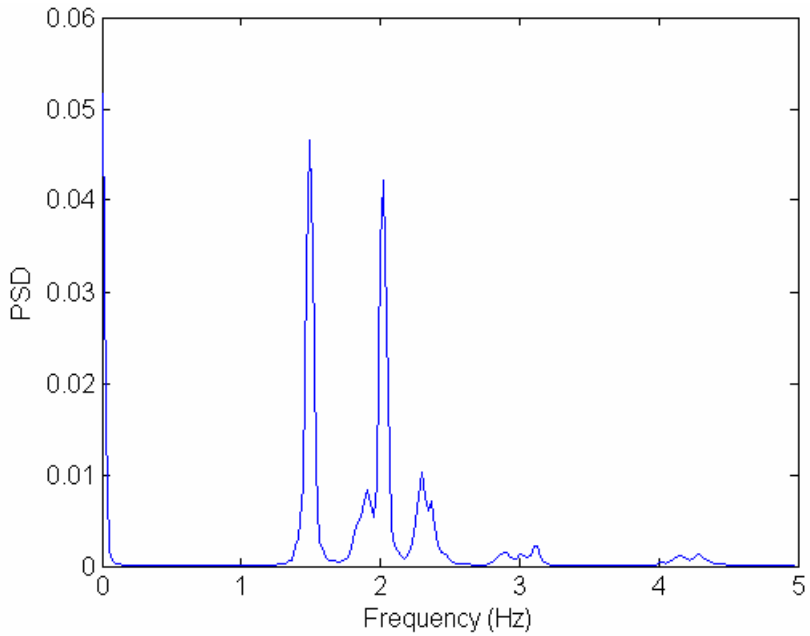

Figure 9.1.17 PSD from Transverse Acceleration Channels

9.2 Database for Structural Parameters

The back propagation neural network technique (e.g., Feng and Bahng 1999; Masri et al. 2000; Yun et al. 2001) was applied to obtain the elemental stiffness values based on the measured dynamic characteristics of the bridge. The neural network-based system identification method has several advantages compared with conventional system identification methods. The neural network approach is more capable of obtaining elemental stiffness values based on the partially and incompletely measured mode parameters due to the limited sensor number, and on only a few lower modes extractable from the vibration signals. Furthermore, it is very convenient to use the neural network to parameterize any properties of the structures, such as the effective shear area, as the unknowns to be identified. In contrast to many system identification methods in which the sensitivity matrix may become unstable especially for complex structural systems, the neural network approach does not require calculation of the sensitivity matrix, and thus can be applied to the complex civil engineering structures avoiding the numerical difficulty.

As shown in Figure. 9.2.1, the neural network consists of an input layer, hidden layers, and an output layer. The relationship between input and output of a neural network can be nonlinear or linear, and its characteristics are determined by the weights assigned to the connections between the neurons in two adjacent layers. Changing these weights will change the input/output relationship of the network. A systematic way of determining the weights of the network to achieve a desired input/output relationship is referred to as a training or learning algorithm. The standard back propagation algorithm was used in this study, for training the neural network to identify structural parameters (the stiffness and the mass matrices of the bridge, and the spring stiffness at the abutments) from measured natural frequencies and mode shapes. The procedure of the neural network-based identification involves the following steps: (1) determining the types of input and output patterns; (2) preparing

the training and testing patterns through FE analyses; (3) training the neural network using the back propagation algorithm; and finally (4) estimating the structural parameters of the baseline FE model by inputting the measured natural frequencies and mode shapes to the well trained neural network.

In the present study, the input pattern consists of the natural frequencies and the mode shapes. The output pattern consists of correction coefficients of structural parameters Training input–output data sets were obtained by extensive FE analyses with different sets of correction coefficients.

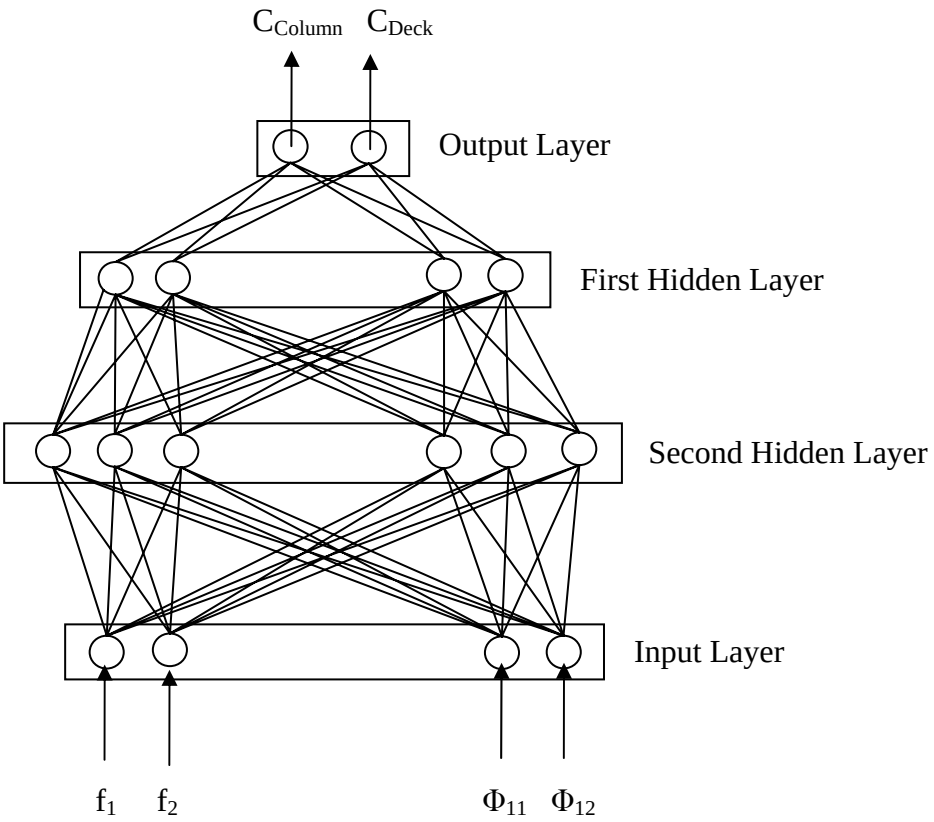

Figure 9.2.1 Architecture of the Neural Network

9.2.1 JRO

The first four modal frequencies and the first modal shape were taken as input, whereas the correction coefficients for the column and the superstructure as output for the neural networks. Training patterns were generated using the computer code SAP2000. Table 9.2.1 shows the moments of inertia of the column and the superstructure based on the design drawings. For training patterns, the values of the moment of inertia are varied from 0.2 to 1.2 times of ones based on the design drawings shown in Table 9.2.1. For each given moment of inertia values the corresponding frequencies are calculated using the program. The back propagation result was not satisfactory. For example, the identified stiffness correction coefficients might be as low as 0.1 of the original stiffness which has no physical insight. However, when the radial basis neural networks were employed, the identification results became quite meaningful.

Table 9.2.1 Moment of Inertia of JRO

Element	Area (m^2)	Moment of Inertia (m^4)	
		I_x	I_y
Deck	5.94	7.63	3.01
Column	3.53	2.51	0.72

Once the neural network is trained, it can be used to identify the stiffness correction coefficients based on the measured modal information. The identified results are shown in Figures 9.2.2 and 9.2.3. It is observed that the column stiffness identified based on measurement is 85% of the one obtained from the design drawings, whereas the superstructure stiffness was 95% of the designed value. In addition, there is a fluctuation in the identified stiffness; the column stiffness changes very little (less than 1%), while the superstructure stiffness fluctuates up to 6%. The change is considered due to the temperature variation. Further study incorporating temperature measurement is suggested.

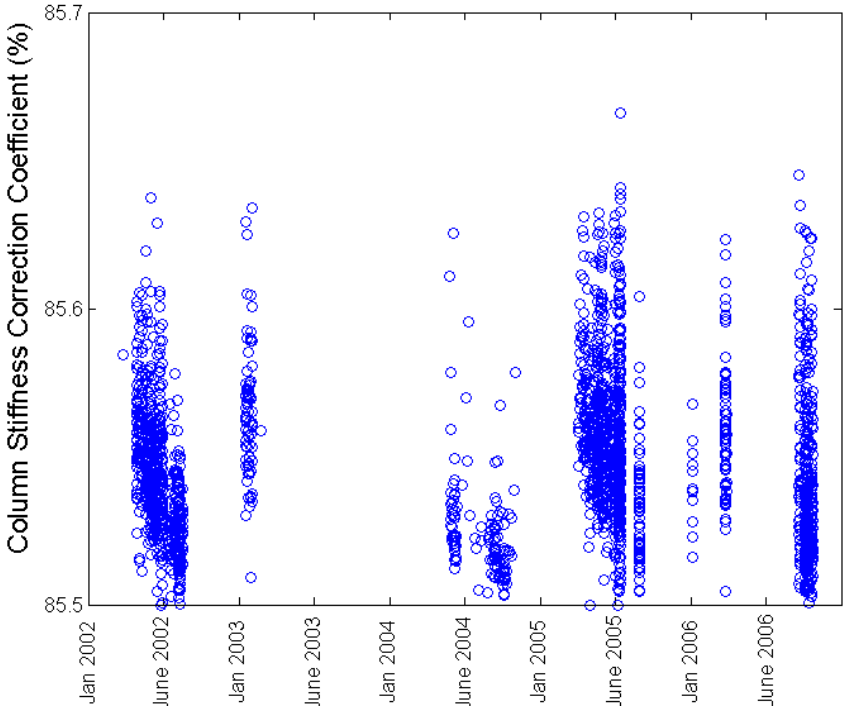

Figure 9.2.2 Long-Term Variation in Column Stiffness

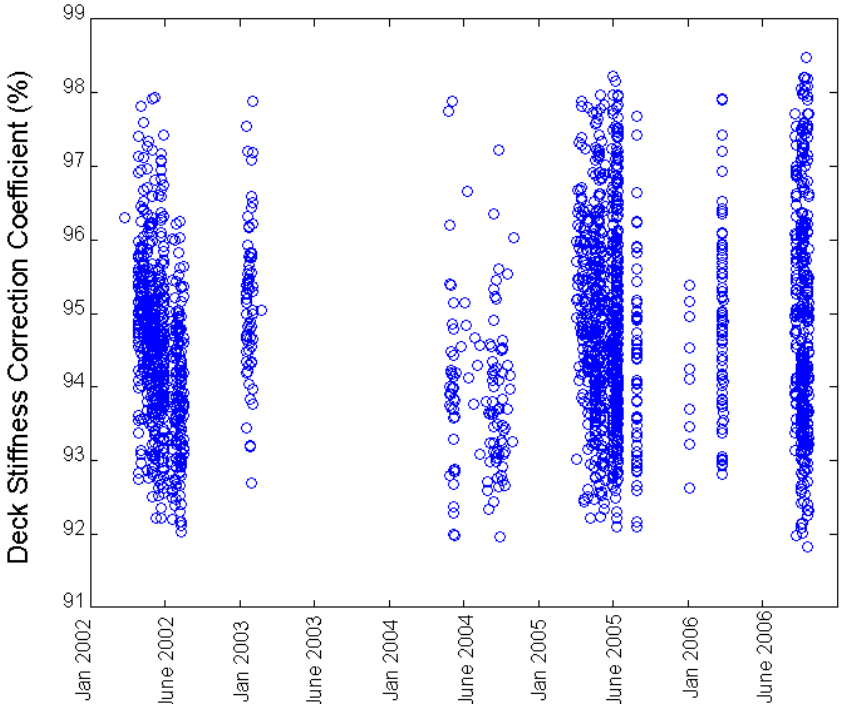

Figure 9.2.3 Long-term Variation in Superstructure Stiffness

9.2.2 WSO

Architecture of Neural Network

Though the input parameters for the neural network can be dynamic characteristics of a structure such as mode shapes, mode frequencies, mode damping, etc., the first three mode frequencies are chosen as the input parameters for the identification of the elemental stiffness of the WSO because of the limited number of the installed accelerometers at the bridge and insufficient information regarding the mode shape.

Since the flexural stiffness is the product of Young's modulus and the moment of inertia of a cross section, the moments of inertia of the column and the superstructure were chosen as the output of the neural network. More precisely, the output of the neural network includes two stiffness correction coefficients, one for superstructure and the other for the columns, and one stiffness correction coefficient of the soil springs at the bridge abutment.

The back-propagation neural network with two hidden layer is selected. Each hidden layer has 10 nodes i.e. neurons. Tangent sigmoid function and pure linear function were used as the transfer function for hidden layers and output layer, respectively.

Training Patterns

Training patterns were generated using the program "OpenSees". Table 9.2.2 shows the moment of inertia of the column and the superstructure from the design drawings and Table 9.2.3 shows the spring stiffness of the abutment boundary condition assumed based on the FHWA recommendation. In Table 9.2.3 the longitudinal and transverse directions of the bridge were assumed as X and Y axes respectively, while the vertical direction is Z axis. To generate the training patterns, the correction coefficients of both the superstructure and columns were varied from 0.7 to 1.0 and

0.5 to 0.9 for the soil springs. For each set of the correction coefficients, the corresponding modal frequencies of the bridge were calculated using "OpenSees". Table 9.2.4 shows the examples of training patterns for the WSO. Totally 4805 training sets were generated.

Table 9.2.2 Moment of Inertia of the Column and the Deck Component (ft^4)

Column		Deck	
I_y	I_z	I_y	I_z
$3.221x10^2$	$3.221x10^2$	$6.340x10^2$	$5.623x10^3$

Table 9.2.3 Spring Stiffness of Abutment Boundary Conditions

Direction	Stiffness (kip/ft)	Direction	Stiffness (kip·ft/rad)
Translation X	$6.586x10^4$	Rotation about X axis	$6.290x10^7$
Translation Y	$1.292x10^5$	Rotation about Y axis	0
Translation Z	$1.480x10^5$	Rotation about Z axis	$3.500x10^5$

Table 9.2.4 Training Patterns for the WSO

No	Input (Frequency)			Output (Correction coefficient)		
	1st	2nd	3rd	$C(I_{column})$	$C(I_{deck})$	C(B.C)
1	1.751	2.086	2.357	0.700	0.700	0.500
2	1.762	2.128	2.381	0.700	0.700	0.600
…	…	…	…	…	…	
4805	2.084	2.509	2.819	1.000	1.000	0.900

Verification of Trained Neural Network

A neural network model was built using "Matlab". To avoid the overfitting problem in neural networks, an early stopping method was employed. Table 9.2.5 shows the target output of the neural networks and the identified one.

Table 9.2.5 Verification of Trained Neural Network

No	Target			Identified from Neural Networks		
	$C(I_{column})$	$C(I_{deck})$	C(B.C)	$C(I_{column})$	$C(I_{deck})$	C(B.C)
1	0.700	0.700	0.500	0.679 (-0.030)	0.684 (-0.022)	0.493 (-0.014)
2	0.700	0.700	0.600	0.715 (0.021)	0.691 (-0.012)	0.569 (-0.051)
3	0.700	0.700	0.700	0.718 (0.025)	0.686 (-0.020)	0.673 (-0.038)
…	…	…	…	…	…	…

Note : The values in parenthesis are the difference between target and identified values

Identified Elemental Stiffness

The correction coefficients for 92 data sets were found by introducing the first three mode frequencies obtained from the data to trained neural network. Figure. 9.2.5 shows the extracted mode frequencies and Table 9.2.6 shows the results of the identified correction coefficients.

Table 9.2.6 Modal Frequencies Identified from Ambient Vibration Records

Date	Input (Hz)			Output		
	First	Second	Third	$C(I_{column})$	$C(I_{deck})$	C(B.C)
2004/ 01/30	1.99	2.42	2.79	0.897	0.946	1.150
2004/ 03/30	1.91	2.42	2.75	0.991	0.930	1.168
2004/ 10/21	1.99	2.38	2.77	0.825	0.937	1.112
2004/ 11/03	1.91	2.40	2.59	0.894	0.819	0.959
2004/ 12/16	1.97	2.40	2.71	0.825	0.938	1.070
2005/ 02/ 11	2.03	2.36	2.81	0.892	0.911	1.071
2005/ 03/ 17	1.99	2.41	2.83	1.009	0.850	1.202
2005/ 05/ 17	1.95	2.40	2.73	0.874	0.937	1.148
2005/ 08/ 02	1.93	2.38	2.73	0.903	0.921	1.160
2005/ 09/ 21	1.95	2.40	2.79	0.940	0.923	1.174
2005/ 09/ 23	1.90	2.35	2.72	0.932	0.876	1.180
2005/ 10/ 28	1.99	2.42	2.78	0.884	0.948	1.141
2005/ 11 /22	1.93	2.63	2.71	0.960	0.934	1.153
2005/ 12/ 23	1.97	2.35	2.75	0.796	0.927	1.114
2006/ 01/ 14	1.99	2.42	2.81	0.930	0.933	1.166
2006/ 02/ 03	1.95	2.38	2.77	0.899	0.921	1.168
2006/ 03/ 13	1.99	2.42	2.85	1.158	0.681	1.265
2006/ 03/ 24	1.97	2.42	2.83	1.008	0.873	1.195
2006/ 05/ 08	1.97	2.40	2.75	0.858	0.940	1.138
2006/ 06/ 08	1.97	2.36	2.71	0.771	0.935	1.018
2006/ 09/ 08*	1.90	2.31	2.68	0.812	0.872	1.148
2006/ 09/ 08**	2.01	2.36	2.66	0.988	0.904	0.462
Average	1.96	2.39	2.75	0.911	0.903	1.107

*: Field test -braking test, ** : Field test - bumping test

The average correction coefficient values were found to be 0.911 for the columns, 0.903 for the superstructure, and 1.107 for soil springs. So the stiffness values of the superstructure and columns are 10% lower than the designed ones. Table 9.2.7 and 9.2.8 show the updated values of the moment of inertia and the spring stiffness of the abutment boundary condition.

Table 9.2.7 Updated Moment of Inertia of Column and Deck

Column (ft^4)		Deck (ft^4)	
I_y	I_z	I_y	I_z
$2.934x10^2$	$2.934x10^2$	$5.725x10^2$	$5.078x10^3$

Table 9.2.8 Updated Spring Stiffness of Abutment Boundary Conditions

Direction	Stiffness (kip/ft)	Direction	Stiffness (kip·ft/rad)
Translation X	$7.29x10^4$	Rotation about X axis	$6.96x10^7$
Translation Y	$1.43x10^5$	Rotation about Y axis	0
Translation Z	$1.64x10^5$	Rotation about Z axis	$3.87x10^5$

9.3 Summary and Design Recommendations

In this chapter, vibration measurement data for the instrumented bridges were presented and analyzed. By means of the neural network-based identification method, structural stiffness values were identified based on the measured modal frequencies and shapes. For JRO, the identified bridge superstructure stiffness was 5% and the column stiffness was 15% lower than the design values. For WSO, the identified stiffness was 10% lower for the superstructure as well as for the column.

From the data collected at JRO over a period of four years, +/- 10% fluctuation in the identified modal frequencies were observed. However, the column stiffness had little fluctuation while the superstructure stiffness fluctuated up to 6% over the four-year observation period. Similar findings were examined for the other two bridges. The identified stiffness values also agreed well with those obtained by using the different identification methods presented in Chapter 6. The fluctuation in the identified stiffness is considered due to change in environmental conditions such as temperature. Further study is suggested by incorporating temperature measurement.

Chapter 10

DEVELOPMENT OF SOFTWARE

This chapter presents a software package developed in this project for identifying structural stiffness based on vibration measurement. The software has a number of functions including data acquisition, modal parameter identification and animation, and more importantly, structural stiffness identification, and database operation. With this software, data from an instrumented bridge can be processed, bridge stiffness identified and stored into a database.

10.1 List of Software Modules

As illustrated in Figure 10.1.1, major functions of the software include

(1) vibration data acquisition and time-history display,
Binary data are acquired and converts to ascii format for storage.

(2) extraction of modal parameters using the frequency domain decomposition (FDD) method, display of modal frequencies and mode shapes, update a modal parameter database

(3) identification of structural elemental stiffness, and

(4) stiffness evaluation in comparison with those in the database, and update of database

For the demonstration purpose, the neural network-based identification method is incorporated into the current version of the software. Other methods developed in this project as described in Chapter 6 can be incorporated into this software.

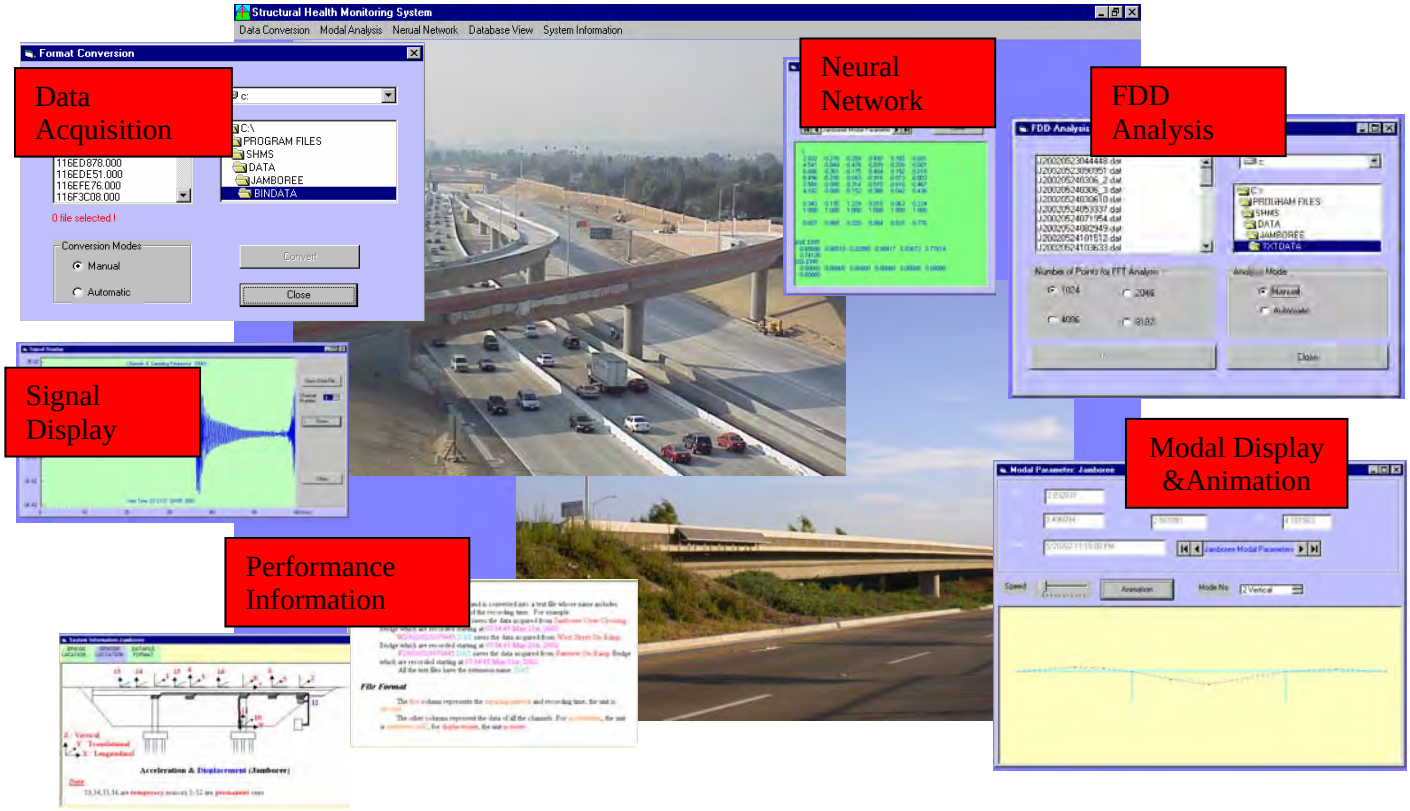

Figure 10.1.1 Major Functions of the Software

In the software package there are three files that are related with the end user:

1. SHMS.exe
2. Folder “Data”
3. Folder “Database”

SHMS.exe

This is the executable file for the software. When it is run the first window will appear as shown in Figure 10.1.2. One can choose a bridge to analyze from the pre-stored drop-down menu.

Figure 10.1.2 Bridge Selection Window

Upon selecting the bridge, the second window will appear as shown in Figure 10.1.3. This is the main interface for the software.

Figure 10.1.3 Main Interface for the Software

The modules of the software are listed as follows:

1. Bridge File
    i. Open Bridge File
    ii. Exit SHM
2. Data Conversion
    i. Convert Format
    ii. Display Signal

3. Modal Analysis
    i. Combine Files
    ii. FDD Analysis
4. Neural Network
    i. Testing
5. Database View
    i. Modal Parameters
    ii. Elemental Stiffness Values
6. Bridge Info
    i. Location Map
    ii. Sensor Configuration
    iii. File Naming Rules

Data Folder

In this folder one can find subfolders. Each has the name of the bridge. Each of them has the information listed below:

(1) Bindata: The raw data obtained from the data logger of the bridge are stored in this folder.

(2) Txtdata: The software converts the binary data to text data save under this folder.

(3) Picture: The pictures representing the bridge should be stored in this folder. They will be used in the software when called.

(4) FDD Control: This text file can be changed depending on the bridge. This file is used for the identification of modal parameters using the frequency domain decomposition method.

(5) Sys: This text file includes the type of sensors e.g. accelerometers, displacement sensors.

(6) Geometry: This text file includes the information of the geometry of the bridge. It is used for the animation purpose.

10.2 Description of Usage of Modules

The instructions for using the modules listed in the previous section are given below:

1.i. Open Bridge File: This module allows user to switch between different bridges and the associated window is shown in Figure10.1.2.

1.ii. Exit SHM: This is to exit the program

2.i. Convert Format: This module allows user to convert binary data to txt data. As shown in Figure 10.2.1, the folder where the binary data are saved can be chosen. After selecting the data, one shall click the "convert" button. There is an option of selecting more than one data files. There are two options for the data conversion: manual and automatic. The latter can be used when more than one file is chosen. All the converted data files are saved in the TXTDATA folder.

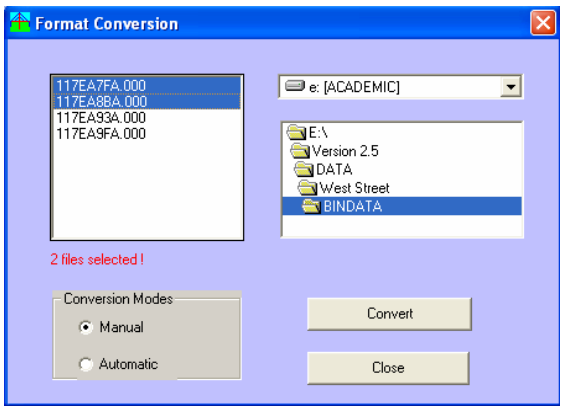

Figure 10.2.1 Data Format Conversion Window

2.ii. Display Signal: This module allows user to see the measurement data. By clicking the "Open Data File" button, one can select a data set from the TXTDATA folder. Furthermore, Channel Number is to selected. By clicking the "Show" button, one can view the time history of the stored data, as demonstrated in Figure 10.2.2.

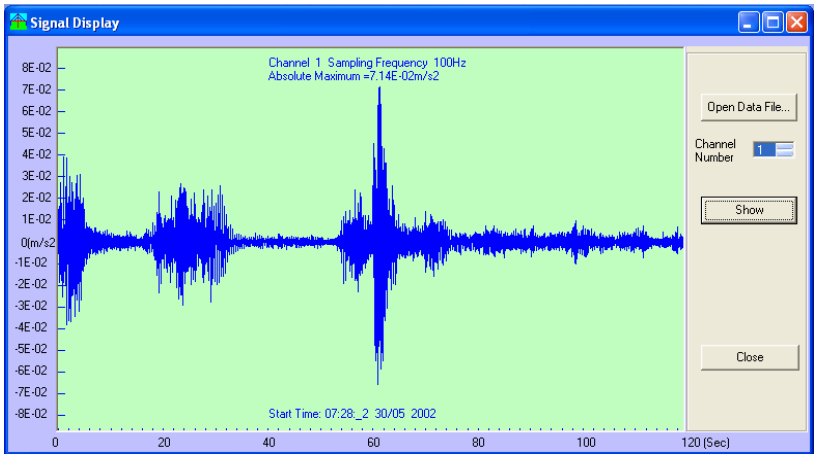

Figure 10.2.2 Time History Display Window

3.i. Combine Files: Several files collected from the bridge can be connected one after another to obtain a longer data file. As shown in Figure 10.2.3 several data can be selected and then click the "Combine" button to save the combined file as a new data file.

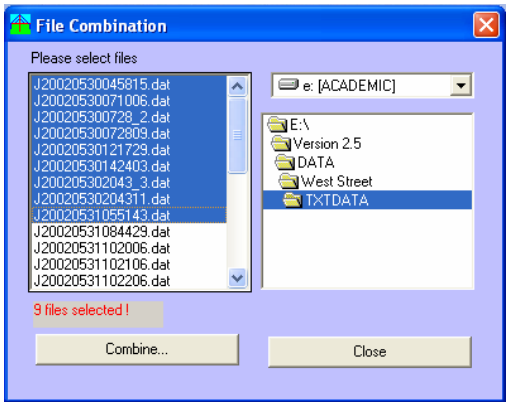

Figure 10.2.3 Data Combination Window

3.ii. FDD Analysis: In this module the FDD analysis can be performed manually by selecting a particular data file to analyze or automatically by analyzing all the data files in the folder. One can choose the number of data points for FFT analysis, as shown in Figure 10.2.4.

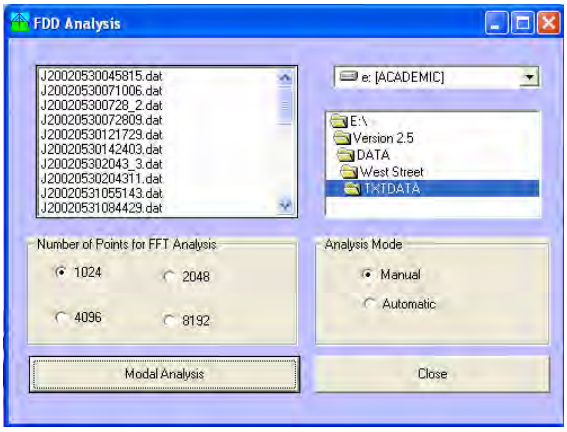

Figure 10.2.4 FDD Analysis Window

4.i. Testing: In this module, stiffness correction coefficients of the bridge structure are identified based on the neural network method (presented in Chapter 6). The identified coefficient values are shown in Figure 10.2.5. The neural network in the software should be pre-trained to established mapping between the modal parameters and the stiffness correction coefficient.

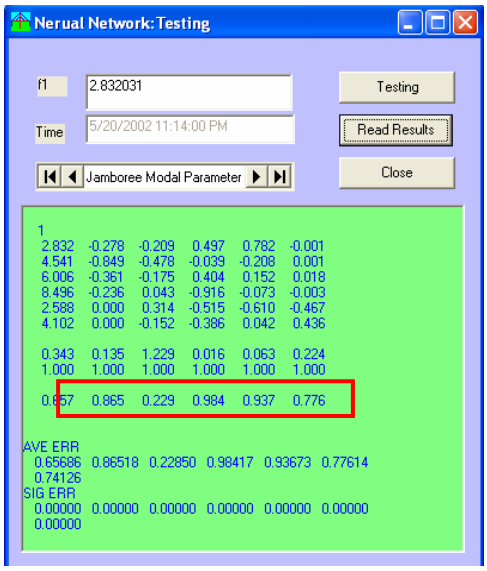

Figure 10.2.5 Neural Network Analysis Window

5.i. Modal Parameters: In this module the identified modal values can be animated. As shown in Figure 10.2.6 for the Jamboree Road Overcrossing, there are four vertical and two transverse modes. Different dates can be chosen using the arrows

next to “Jamboree Modal Parameters”. Different modes can be selected using the arrows next to “Mode No”.

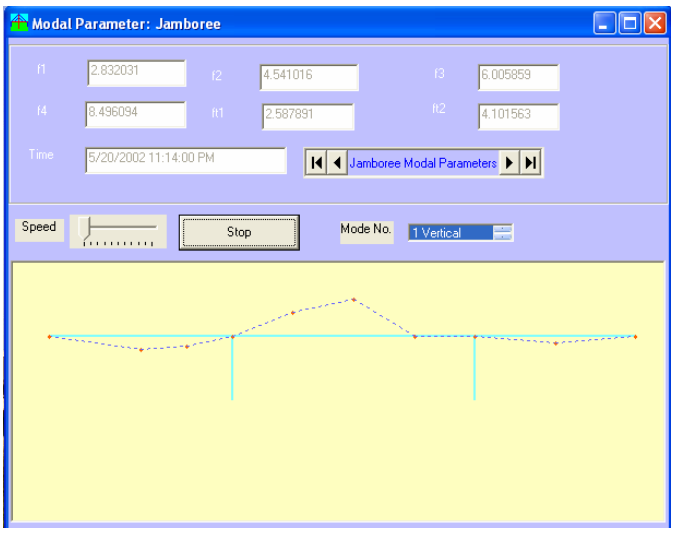

Figure 10.2.6 Animation Window

6.i. Location Map: Location of the bridge is stored under the bridge information. Figure 10.2.7 shows the location of the Jamboree Road Overcrossing as an example.

Figure 10.2.7 Location Map Window

6.ii. Sensor Configuration: Locations of the sensors are stored under the bridge information. Figure 10.2.8 shows the sensor locations at the Jamboree Road Overcrossing as an example.

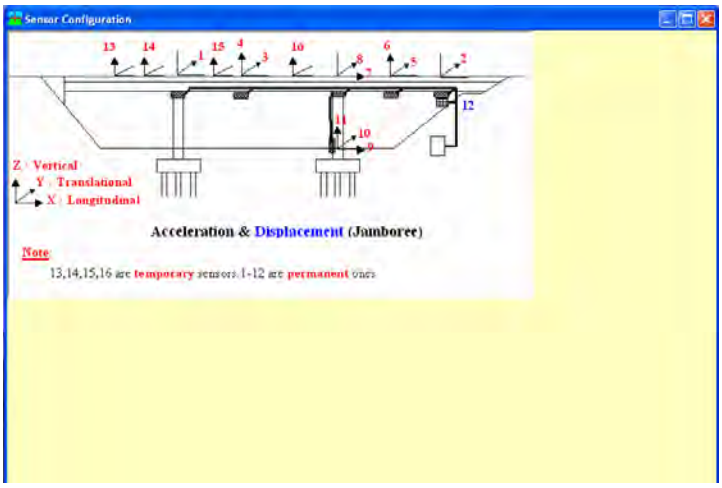

Figure 10.2.8 Sensor Configuration Window

6.iii. File Naming Rules: Format of the names for the data files is explained in Figure 10.2.9.

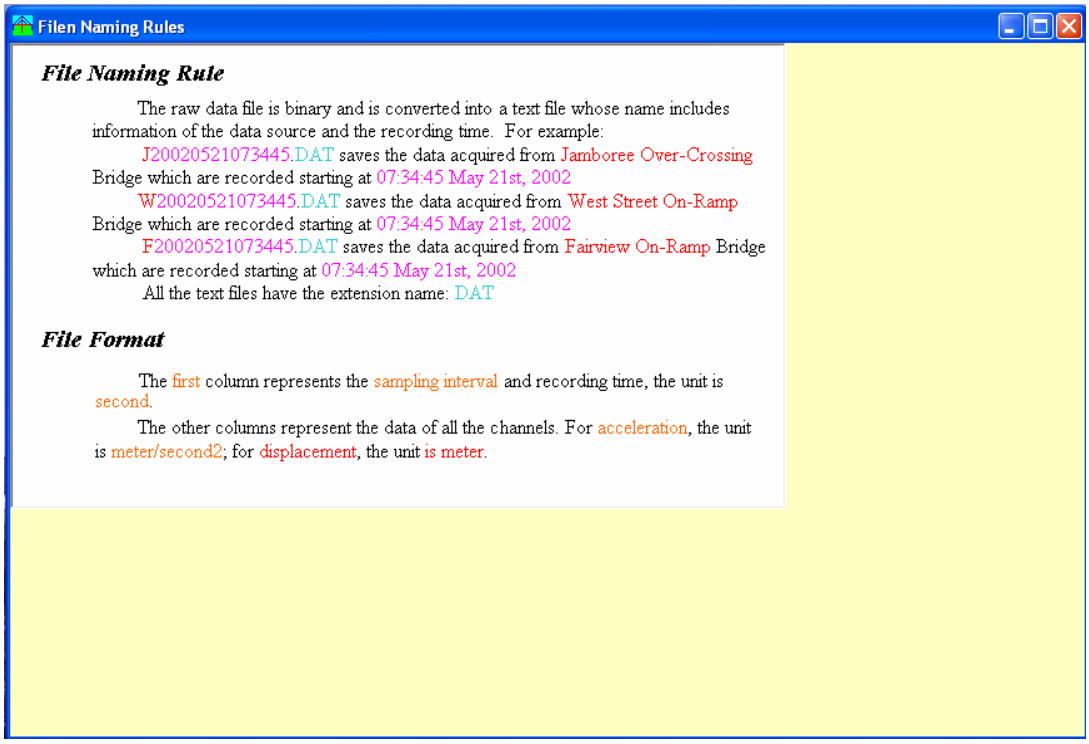

Figure 10.2.9 File Naming Window

Chapter 11

CONCLUSIONS AND RECOMMENDED FUTURE WORK

This project developed a number of methods for identifying element stiffness of bridge structures based on structural vibration measurement. These methods were validated by uniquely large-scale shaking table tests of realistic bridge models. Using these methods and a software package developed in this project, a stiffness baseline was established for each of the three highway bridges instrumented with accelerometer and strain sensor systems. In addition, database for the baseline was developed based on measurement of traffic- and earthquake-induced vibration data over the last few years.

11.1 Conclusions

The following conclusions can be made from this study:

1. Identification of changes in structural component stiffness based on measurement of traffic- and/or seismic-induced vibration can be a powerful tool for assessing global structural condition in an automatic, real-time, objective and quantitative manner. The use of element stiffness as the indicator of structural "health" condition enables not only quantification but also location of structural damage and deterioration.
2. It is proposed to use traffic excitations to identify bridge superstructure stiffness. For this purpose, a unique traffic excitation model was developed by incorporating video-based partial traffic monitoring information, which is more realistic than the conventional assumption of spatially-uncorrelated white noise. Bayesian updating and neural network methods were developed for identifying bridge structural element stiffness.
3. The identified stiffness at the bridge superstructure and substructure (columns) of the three instrumented new bridges are up to 15% lower than their design values. As a result, a stiffness baseline was updated from the design values for each of the bridges and it can be used for long-term monitoring.
4. Up to 6% fluctuations in the identified stiffness was observed for one of the bridges over a four-year period. This is considered due to change in environmental conditions such as temperature.
5. Static and dynamic loading tests were conducted on one of the bridges using water trucks. From the strain observation during the static load test, Up to 5% variations were observed in the identified modal frequencies between bumping and breaking tests. This is considered due to the change in bridge vibration amplitudes.

6. For detection and evaluation of seismic damage in bridge columns, it is proposed to use earthquake input and bridge response to identify change in column stiffness. In addition to the neural network method, an extended Kalman filter method was also developed in this project that can deal with nonlinear structural response and instantaneously identifying and quantifying change in column stiffness in real time during a damaging earthquake event.
7. The effectiveness of the seismic damage evaluation methods was verified by a large-scale shaking table tests of multi-bent, multi-span bridge models. Locations and extent of stiffness degradations in the bridge columns were successfully identified based only on the seismic (acceleration) responses of the bridge, as the bridge was progressively damaged to different extents by seismic excitations. The identified locations and extents of stiffness degradation were verified by the strain measurement and visual inspection. The shaking table tests conducted in this study represented the first effort in validating seismic damage evaluation methods using a realistic structural model subjected to realistic seismic damage

11.2 Recommended Future Work

This project has demonstrated the potential of using the sensor technology for long-term and real-time structural health monitoring and post-event damage detection. Meanwhile, this study also identified key issues, as listed below, that must be addressed before we can successfully implement the sensor and monitoring technology to majority of the Caltrans bridges for the purposes of structural maintenance and post-event damage assessment.

1. Methods must be developed to further translate the structural stiffness reduction identified based on vibration measurement into information regarding the remaining bridge load-carrying capacity.
2. The baseline updating methods based on vibration measurement and stiffness identification developed in this study can also be applied to existing old bridges (that represent the majority of the Caltrans inventory) in the following two ways; one is for establishing the current baseline of the bridge for its future damage detection and deterioration assessment, and the other is for assessing the ongoing "health" if a database of similar types of bridges exist for the comparison purposes. Obviously the later requires additional effort to monitor and study different types of bridges and establish a long-term database.
3. This study focused on concrete box-girder bridges that represent the majority of the Caltrans highway bridges. The applicability of the methods developed in this study to special long-span bridges, such as the Vincent Thomas Bridge, should be investigated in the future.

REFERENCES

Aktan E A, Farhey D N, Helmicki A J, Brown D L, Hunt V J, Lee K-L and Levi A (1997), "Structural Identification for Condition Assessment: Experimental Arts." Journal of Structural Engineering, Vol.123, No.12, pp.1674- 1684

Aktan E A, Catbas N F, Grimmelsman K A, and Tsikos C J (2000). "Issues in infrastructure health monitoring for management." Journal of Engineering Mechanics, Vol.126, No.7, pp.711-724.

Asmussen J. C. and Brincker R. (1996), "Estimation of Frequency Response Function by Random Decrement." Proceeding of 14th IMAC, Dearborn Michigan, pp. 246-252.

Beck J. L. (1989), "Statistical System Identification of Structures." Proceeding of 5th International Conference on Structural Safety and Reliability (Eds Ang A. H.-S., Shinozuka M. and Shuëller G. I.).

Beck J. L. and Au S.-K. (2002), "Bayesian Updating of Structural Models and Reliability Using Markov Chain Monte Carlo Simulation." Journal of Engineering Mechanics, Vol. 128, No. 4, pp. 380-391

Beck J. L. and Katafygiotis L. S. (1998), "Updating Models and Their Uncertianties I: Bayesian Statistical Framework." Journal of Engineering Mechanics, Vol. 124, No. 4, pp. 445-461.

Beck J. L. and Yuan K.-V.(2004), "Model Selection Using Response Measurements: Bayesian Probabilistic Approach." Journal of Engineering Mechanics, Vol. 30, No. 2, pp. 192-203

Bolton R., Stubbs N., Park S. and Choi S. (2001), "Documentation of Changes in Modal Properties of a Concrete Box-Girder Bridge Due to Environmental and Internal Conditions." Computer-Aided Civil and Infrastructure Engineering, Vol. 16, pp. 42-57.

Brincker R., Zhang L. and Andersen P. (2001), "Model Identification of Output-Only Systems Using Frequency Domain decomposition." Smart Materials and Structures, 10, pp. 441-445.

Caicedo J. M., Dyke S. J. and Johnson E. A. (2004), "Natural Excitation Technique and Eigensystem Realization Algorithm for Phase I of the IASC-ASCE Benchmark Problem: Simulated Data." Journal of Engineering Mechanics, Vol.130, No.1, pp. 49-60.

Catbas, N F and Aktan E A (2002), "Condition and Damage Assessment: Issues and Some Promising Indices." Journal of Structural Engineering, Vol.128, No.8, pp. 1026-1036.

Cebon D. (1999), Handbook of Vehicle-Road Interaction, Swets & Zeitlinger Publishers, Lisse, the Netherlands.

Chang P C and Liu S C (2003) “Recent Research in Nondestructive Evaluation of Civil Infrastructures.” Journal of Materials in Civil Engineering, Vol.15, No.3, pp. 298-304.

Chen, Y. B. and Feng, M.Q., (2003). “Technique to improve the empirical mode decomposition in the Hilbert-Huang transform”, *Journal of Earthquake Engineering and Engineering Vibration*, Vol. 2, No. 1, pp 75-86.

Deodatis G., Fijimoto Y., Ito S., Spencer J. and Itagaki H. (1992), “Non-periodic inspection by Bayesian method I.” Probability Engineering Mechanics, Vol.7, No.4, pp191-204.

Ito, S., Deodatis G., Fujimoto Y., Asada H. and Shinozuka, M. (1992), “Non-periodic inspection by Bayesian method II: Structures with elements subjected to different stress levels.” Probability Engineering Mechanics, Vol.7, No.4, pp205-215.

Doebling S. W., Farrar C. R., Prime M. B. and Shevitz D. W. (1996), “Damage Identification and Health Monitoring of Structural and Mechanical Systems from Changes in their Vibration Characteristics: A Literature Review.” Los Alamos National Laboratory Report, LA-13070-MS.

Federal Highway Administration (FWHA), (1995), “Recording and Coding Guide for the Structure Inventory and Appraisal of the Nation’s Bridges.” U.S. Dept. of Transportation, Washington, D.C.

Feng M. Q. and Kim J. M. (1998), “Identification of a Dynamic System Using Ambient Vibration Measurements.” ASME Journal of Applied Mechanics, Vol.65, No.2, pp. 1010-1023.

Feng M. Q. and Bahng EY. (1999), “Damage Assessment of Jacketed RC Columns Using Vibration Tests.” Journal of Structural Engineering, 125(3): 265-271.

Feng, M. Q. and Kim, D.K. (2001). “Long-Term Structural Performance Monitoring of Two Highway Bridges”, *Technical Report of the California Department of Transportation*

Feng M. Q., Kim D. K., Yi J-H and Chen Y. (2004), “Baseline Models for Bridge Performance Monitoring.” Journal of Engineering Mechanics, Vol.130, No.5, pp. 562-569.

Garibaldi L., Giorcelli E. and Piombo B. A. D. (1998), “ARMAV Techniques for Traffic Excited Bridges.” ASME Journal of Vibration and Acoustics, Vol.120, No.3, July, pp. 713-718.

Ghanem R, Ferro G. (2006), “Health Monitoring for Strongly Non-Linear Systems Using the Ensemble Kalman Filter.” Structural Control and Health Monitoring, in-press.

Ghanem R, Shinozuka M. (1995), “Structural System Identification I: Theory.” Journal of Engineering Mechanics, 121(2): 255-264.

Hera A. (2004), “Application of Wavelet Approach for ASCE Structural Health Monitoring Benchmark Studies.” Journal of Engineering Mechanics, Vol. 130, No. 1, pp. 96-104.

Hibbeler R. C. (2002), Structural Analysis, Prentice-Hall Inc., Upper Saddle River, NJ, USA.

Hoshiya S, and Saito E. (1984), “Structural Identification by Extended Kalman Filter.” Journal of Engineering Mechanics, 110(12): 1757-1770.

Huang C. S. (2001), “Structural identification from Ambient Vibration Measurement Using the Multivariate AR Model.” Journal of Sound and Vibration, Vol.241, No.3, pp. 337-359.

James III G. H., Garne T. G. and Mayes R. L. (1996), “Modal Parameter Extraction from Large Operating Structures Using Ambient Excitation.” Proceedings of the 14th IMAC, Dearborn Michigan, pp. 77-83.

Jenson J. L., Kirkegaard P. H. and Brincker R. (1992), “Modal and Wave Load Identification by ARMA Calibration.” Journal of Engineering Mechanics, Vol.118, No.6, pp. 1268-1273.

Kalman RE. (1960), “A New Approach to Linear Filtering and Prediction Problems.” Journal of Basic Engineering, 82(1), 35-45.

Kim J.T., Ryu Y.S., Cho H.M., Stubbs N., (2003) “Damage Identification in Beam-Type Structures: Frequenncy-Based Method vs Mode-Shape-Based Method”, Engineering Structures, 25, 57-67.

Koh C. G., Qiao G. Q. and Quek S. T. (2003), “Damage Identification of Structural Members: Numerical and Experimental Studies”, Structural Health Monitoring, Vol. 2, No. 1, pp. 41-55.

Lam H. F., Katafygiotis L. S. and Mickleborough N. D. (2004), “Application of a Statistical Model Updating Approach on Phase I of the IASE-ASCE Structural Health Monitoring Benchmark Study.” Journal of Engineering Mechanics, Vol. 130, No.1, pp. 34-48.

Loh CH, Chung ST. (1993), “A Three-Stage Identification Approach for Hysteretic Systems.” Earthquake Engineering and Structural Dynamics, 22: 129-150.

Loh CH, Tou IC. (1995), “A System Identification Approach to the Detection of Changes in Linear and Non-linear Structural Parameters.” Earthquake Engineering and Structural Dynamics, 24: 85-97.

Masri S., F., Smyth, A. W., Chassiakos, A. G., Caughey, T. K., and Hunter, N. F., (2000) ‘‘Application of neural networks for detection of changes in nonlinear systems”. Journal of Engineering Mechanics, Vol.126, No.7, pp.666-676.

National Bridge Inspection Standards (NBIS), (1996), Code of Federal Regulations, No. 23CFR650, U.S. Government Printing Office, Washington, D.C., 238–240.

Ou J. and Wang G. (1998), Random Vibration of Structures, (in Chinese), Higher Education Pub., Beijing, P.R. China

Pan T-C and Li J. (2002), “Dynamic Vehicle Element Method for Transient Response of Coupled Vehicle-Structure Systems.” Journal of Structural Engineering, Vol.128, No.2, pp. 214-223.

Papadimitriou C., Beck J. L. and Katafygiotis L. S. (2001), “Updataing Robust Reliability Using Structural Test Data.” Probabilistic Engineering Mechanics, 16, pp. 103-113.

Park S., Stubbs N., Sikorsky C., (1997) “Linkage of Nondestructive Damage Evaluatin to Structural System Reliablity”, Proceedings of Smart Structural and Material Symposium, SPIE, San Diego.

Park S., Stubbs N., Bolton R., Choi S., Sikorsky C., (2001) “Field Verification of the Damage Index Method in a Concrete Box-Girder Bridge via Visual Inspection”, Computer-Aided Civil and Infrastructure Engineering, 16, 58-70.

Parzen E. (1962), Stochastic Processes, Holden-Day Inc, San Francisco, USA.

Peeters B., Maeck J. and De Roeck G. (2001), “Vibration-Based Damage Detection in Civil Engineering: Excitation Sources and Temperature Effects.” Smart Materials and Structures, 10, pp. 518-527.

Pesterev A. V., Bergman L. A., and Tan C-A (2004), “A Novel Approach to the Calculation of Pothole-Induced Contact Forces in MDOF Vehicle Models.” Journal of Sound and Vibration, 275, August, pp. 127-149.

Pesterev A. V., Yang B., Tan C-A, and Bergman L. A. (2003) “Assessment of Pothole-Induced Tire Forces in a General Linear Vehicle Model.” Proceedings of the ASCE Engineering Mechanics Conference, Seattle, Washington, July.

Phares B M, Washer G A, Rolander D D, Graybeal B A and Moore M (2004), “Routine Highway Bridge Inspection Condition Documentation Accuracy and Reliability.” Journal of Bridge Engineering, Vol.9, No.4, pp. 403-413

Rytter A. (1993), “Vibration Based Inspection of Civil Engineering Structures.” PhD dissertation, University of Aalborg, Denmark

Safak E. (1991), “Identification of Linear Structures Using Discrete-Time Filters.” Journal of Structural Engineering, 17(10): 3064-3085.

Safak E. (1989), “Adaptive Modeling, Identification and Control of Dynamic Structural Systems. I: Theory.” Journal of Engineering Mechanics 1989; 115(11): 2386-2405.

Schenk C. A. and Bergman L. A. (2003), “Response of Continuous System with Stochastically Varying Surface Roughness to Moving Load.” Journal of Engineering Mechanics, Vol.129, No.7, pp. 759-768.

Sohn H., Farrar C. R., Hemez F. M., Shunk D. D., Stinemates D. W. and Nadler B. R. (2003), “A Review of Structural Health Monitoring Literature: 1996-2001.” Los Alamos National Laboratory Report, LA-13976-MS

Shen F., Zheng M., Feng D. and Xu F. (2003), “Using the Cross-Correlation Technique to Extract Modal parameters on Response-only Data.” Journal of Sound and Vibration, Vol.259, No.5, pp. 1163-1179.

Shinozuka M. and Kobori T. (1972), “Fatigue Analysis of Highway Bridges.” Proceedings of the Journal of Structural and Civil Engineering, 208, December, pp. 137-148.

Sikorsky, C. (2005), “A Strategy to Implement Structural Health Monitoring on Bridges.” Sensing Issues in Civil Structural Health Monitoring, Springer, Dordrecht, The Netherlands, pp.43-53, Farhad Ansari (Ed.).

Straser EG, Kiremidjian AS. (1996), “Monitoring and Evaluating Civil Structures Using Measured Vibration.” Proceedings of 14th International Modal Analysis Conference, pp. 84–90.

Stubs, N., Park, S., and Sikorsky, C. (2000), “A global Non-Destructive Damage Assessment Methodology for Civil Engineering Structures.” International Journal of Systems Science, Vol. 31 (11), pp. 1361-1372.

Turner J. D. and Pretlove A. J. (1988), “A Study of the Spectrum of Traffic-Induced Bridge Vibration.” Journal of Sound and Vibration, Vol.122, No.1, pp. 31-42.

Udwadia FE, Sharma DK, Shah PC. (1988), “Uniqueness of Damping and Stiffness Distributions in the Identification of Soil and Structural Systems.” Journal of Applied Mechanics, 45: 181-187.

Vanik M. W., Beck J. L. and Au S. K. (2000), “Bayesian Probabilistic Approach to Structural Health Monitoring.” Journal of Engineering Mechanics, Vol. 126, No. 7, pp. 738–745.

Yang B., Tan C-A and Bergman L. A. (2000), “Direct Numerical Procedure for Solution of Moving Oscillator Problems.” Journal of Engineering Mechanics, Vol.126, No.5, pp. 462-469.

Yang J. N. and Lin S. (2005), “Identification of Parameter Variations of Structures Based on Least Squares Estimation and Adaptive Tracking Technique.” Journal of Engineering Mechanics, Vol. 131, No. 3, pp. 290-298.

Yang JN, Lin S, Huang H, Zhou L. (2005), “An Adaptive Extended Kalman Filter for Structural Damage Identification.” Structural Control and Health Monitoring, in-press.

Yuen K.-V. and Beck J. L. (2003), “Updating Properties of Nonlinear Dynamical Systems with Uncertain Input.” Journal of Engineering Mechanics, Vol. 129, No. 1, pp. 9-20

Yuan K.-V., Beck J. L. and Au S. K. (2004), “Structural Damage Detection and Assessment by Adaptive Markov Chain Monte Carlo Simulation.” Structural Control and Health Monitoring, 11, pp. 327-347.

Yuen K.-V., Beck J. L. and Katafygiotis L. S.(2002), “Probabilistic Approach for Modal Identification Using Non-Stationary Noisy Response Measurement Only.” Earthquake Engineering and Structural Dynamics, 31, pp. 1007-1023.

Yun CB, Shinozuka M. (1980), “Identification of Nonlinear Structural Dynamic Systems.” Journal of Structural Mechanics, 8: 187-203.

Yun, C. B., Yi, J. H., and Bahng, E. Y. (2001). ‘‘Joint damage assessment of framed structures using a neural networks technique.’’ Engineering Structures, 23(5), 425-435.